Dynamic reservoir characterization from overburden time-lapse strains

Alejandro García Azuero

Submitted for the degree of Doctor of Philosophy

Heriot-Watt University
Institute of Petroleum Engineering
December, 2011

The copyright in this thesis is owned by the author. Any quotation from the thesis or use of any of the information contained in it must acknowledge this thesis as the source of the quotation or information.

Abstract

Accurate reservoir depletion or pressure change patterns are of great value when planning infill drilling programs for field development, as well as when monitoring injection wells and swept/unswept areas. In addition, a precise dynamic geomechanical description of the reservoir and overburden stress state could prevent costly undesired effects on the production infrastructure such as sea floor subsidence, casing shear and well failure. Dynamic characterization of reservoirs, until recently, had only well data to rely on, which apart from the inherent uncertainties (e.g. due to formation damage), provides no direct information on what is taking place between the wells. The advent of time-lapse seismic at the end of the 1990s meant that this gap could be bridged, providing measurements of the changes taking place in the subsurface.

In its origins, time-lapse seismic was conceived as a tool to image intra-reservoir fluid movements via the dependency of reflection amplitudes on acoustic impedance, which is affected by fluid saturation changes in the porous reservoir rocks. However, depletion induced velocity changes are also non negligible. Furthermore, the reflectors may undergo deformation and displacement where compaction and subsidence are involved. As a consequence, analysis of amplitude changes is not straightforward, since in most cases, amplitudes have been shifted by a non negligible time difference or time-shift, presenting not only challenges, but also new possibilities. It is in the possibilities of these time-shifts that the present study is based.

This research presents a novel method which numerically solves the static field problem in a multilayered heterogeneous media, relating overburden strain to reservoir depletion. It builds up on previous works based on Geertsma type solutions requiring a homogeneous half-space. This technique makes it possible to estimate the reservoir's stress state, strain and pressure changes from measured overburden strain by considering the earth as a linear filter with reservoir compaction and overburden strain as parameters. However, some a priori knowledge is needed in the form of a rough subsurface model and a preliminary geomechanics simulation in order to approximate the transfer functions as Wiener filters.

In this thesis, the Wiener filter concept has been applied to three real North Sea fields. First, to the Elgin field, an HP/HT shallow marine Upper Jurassic sandstone reservoir located in the UK sector of the North Sea. Then, to the Ekofisk and South Arne fields, both compacting chalk reservoirs in the Norwegian and Danish sector of the North Sea respectively. Additionally, by using a synthetic example the method has been validated and compared with a linear inversion approach using a Geertsma type Green's function achieving higher accuracy. The project involved not only the development and application of the method itself, but the calculation of time-strains from the measured seismic and the construction and implementation of full field geomechanical models.

To my family

“For years the Empty Quarter had represented to me the final, unattainable challenge which the dessert offered. Suddenly it had come within my reach. I remembered my excitement when Lean had casually offered me the chance to go there, the immediate determination to cross it, and then the doubts and fears, the frustrations, and the moments of despair. Now I had crossed it. To others my journey would have little importance. It would produce nothing except a rather inaccurate map which no one was ever likely to use. It was a personal experience, and the reward had been a drink of clean, nearly tasteless water. I was content with that.”

Wilfred Thesiger (Brtisish explorer), 1910-2003
Arabian Sands, 1959

Acknowledgements

First and foremost, I would like to thank my parents for their endless support and for always being there for me. To them I dedicate not only this work but my life: achievements, failures, joys and sorrows, for they made me what I am and for that I will always be grateful. Muchas gracias papas, los quiero mucho. My most sincere thanks go also to the rest of my family: my brother, Pilar and nieces for bringing new joy to the family and "la patota" for all the wonderful moments, all the support and love. Thank you all.

To Colin MacBeth for having given me the chance of making part of ETLP, the prestige of ETLP has opened great opportunities for my future professional development. I would also like to thank the rest of the ETLP team past and present, students and staff, for their support, guidance, ideas and simply for their friendship. To previous students Margarita Corzo, Neil Hodgson and Fabian Domes for the inherited research experiences, advice, discussions and the odd Matlab script. Special thanks go to Yi and Hamed for having to endure this long my stress relief pranks. To Asghar Shams for sharing his Ekofisk and general chalk experience. I am also very grateful with the late Mr. Nelson Briceño and Prof. Andreas Hördt for giving me the opportunity to become a geophysicist and to Andreas also for introducing me to the concept of Wiener filters, his ideas found fertile ground on this Thesis. I am also grateful with the thesis examiners Jorg Herwanger and Asghar Shams, for taking the time to read and evaluate this work.

This reaserch would not have been possible without the ETLP sponsors phases III and IV: BG Group, BP, Chevron, ConocoPhillips, OHM, ENI, Encana, ExxonMobil, Ikon Science, Landmark, Maersk, Marathon, Norsar, Petrobras, Shell, Statoil, Total and Hess and the direct and valuable help from Alexandre Bertrand (ConocoPhillips), Ole V. Vejbæk and Christian R. Schiott (Hess). Special thanks to Andrea Grandi (Total) for his support and guidance that allowed me to shape the Wiener filter technique to the way is presented in this thesis. I would also like to thank Ian Jack and the SEG Foundation for their support that helped me ease the economical burdens of a student life.

And last but not least to all my Edinburgh friends: the Banana Republic Movie Club for sharing my awful movie taste, to Mattteo Lupi for stoically enduring the Heavy Metal

breakfasts, to my climbing partners Jon, James and Carlos for sharing my passion, to Oscar and Susana for letting me squat at their place during my “transition time” and to all my “parceros” back home and the ones scattered around the globe, thank you all for all the experiences we have shared and for the many more to come and above all, thank you for your friendship you kept sane despite the PhD.

Contents

List of tables

List of figures

Chapter 1

1 Overview

This chapter introduces the reader to both 4D-seismic and geomechanics as reservoir management tools. It gives a brief historical account of compacting reservoirs and thus the facts that gave birth to time-lapse seismic, and explains the now growing need for fully-coupled fluid-flow and geomechanics simulators for reservoir characterization. This sets up the background of this research project.

1.1 History of compacting reservoirs

In 1984 the Ekofisk field, located in the central graben in the southern part of the Norwegian sector of the North Sea, set a stark reminder that some subsurface processes are far from understood when the first signs of subsea ground subsidence were recognized. It was not until then that several measurement mechanisms were used to determine the rate of subsidence; e.g. compaction logs, bathymetry and satellite geolocation of the platforms. After some months, it became clear that the seabed was sinking at a rate of about 40 to 50 centimetres per year (Kvendseth, 1988). In April/May of 1985, there was sufficient data to be able to say that the platforms lay about 2.5 meters deeper in the water than when they were installed, see Figure 1.1.

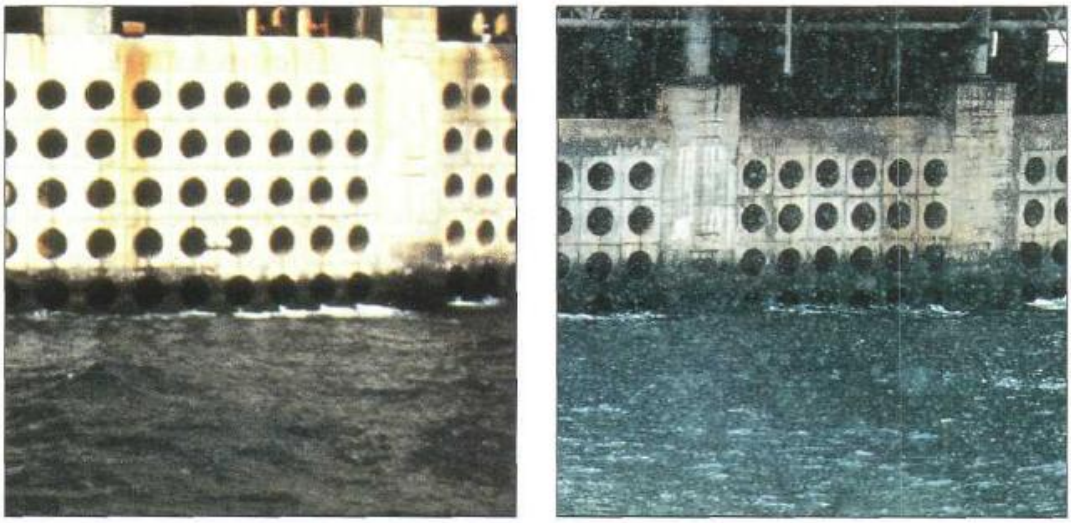

Figure 1.1 Pictures of the Ekofisk Tank, in 1973 (left) and 1986 (right) evidencing sea floor subsidence (Kvendseth, 1988).

The events surpassed by far any previous estimates on seabed subsidence and reservoir compaction (Sulak & Danielsen, 1989). Before 1984 the then operator of the field, Phillips Petroleum Co., never realized that they were facing subsidence and compaction issues, but literature indicated that several operators in various parts of the world had experience dealing with compaction monitoring, especially at Wilmington (Pierce, 1970) and Gröningen (Loos, 1973).

In the Gröningen field (onshore Holland), reservoir compaction has been reported and monitored since 1964. In 1967, the use of radioactive markers was introduced for compaction monitoring and in 1982, Schlumberger's four-detector formation subsidence monitoring tool (FSMT) was introduced (Mobach and Gussinklo, 1994). Based on Gröningen's experience, an appraisal programme was initiated with time-lapse surveys performed with cased-hole neutron tools in addition to radioactive markers and FSMT (Menghini, 1989), in order to determine the magnitude and areal extent of the formation compaction at Ekofisk. The results (Figure 1.2) showed a compaction rate of up to 40 cm/year in the reservoir section, but no evidence of overburden strain was found. This technique, although useful, proved expensive, since a dedicated near vertical well had to be drilled only for FSMT monitoring purposes.

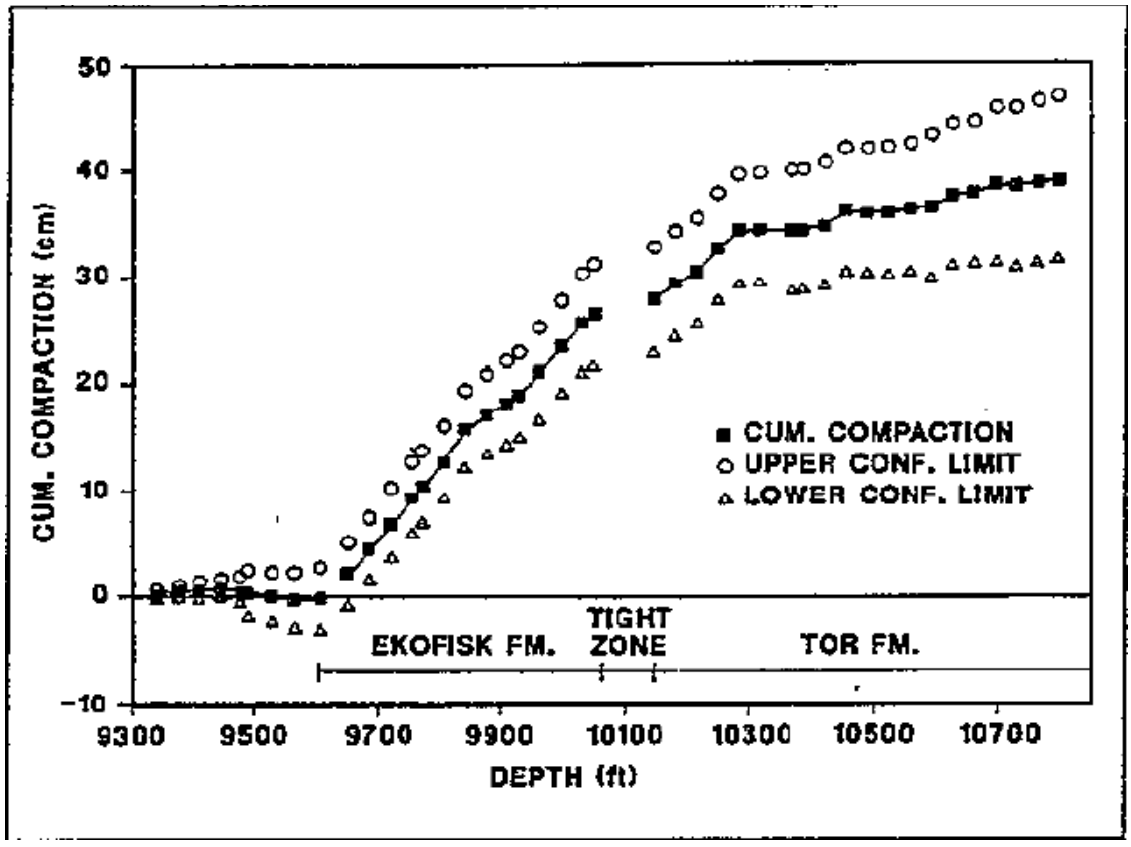

Figure 1.2 Compaction measurements in Well 2/4 C-11 of the Ekofisk field between Oct. 1986 and Oct. 1987 (Menghini, 1989).

Field	Area	Geology	Year	Reference
Goose Creek	Texas	Unconsolidated sands and thin shales	1918-1925	Pratt and Johnson, 1926
Wilmington	California	Unconsolidated sands and thin shales	1928-1966	Allen and Mayuga, 1970
Buena Vista	California	Unconsolidated sands and thin shales	1932-1959	Yerkes and Castle, 1970
Huntington	California	Unconsolidated sands and thin shales	1933-1965	Yerkes and Castle, 1970
Inglewood	California	Unconsolidated sands and thin shales	1911-1963	Yerkes and Castle, 1970
Bare	Orinoco Venezuela	Unconsolidated sands	1973	Nagel, 2001
Various Fields	Lake Maracaibo	Unconsolidated sands	1962	der Knaap and der Vlis, 1967
Gröningen	Netherlands	Sandstones	1967	Loos, 1973
Sarawak	Malaysia	Carbonates	1982	van Ditzhuijzen and de Wool, 1984
Ekofisk	North Sea Norway	Chalk	1984	Kvendseth, 1988

Table 1.1 Some of the most recognized cases of production-induced compaction, from Goose Creek, 1918 to Ekofisk, 1984.

Compaction and subsidence observations have been reported from the North Sea, to Venezuela (Ramirez and Zubillaga, 1987), to the western coast of the US (Nagel, 2001) and the Gulf of Mexico (Rickett et al., 2006) to Southeast Asia (van Ditzhuijzen & de Wool, 1984), highlighting the ubiquity of the phenomenon. Subsidence at the Wilmington and Ekofisk oil fields are two of the most widely recognized examples due both to the magnitude of subsidence as well as the cost of remediation. However, other lesser reported subsidence cases are a challenge for a number of reservoirs. In Venezuela, surface subsidence due to reservoir depletion has led to severe flooding along the coast of Lake Maracaibo and in the Netherlands subsidence at the large

Gröningen gas field, though only on the order of tens of centimetres (Nagel, 2001), poses significant challenges since large portions of the Netherlands are below sea level and protected by dikes. Table 1.1, shows a variety of the most recognized cases of hydrocarbon production-induced compaction, some as early as 1918 at the Goose Creek field in Baytown Texas, where the entire Gaillard Peninsula which originally jutted into the middle of Tabbs Bay, disappeared by 1926, Figure 1.3.

Figure 1.3 Top, maps of the San Jacinto Bay area between 1917 and 1926, showing the sinking of the Gaillard Peninsula and part of the surrounding marshlands. Bottom left, shows the wellheads in 1926 where elevated walks and plank roadways had to be built to connect them to the mainland. Bottom right, two geologists sent to investigate in 1926, find that the problem is not restricted to the former peninsula, but to the entire Goose Creek field (Pratt and Johnson, 1926, and Albert, 2001).

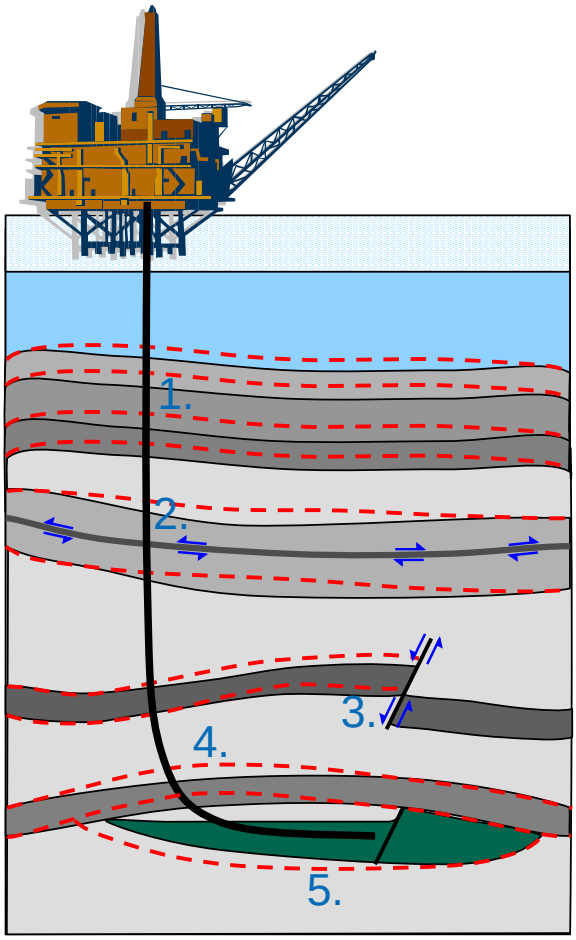

Figure 1.4 Cartoon illustrating production induced subsurface deformation, the red dashed lines indicate the pre-production state: 1) shallow overburden/ seafloor subsidence, 2) bedding parallel slip, 3) fault reactivation, 4) fracturing of seal, gas clouds in overburden and well failure in extension, 5) Reservoir compaction and porosity and permeability reduction. Redrawn after (Herwanger, 2007).

Reservoir compaction and surface, or seabed, subsidence has many impacts, challenges, solutions, and even benefits. Figure 1.4 shows some of the issues associated with compacting reservoirs, e.g. bedding parallel slip, fault reactivation, seal fracture and well failure. Seabed subsidence at the Ekofisk field, for example, resulted in the need for a jack-up of the platforms in 1987 (Figure 1.5), the barrier placement in 1989, and the Ekofisk II redevelopment in 1998 (Kvendseth, 1988). Likewise, subsidence has also led to significant pipeline concerns due to excess compressional or tensional strain. At the same time, reservoir compaction, has led to numerous casing deformations and poses a notable challenge for well completion, where in the Ekofisk case, wells had to be redrilled after 10-14 years (Yudovich et al., 1989). Nonetheless, reservoir compaction also provides significant drive energy for hydrocarbon recovery and greatly contributes to increased production and reserves in the form of what is known as *compaction drive*.

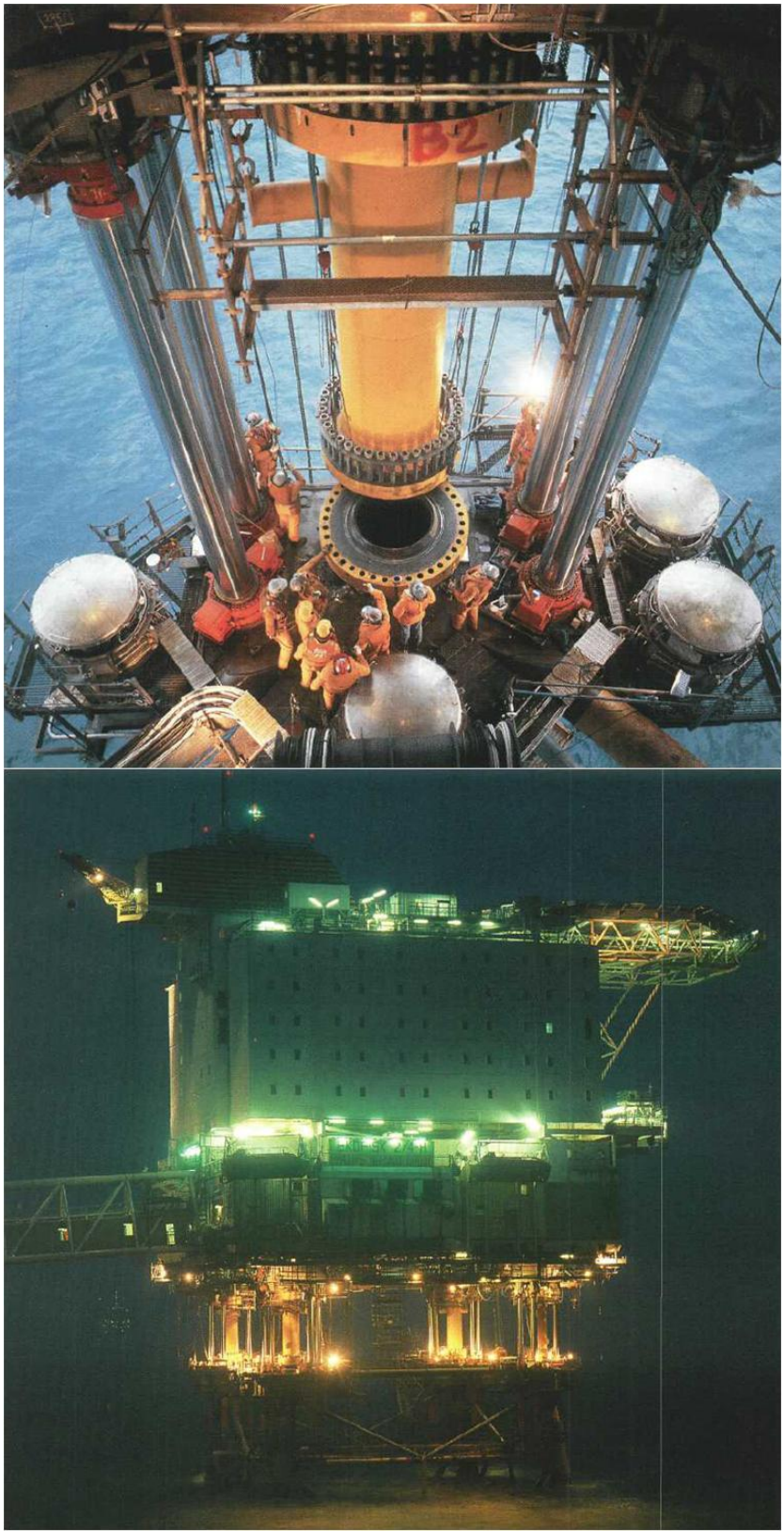

Figure 1.5 Jacking up of the Ekofisk platform and installation of leg extensions. After installation of the hydraulic jacks the platform legs were cut just below the deck, and bolted flanges welded on to the legs followed by fitting of 6 metre long extension spools. Top, jacking up of Platform 2/4H (The Hotel). It took less than 12 hours to elevate the platform before the extension spools could be slid into place. Bottom, after only 21 hours and 43 minutes the job on the platform 2/4H was finished (Kvendseth, 1988).

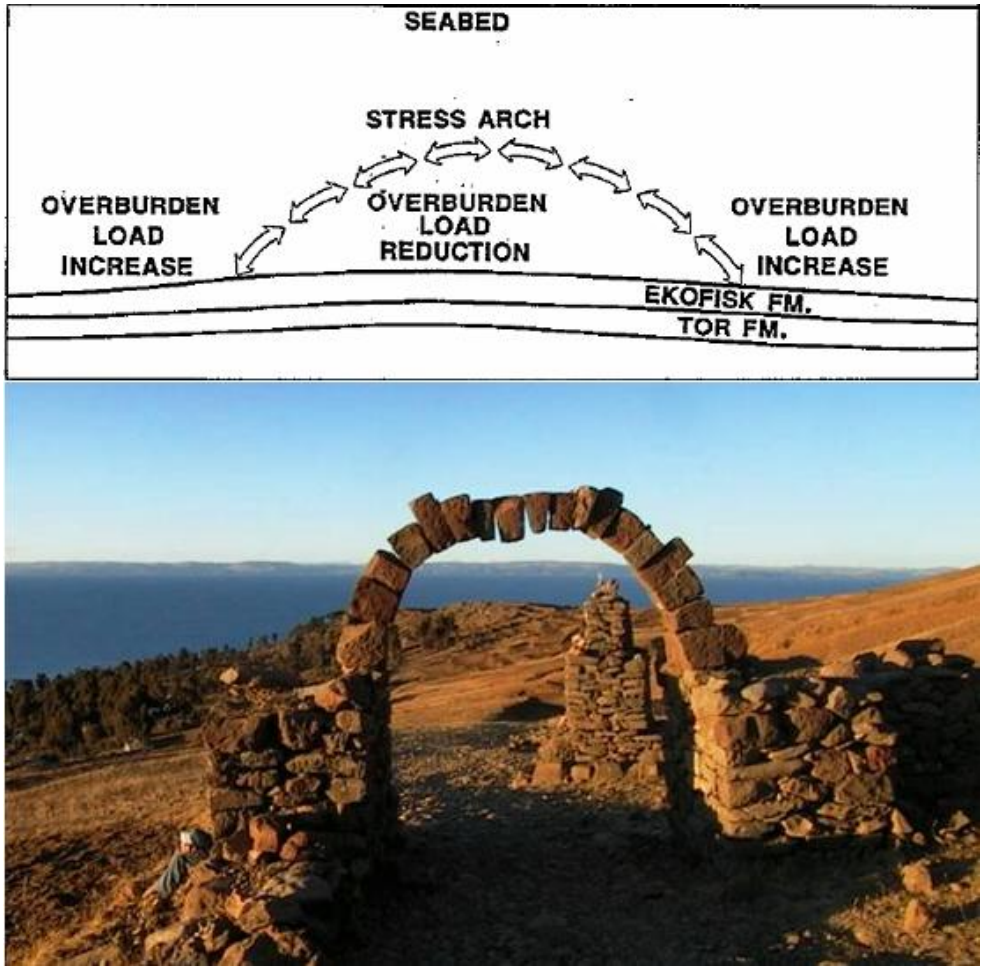

Figure 1.6 Top, schematic of stress arching at Ekofisk due to reservoir depletion and overburden subsidence, after (Sulak and Danielsen, 1989). Bottom, arch of Inca ruins at the Amantani Island in Lake Titicaca, Peru, illustrating the principles of *stress arching*. Source: http://www.hat.net/

1.2 Reservoir compaction and rock mechanics

The reason the overburden deforms in response to reservoir compaction is related to a reaccommodation of the stress field in the sediments. The load or weight of the overburden, initially fully supported by the reservoir's rock matrix and pressurized fluid, loses ground as the reservoir compacts in response to depletion. Hence, the lowermost part moves downward and the rest of the overburden follows if no layer strong enough exists to support the load. The overburden, however, has some ability to resist downward displacement. Consequently, the upper intervals are not displaced downwards as much as the lower layers; therefore, the overburden above the depleted

region is extended vertically. As a result, some load is redistributed from the top of the structure to the flanks giving rise to what is known as a *stress arch*, analogous to the ancient Inca arches, as displayed in Figure 1.6, where the entire load of the structure is supported at the flanks. The effect is significant because it reduces the vertical stress at the centre substantially. At Ekofisk for example, up to Feb. 1989, the vertical stress reduction was estimated to be near 1000 psi (6.9 MPa), due to a seafloor subsidence of about 1.0 ft (0.23 m) for every 1.9 ft (0.58 m) of reservoir compaction, as shown by Sulak and Danielsen (1989) and Johnson et al. (1989). Stress arching and overburden subsidence, have the effect of reducing vertical stress while increasing lateral compression and thus, increasing shear stress (Figure 1.7). As a consequence, associated bedding plane slip and overburden shear may take place where horizontal stresses are high (inside the stress arch) and normal faulting where horizontal stresses are low (flanks of the stress arch) provided the differential stress exceeds a critical value.

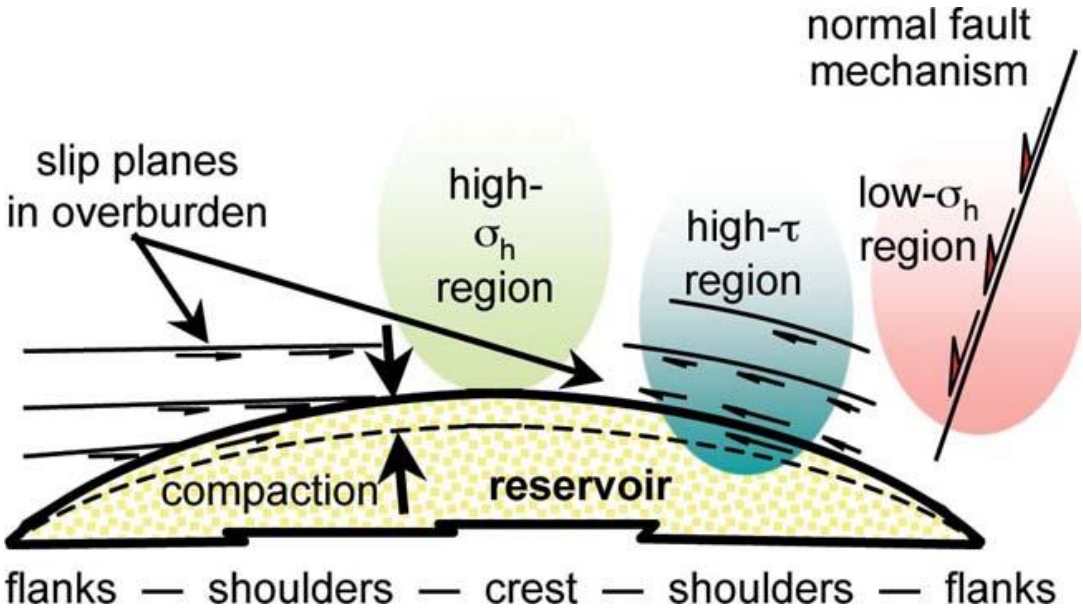

Figure 1.7 Schematic view of stress changes in the overburden due to reservoir compaction (Dusseault et al., 2007).

Changes in horizontal strain may give rise to different well failure or casing damage mechanisms; i.e. overburden shear damage along horizontal interfaces, shearing at the crest or shoulders of the reservoir, and compression and buckling damage within the production interval (Figure 1.8), primarily around perforations, where the casing is weaker (Bruno, 2002).

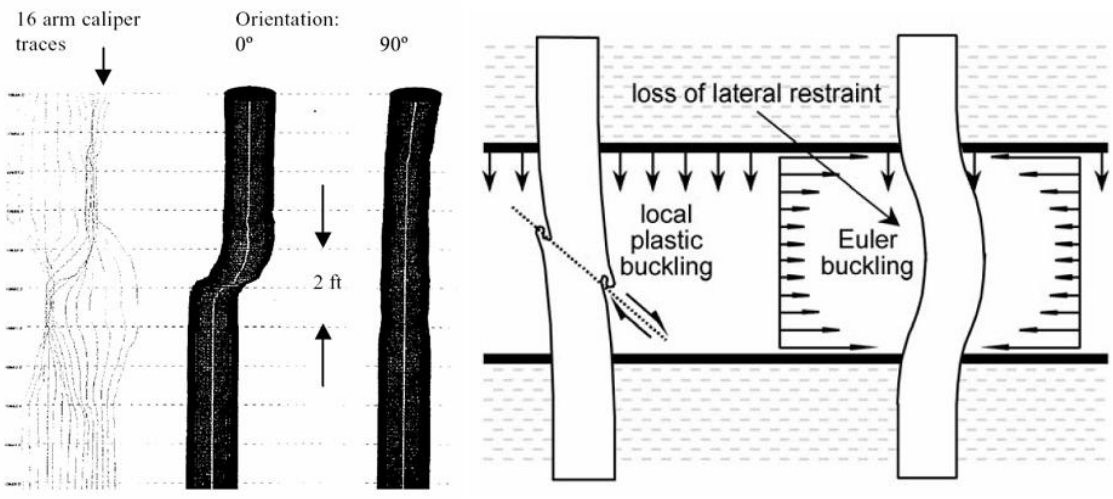

Figure 1.8 Left after (Bruno, 2002): Sample casing shear deformation noted in calliper logs in a gas well in Southeast Asia. Right after (Dusseault et al., 2001), sample cases of well failure; Euler buckling and plastic buckling due to reservoir compaction.

In order to mitigate or prevent any issues associated with compaction, a detailed dynamic description of the subsurface is necessary. Such a description could in principle be achieved with direct measurements. However, sparseness and cost of data favours indirect computational methods. For the latter case, accurate prediction of any kind of subsurface deformation requires that the mechanical properties not only of the reservoir rock, but of all its surroundings to a reasonable extent, be determined in conjunction with its initial stress state. These can then be combined with such information as reservoir pressure and field structure to calculate the amount of compaction and the resulting surface deformation. Mainly two different approaches exist to address the problem; one based on analytical solutions and the other one on numerical computations.

1.3 Reservoir geomechanics

In the 1990s the advent of 4D seismic provided a new tool to describe geomechanical phenomena in the reservoir. The large scale development of viscous oil, high-porosity offshore reservoirs, high-pressure high-temperature (HP/HT) cases, and fractured

carbonates with severe stress sensitivities raised awareness on geomechanics as a vital aspect of reservoir management.

Previously, the science of geomechanics was a scattered group of applications of rock, soil, and fracture mechanics used separately to deal with a variety of problems in drilling, production, completion, and reservoir engineering. Nonetheless, geomechanics has become the common thread that binds together geophysics and many engineering disciplines for field development and especially for non-conventional oil and enhanced oil recovery. Additionally, the fact that about 60% of the world's oil reserves are in the form of heavy oil in weak sandstones (International Energy Agency, 2005), suggest that geomechanics and seismic monitoring will attain central stage in decades to come.

1.4 Time-lapse (4D) seismic: linking geomechanics and geophysics

Increased sophistication in seismic acquisition, processing, and imaging techniques, have made imaging of detailed structural and stratigraphic variations within the reservoir possible, and in some cases variations in the distribution of reservoir properties and fluids. These detailed reservoir descriptions have provided the basis of seismic reservoir characterization. However, since changes in fluid saturation and pore fluid pressure can often give rise to detectable seismic changes, the use of time-lapse seismic data seemed a natural next step for dynamic reservoir characterization.

The first mentions in the literature of time-lapse seismic monitoring, can be traced back to 1983 by Greaves et al. (1983) of Arco Oil & Gas. Their research was aimed at testing the ability of 3D seismic data to assess enhanced oil recovery (EOR) methods, particularly in-situ combustion. Since one measure of EOR efficiency is the actual fraction of the reservoir rock volume acted upon by the enhancement process, a duplicate 3D seismic programme was carried out before and during combustion, at the Holt Field in north-central Texas, so that the areal extent of the burn process and direction of propagation could be mapped. A third identical study was later acquired, within a 15 month period for all three, so that a complete set of preburn, midburn and postburn surveys were available for combustion propagation monitoring. The results were published by Greaves and Fulp (1987). Acquisition and processing parameters for

all campaigns were identical, so that a direct comparison between the individual data sets could be made.

The basic premise behind the project was that as the combustion process substantially increases the temperature and gas saturation within the affected reservoir zone, both the reservoir density and seismic velocity will change, which in turn would produce measurable changes in reflection amplitude. Figure 1.9, displays line 14, a 2D north-south section at preburn, midburn and postburn times. The line shows a "bright spot" at the top of the Holt sand that increases in amplitude and lateral extent after the combustion process was started.

Additionally, amplitude difference volumes were generated by subtracting the envelope amplitude traces from the preburn data volume from their counterpart traces in the midburn and postburn data volumes, generating "difference volumes." Figure 1.10 shows horizon slices at the top of the Holt sand, from the envelope amplitude difference volumes. The midburn difference shows a positive amplitude anomaly in the south western side of the data. This corresponds to the bright spot development observed in line 14 (Figure 1.9). The postburn difference shows that the bright spot grew to cover most of the area within the production wells, and the maximum amplitude of the difference anomaly increased by about 10 percent.

The results obtained by Greaves and Fulp (1987) in their early and successful use of time-lapse seismic, proved the ability of the method for reservoir monitoring. However, despite the encouraging results, time-lapse seismic was severely limited at the time by the then attainable imaging resolution and repeatability. Which for the particular case of the Holt sandstone reservoir required a signal of around 100 Hz. This was possible only given the shallow depth of the reservoir, and that being onshore the geophones were required to be permanently in place to ensure proper survey repeatability. Nevertheless, their ideas stayed "dormant" awaiting acquisition and processing developments.

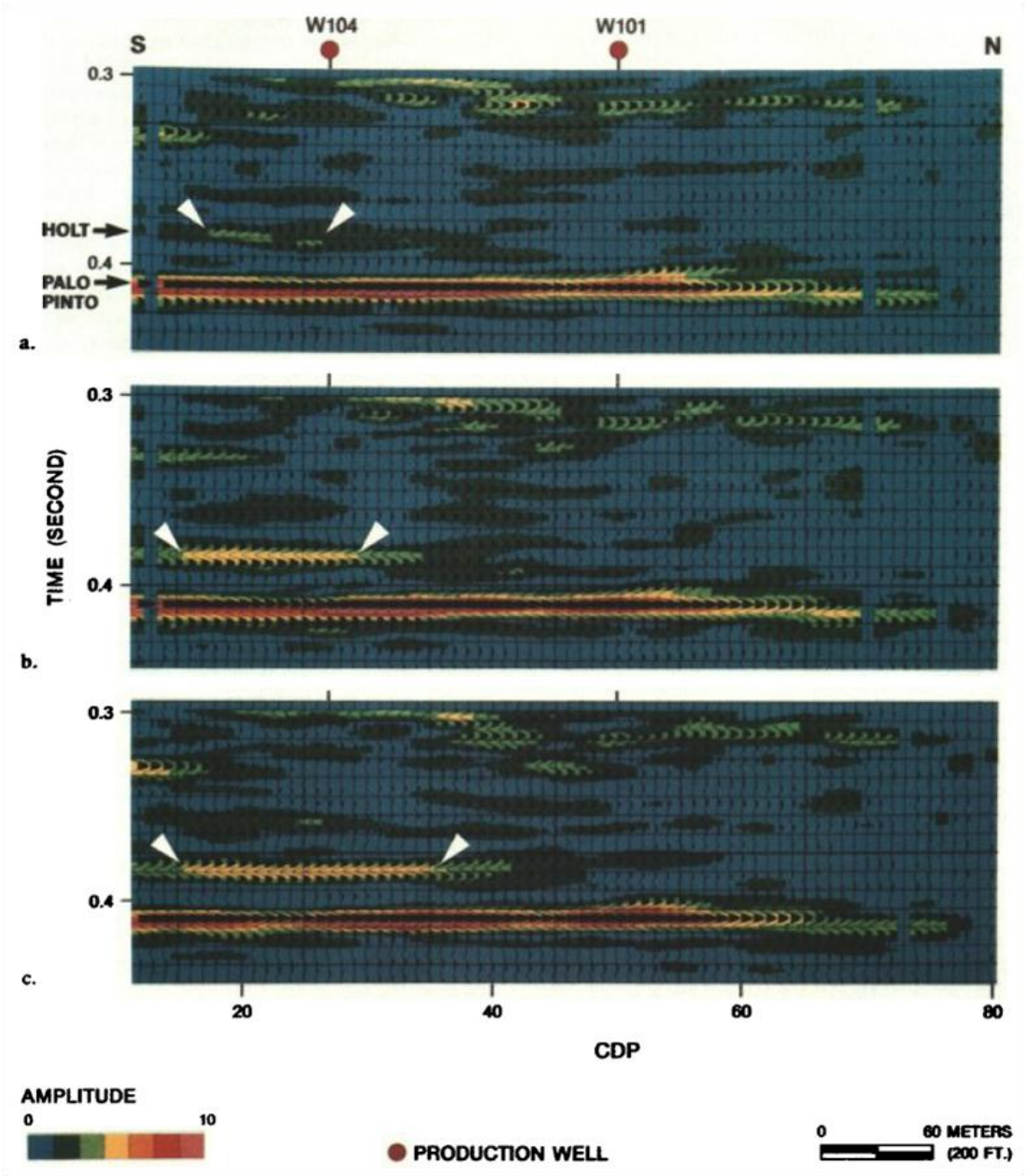

Figure 1.9 Line 14, displaying preburn (a), midburn (b), and postburn (c) sections from the 3D seismic volumes. Dip was removed by static shifts before display. A bright spot was created at the top of the Holt sandstone (see arrows which increased in amplitude and lateral extent with time (Greaves and Fulp, 1987).

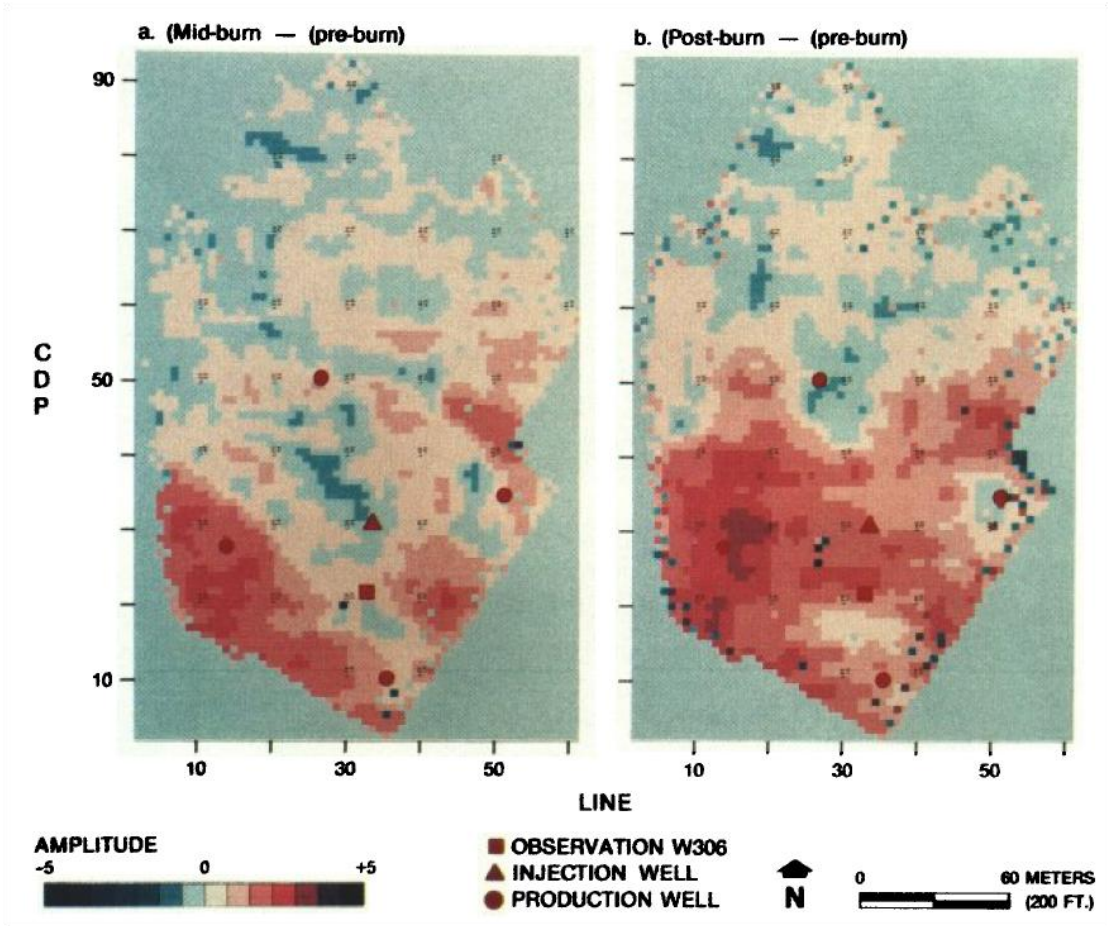

Figure 1.10 Time slice at approximately 385ms at the top Holt sandstone using difference volumes of the envelope amplitude; midburn (a) and postburn (b). Bright spots occur as positive anomalies. Well locations are marked for position in the subsurface at the top of the Holt sandstone (Greaves and Fulp, 1987).

With respect to compacting fields, it was not until 1998 that Key et al. (1998) published a development plan for seismic monitoring in the Ekofisk field. The plan included a detailed reservoir characterization and the construction of a new fluid-flow simulator to provide the primary tools to manage the redevelopment. Part of this process was an in-depth evaluation of the seismic response by forward modelling with the extensive well data. The results were published in 2002 (Guilbot and Smith, 2002). Since it was the first of these studies focused on compaction monitoring, it was also the first concerned with the accurate magnitude of the travel-time changes and the compaction and velocity changes estimates that could be derived from them. The paper presented a method to constrain depth conversion in a time-lapse consistent way to account for subtle velocity changes in the overburden and reservoir. The importance of accurately capturing these changes was to correctly estimate the magnitude of compaction.

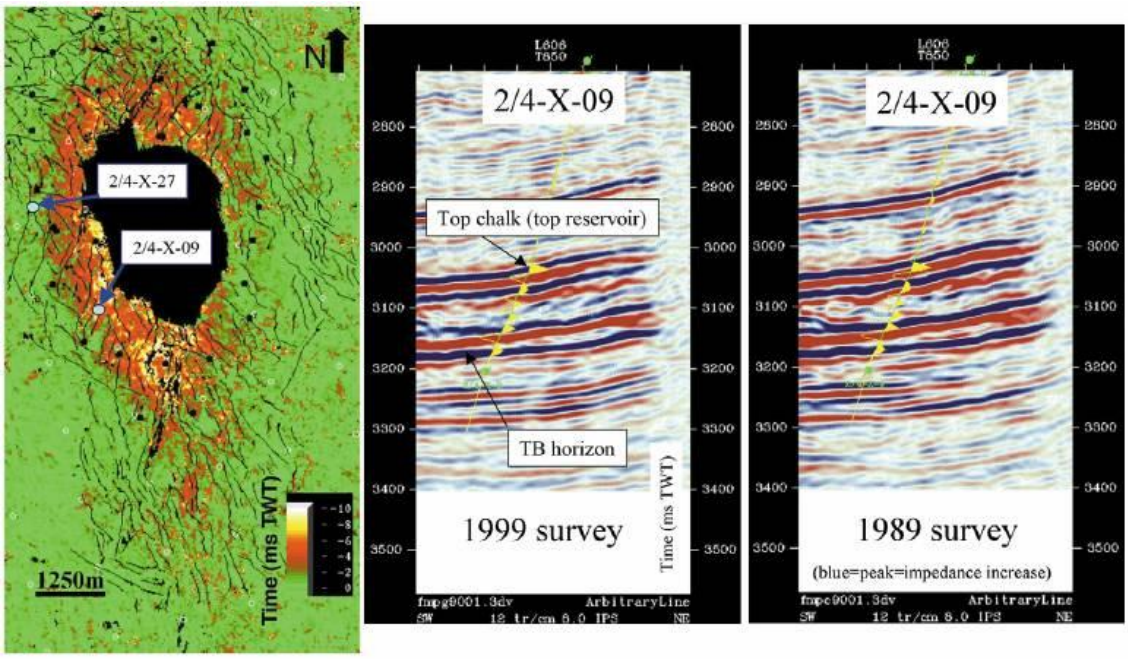

Figure 1.11 Left: time compaction map of Ekofisk Formation. The compaction is mainly located on the western flank of the field and is relatively large, between 2 and 10 ms TWT. Right: time seismic section around well 2/4-X-09 drilled in 1997. The synthetic trace in yellow, has been calibrated for the 1999 survey and is displayed on top of the 1999 (middle) and 1989 (right) surveys. Source: (Guilbot and Smith, 2002).

The resulting time-shift map Figure 1.11, agreed with the observations and compaction estimates from wells. Well 2/4-X-09 located in a strongly compacted area, showed a strong time subsidence effect at the top of the reservoir (10 ms TWT) and a decrease of this subsidence down to base reservoir (near TB horizon), as compared with the synthetic seismic trace calibrated for the 1999 survey.

It was not until late 2002, shortly after the Ekofisk publication, that Hall et al. (2002) introduced the now widely used term of *time-shifts* when referring to the travel time differences between base and monitor surveys. Their work presented a systematic method of *interpreted warping* for calculating the corresponding time-shifts. It was applied at the Valhall field in the Norwegian North Sea; like Ekofisk, another compacting chalk reservoir. The technique can be summarized as a full trace by trace cross-matching of 4D seismic data, on small data volumes positioned on selected horizons, to resolve the spatial (temporal) shifts between surveys. Warping allows the

significant misalignment in 3D (x, y, t) of seismic data volumes acquired at different times, e.g., due to reservoir compaction and overburden subsidence, to be resolved and can at the same time be used as an interpretable time-lapse attribute, Figure 1.12.

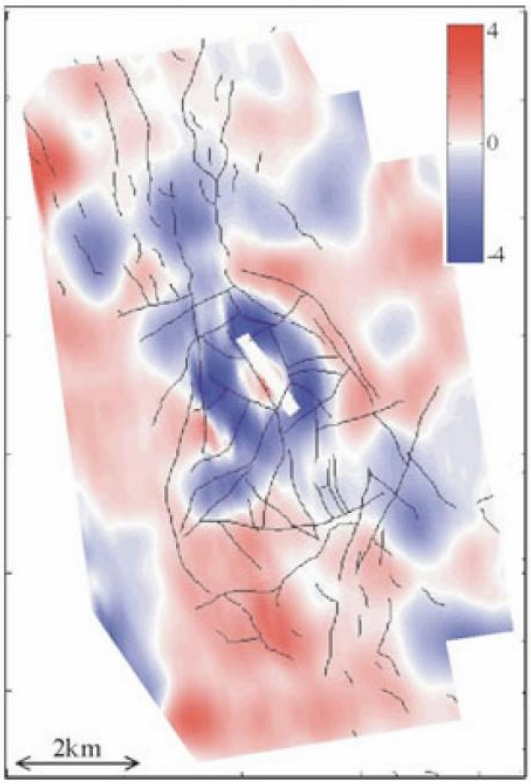

Figure 1.12 Warp map at the top of the chalk showing the relation between the anomalies and large scale faulting. Source (Hall et al., 2002).

Figure 1.12 shows the warp map at the top of the chalk for the Valhall field obtained by Hall et al. (2002). Some correlation can be inferred between the warp anomalies and large scale faulting, but other lineaments exist suggesting additional faults may be highlighted by the 4D analysis.

1.4.1 Time-shifts, travel-time and velocity changes

The original intent of 4D seismic was to image reservoir changes via the dependency of seismic reflection amplitudes on velocities and density, which are affected by fluid saturation in the porous reservoir rocks. However, the velocities also depend on elastic

properties, and stress state of the reservoir and surrounding rock. Moreover, in addition to velocity changes in the subsurface, the reflectors may undergo deformation and displacement where compaction and subsidence are involved. This presents challenges as well as new possibilities, when considering the amount of information potentially contained in the time-shifts as a single 4D attribute. As a result, it is important to note that the 4D time-shifts capture the combined effects of velocity and thickness changes within a given layer. It is therefore crucial to distinguish between the two effects, both for the reservoir section and the surrounding material.

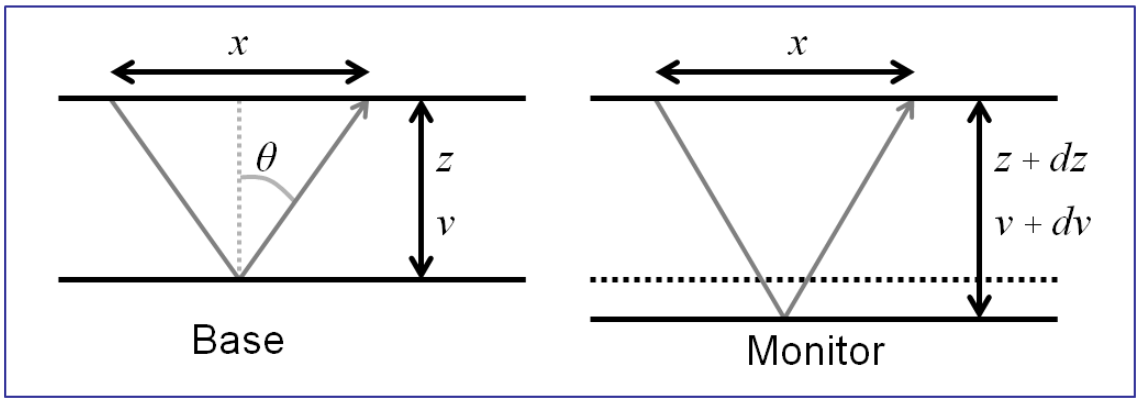

Figure 1.13 Representation of an overburden offset ray both for base (left) and monitor survey (right) after reservoir compaction. Redrawn after Landrø and Stammeijer (2004).

Consider a single layer with thickness z and a P-wave velocity v that is experiencing vertical strain and velocity changes as a result of production, as shown in Figure 1.13. Assuming normal-incidence, the normalized time-shift to the lowest order can be expressed as

$$\frac{dt}{t} = \frac{d\left(2z/v\right)}{2z/v} \approx \frac{\Delta z}{z} - \frac{\Delta v}{v} \tag{1.1}$$

as introduced in 2004 by Landrø and Stammeijer (Landrø and Stammeijer, 2004). In the same way, exploiting the fact that travel time and acoustic impedance (AI) changes exhibit different sensitivities for velocity changes and compaction, they obtained

$$\frac{dAI}{AI} = \frac{d(\rho v)}{\rho v} \approx \frac{\Delta \rho}{\rho} + \frac{\Delta v}{v} \tag{1.2}$$

Landrø and Stammeijer presented two new seismic methods for monitoring compacting reservoirs, one based on measured seismic prestack traveltime changes, and the other based on poststack traveltime and amplitude changes. Both methods relied on near- (*N*) and far-offset (*F*) observations to resolve independently thickness and velocity changes via the relation

$$\frac{\Delta z}{z} = \frac{\left(1+\tan^2\theta_F\right)\frac{\Delta t_N}{t} - \left(1+\tan^2\theta_F\right)\frac{\Delta t_F}{t}}{\tan^2\theta_F - \tan^2\theta_N}, \tag{1.3}$$

$$\frac{\Delta v}{v} = \frac{\frac{\Delta t_N}{t} - \frac{\Delta t_F}{t}}{\tan^2\theta_F - \tan^2\theta_N} \tag{1.4}$$

where θ corresponds to the seismic ray angle through the layer (Figure 1.13) and t corresponds to the two-way travel time thickness after NMO correction. On the other hand, by postulating the basic relationship between density and compaction:

$$\frac{\Delta\rho}{\rho} = -a_0\frac{\Delta z}{z} - a_1 \tag{1.5}$$

estimates for compaction and velocity changes in equation (1.2) can be calculated using

$$\frac{\Delta z}{z} = \frac{\frac{\Delta t}{t} + \frac{\Delta AI}{AI} + a_1}{1-a_0} \tag{1.6}$$

$$\frac{\Delta v}{v} = \frac{a_0\frac{\Delta t}{t} + \frac{\Delta AI}{AI} + a_1}{1-a_0} \tag{1.7}$$

where a_0 and a_1 are empirical parameters depending upon initial reservoir conditions. However, the introduction of these parameters, and the lack of physical support behind them and the fact that the results were limited only to uniform isotropic horizontal layers and required high quality prestack data for both surveys, severely limited the applicability of the approach. Hatchell and Bourne (2005) published one of the most controversial and henceforth referenced papers on the subject. Based on observations of

time-lapse seismic data from several locations around the world and a previous work by Hatchell et al. (2003), they proposed a simple linear model relating seismic velocity changes to vertical normal strain. Their observations also suggested that the velocity-strain dependence is larger for rock elongation than for rock contraction.

Consider the time-shift due to a single thin horizontal layer of thickness, *z*, and P-wave velocity, *v*. Let the traveltime for a normal-incidence P-wave be *t*. Changes in traveltime due to small changes in layer thickness and velocity, such that $\Delta z/z \ll 1$ and $\Delta v/v \ll 1$, may be expressed as

$$dt = \left(\frac{\partial t}{\partial z}\right)_v dz + \left(\frac{\partial t}{\partial v}\right)_z dv \tag{1.8}$$

Evaluating the partial derivatives for $t=z/v$ leads to

$$\frac{dt}{t} = \frac{dz}{z} - \frac{dv}{v} \tag{1.9}$$

Which is nothing but relation (1.1) though, more elegantly derived, as presented by Hatchell and Bourne (2005). In this limit, the fractional change in traveltime across the layer is simply the difference between the fractional change in path length and velocity. For this geometry, the fractional change in path length is exactly equal to the average vertical strain over the layer, ε_{zz}. The remaining unknown in this expression is the fractional change in seismic velocity, which in the general case will be anisotropic (Sayers, 2005). However, in the case of normal incidence P-waves, Hatchell and Bourne proposed that fractional changes in velocity also occur in proportion to fractional changes in path length, such that $dv/v = -R\,\varepsilon_{zz}$. So it follows from equation (1.9) that the fractional change in traveltime becomes

$$\frac{dt}{t} = (1+R)\varepsilon_{zz} \tag{1.10}$$

where the dimensionless value, *R*, denotes the ratio between traveltime changes due to velocity changes and path length changes. In sedimentary rocks seismic velocity depends strongly on porosity (or, equivalently, density) and as a result there are well known and commonly used regressions between velocity and porosity; Figure 1.14

shows the R-values versus porosity for several rock physics models published by Mavko et al. (1998).

The total change in P-wave traveltime, Δt, over a finite sequence of layers is then

$$\Delta t = \int_0^z (1+R)\frac{\varepsilon_{zz}}{v}\,dz \tag{1.11}$$

This formulation implies that time-lapse time shifts, seafloor subsidence, and reservoir compaction can all be directly related and calibrated to each other.

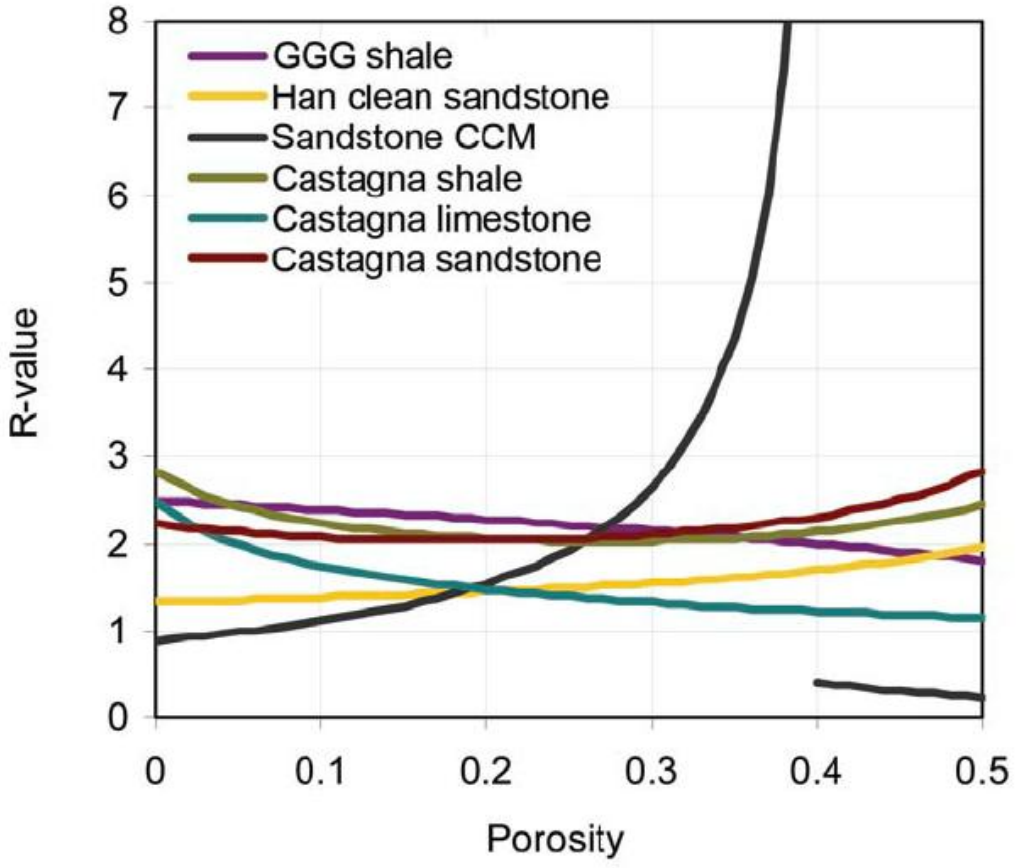

Figure 1.14 R-values versus porosity for a number of common rock properties. Source (Hatchell and Bourne, 2005).

However, there is still some controversy regarding the consistency of the R-factor. Hatchell and Bourne suggested that based on a number of case studies typical 'R' values for the overburden are between 4 to 6 and 1 to 3 within the reservoir. On the other hand,

Staples et al. (2007) propose ‘R’ factors in excess of 10 for some sandstone HP/HT reservoirs where values of up to 50 are documented in literature (Garcia et al., 2010). The case for ‘R’ is not helped by available hard data, as lab data appears contradictory. In Ekofisk, using core data Janssen et al. (2006) reported values up to 30. In contrast, values of ‘R’ from measured time-shifts in combination with a single compaction log are consistent with those proposed by Hatchell and Bourne. In any case, the R-factor is a robust and simple way to discriminate physical strain and velocity changes from measured time-shifts, which in the absence of a more consistent approach, remains the preferred method.

1.5 Thesis aims and outline

The possibility of calculating vertical strains and velocity changes from measured time-shifts opens up a whole new set of tools for reservoir monitoring. Notwithstanding the possibility of using overburden time-lapse attributes for reservoir and overburden characterization. The reason for using overburden information to indirectly infer what is going on in the reservoir is justified by the fact that most compacting reservoirs offer massive challenges for reservoir imaging; e.g. the HP/HT gas condensate reservoirs in the North Sea Central Graben area have very low seismic reflectivity and some of the high porosity chalk fields usually gas clouds making the use of conventional seismic attributes impractical. In order to exploit overburden information an integrated understanding of the reservoir and its surroundings is required, whereby changes in the subsurface, e.g. vertical strains or velocity changes, can be unequivocally linked to specific production related changes inside the reservoir.

This project, aims precisely to integrate all available time-lapse information via a geomechanical characterization of the subsurface. By using measured overburden time-strains and understanding their relationship with reservoir changes, it is possible to calculate the reservoir compaction and effective stress changes. This has been attempted before by Hodgson et al. (2007), where by treating the subsurface as a single elastic material a Geertsma type Green’s function (Segall, 1992) was used to perform a linear inversion for reservoir pore pressure changes. However, this approach neglects the effects of structure and heterogeneity.

In this thesis I present a method which treats the overburden as a linear filter and makes substitution of the Green's function by a more general transfer function. As long as the process can be regarded as linear, the transfer function together with some a priori knowledge can be approximated as a Wiener-filter (Gonzalez and Wintz, 1983). In the following chapters, I will develop and validate the Wiener-filter method and use it with three real data sets as follows:

Chapter 2

The Wiener-filter method is developed and compared to a Geertsma type Green's function using a synthetic example.

Chapter 3

Application to the Elgin field, an HP/HT sandstone reservoir with one monitor survey comprising four years of production. The time-shifts and geomechanical model used for the calculations were supplied by the operator.

Chapter 4

Application to the Ekofisk field, a high porosity chalk reservoir. The time-lapse data consists of four monitor surveys. As part of this study a field-wide geomechanical model was constructed and all time-shift sets were calculated using a 3D-warping technique.

Chapter 5

Application to the South Arne field, also a chalk reservoir with one monitor survey. High quality data permit the use of other time-lapse seismic attributes to provide a more robust final interpretation. Additionally, various sets of time-shifts (both calculated here and supplied by the operator) were used to test the robustness of the time-shifts themselves. A full field geomechanical model was constructed based on an old geomechanical model and an updated reservoir model.

Chapter 6

A synthetic Ekofisk-like ray-tracing model is set up, including compaction, to investigate the effects of overburden velocity changes on the measured time-shifts. Additionally, the lateral components of the 3D warp vector (lateral shifts) are analyzed in search of potential additional information for reservoir management.

Chapter 7

Presents a summary and conclusions of this project in addition to recommendations for a possible follow up and future applications of this research.

Chapter 2

2 The Earth as a Linear-filter

Any attempt of quantitative reservoir monitoring from measured time-lapse seismic, requires some kind of inversion process. This entails the solution of a static field propagating in a heterogeneous, irregular, layered media. However, such a system does not have an analytical solution. Various numerical and semi-analytical methods have been developed to relate overburden strain to reservoir compaction and associated depletion, nonetheless only a handful tackle the inverse problem; mostly from surface subsidence measurements.

Continuous advances in seismic acquisition and processing and widespread use of 4D-seismic, have made available reliable observations of time-lapse time-shifts, which are related to production induced subsurface deformations. Here a semi-analytical method is proposed which by treating the subsurface as a linear causal system, allows substituting the unknown Green's function with linear filters that can be calculated directly from the data itself (be it real or simulated). This approach permits a very fast and robust solution of both the forward and inverse problems. No assumptions are made about the reservoir's behaviour; the only requirement is that the overburden obeys linear elasticity. The method is here tested with a synthetic example and compared against a linear inversion of a Geertsma type Green's function.

2.1 Introduction

The problem posed by a field propagating in a multilayered media is common to many physical systems, therefore research regarding layered structures abounds. On the subject of poroelasticity, various authors have studied and derived analytical solutions for elastic deformations in a homogeneous halfspace. However, such analytical solutions are based on the assumption that 1) the Earth's crust is a semi-infinite ideal elastic body, and 2) deformations are caused by a hydrostatic pressure change in a spherical or point-source, and as a consequence, the observation point needs to be far away from the source, for the point-source assumption to hold. One of the first of these point-source solutions is known as Mogi source (Mogi, 1958), and has been widely used in volcanology for the understanding of plumbing systems and their eruptive mechanisms with respect to surface deformations and displacements.

Nearly a decade later Geertsma (Geertsma, 1966) developed a model describing surface subsidence and reservoir compaction, in which the depleting reservoir is part of a homogeneous linear elastic medium. By using the displacement solution for a nucleus of thermoelastic strain in a half-space with a traction-free surface (Mindlin and Cheng, 1950), Geertsma derived a semi-analytical solution for a thin disc-shaped reservoir. Segall (1992) presented a more systematic semi-analytical approach to calculate the displacements and stresses caused by fluid extraction in a reservoir within the limits of linear poroelasticity, where Geertsma's results (Geertsma, 1973) are recovered as a special case. Carnec and Fabriol (1999) used the Mogi point source solution to monitor and model land subsidence at the Cerro Prieto geothermal field in Baja California, Mexico, using interferometric synthetic aperture radar InSAR for subsidence measurements.

However, Geertsma's solution as mentioned above is limited to a homogeneous elastic half-space. Later works included the effects of a rigid basement (van Opstal, 1973) and a plane-layered elastic medium (Fares and Li, 1988) involving an infinite series of images. Both approaches are limited to media with two interfaces and therefore to a two-layered model of the subsurface. A natural choice to overcome these simplifications in search of a general solution will be to extend the closed solutions of elastodynamics, (Bouchon, 1981 and Kennett, 1983), to the limit of zero frequency. Nevertheless, this leads to undesired numerical instabilities (Kuvshinov, 2007a). For this reason

propagation of static fields in layered structures are analyzed numerically mainly by one of the following methods: Finite Elements (Boade et al., 1989) and (Settari and Mourits, 1998), Boundary Element (Pan, 1997) and (Fokker et al., 2007), Finite Differences (Vasco et al., 2000) and the image source technique (Chow et al., 1991). Although all these methods can be used for the inverse process, they require carrying out a full field simulation for as many reservoir cells in order to generate the respective Green's function. Thus, the involved computational effort has kept these inversion schemes away from widespread use.

Therefore, successful inversion schemes have been so far confined to the simplest of Green's functions; i.e. a Geertsma type solution following Segall's approach. Under this methodology, Du and Olson (2001) developed a forward/inverse model relating surface subsidence and reservoir pressure change, and validated it using two synthetic examples. Hodgson et al. (2007) extended this to invert subsurface displacements measured as time-lapse time-shifts at the Genesis Field in the Gulf of Mexico. Nonetheless, despite its shortcomings a generalization of Geertsma's model accounting for logarithmic pressure profiles and finite reservoir thicknesses is used by Shell on a regular basis (Kuvshinov, 2007b). Although encouraging, the results put in evidence the need for a more complete solution, to account for structure and especially different material contrasts.

The perfect candidate would be a semianalytical method able to incorporate as much knowledge of the subsurface as possible but avoiding excessive computational hurdles. Under conventional techniques, additional information comes in hand with more complex behaviours and thus, extended computational time. But by assuming only the whole process to be linear and time invariant, all complexity between a given input and its output, can be incorporated as a linear filter process. Whereby, regardless of the system's complexity, once the filter is known any forward or inverse modelling can be carried out in a matter of seconds by a simple convolution operation.

2.2 Background to linear filters

Linear digital filters have long been used in seismic data processing and other geophysical problems. The basic principle underneath a linear filtering process is composed of an input signal and the desired and actual output signals. Consequently it is possible by minimizing the difference between the desired and actual filter outputs, to solve for the so-called optimum, or least squares filter. Commonly known as the "Wiener" filter (Robinson and Treitel, 1967), this solution is characterized uniquely by its respective transfer function. This transfer function might be the reciprocal of a mechanical impedance function in the case of structures, e.g. the acoustic impedance in the case of seismic waves. In electrical circuits, it may represent a filter interpreted very generally as any linear process definable by a convolution operation. Whereas, in most situations, the transfer function might simply represent some poorly understood or very complex (but useful) linear relation between two arbitrary signals (Otnes and Enochson, 1978).

2.2.1 Green's functions versus transfer functions

Let there be a Green's function $g(\mathbf{x},t|\mathbf{x_0},t_0)$, that is, the impulse response of a structure (velocity, displacement, etc.) at point ***x*** and time *t*, when excited by a pulse at point $\boldsymbol{x_0}$ and time t_0. The impulse response function is defined by

$$L^{(n)}\left\{g(\mathbf{x},t|\mathbf{x_0},t_0)\right\} = A\delta(\mathbf{x}-\mathbf{x_0})\delta(t-t_0) \tag{2.1}$$

where $L^{(n)}\{\ \}$ represents an nth degree differential equation, or system of such equations that describes the structure in question; *A* is a constant that usually carries the dimensions transmitted by the pulse and $\delta(\mathbf{x})$ is the Dirac delta function.

As a consequence, any perturbation of a structure or excitation function $p(\mathbf{x}_0,t_0)$, with arbitrary distribution can be expressed as a sum of localized pulses as

$$p(\mathbf{x},t) = \int p(\mathbf{x}_0,t_0)\delta(\mathbf{x}-\mathbf{x_0})\delta(t-t_0)d\mathbf{x}_0dt_0 \tag{2.2}$$

In the same way, the resultant response $u(\mathbf{x},t)$, to the excitation function can be written as the sum of the individual impulse responses

$$u(\mathbf{x},t)=\frac{1}{A}\int p(\mathbf{x}_0,t_0)g(\mathbf{x},t\,|\mathbf{x_0},t_0)d\mathbf{x}_0dt_0 \tag{2.3}$$

Let us now think of a more general scenario governed by the following linear differential equation

$$L^{(n)}\{y\}=h(t), \tag{2.4}$$

subject to the initial conditions $y(0)=y'(0)=0$ and where $h(t)$ is not restricted to a Dirac delta function. Thus the Laplace transform reads

$$Y(s)=\frac{1}{P^n(s)}H(s) \tag{2.5}$$

where $Y(s)$ and $H(s)$ are the Laplace transforms of $y(t)$ and $h(t)$ respectively, and $P^n(s)$ is an nth degree polynomial in s. The solution $y(t)$, to equation (2.4) can be obtain readily by applying the inverse transform (Boeas, 1983). However, solving linear differential equations in this fashion requires knowledge of the unspecified Laplace transform $H(s)$, in which case the system could be solved by use of Green's functions. Now consider the ratio

$$\frac{Y(s)}{H(s)}=G(s)=\frac{1}{P^n(s)}, \tag{2.6}$$

which depends only on the properties of the system. Here $G(s)$ is known as the transfer function, because one can transfer the input $H(s)$ in to the output $Y(s)$ by the product $G(s)\cdot H(s)$.

Consider now equation (2.1) as a special case of equation (2.4) where the forcing function $h(t)$ has been replaced by an impulse $\delta(t)$. However, the transfer function, i.e. the Laplace transform of $g(t)$, $G(s)$, remains unchanged as given in equation (2.6).

Therefore, one can calculate the transfer function of a system by imposing on it an impulse forcing, where the Laplace transform of the response is the transfer function.

As a consequence, from equation (2.6)

$$Y(s) = G(s)H(s), \tag{2.7}$$

or from the convolution theorem (Arfken and Weber, 2001)

$$y(t) = g(t) * h(t) \tag{2.8}$$

That is, the convolution of the impulse response with a particular input gives the response of the system. In other words, the Green's function is a special case of transfer function; i.e. where the forcing function is known and can be described by a Dirac delta function. Another special type of transfer function is the Wiener filter, especially useful when no mathematical description of the system exists.

2.2.2 The Wiener filter formulation

It is customary to write discrete linear inverse problems as a system of equations

$$\mathbf{G}(\mathbf{m}) \rightarrow \mathbf{Gm} = \mathbf{d} \tag{2.9}$$

Where **m** represents the set of physical parameters that characterize a model, **d** is a set of observed data and **G** is the function/s that relates **m** and **d**.

The *forward problem* consists of finding **d** given **m**, solving the system **Gm**. More often than not, this involves solving a system of differential equations, and thus the use of Green's functions and a solution of the type of equation (2.3). The *inverse problem* is that of finding **m** given **d**, which requires finding the best approximate solution, or the set **m**, that produces the smallest misfit. Solving by least squares involves minimizing with respect to **m** the objective function $F(\mathbf{m})$ (Menke, 1984) given by

$$F(\mathbf{m}) = \|\mathbf{Gm} - \mathbf{d}\|_2^2 \tag{2.10}$$

There is a third case, that of the *system identification problem*, or determining **G** given samples of **m** and **d**. As explained above, such a system can be described via linear filter theory and characterized by the convolution $\mathbf{G} * \mathbf{m}$, once the impulse response has been calculated. Note, that here **G** operates as a linear-filter, thus from here onwards it will be identified as **f**, to avoid confusion with conventional Green's function. As a consequence, applying least squares one reformulates the objective function (2.10) to minimize now with respect to **f** (Gubbins, 2004)

$$F(\mathbf{f}) = \|\mathbf{f} * \mathbf{m} - \mathbf{d}\|_2^2 \tag{2.11}$$

The resulting filter elements f_i, correspond to having found the coefficients of a linear differential equation that best describe (in a least-squares sense), the structure or process under consideration.

The power of linear filters and the reason they are used in this thesis, lies not only in the fact that it is possible to describe any linear process regardless of its complexity, but also in that the inverse problem can be solved just as easily. To this purpose, the inverse filter is used; that is the filter $\mathbf{f}^{-1}$, which has the property

$$\mathbf{m} = \mathbf{f}^{-1} * \mathbf{d}, \tag{2.12}$$

in a process known as Wiener deconvolution (Gonzalez and Wintz, 1983).

2.3 The application of Wiener filters

The relative ease with which surface measurements are acquired in comparison with the sparseness of direct underground (i.e. down-hole) measurements, has lead to the development of a myriad of techniques where surface measured data can be inverted into subsurface properties, e.g. seismic, gravimetric and magnetic surveys, tiltmeter data, satellite interferometry, etc. Of highest relevance for geomechanics and reservoir

monitoring are time-lapse seismic attributes, specifically time-shifts as a direct measure of production-induced subsurface displacements. These measured overburden time-shifts, given a Green's function or in its absence, any other type of transfer function, could be used to track changes in reservoir pressure. It is therefore possible to formulate the problem as a system identification problem, and thus calculate the transfer function as a Wiener filter from the measured data directly.

However, to calculate the transfer function **f**, one needs to solve equation (2.11), which requires knowledge of both **m** and **d**. It is theoretically possible to calculate the earth's impulse response directly from say, a well test and a base and monitor seismic surveys before and after such a test. Most likely, however, monitor surveys are acquired long after several wells have entered production, making the calculation of a transfer function difficult at best. Nonetheless, in the absence of suitable field data, a geomechanics simulator can be used to estimate the structure's impulse response. Although a rough earth model will do the job, this step allows the inclusion of all available information into the approximated transfer function. Figure 2.1 describes schematically the process through which a structure's transfer function can be approximated and applied with the following steps:

1. Selecting the appropriate input and output set; i.e. selecting/simulating a localized production/injection area and its associated overburden displacement.
2. Once a suitable input and output are known, the system's Green's function or Wiener filter can be calculated, by solving the set of normal equations (2.11).
3. Having calculated the Wiener filter f, it can be used either in forward mode by convolving the filter with known or simulated reservoir data, or in inverse mode, where overburden strains (calculated via equation (1.10) from measured overburden time-lapse time-strains) are deconvolved to invert for the reservoir data.

A similar approach is widely used in seismology in what is known as the empirical Green's function method, where recorded small magnitude earthquakes (usually the aftershocks) are used as Green's functions to describe larger magnitude events (Irikura, 1986; Velasco et al., 1994).

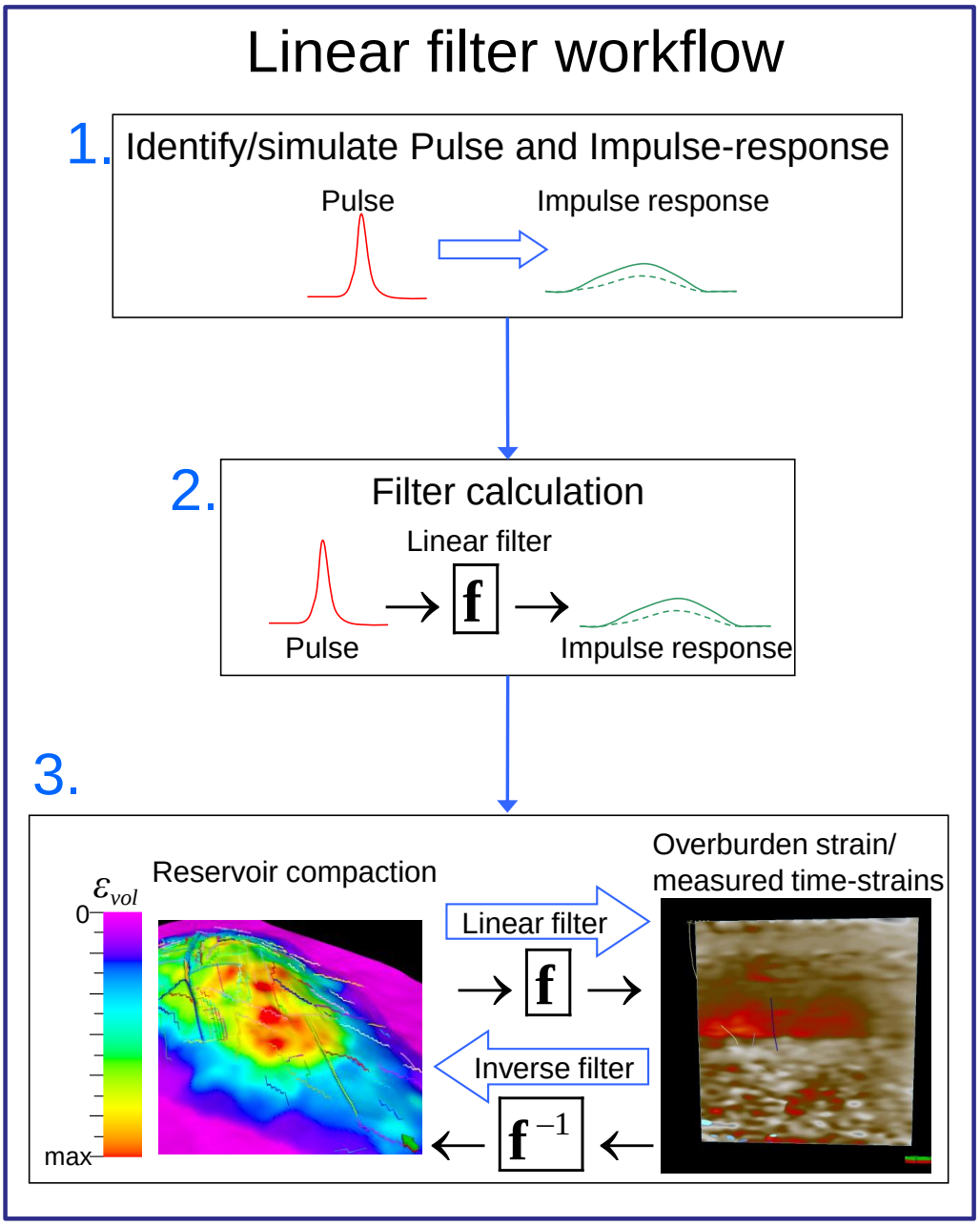

Figure 2.1 Workflow chart explaining how to calculate and use linear filters in time-lapse seismic data for reservoir monitoring.

Following the procedure described above, it will be desirable to calculate the impulse response **f**, as a function of reservoir pressure change. However, reservoirs seldom behave in a linear elastic fashion (Audet and Fowler, 1992), i.e. highly depleted reservoirs will display different elastic behaviour than at initial conditions, and a range of inelastic deformation mechanism is reported, including plastic deformations, pore collapse and for some chalk reservoirs water weakening. Nevertheless, since the overburden materials do not experience any significant changes in their constituency

and only react to reservoir deformation (Vasco and Ferretti, 2005), for the purpose of this thesis they are considered as essentially elastic. Thus, regardless of how the reservoir deforms, the induced overburden displacements is here regarded as elastic.

Thus, as it is ultimately reservoir volume changes that induce the overburden deformations, one can assume the following relationship to be linear

$$\boldsymbol{\varepsilon}_{zz} = \mathbf{f} * \boldsymbol{\varepsilon}_{vol} \tag{2.13}$$

where ε_{vol} is volumetric strain at the reservoir and ε_{zz} is overburden vertical strain. In this formalism, the inverse process is given by

$$\boldsymbol{\varepsilon}_{vol} = \mathbf{f}^{-1} * \boldsymbol{\varepsilon}_{zz} \tag{2.14}$$

with $\mathbf{f}^{-1}$, the inverse filter. Once the Wiener filter, or its inverse are known, it is fairly simple to either deconvolve measured time-shifts (converted to/fom vertical strains via the R factor –equation 1.10) for reservoir volume changes, or to forward model overburden displacements from known or modelled reservoir compaction/depletion. The desirability of the inverse filter is evident, in that it provides valuable reservoir information from surface measurements. Whereas the importance of the forward filter, lies in its use in 4D seismic feasibility studies, or as a fast method to calibrate the R-factor from modelled reservoir compaction and altogether as a measure of accuracy of the simulation. This ability to go easily back and forth proves the perfect tool to close the loop between seismic and simulator, providing valuable information at all stages in the seismic history matching process. However, in order for the Wiener filters to be applicable in the way proposed in this thesis, the filters have to obey two conditions: to be time and space invariant. Time invariance implies that a filter calculated at a time t_1 is still valid at a time $t_2 \neq t_1$. Similarly, space invariance (a consequence of convolution 2.13) entails that a filter calculated from a source $\varepsilon_{vol}(\mathbf{x}_1)$ is still a valid solution for a source $\varepsilon_{vol}(\mathbf{x}_2)$ with $\mathbf{x}_2 \neq \mathbf{x}_1$. In this thesis I assume the system to always obey time invariance and that the effects of space variability are locally negligible; i.e. that a few filters calculated in different parts of the reservoir are sufficient to accurately describe the system. Therefore use of equations 2.13 and 2.14 implies interpolation of the solution between source locations.

2.4 Synthetic example

To prove the applicability of linear filters as a tool for reservoir compaction monitoring from observed overburden strains, a synthetic model is constructed. It is based on a North Sea chalk reservoir (see chapter 5 for more details), where the actual poroelastic properties have been preserved; only the reservoir initial conditions and production scenario have been altered. The reservoir structure is that of an elongated anticline, comprising a highly fractured, high porosity, carbonate reservoir. Additionally, the poroelastic properties are not homogeneous; different elastic constants are defined for each formation and vary laterally inside the reservoir. Table 2.1 shows the ranges of Young's modulus and Poisson's ratio used. Figure 2.2 shows the model's Young's modulus in the top reservoir layer, plus a cross-section of the reservoir interval. The reservoir's geomechanical properties are calculated based on the reservoir model and using published (Fjær et al., 2008) empirical relations as function of chalk porosity.

Layer No.	Young's modulus GPa	Poisson's ratio	Formation
1-4	0,2	0,11	
5-6	0,3	0,11	
7-9	0,4	0,11	
10-12	0,5	0,11	Lark Fm.
13-14	0,6	0,11	
15-16	0,7	0,11	Horda Fm.
17	1,48	0,11	Balder Fm.
18	1,48	0,11	Sele Fm.
19	1,5	0,11	Lista Fm.
20-24	0.26-7.34	0.11-0.34	**Ekofisk Fm.**
25	0.54-7.34	0.11-0.31	Tight zone
26-32	0.18-7.34	0.11-0.35	**Tor Fm.**
33-42	2	0,11	Underburden

Reservoir chalk

Table 2.1 Elastic moduli of the simulation model.

The earth model consists of 105x106x42 cells including 3 cells of sideburden in each direction. Vertically, the model extends from the seabed down to the rigid basement,

with the reservoir at about 2.9 km depth and comprising layers 20 to 32. Excluding the sideburden, the grid is regular in horizontal direction, with cell size 50x100m. A regular grid is a necessary condition consequence of the convolution operation (2.13) which requires regularly sampled data.

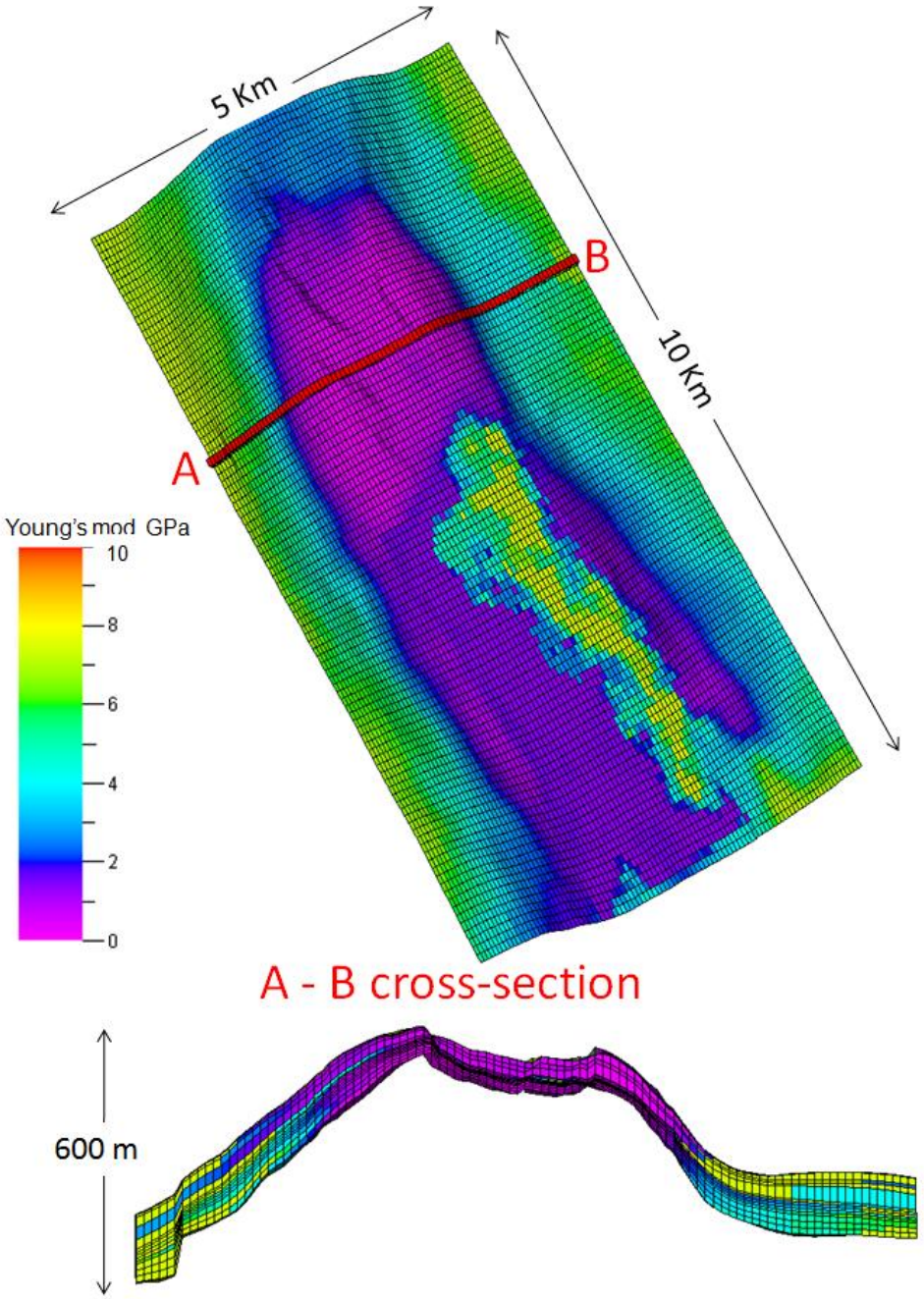

Figure 2.2 The figure shows the Young's modulus at the top reservoir and a corresponding cross-section.

By assuming that the earth (overburden) can be described by a Wiener filter linking volume changes inside the reservoir to overburden strain, we are able to estimate changes of the reservoir from measured time-strains (provided a known R factor), or vice versa. The assumption however, entails that the filter does not change with time, i.e. that the system in question is time invariant. Moreover, in order to be able to calculate the filter, a set of initial conditions is needed; that is some input and output of the system, i.e. a change in the reservoir volumetric train $\boldsymbol{\varepsilon}_{vol}$ and the corresponding overburden strain $\boldsymbol{\varepsilon}_{zz}$.

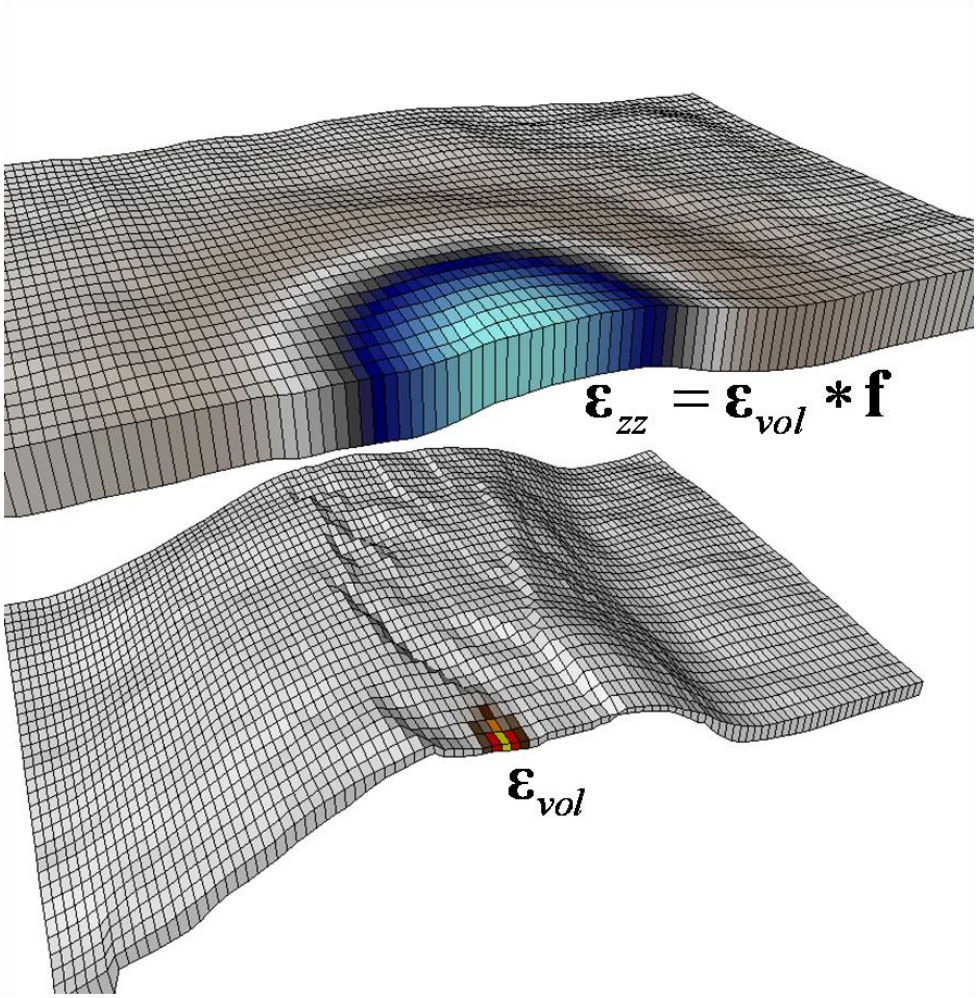

Figure 2.3 Sample of synthetic reservoir volumetric strain and overburden vertical strain used to calculate the subsurface's Wiener filter.

In order to calculate the required Wiener filters, synthetic impulse sources are placed at different locations and are used to calculate the impulse response. The synthetic sources

are one-cell 1 MPa pressure changes with no lateral extension. The sources are then input into a geomechanical simulator whereby the required filter input and output parameters, i.e. reservoir volumetric strain and overburden displacements are created (Figure 2.3).

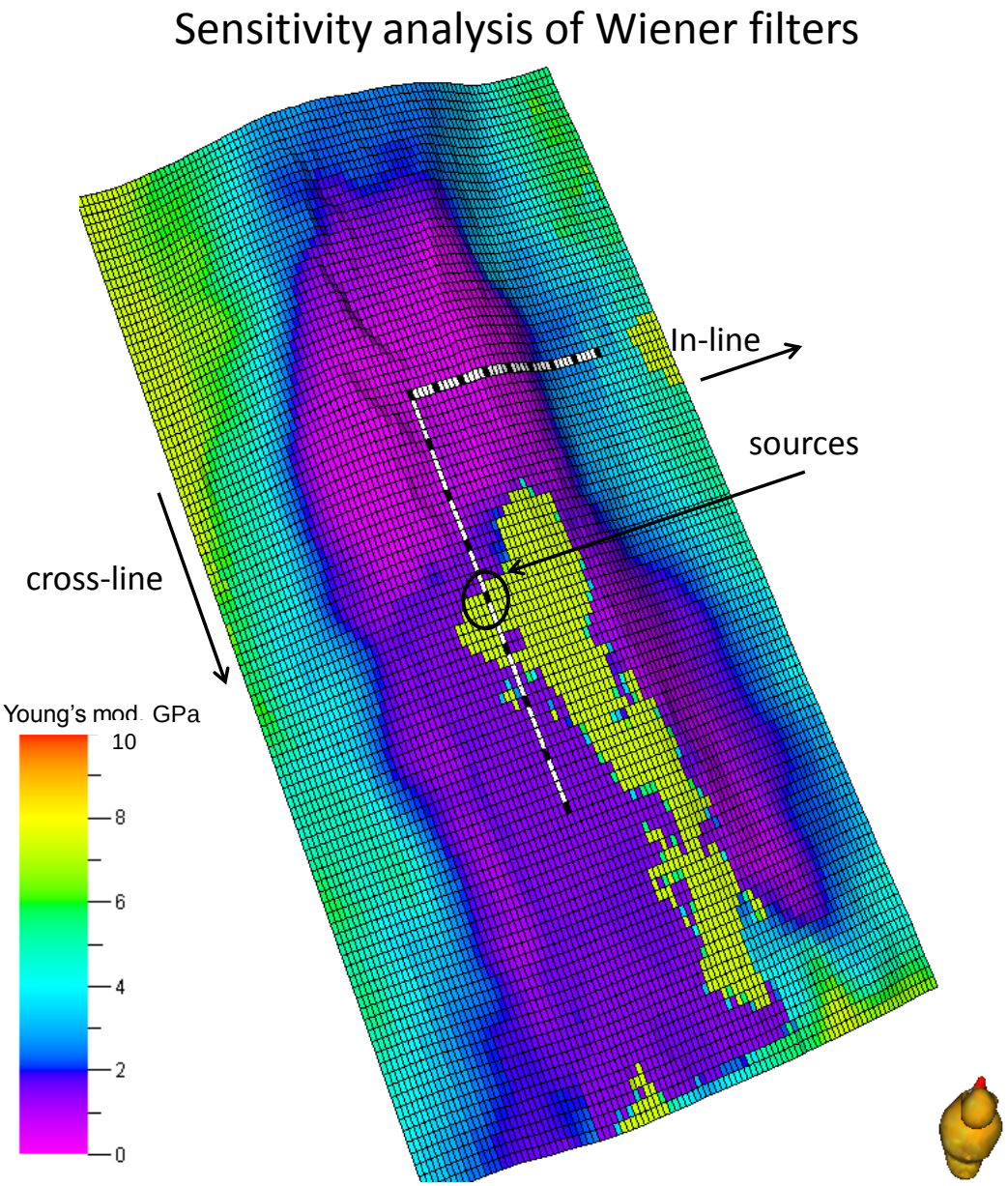

Figure 2.4 Position of sources (black rectangles) for the sensitivity analysis, relative to the top reservoir layer. The yellow area on top of the anticline corresponds to a pinchout of the reservoir formation.

2.5 Sensitivity analyses

Since linear filters are applied by convolution, this implies that lateral heterogeneity (space variability of reservoir properties and structure) should have negligible effect on the solution. For example, if a filter f has been calculated with a source $\varepsilon_{vol}(\mathbf{x}_1)$ as input, such that $\varepsilon_{zz}(\mathbf{x}_1) = f * \varepsilon_{vol}(\mathbf{x}_1)$, the same filter should also be a solution of source $\varepsilon_{vol}(\mathbf{x}_2)$ with $\mathbf{x}_1 \neq \mathbf{x}_2$ such that $\varepsilon_{zz}(\mathbf{x}_2) = f * \varepsilon_{vol}(\mathbf{x}_2)$. In order to test the validity of the previous statement, a sensitivity analysis is made, whereby several sources are placed in in-line and cross-line direction, as shown in Figure 2.4.

The test consists of calculating the Wiener filter for the labelled *source 1*, and applying it both for forward and inverse modelling (equations (2.13) and (2.14) respectively) to nine different sources (including itself), in both in-line (Figure 2.5) and cross-line (Figure 2.6) directions. This should give a combined measure of the errors associated with dipping structure and lateral inhomogeneity. The figures show a cross-section illustrating the position, structure and mechanical properties (Young's modulus) for each source.

For forward modelling (blue line), the Wiener filter calculated from source 1 (i.e. simulated reservoir volumetric strain and overburden vertical strain) is convolved with all the sources volumetric strain to estimate the overburden's vertical strain at a given horizon, corresponding to layer 16 of the model roughly 500m above the reservoir. Note that this implies applying the same filter at different locations. The curves show the normalized root-mean square error or NRMSE (as defined by Kragh and Christie, 2002) of the estimated maps compared with the "real" simulated overburden strain. In the inverse modelling scenario (red line), the simulated overburden strain from all sources at the same horizon (16) is deconvolved with the filter from source 1 to estimate all the volumetric strains of the corresponding sources. The NRMSE for the inverse estimation is relative to the sources' true simulated volumetric strain.

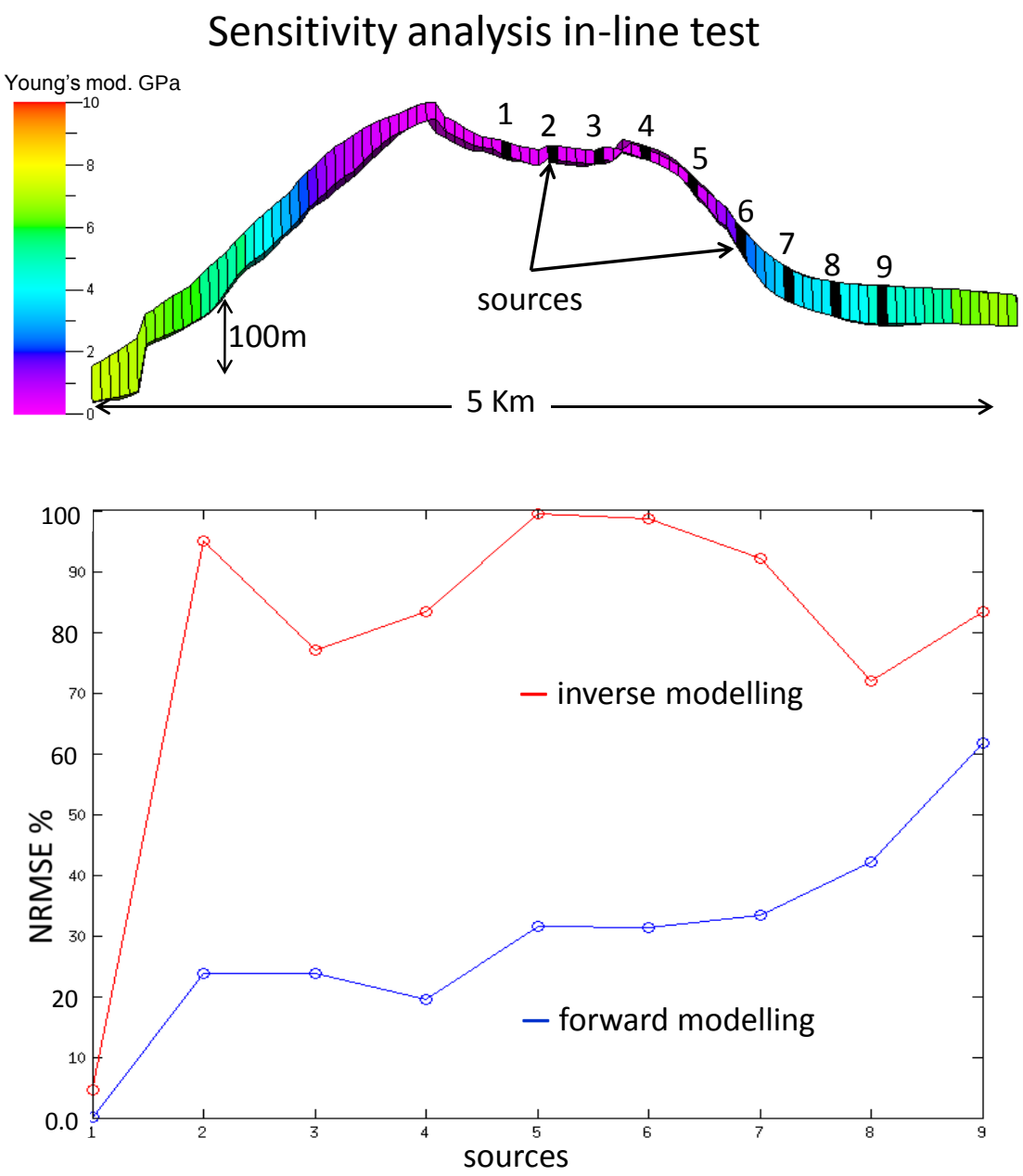

Figure 2.5 Test results in the in-line direction, for both forward an inverse modelling. The top cross-section illustrates the position, structure and mechanical properties (Young's modulus in GPa) of the in-line sources relative to the model's reservoir layer, as shown in Figure 2.4. The bottom curves are the NRMS error with respect to the simulation results.

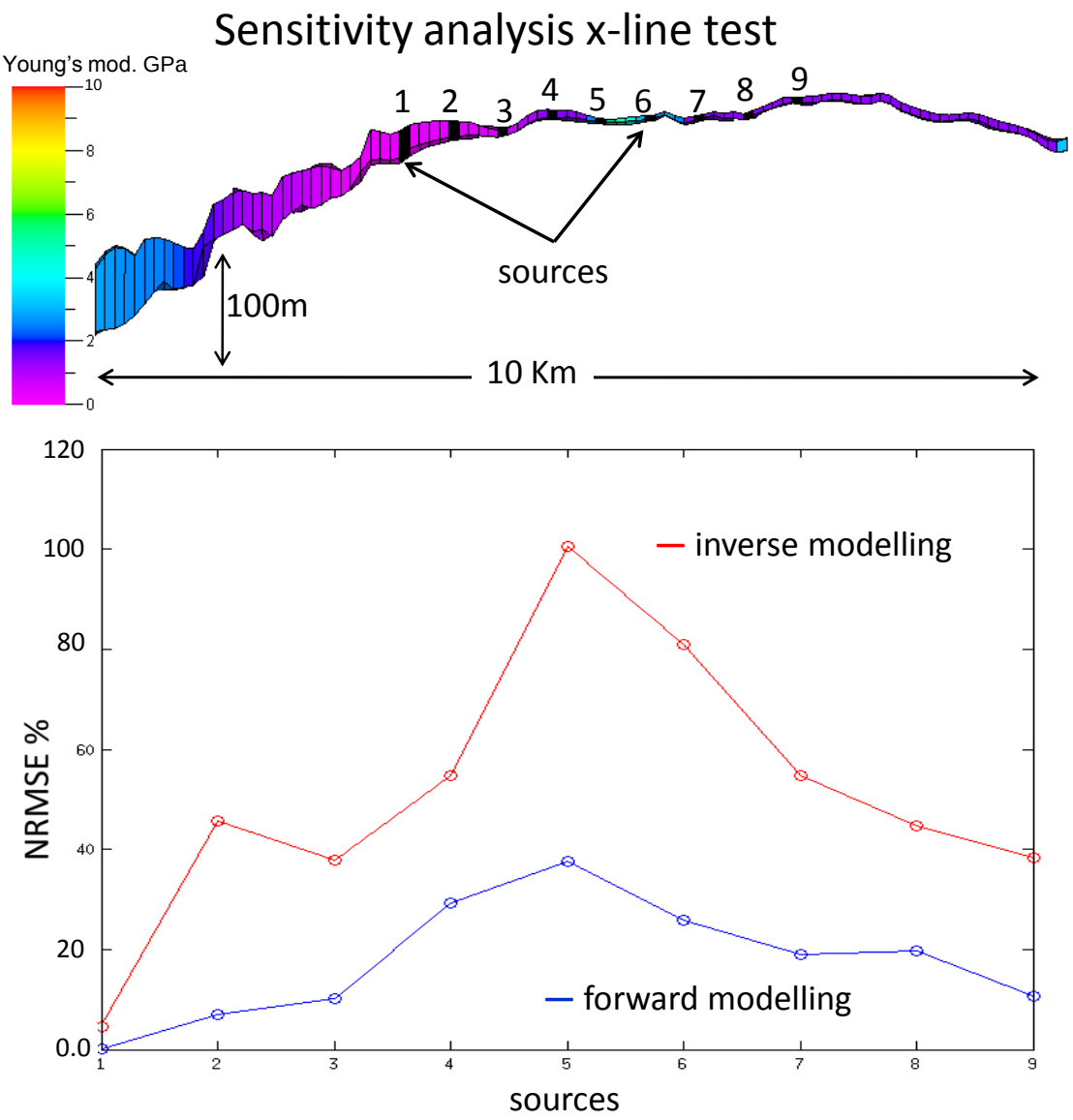

Figure 2.6 Test results in the cross-line direction, for both forward an inverse modelling. The top cross-section illustrates the position, structure and mechanical properties (Young's modulus in GPa) of the cross-line sources relative to the model reservoir layer, as shown in Figure 2.4. The bottom curves are the NRMS error in relation with the simulation results.

The forward modelling error for the in-line test, behaves as one would expect; it increases as one moves farther away from the filter's source. However, the inverse modelling error appears fairly erratic revealing the ill-conditioned nature of the problem; i.e. uniqueness and stability issues. These traits are common to all inversion problems (Aster et al., 2005; Tarantola and Valette, 1982; Tikhonov and Arsenin, 1977), therefore the existence of different a priori constrains and regularization techniques. Both Du and Olson (2001) and Hodgson et al. (2007) faced ill-conditioning

when inverting a Geertsma-type Green's function and tackled it by using first order Tikhonov regularization and a constraining term based on an initial model. Wiener filters differ with Green's functions in that inversion occurs when approximating the system as opposed to the system parameters. Therefore, calculation of Wiener filters being an inverse problem is no different and also experience ill-conditioning. In this study I have addressed stability by adding also first order Tikhonov regularization in the objective function 2.11. However, no constraining terms have been included, since being this a new technique it is not yet clear how the solution of the filter can be constrained. Nonetheless, non-uniqueness is addressed by inverting from the overburden directly to the reservoir grid and calculating a model-based Wiener filter, which should reduce considerably the number of possible solutions. Still, nonuniqueness is intrinsic to potential field problems which are analogous to the present problem of a deformation field (strain) due to reservoir compaction. Thus, nonuniqueness inevitably arises in inverse modelling both with Green's functions and Wiener filters. The reason being that nonuniqueness is a characteristic of rank-deficient (i.e. zero eigenvalues) discrete linear inverse problems. Therefore, models, $\mathbf{m}_0$, that lie in the null space of **G** are nontrivial solutions to $\mathbf{G}\mathbf{m}_0 = 0$, or in the same way nontrivial solutions to $\mathbf{f}^{-1} * \mathbf{d} = 0$ and any linear combination of these null space solutions can be added to a particular model satisfying equations 2.9 or 2.12 respectively without affecting the fit to the data.

Therefore, a sharp localized source in the reservoir (**m**) as those used in this example, yields a smaller NRMSE for forward modelling than the inverse modelling from the more laterally spread overburden strain (**d)**. As a consequence, the nature of the problem dictates that as the deformation field spreads in the subsurface and the spatial wavelength of the deformation increases, the more under-determined the system becomes and thus, the higher NRMSE. On the other hand, for the cross-line test (Figure 2.6) the error is biggest where the reservoir is thinnest, i.e. where the reservoir formation has almost all been eroded (sources 5 and 6).

In general, it can be concluded that the inverse modelling error will always be larger than the forward case regardless of the method used for the inversion. The basis of this lies in that as the "strain field" propagates out from the source, resolution is lost with distance. Thus, the farther away the observation point is, the more "diffuse" the

reproduction of the source will become. For this reason, the vertical resolution is also put to test (Figure 2.7).

In order to examine vertical resolution, the overburden vertical strains at layers 10 to 19 generated by cross-line sources 1, 2 and 3, were deconvolved using the filter from source 1 and compared with the simulated corresponding volume changes. The NRMS error demonstrates that the farther one "looks" from the reservoir more information is lost, resulting in a higher NRMS. However, of particular importance is the behaviour at horizon 15, where the error is highest; a consequence of the structure of that particular horizon, which presents a "bump" right on top of where source 1 is located.

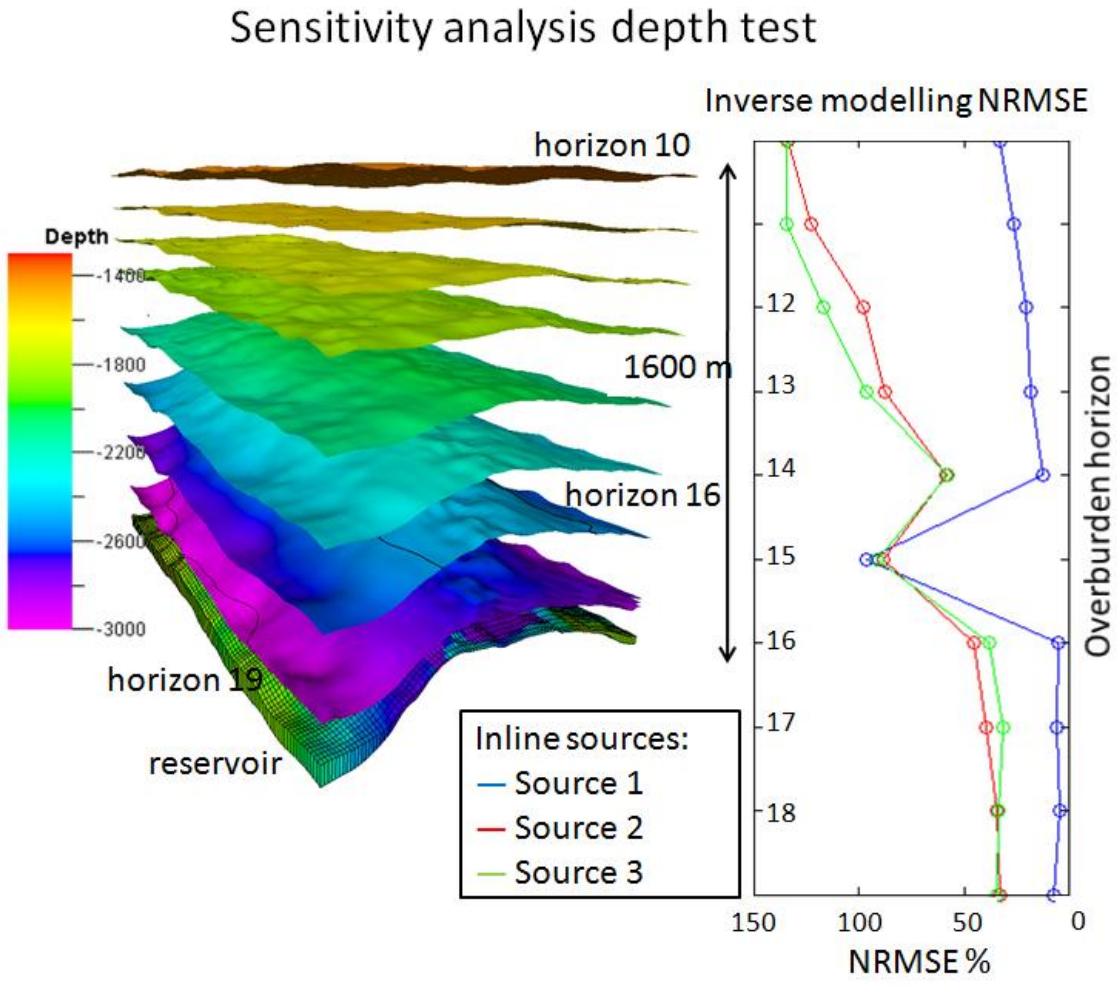

Figure 2.7 Vertical resolution test, showing the relative position of the analyzed overburden horizons relative to the reservoir (left), and the NRMS error (right) of inverse modelling cross-line sources 1 to 3 from horizons 10 to 19.

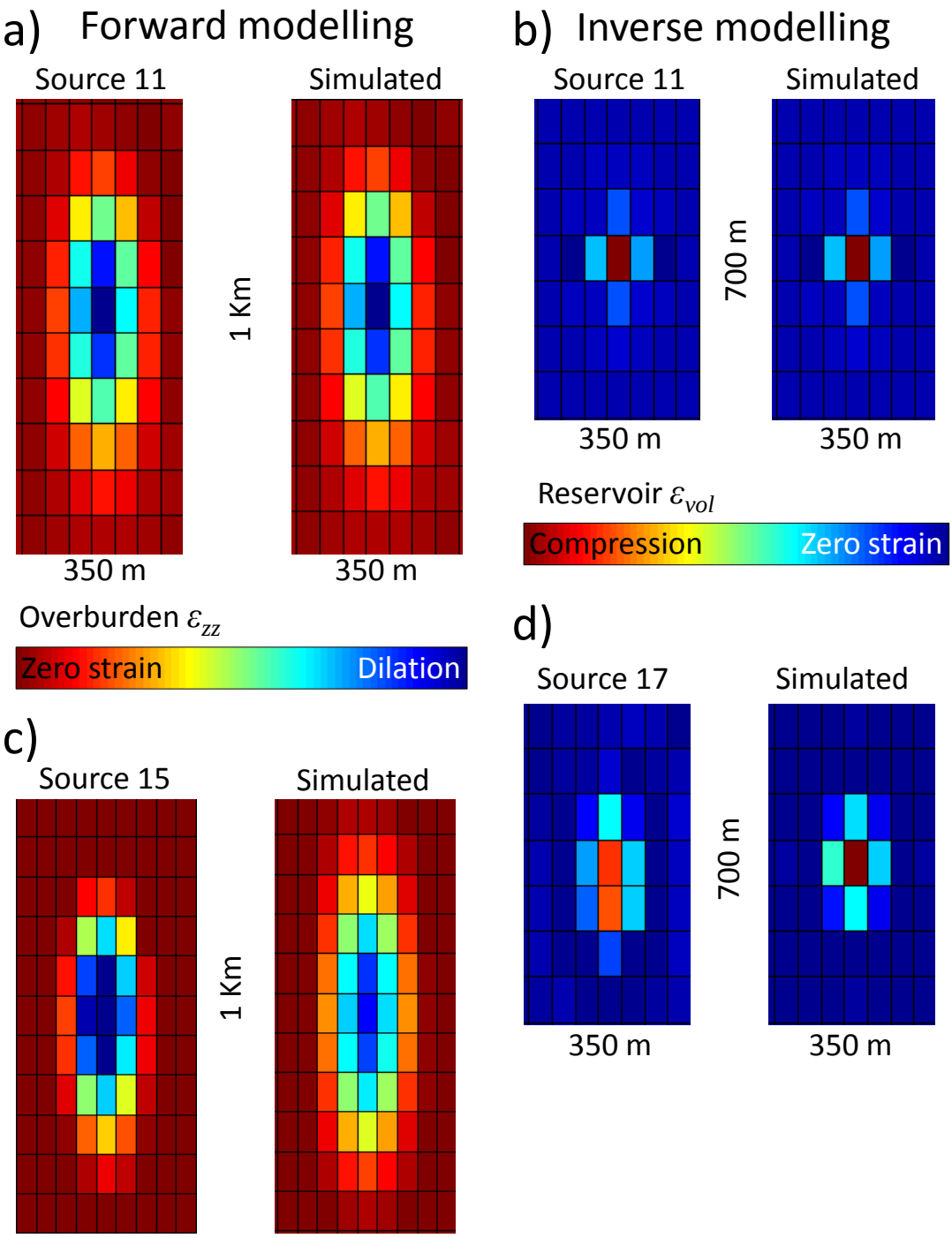

Figure 2.8 Zoomed-in map view of the vertical strains at horizon 16 for forward modelling (a and c) and reservoir volumetric strain (b and d) for inverse modelling. In both cases, the dimensions of the zoomed-in are are shown i.e. 1km x 350m for the vertical strains and 700m x 350m for the volume changes.

On the whole, the NRMS values appear too high, the cause of which is better to examine up-close. Figure 2.8 shows a close up of the simulated and estimated overburden strains and reservoir volumetric strain for two sources; 1 and 5 for forward modelling (a and c) and 1 and 7 (b and d) for inverse modelling. In the notation used *source 11* represents the Wiener-filter determined from source 1 convolved with source 1 (volumetric train at source at location 1) to forward model the corresponding subsurface strains. In the same way, source 15 refers to the resulting strains of convolving filter 1 with in-line source 5 (volumetric train at source at location 5). Similarly, the reservoir's volume changes for sources 11 and 17 correspond to overburden strain of source 1 deconvolved with filter 1 and overburden strain of in-line source 7 deconvolved with filter 1. In all four cases, the "true" simulated strains and volume changes are displayed side by side of the estimated maps.

So far it has been shown that the Wiener filter formalism can be employed for subsurface characterization with reasonable accuracy. Still, the question remains of whether that technique represents an improvement over existing inversion schemes. For instance, a Geertsma type Green's function as used by Du and Olson (2001) and Hodgson et al. (2007). In contrast to linear filters, Geertsma's linear inversion takes about 100 times more computational time, and this excludes the additional time it takes to find an optimum damping coefficient (Gubbins, 2004). On top of this, Geertsma calls for a homogeneous half space involving a guess as to which single material better approximates a complex subsurface. After multiple tests, the best fit between Geertsma and the simulation model is achieved with a Young's modulus of 0.1 GPa and a Poisson's ratio of 0.1. Note that this value for the Young's modulus is considerably lower than all the values used in the reference geomechanical model (Table 2.1). For this reason, only three points are modelled, corresponding to cross-line sources 1, 2 and 5. Geertsma's advantage however, lies in that it does not require a geomechanical simulation, though it still needs a gridded model of the subsurface.

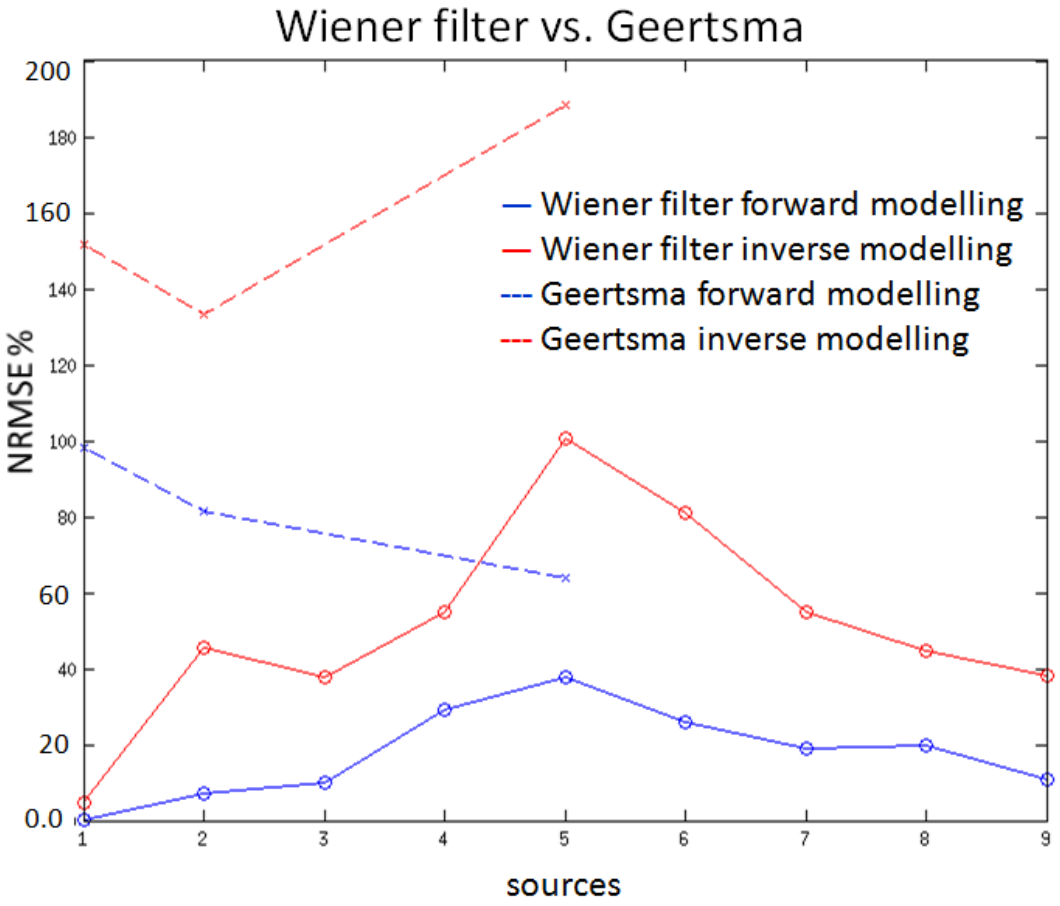

Figure 2.9 NRMS error employing Wiener-filters (solid lines) and Geertsma type Green's functions (dashed lines), both for forward (blue lines) and inverse modelling (red lines) of overburden strains. Only three points have been calculated using Geertsma, as it is computationally more expensive.

The NRMS error of the two methods is shown in Figure 2.9, for both forward and inverse modelling, with the dashed lines corresponding to Geertsma Green's function and the solid lines to the Wiener filters. The Wiener filter approach consistently shows a lower NRMS error, about a third if no less than that of the linear inversion. A close-up of the Geertsma solutions (Figure 2.10) reveals large dissimilarities between the calculated and the simulated maps. Note that the scale between the maps varies, a consequence of over-smoothing when forward modelling, or instability of the inversion to map small changes.

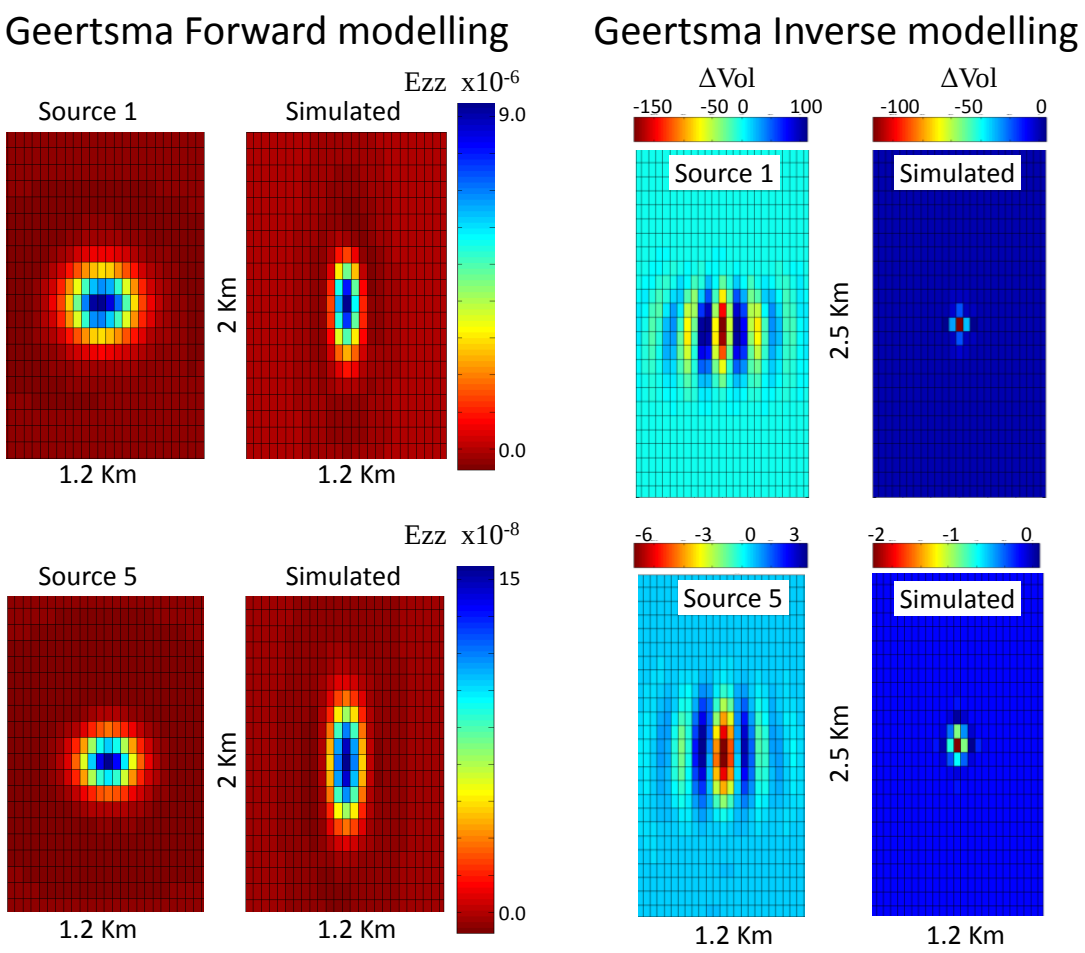

Figure 2.10 This maps, in analogy to Figure 2.8, show a close-up of the estimated overburden vertical strains calculated with Geertsma's equations (a and c), for sources 1 (a) and 5 (c). The right figures correspond to the inverted reservoir volume changes also for sources 1 and 5 (b and d respectively). For all cases the actual simulated maps are displayed adjacent to the calculated ones.

When considering the Wiener filter results, it is worth noting that the errors, although high, correspond for the sources in question, to localized perturbations where minute differences yield high NRMS values. Therefore, for wider distributions where more data points contribute to the estimates, the NRMS error is expected to be lower, as will be shown in the next section. Additionally, carefully selected source locations produce an equal number of estimates that when stacked together result in a more robust final estimate.

2.6 Full field tests

A full field one way coupled geomechanical simulation was performed using a history matched reservoir model from the South Arne field. Details about the model and field will be given in Chapter 5. Suffice to say that the reservoir is composed of two formations, Ekofisk and Tor, separated by a low porosity low permeability interval at the bottom of the Ekofisk formation, known as the Tight zone.

In dealing with multilayered reservoirs, Wiener filters are especially handy; only now synthetic sources are stacked on top of each other, one for each flow unit. Assuming such units to be isolated and that no interaction takes place between them, the total overburden strain can be regarded as the sum of the strains generated separately by each of the reservoir formations. Thus, by knowing the fraction of the total measured overburden strain caused by each reservoir interval at the different source locations, one can apply the corresponding filters as appropriate.

The resulting simulated overburden vertical strains at layer 16 (roughly 500m above the top reservoir) are used to estimate the reservoir volumetric strain. In total, eight sources are employed, four per each reservoir formation, to calculate an equal number of filters. The sources are distributed as shown in Figure 2.11 and located in areas of high well activity. The procedure followed is analogous to real measured time-strains being used instead of simulated strains; i.e. the simulated vertical strains at the selected overburden layer are used both for the Gertsma inversion and the Wiener filter deconvolution. Figure 2.12 shows a comparison between the true simulated strains (Figure 2.12a and d), the Wiener filter estimates (Figure 2.12b and e) and Geertsma's linear inversion (Figure 2.12c and f). The Wiener filter estimated volume changes for the Ekofisk and Tor formations have an NRMS of around 36% and show an impressive amount of detail; i.e. faults and individual injectors and producers can be resolved. Geertsma on the other hand, has an NRMS about twice as much as the Wiener filters and although it captures the overall distribution remarkably well, the small details are lost due to over smoothing. In short, Wiener filters are twice as accurate as the Geertsma type Green's functions with considerably faster computing time.

Figure 2.11 The red circles show the location of the sources used to estimate the Wiener filters. A total of eight stacked synthetic sources were employed, four per each reservoir unit, to calculate an equal number of filters.

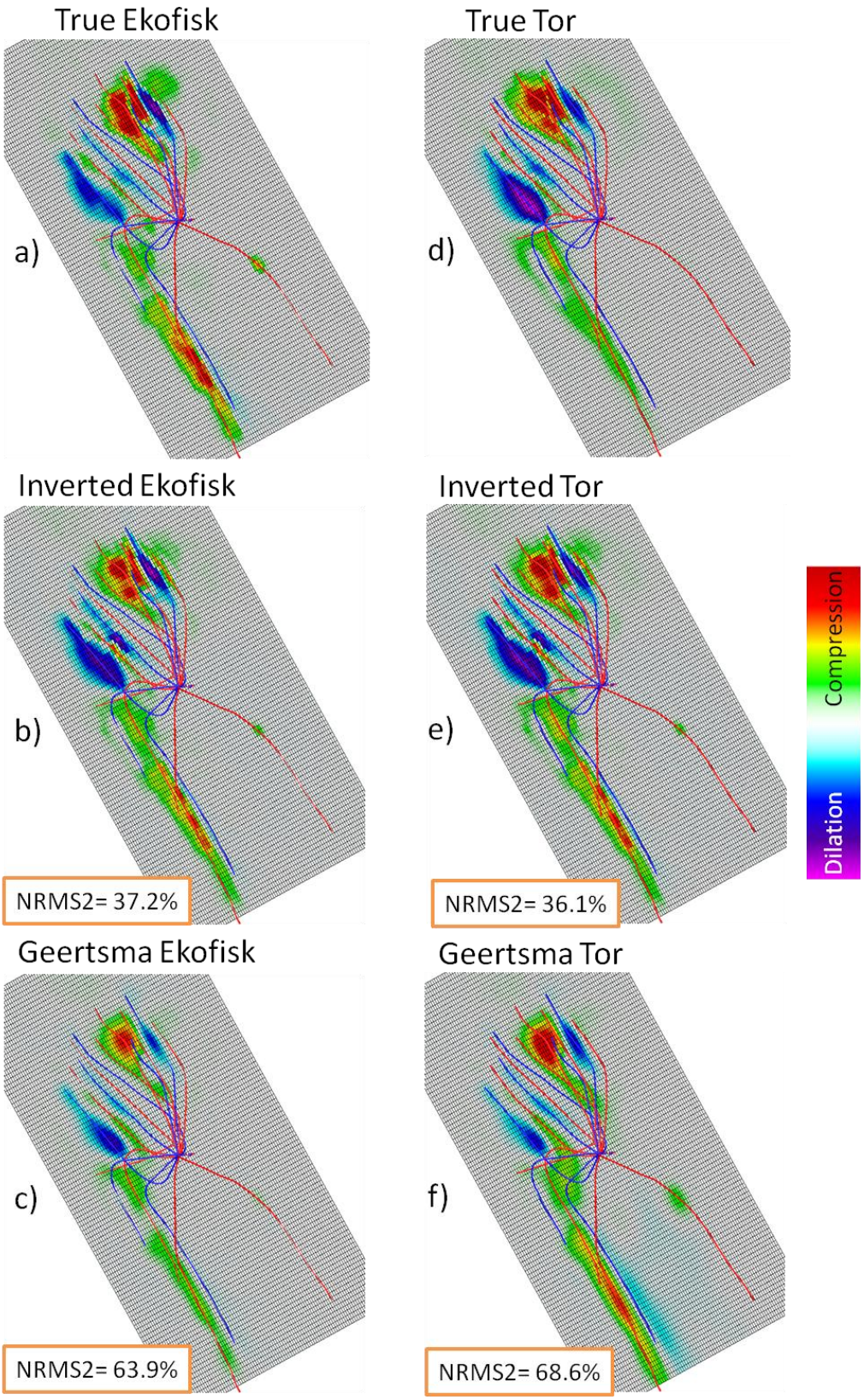

Figure 2.12 True simulated reservoir volume changes for the Ekofisk (a) and Tor (d) formations, for comparison with estimates using Wiener filters (b and e) and estimates from Geertsma's linear inversion (c and f). The NRMS of both estimation processes is also shown.

2.7 Summary

The proposed methodology has proven successful and accurate for recovering reservoir volume changes. By numerically calculating the transfer function complicated and compartmentalized structures can be accurately described. In addition, complex distributions of reservoir compaction/depletion can be estimated, with the potential of being able to resolve multiple reservoir units

The Wiener filter technique is fast and robust and the final modelling error although still high, represents a considerable improvement when compared with the widely used Geertsma approach. Although the use of a geomechanical simulation to calculate the impulse response can be seen as a drawback, the method is unique in that given the correct measured data, the Wiener filters could be calculated directly from it. As a consequence, the method requires some user interaction and knowledge of the model in order for an optimum set of transfer functions to be calculated. Moreover, the method's ability to go backwards and forwards between seismic and simulator makes it the perfect tool for "closing the loop" for dynamic reservoir characterization. Once the Wiener filter has been computed, it is only a matter of doing a convolution or deconvolution to go from simulator to seismic or vice versa.

Chapter 3

3 The Elgin field: An application to overburden strain inversion

In this chapter, the concept of linear filters described previously in chapter 2, is applied to observed data from the Elgin field. Elgin is an HP/HT gas condensate sandstone reservoir located in the South Central Graben Area, in the UK sector of the North Sea. Measured time-shifts from a five year time-lapse period are then converted to physical vertical strains by means of the R-factor. Values for 'R' are readily available from literature and have been obtained by comparing simulated physical strains with measured time-strains. Subsequently, vertical strains are deconvolved with the calculated Wiener filters to estimate the reservoir's volumetric strain and effective stress changes for the three separate reservoir sands. The estimates are compared with simulations from history-matched geomechanical and reservoir models.

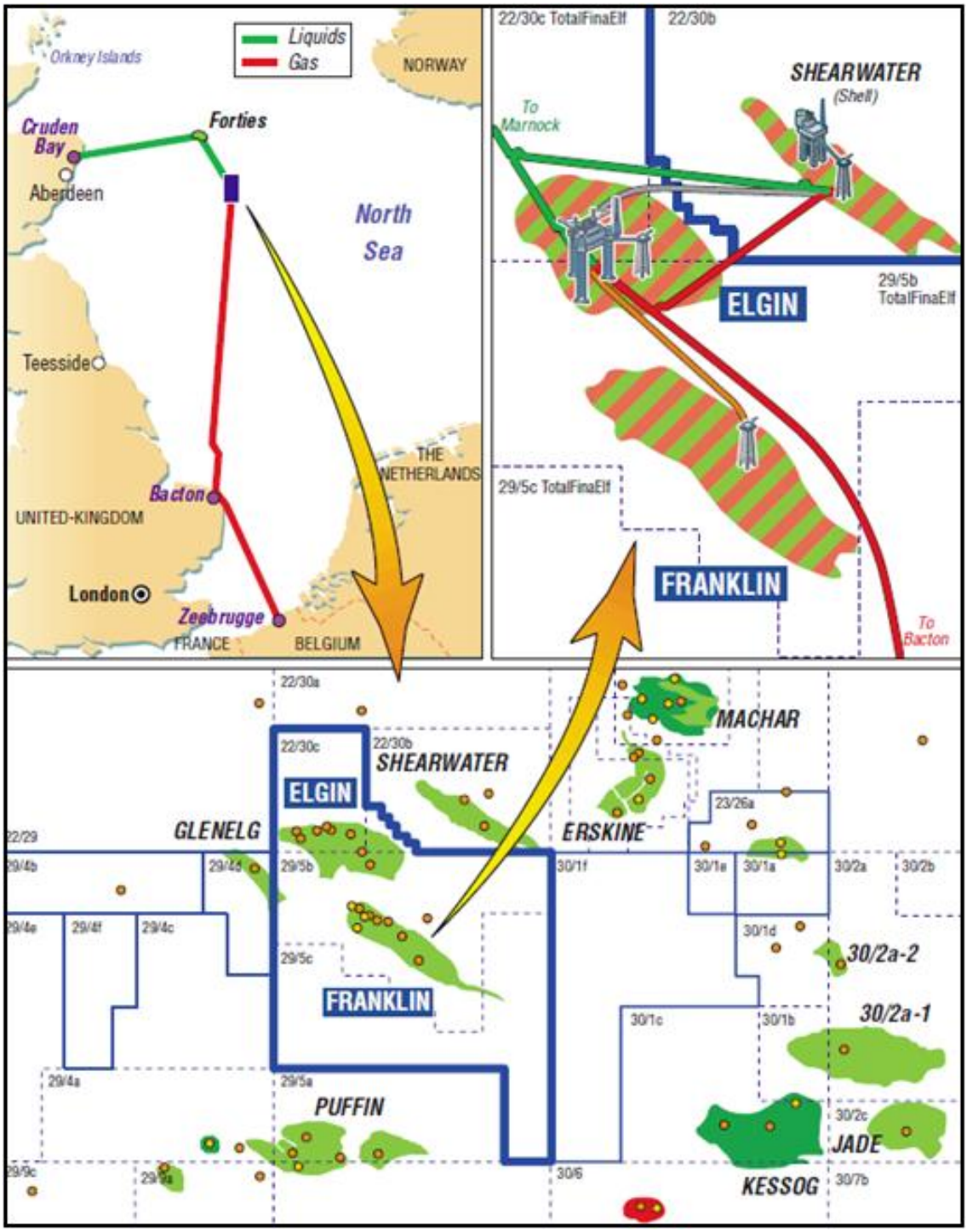

Figure 3.1 Location of the Elgin field, 240 km east of Aberdeen, in the hub of the Central Graben area (TOTAL S.A., 2002).

3.1 Field description

The Elgin field is located 240 km east of Aberdeen in the UK sector of the North Sea, in the South Central Graben area in blocks 22/30b, 22/30c and 29/5b (Figure 3.1). Elgin was discovered in 1991, following the discoveries of neighbouring Franklin (1986) and Shearwater (1988). These fields are remarkably deep compared to most North Sea reservoirs, resulting in much higher reservoir pressures and temperatures. As a result, the joint Elgin/Franklin development was hailed as the world's largest HP/HT project of the time.

The formations in the Central Graben basin cover a complex geological setting resembling a fractured bowl. The Elgin field comprising a faulted anticline lies almost six kilometres below the seabed and contain high pressure, high temperature gas condensate. Normal faulting during the Cretaceous sedimentation divided the Jurassic reservoir into numerous isolated fault blocks, Figure 3.2. The main reservoir comprises very fine grained, shallow marine sandstone of the Upper Jurassic Fulmar Formation, locally named the Franklin sand. Three main reservoir units are identified, from top to base: Fulmar C sands, of moderate reservoir quality; Fulmar B sands with the best reservoir properties are the main contributor to production; and Fulmar A sands generally of poor quality. The overall Fulmar sand pay thickness is about 170 m with an average porosity of about 19 %. The good reservoir quality is due to the significant amount of porosity preserved by the extreme overpressure and favorable diagenetic processes. The combination of extreme reservoir conditions with an initial pressure of 16,000 psi (110 MPa) and temperatures of 190°C meant that production could not start until 2001, once these challenges could be addressed.

The source rocks of the Franklin sands are various; i.e. the shales and coals of the Upper and Middle Jurassic periods. The main sources are the claystones of the Heather Formation and of the overlaying Kimmeridge Clay Formation, and Middle Jurassic coals and Carbonaceous shales of the Pentland Formation. Initially trapped hydrocarbons were oils and conversion to gas began during the Early Pliocene, with significant gas generation due to the high burial rate in the Plio-Quaternary phase. These hydrocarbons are sealed in the reservoir by Upper Jurassic shales and Lower Cretaceous marls (Burns et al., 2005).

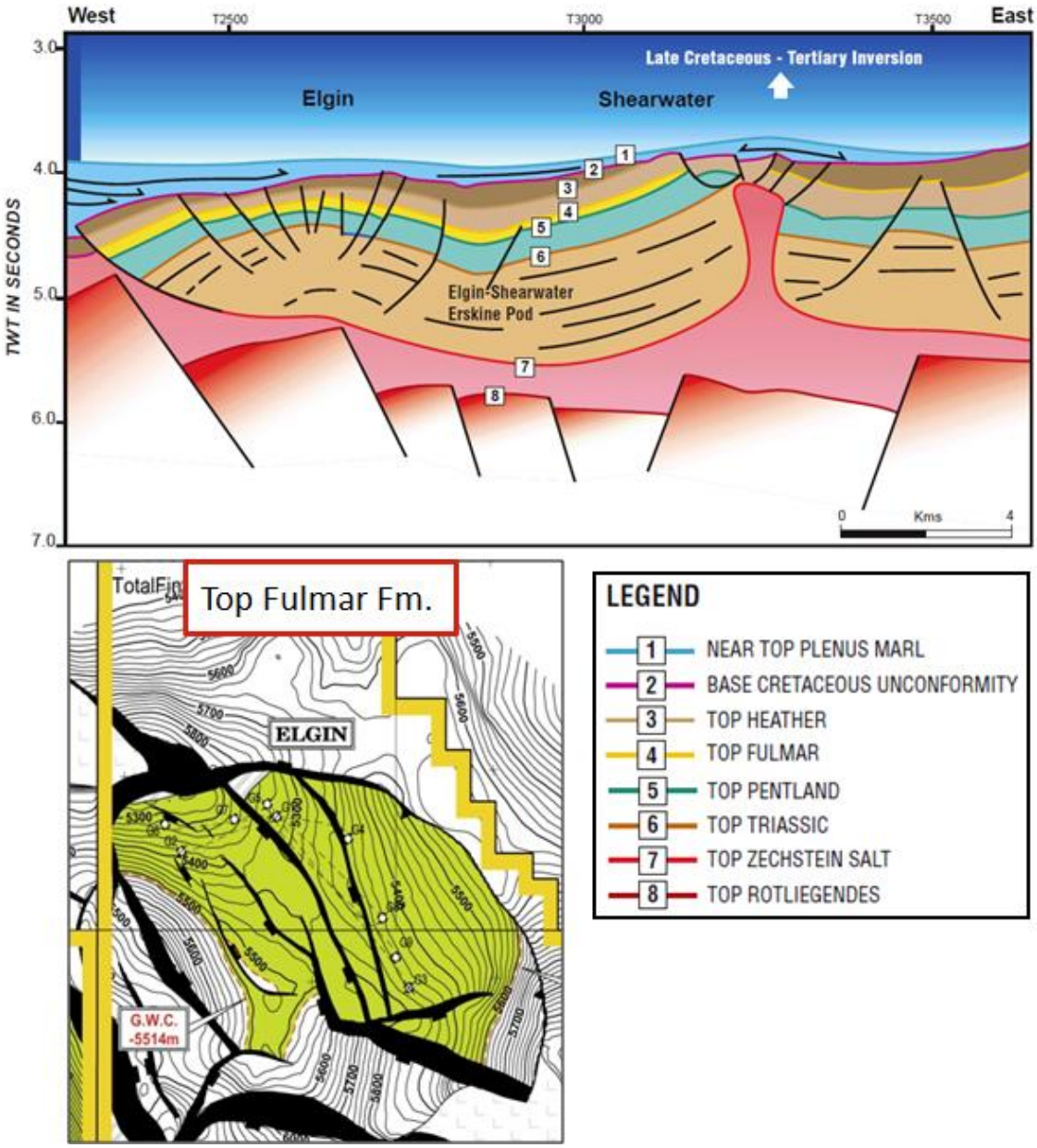

Figure 3.2 Geological cross section of Elgin and Shearwater (top) and depth map (bottom left) of Elgin's reservoir sands of the Fulmar formation. (TOTAL S.A., 2002)

3.2 The 4D seismic campaign

A case study presented in 2003 by Hatchell et al. (2003) found that production at neighbouring Shearwater Field gave rise to geomechanical effects that could be measured with time-lapse seismic throughout much of the subsurface in and around the reservoir. He reported that, small variations in layer thickness and seismic velocities manifested themselves as time-shifts between the base and monitor survey. Encouraged by this case study, in order to monitor the field depletion and well casing integrity issues at Elgin and Franklin, a 4D seismic feasibility study was carried out in 2004. Coupled geomechanics and reservoir model of four different history matched scenarios were initially considered (Figure 3.3). Fault transmissibilities were varied on Elgin, in particular between the undrilled SE block and the eastern aquifer. On Franklin varying degrees of communication were assumed within the downdip part of the field (Taylor et al., 2007). Synthetic 3D ray tracing was used in order to determine the overburden time-shifts. The corresponding modelled time-shifts are shown in Figure 3.4.

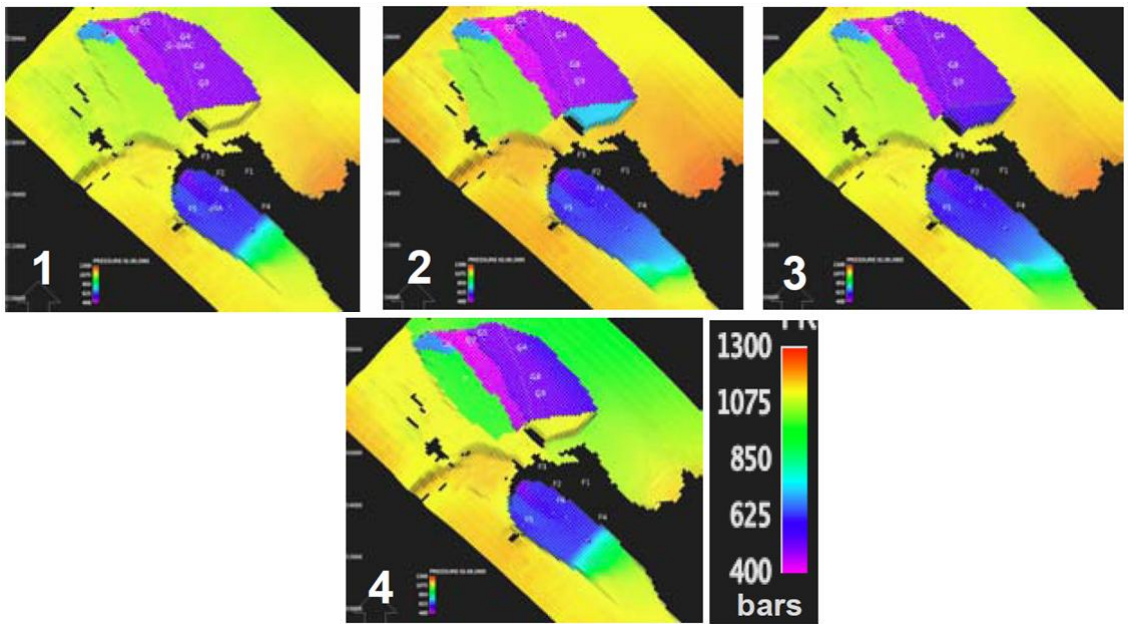

Figure 3.3 Four different history matched reservoir depletion scenarios for the Elgin and Franklin Fields (Taylor et al., 2007).

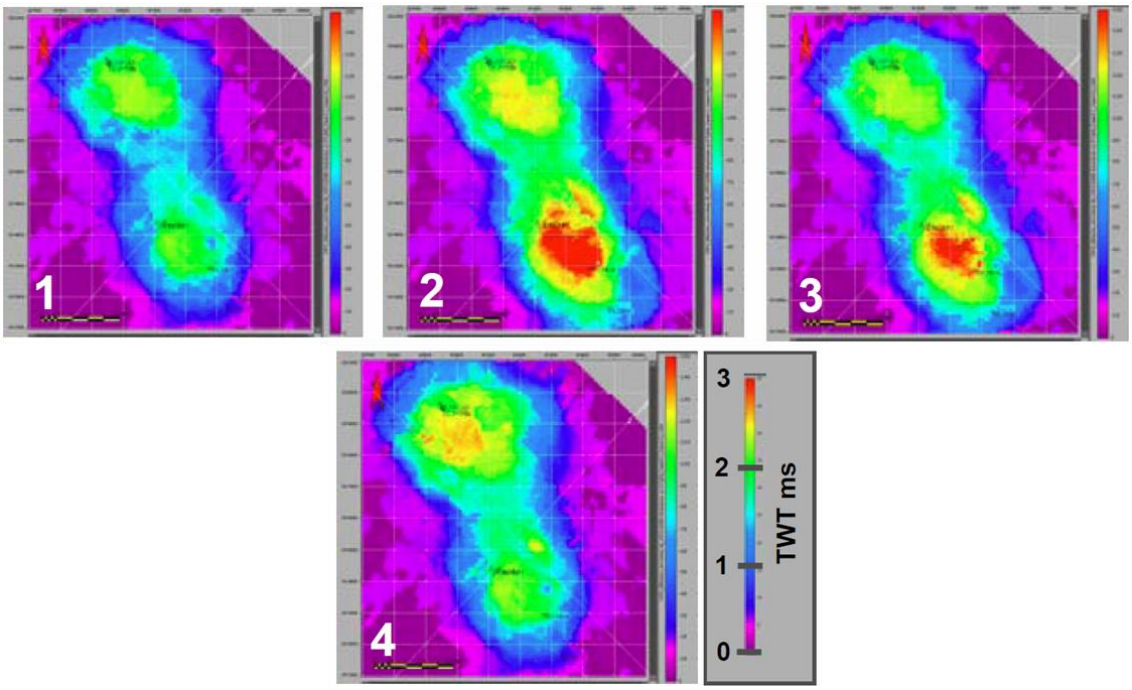

Figure 3.4 Modelled time-shifts at the top of the reservoir (Top of Plenus Marl) for the corresponding reservoir models shown in Figure 3.3 (Taylor et al., 2007).

The modelled time-shifts indicated that meaningful and measurable travel-time differences between the monitor and baseline surveys of up to 3 ms could be expected. Therefore a 4D project followed, culminating in the acquisition of a monitor survey in 2005 with a 1996 baseline. The 2005 survey was acquired with parameters that, as far as possible, matched those of the base survey. It also included a large part of the Shell-operated Shearwater Field, as well as the Glenelg and West Franklin fields that in 2005 were yet to be produced.

The 1996 baseline survey covers an area of 290 km^2 and was acquired interleaved with a single source and 6 cables, 4600m long, with 75m spacing. Final bin size is 12.5m by 18.75m (Taylor et al., 2007). The two surveys went through identical parallel processing sequences. Time and depth processing were carried out using the same velocity field, phase, time and amplitude corrections derived from the baseline and applied to both surveys. The time-shifts were calculated using an in-house warping inversion (Williamson & Cherrett, 2007; Grandi et al., 2009), where the warp field is calculated by a least-squares inversion that minimizes the difference between the traces of the base and monitor survey.

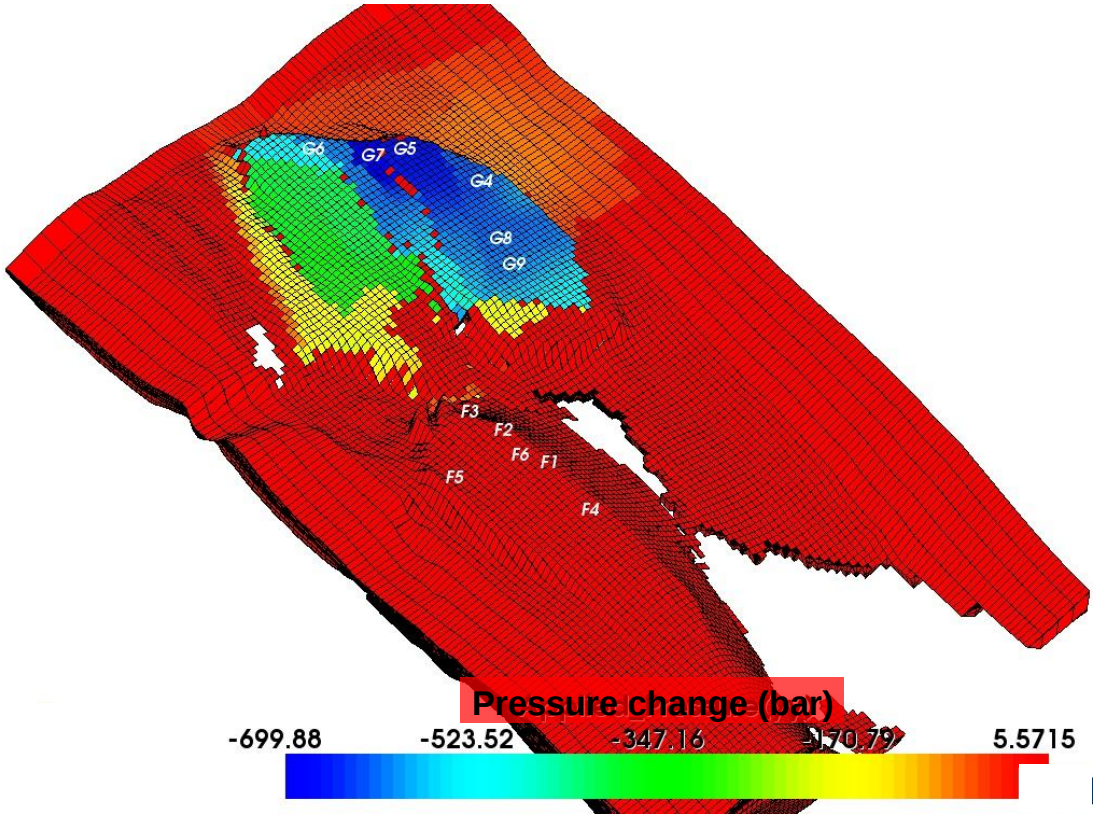

Figure 3.5 Elgin and Franklin reservoir section of the full field geomechanical model grid.

3.3 Geomechanical full field model

Both the reservoir and geomechanical simulation models used in this study have been supplied by the operator. The reservoir part of the geomechanical model covers both the Elgin and Franklin fields as presented by de Gennaro et al. (2008) and is composed of 65×140×34 cells, which comprise the C, B and A Fulmar sands, and the Pentland formation (Figure 3.5). Starting with the reservoir grid, 56 overburden layers are added extending the model up to the seabed. The extended grid is further embedded in a sideburden and underburden to diminish undesired boundary effects (Figure 3.6). The resultant extended geomechanical model is composed of 83×158×99 cells. The mechanical behavior of the model is assumed to be linear-elastic and isotropic. The behaviour of the faults is considered to be elastoplastic and governed by the normal and shear stiffness. The values used (shown in Table 3.1) are from the de Gennaro et al. (2008) study.

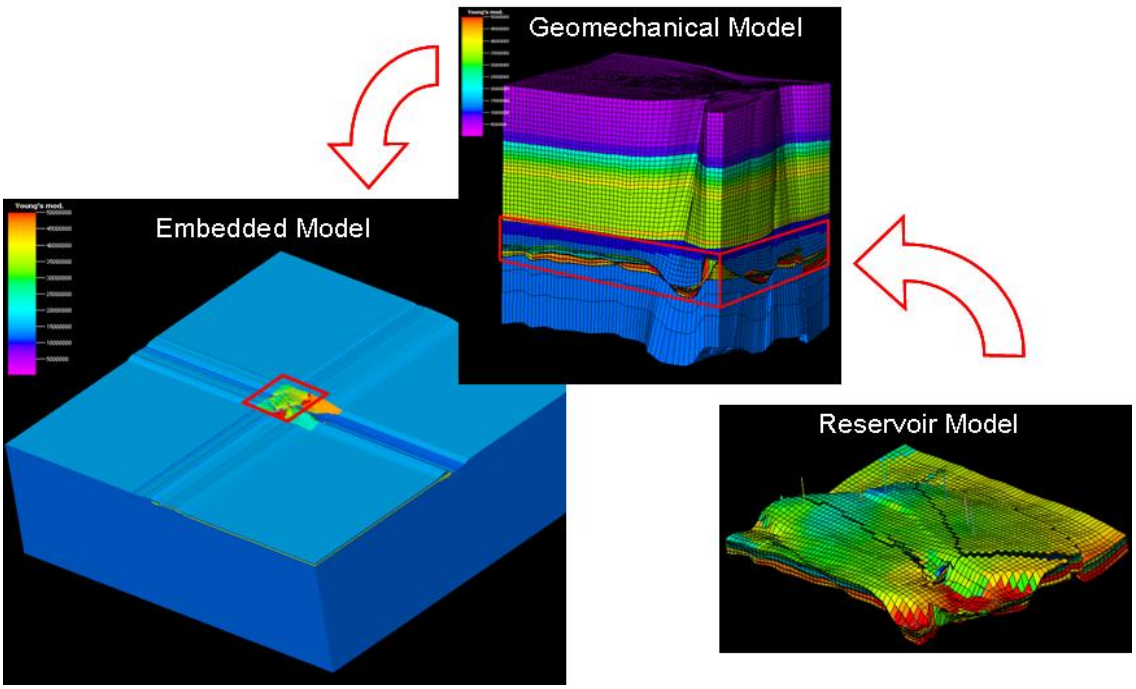

Figure 3.6 Schema showing how the extended geomechanical model is created starting from the reservoir grid.

Layer No.	Young's modulus GPa	Poisson's ratio	Formation
1 to 11	2,86	0,31	Nordland and Hordland Group
12 to 26	4,85	0,31	Nordland and Hordland Group
27 and 28	9,00	0,31	Paleocene Formations
29 to 36	31,50	0,31	Cretaceous Formations (Chalk Group)
37 to 45	34,00	0,31	Cretaceous Formations (Chalk Group)
46	43,00	0,33	Cretaceous Formations (Chalk Group)
47	34,00	0,31	Cretaceous Formations (Chalk Group)
48 to 56	11,30	0,33	Cretaceous Formations (Cap Rock)
57 to 61	4.9-59	0,17	**Franklin C**
62 to 70	3.7-74	0,13	**Franklin B**
71 to 74	23-74	0,10	**Franklin A**
75 to 90	36,00	0,10	Pentland
91 to 99	12,00	0,35	Underburden

Table 3.1 Poroelastic properties of the Elgin geomechanical model.

3.4 Computation of the transfer functions

At the time of the monitor survey (2005), production had been going on simultaneously in all wells for four years and the pressure drop is expected to have spread throughout most of the reservoir area and wells have long since interacted with each other. Thus, it is not feasible to use real production data in order to calculate the system's Wiener filter as described in Section 2.3. For this reason, a geomechanical model (Visage coupled to Eclipse) was used. To this end, synthetic sources were placed in locations with an anticipated small amount of lateral heterogeneity, e.g. porosity and permeability, in order to ensure a smooth pulse and correspondingly a well behaved impulse response. The synthetic sources or pulses in this case, are pressure changes that consist of a 1 MPa peak that decays to zero in the next 5 neighbouring cells (Figure 3.7). This distribution is then fed into the geomechanical simulator to obtain the associated reservoir volumetric strain and the overburden vertical strain, allowing calculation of the impulse-response.

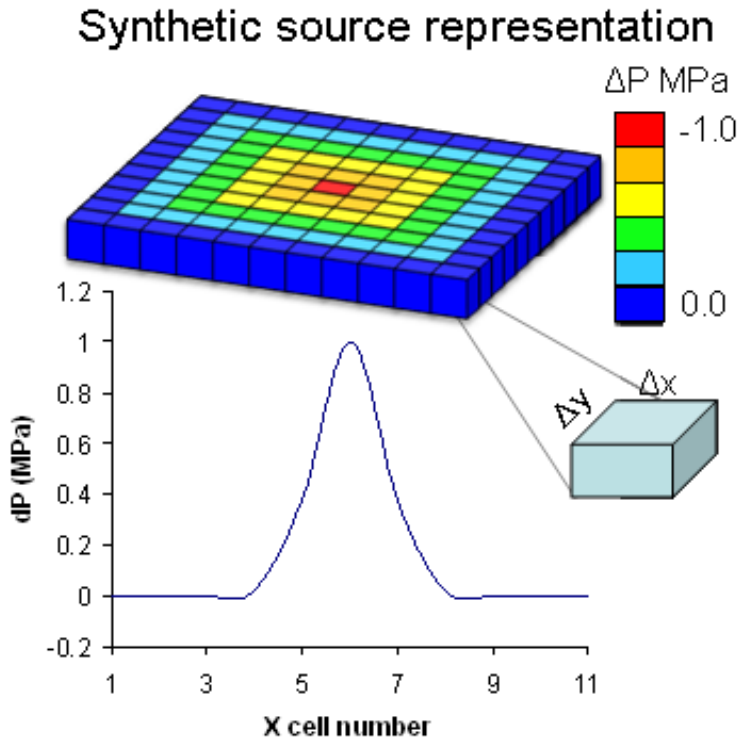

Figure 3.7 Synthetic sources used to simulate the system's impulse-response. The source consists of a 1 MPa peak that decays exponentially to zero in the next 5 neighbouring cells.

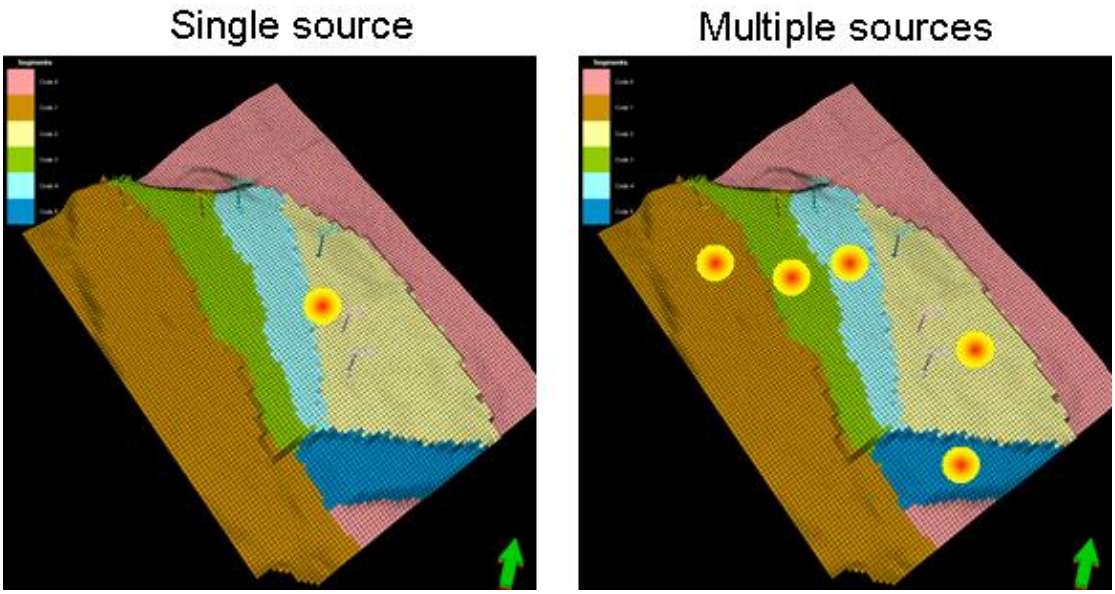

Figure 3.8 Source locations for the single source study (left) and multiple source study (right). The different colours correspond to the different reservoir compartments in the Fulmar C (top reservoir).

In part to test the robustness of the method, but mainly to investigate the dependency on the source locations, two separate studies are carried out: a single source placed roughly in the middle of the reservoir and five sources, each placed in the centre of one of the reservoir's compartments (Figure 3.8). Note that each "source location" actually contains several sources stacked together; one for each of the reservoir's flow units (in this case three). This allows assessment of the discrimination of the contributions from all reservoir layers, and thus a separate inversion of each one. Once the set of Wiener filters for the subsurface model have been calculated, the measured time strains can be deconvolved in order to estimate the reservoir's volumetric strain. However, first the measured time-strains have to be transformed to actual physical vertical strains. This is achieved using equation (1.10). The R-values used for this study are the same as those used by Gennaro et al. (2008); i.e. 50 for the overburden, 8 for the cap rock and 2 for the reservoir and underburden (Figure 3.9).

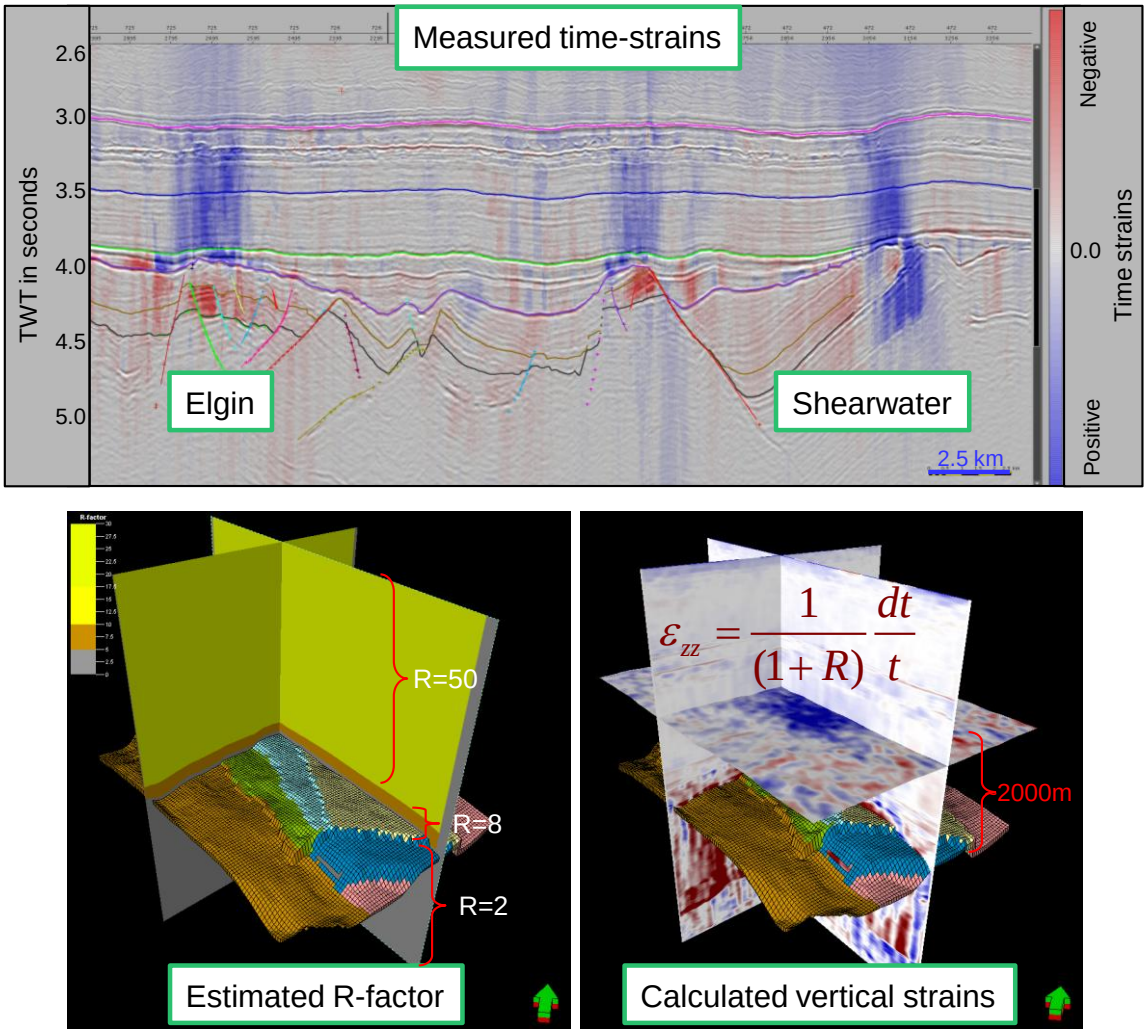

Figure 3.9 Illustrating the process to calculate physical vertical strains from measured time-strains. The top figure shows measured time-strains for Elgin and Shearwater fields (image courtesy of Total E&P UK). With help of the estimated R-factors for the subsurface (bottom left figure), the vertical physical strains (bottom right figure) are calculated using Hatchell and Bourne's relation.

Also shown in Figure 3.9 (bottom right) are the vertical strains of the Hod formation, roughly 2000m above the top reservoir, selected for the subsequent analysis. The strains are vertically averaged for the cells between the geomechanical model layers, in order to increase the signal to noise ratio and to ensure equivalence between modelled and calculated strains.

3.5 Wiener filter results

Before discussing the results, it is worth considering what can be learned in terms of reservoir management from the estimated volumetric strains. One of the biggest concerns for reservoir engineers is porosity and porosity changes far from control wells. This can be described in the hydrostatic case by the expression (Settari and Mourits, 1998)

$$\Delta\phi = [c_b(1-\phi_0) - c_s](\Delta p - \langle \Delta\sigma \rangle) \tag{3.1}$$

where c_b is the bulk compressibility and c_s the solid grain or rock matrix compressibility. The bulk compressibility c_b, is defined as the inverse of the bulk modulus K, and the matrix compressibility c_s which, after some algebraic manipulation can be expressed as

$$c_s \approx c_b \left(\frac{2-\phi_0}{1-\phi_0} \right). \tag{3.2}$$

The initial porosity ϕ_0 and the pressure change Δp can be obtained from the reservoir model, or calibrated from well data. The mean effective stress change $\langle \Delta\sigma' \rangle$ defined as

$$\langle \Delta\sigma' \rangle = \langle \Delta\sigma \rangle - \alpha \Delta p \tag{3.3}$$

with $\langle \Delta\sigma \rangle = \frac{1}{3}(\sigma_1 + \sigma_2 + \sigma_3)$ the mean stress or first stress invariant and α the Biot coefficient, can be easily derived from Hooke's law and is given by

$$\langle \Delta\sigma' \rangle = K \varepsilon_{vol} \tag{3.4}$$

Thus, the mean effective stress change can readily be obtained directly from the inverted volumetric strain ε_{vol}, nonetheless, this requires that a reasonable estimate of the bulk modulus K, for the reservoir formation is known. The value of calculating the mean effective stress changes, lies in that it is not possible to estimate directly pore

pressure changes from overburden inversion, only mean effective stress changes are measurable through the induced reservoir volumetric strain.

3.5.1 Results using a single source location

Having calculated the set of Wiener-filters for the three reservoir units, using the single source location shown in Figure 3.8, the measured vertical strains are deconvolved with the respective inverse filters. Time-strains from all overburden layers are inverted, and the results from the Hod formation selected given that the respective time-strains show a higher signal to noise ratio when compared with the other formations. Additionally, the results from all overburden formations are stacked together (*overburden stack*) with all estimations equally weighted (i.e. arithmetic mean of all the estimated maps).The results are compared with simulated volumetric strains from Visage coupled to a history-matched Eclipse-300 reservoir model corresponding to the time lapse period.

Figure 3.10 shows the inverted results for the Fulmar C sand. Taking the Visage simulated results as reference, several features are evident: the larger extensions at the reservoir boundaries including the south panel (yellow arrows), also the absence of compaction around the G8 well and the large compaction on the NW corner outside the reservoir area (red circles). In addition to this, note the smaller magnitudes in volumetric strain of the overburden stacked inversion. Of similar characteristics are the results from the Fulmar B inversion (Figure 3.11).

The Fulmar A inversions (Figure 3.12), are more peculiar in the sense that the inversion from the Hod Formation alone is dominated by an anomaly near G8, roughly in the same position as that of the upper reservoir sands, though of opposite sign. Nevertheless, as with the previous two cases, the overburden stacked inversion, although smaller in magnitude is more consistent with the simulated results and also shows larger extensions outside the boundaries of the reservoir. The persistent trait of the overburden stacked inversions having smaller magnitude has its cause in that the inverted overburden strains for some of the horizons are smaller than they should be. This suggests that the assumption of a constant R-factor for all the overburden is invalid and should be revised for individual overburden formations.

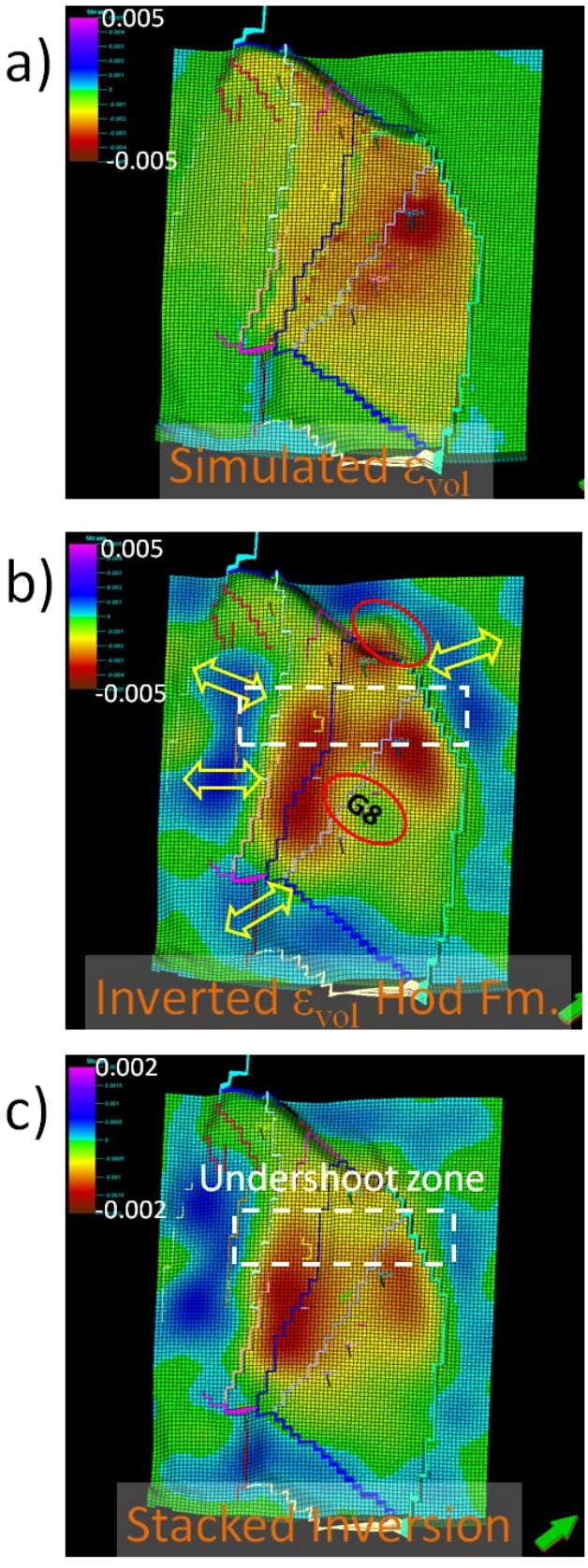

Figure 3.10 Volumetric strain for the Fulmar C sand (upper reservoir), for the single source location study. Map (a) corresponds to the Visage simulated results, as obtained from a coupled history-matched Eclipse-300 reservoir model, compared with inversions using time-strains from the Hod formation only (b), and time-strains from all overburden layers (c). The stacked inversion (c) is the result of averaging inversions of time-strains at all overburden layers.

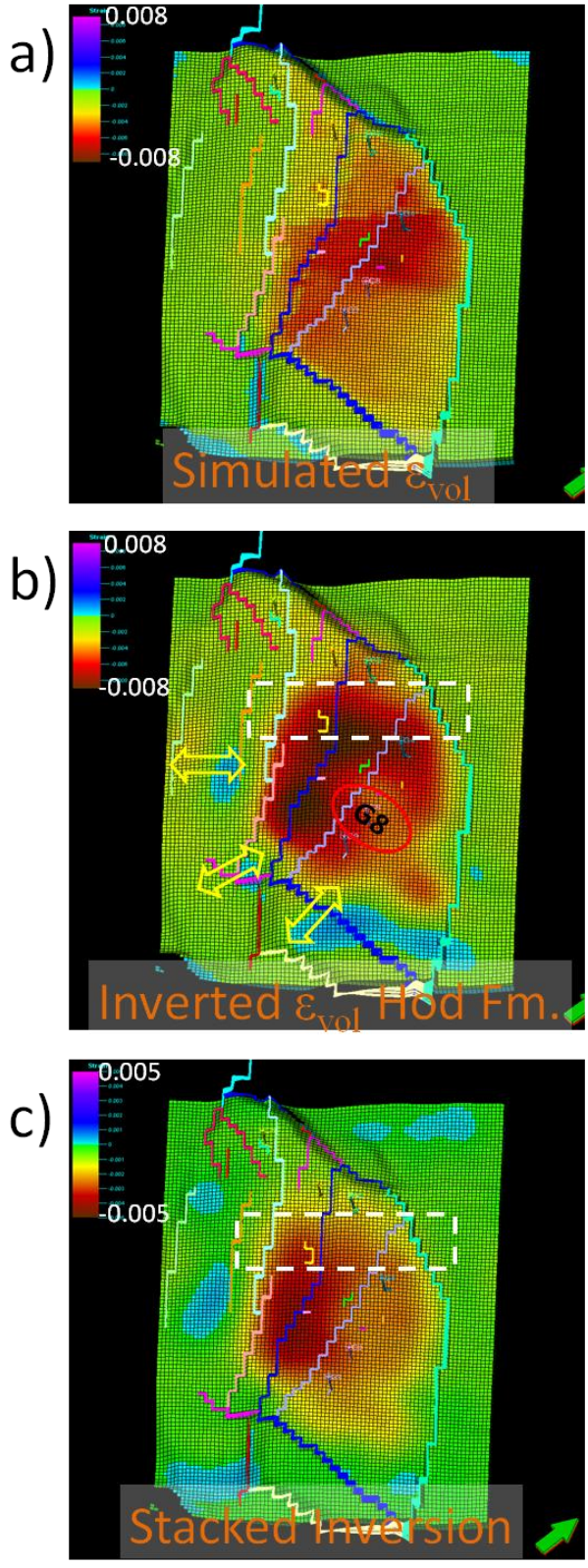

Figure 3.11 Volumetric strain for the Fulmar B sand (mid and main reservoir), for the single source location study. Map (a) corresponds to the Visage simulated results, as obtained from a coupled history-matched Eclipse-300 reservoir model, compared with inversions using time-strains from the Hod formation only (b), and time-strains from all overburden layers (c). The stacked inversion (c) is the result of averaging inversions of time-strains at all overburden layers.

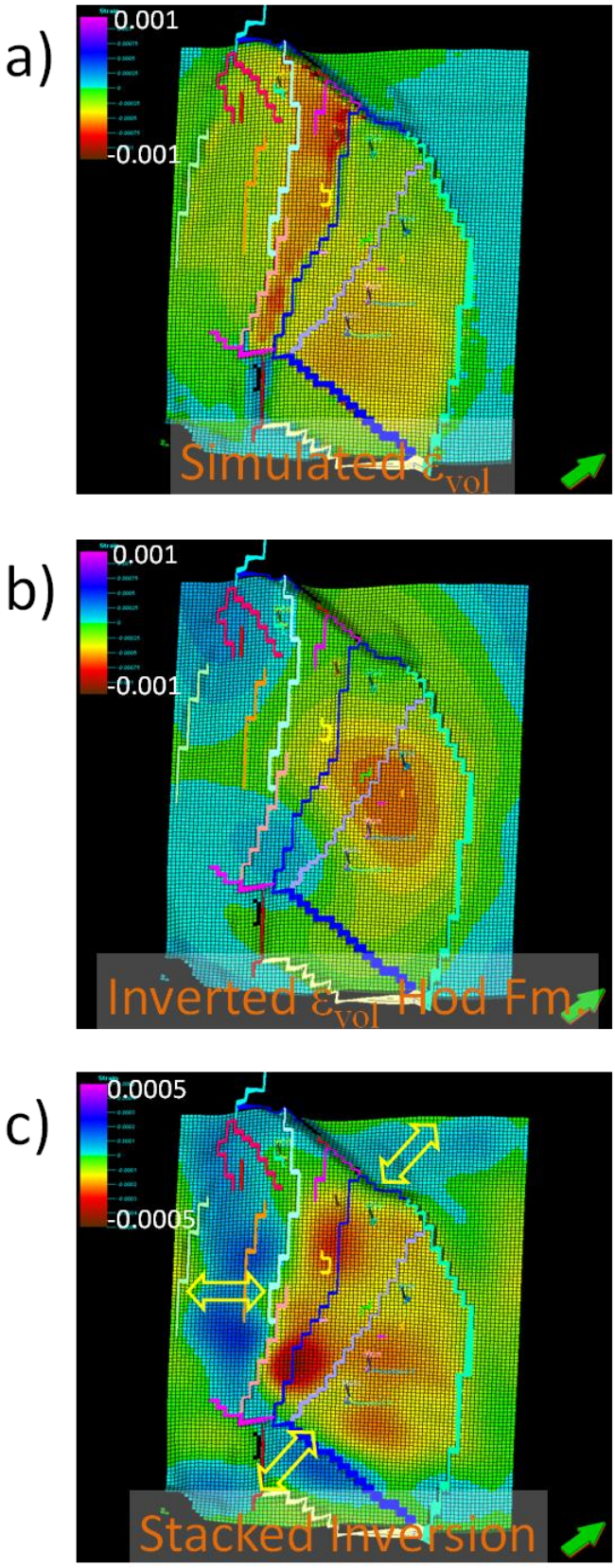

Figure 3.12 Volumetric strain for the Fulmar A sand (lower reservoir), for the single source location study. Map (a) corresponds to the Visage simulated results, as obtained from a coupled history-matched Eclipse-300 reservoir model, compared with inversions using time-strains from the Hod formation only (b), and time-strains from all overburden layers (c). The stacked inversion (c) is the result of averaging inversions of time-strains at all overburden layers.

3.5.2 Results using multiple source locations

The inversions using multiple source locations (Figure 3.13), has clearly higher resolution and contrast when compared with the single source analysis shown above, but the main features are preserved. Overall, larger than expected extensions at the reservoir boundaries are observed (yellow arrows). This could be caused by a) smaller pressure support and/or b) smaller fault transmissibility or c) inversion artefacts. Similarly, the south panel shows no evidence of compaction for the C and B sands, thus if it initially contained hydrocarbons, they should still be in place. The persistent anomaly near G8 (centre of the reservoir) is now more obvious and indicates that no depletion is taking place in that area. The striking feature at the north end of compaction on top of the extension (red circle Figure 3.13 a and c) at opposite ends of the fault hints to fault activity. Results from Fulmar A suggest indirect depletion from the west and south panels, i.e. that fluids are flowing into the above formations or that pressure is diffusing, which could explain the high relaxation on the west panel in Fulmar B.

Using equation (3.4) and the inverted volumetric strain gives the mean stress changes in the reservoir (Figure 3.14). The anomaly around G8 discussed before is also visible. It appears as a zone with relatively no changes in stress, surrounded by increasing stress from depletion. In order to rule out the possibility of the anomaly being an artefact of the method, the time-strains are integrated vertically along the reservoir interval to yield what are called interval time-strains (Grandi et al., 2009; De Gennaro et al., 2010). As opposed to “normal” time-shifts, the interval variant shows only the accumulated time-strains inside the integration interval, instead of a stack of all the changes to the surface. The interval time-strains for the Fulmar B sand (Figure 3.15), also show the anomaly around the G8 well (Grandi et al., 2010). Recall that the Wiener filter estimated parameters are calculated from strains 2000m above the reservoir and that the interval time-strains correspond to changes at the reservoir level only. Therefore, by comparing the interval time-strains with the estimated volumetric strain and effective stress changes, it can be concluded that unless the artefact has been introduced during seismic processing, it is real and not caused by the linear filter method. In this case, by highlighting an area insensitive to depletion, it reveals a zone either with aquifer support or a facies change and thus, poor reservoir quality. The aquifer hypothesis has now been discarded since no water is being produced in any of the nearby wells.

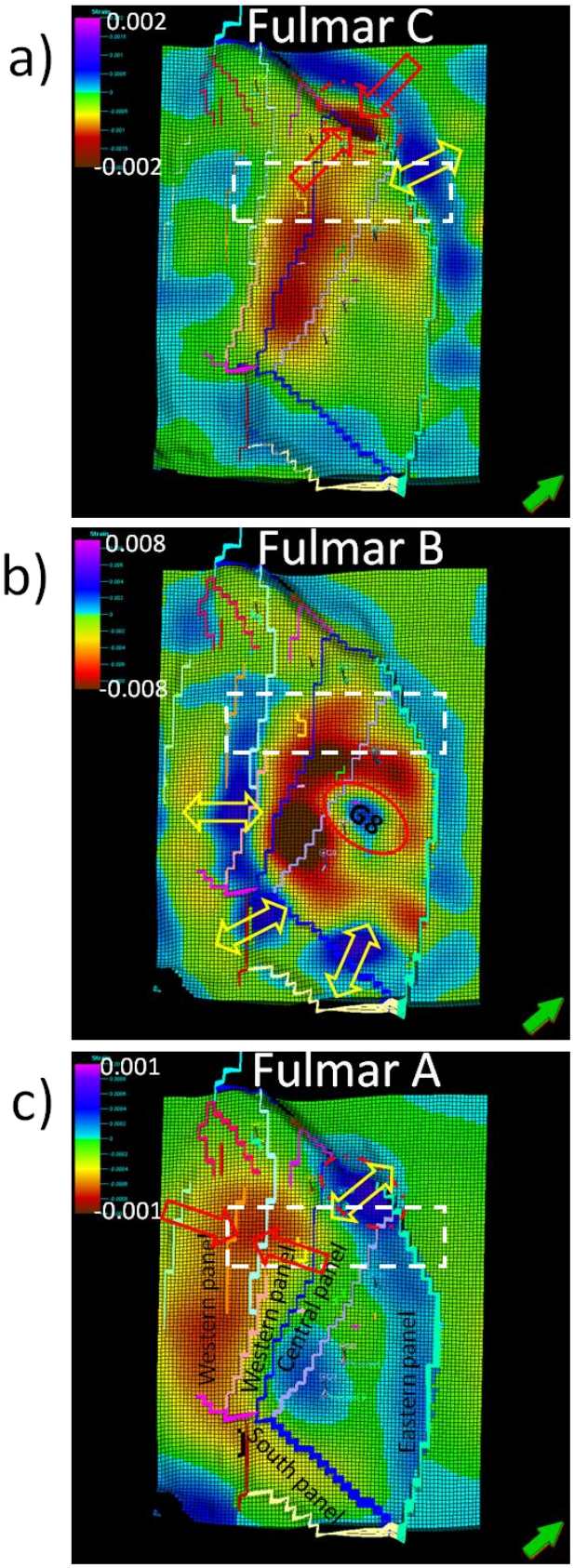

Figure 3.13 Inverted volumetric strain for the three reservoir units: Fulmar C (a), Fulmar B (b) and Fulmar A (c). The inversions are from averaged time-strains at the Hod formation and where obtained using multiple source locations i.e. one source per reservoir compartment.

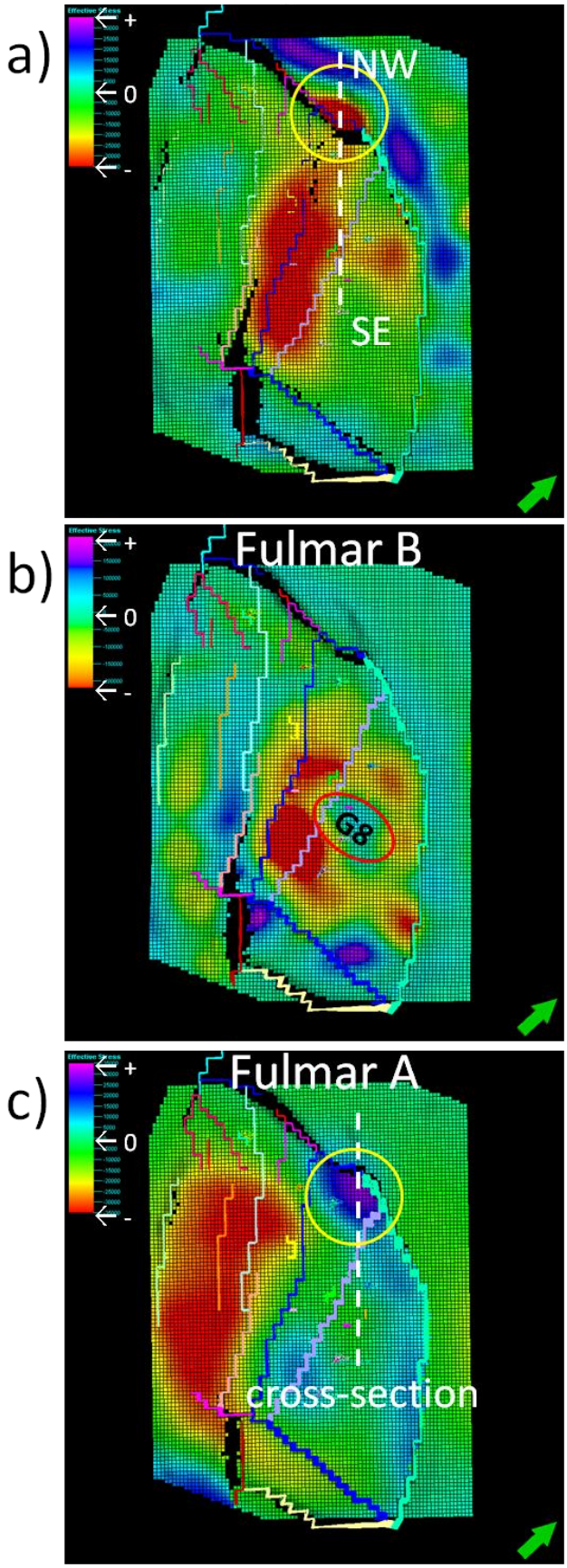

Figure 3.14 Calculated mean stress for the three reservoir units: Fulmar C (a), Fulmar B (b) and Fulmar A (c). The SE-NW cross section is shown in Figure 3.16.

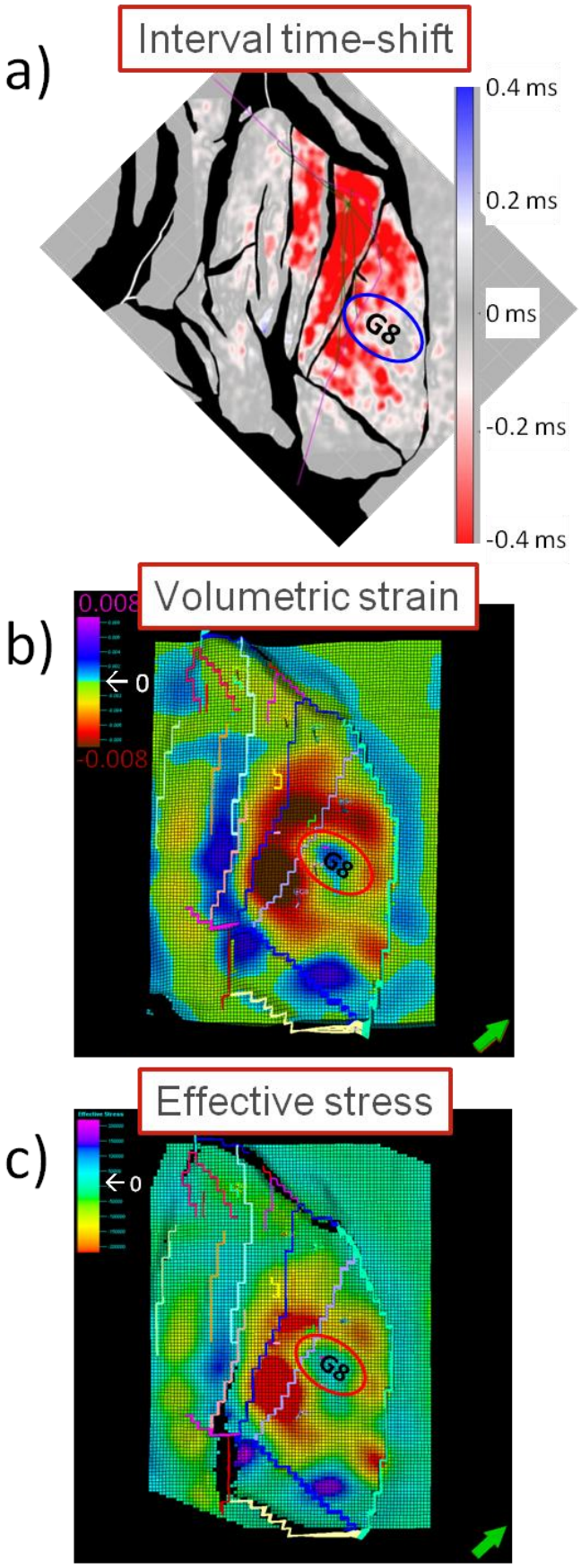

Figure 3.15 Comparison of interval time-strains (a) with overburden derived volumetric strain (b) and effective stress changes (c) at the Fulmar B sand. All maps show the anomaly around G8.

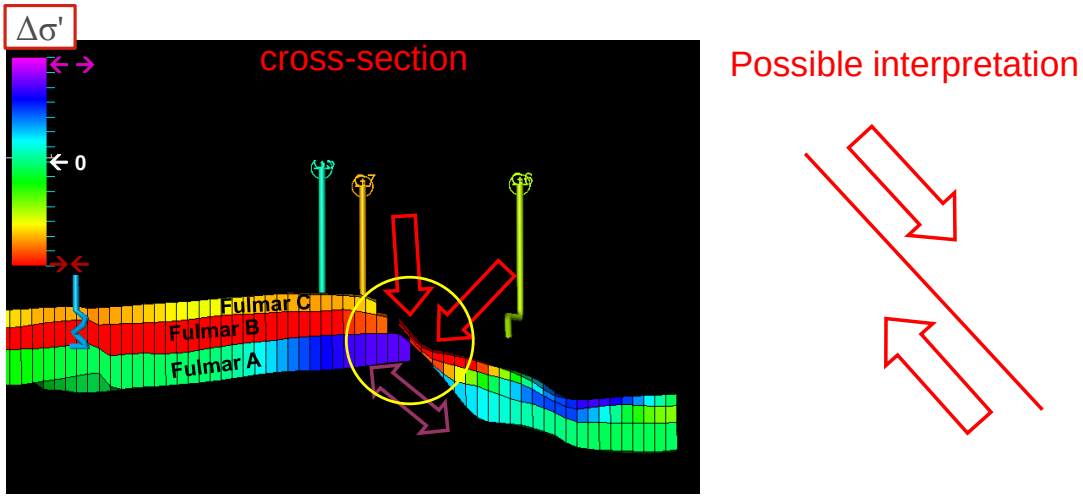

Figure 3.16 NW-SE reservoir cross section of inverted reservoir mean effective stress change, showing clearly the compression at the top caused possibly by lateral shifts of the sideburden on top of underburden relaxation across the fault.

There are no significant compressive stresses in the reservoir area of Fulmar A enforcing the undepleted scenario. The feature at the NW corner in Fulmar C (Figure 3.14a and c) shows accumulation of compressive stress opposite to extensive stress across the north fault in Fulmar A; a cross section is shown Figure 3.16 for easier interpretation. The cross section reveals a build-up of compressive stress on the top reservoir and along the fault underlined by expansive stress (relaxation) on the Fulmar A sand. Such a stress load after sufficient build up may cause the fault to slip as illustrated on the right-side cartoon. Indeed a seismic event caused by a fault-slip of such characteristics was observed in 2007 in the Elgin area. Taking into account that the monitor survey took place in 2005, and if the above discussed fault reactivation is correct, this method could be used to monitor stress accumulation. Accumulation of shear stresses like this on the reservoir flanks, are not uncommon in depleting reservoirs as described in Section 1.2. Note also that the observed mean effective stress is a mean of the normal stress components only, no shear components can be measured in this way. Nonetheless, the distribution of opposing stresses along the fault hints to the presence of shear build-up. However, depletion from outside the main reservoir, i.e. across the fault, is also a possibility.

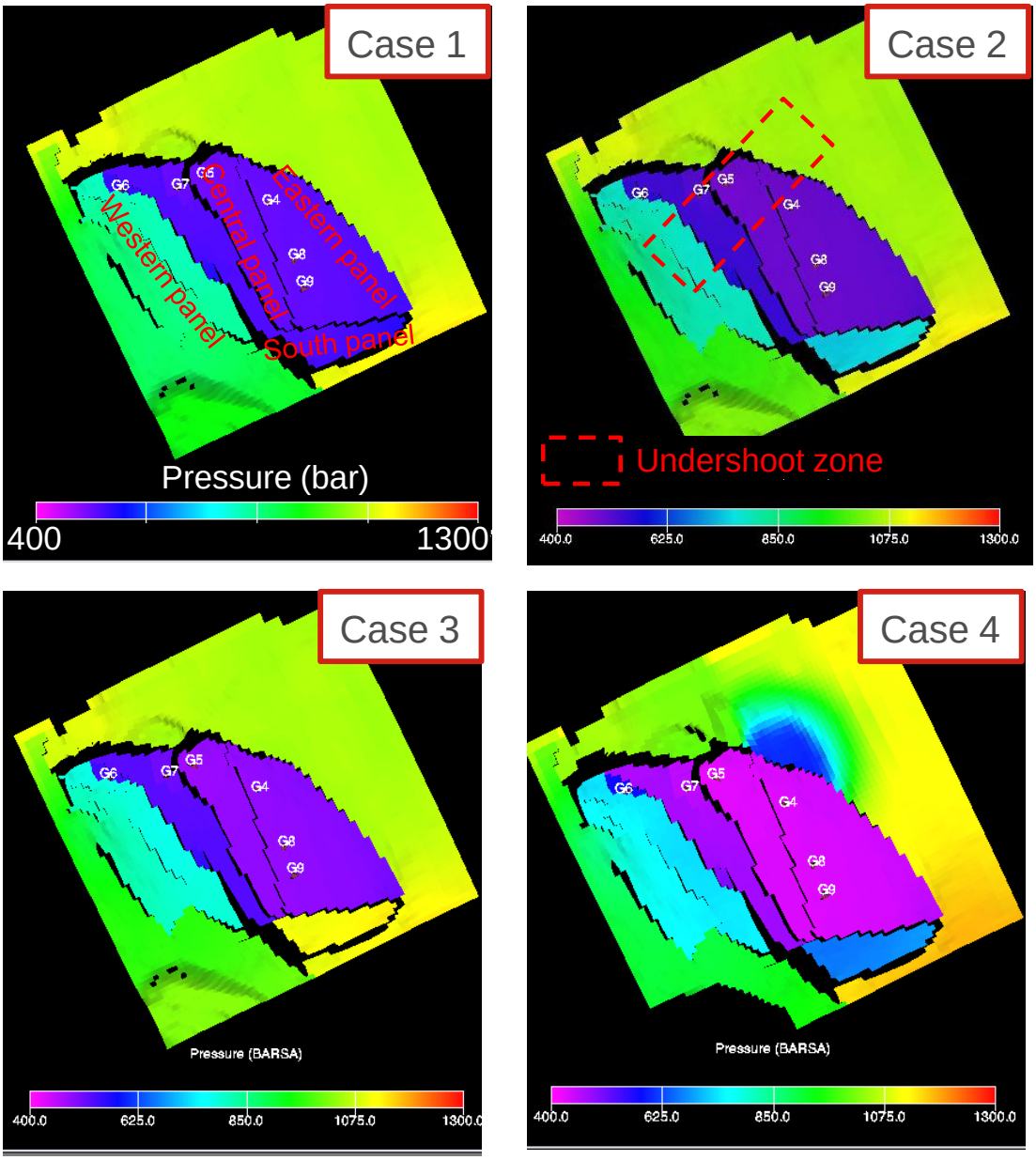

Figure 3.17 Reservoir pressure scenarios used to investigate compartmentalization: case 1; fully open faults; case 2 partially open faults; case 3 completely sealing faults; case 4 different configuration of partially sealing faults allowing for depletion north of the reservoir (Grandi et al., 2010).

Grandi et al. (2010) in a study aimed at understanding compartmentalization in Elgin, compared measured time-strains in the overburden with simulated strains corresponding to different history matched reservoir models in order to identify the most likely scenario. The reservoir models differ solely in fault transmissibility and thus, only the depletion patterns vary in the input of the geomechanical simulations (Figure 3.17). Strains at the top of the BCU formation (cap rock) were compared. However, in the undershoot area affecting the north-west part of the reservoir, the quality of the time-

shifts and uncertainties of the earth model do not allow an unambiguous answer. On the other hand, it has been shown that the Wiener-filter estimations can be used in the selection of optimum reservoir parameters during the history matching process.

Estimated volumetric strains and stress changes do not show any activity on the south panel, thus proving the scenario where the panel's bounding faults are sealing (case 3 Figure 3.17). In addition, the strong compaction north of the central panel outside the reservoir, besides possible fault activity as discussed above, hints to partially sealing faults and depletion outside the reservoir (case 4 Figure 3.17). As a consequence, the Wiener filter estimates do give meaningful information in terms of compartmentalization and fault transmissibility not directly available otherwise, with the potential of substantially speeding up and guiding the history matching process.

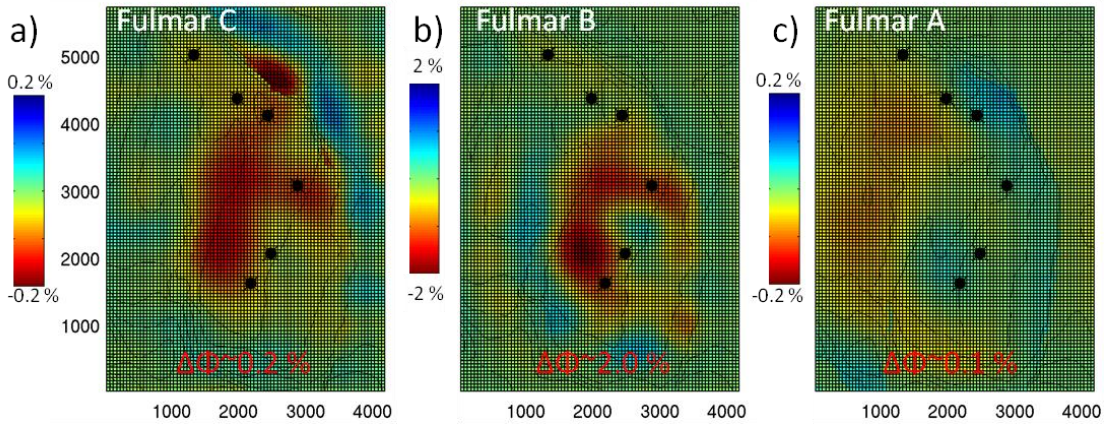

Figure 3.18 Calculated porosity changes in percentage for the three reservoir units: Fulmar C (a), Fulmar B (b) and Fulmar A (c).

The distribution of the calculated porosity changes (Figure 3.18), obtained from the estimated volumetric strain and mean stress change as given by equation (3.1), validates the previous observations and gives no additional information, since the dominant term is the volumetric strain. Porosity changes in Fulmar B are considerable ~2% and a factor of ten bigger than for the other sands. However, 2% is still too low to be clearly measurable by new infill wells.

3.6 Conclusions

In the case of Elgin, where seismic quality inside the reservoir is poor and reservoir conditions make drilling of infill wells very challenging, the choices for dynamic reservoir characterization are limited. Nonetheless, the use of Wiener-filters proves to be a valuable addition for the analysis of seismic time-lapse data.

The single source location analysis, especially comparing the results from the Hod formation with the stack of all overburden formations, puts in evidence that even though the time-strains at Hod are of good quality, the formation is too shallow, and hence high resolution information is lost. The simple arithmetic average used in overburden stacking although probably too simple an approach, makes clear that an R factor of 50 for all the overburden formations is incorrect. This could be easily overcome by taking a normalized average of the different estimates, but with the drawback of losing the scale of the results.

The multiple source location approach as expected yields better results, in terms of higher resolution and contrast, however this also has the drawback of computational time. Nonetheless, the linear filters need only be calculated once and could be used to deconvolve any future monitor survey. Or if such is the case, the forward filters could be used for feasibility studies.

The inverted results consistently show larger extensions at the reservoir boundaries, which may indicate that the pressure support is less than expected. This is caused either by a lower pressure from the aquifer and/or smaller fault transmissibility of the faults that delimit the reservoir. However, given the apparent permeable nature of the intrareservoir faults, the latter reason seems unlikely. Also consistent is the absence of compaction, or in that case, of any sign of depletion in the south panel for any of the three sands. This means that the area should still be at virgin pressure regardless of hydrocarbon content. Along the same line, the apparent depletion shown north of the central panel outside the reservoir is consistent with at least one of the history matched realizations, proving the technique's potential for reservoir engineering and integrated reservoir management guiding the history matching process.

The persistent anomaly at the centre of the Eastern Panel near the G8 well, observed also on the warping results within the reservoir (Grandi et al. 2010), can be tentatively interpreted as facies degradation. A fact that could not have been observed otherwise unless by drilling a well, in which case it would have been too late. There is evidence to suggest that the calculation of the mean stress changes, does indeed provide a way to measure stress accumulation that may lead to fault reactivation, as supported by the 2007 microseismic event. It is plausible, that with higher resolution on the stress accumulation map, areas that represent a hazard in terms of well stability could be identified.

Finally, the porosity change maps do not provide much additional information, as the amplitudes of up to 2%, lay inside the uncertainty of the estimated initial porosity. Nonetheless, the distribution of reservoir compaction and associated porosity changes go in hand with the expected depletion. As a consequence, and given the evidence for weaker aquifer support, Elgin is a case of mainly compaction drive.

Chapter 4

4 Application to the Ekofisk field: Multi-vintage time-lapse analysis

The Ekofisk field, one of the largest North Sea oil fields, was brought on stream in 1971. The reservoir rock consists of largely high porosity chalk of Maastrichtian through Upper Danian age. Water injection started fully in 1989 after sea floor subsidence of up to 5m was discovered. However subsidence did not stop and continued to about 8m in 2000 in part due to water weakening of the chalk. The massive compaction by 1987 caused seven platform decks to be jacked up at a cost of U.S. $ 1 billion (Suiak & Danielsen, 1989), in addition to numerous well failures.

The potential of seismic time-lapse monitoring to help in evaluating this process was recognized early, resulting in a 3D baseline survey acquired in 1989, with subsequent monitors in 1999, 2003, 2006 and 2008 leading ultimately in 2010 to the installation of a permanent seismic cable system or Life of Field Seismic (LoFS). In this chapter the five towed streamer time-lapse surveys are analyzed. Time-shifts are calculated and examined using Wiener filters and a geomechanical model. Despite the field's complexity, the estimated compaction and effective stress changes can be correlated with well activity and give valuable information; i.e. to identify water fronts and sweep efficiency, drainage areas, hydraulic fracturing and an indication of fault transmissibility.

4.1 Field description

The Ekofisk field is located in the Central Graben area in the Norwegian sector of the North Sea (Figure 4.1). The source rock is upper Jurassic to lower Cretaceous shales of the Mandala formation (Beaumont and Foster, 2001). The reservoir rock is a fine-grained limestone deposited after the Central Graben rift formed, creating a continuous body in the North Sea region covering more than 500,000 km^2, with an average thickness of about 500m, known as the Chalk Group (Japsen, 1998). The traps are salt-generated structures medium to highly fractured; a result of post-diapiric salt movement, faulting and differential compaction (Meling and Lehne, 1993). The Ekofisk field is an elongated four-way closure anticline.

The south-western part of the Norwegian continental shelf, called the Greater Ekofisk Area, contains eleven major chalk fields, of which Ekofisk, the first to be discovered, is the largest. Figure 4.2 shows the size and location of some of the fields. The producing horizons at Ekofisk are the Ekofisk and Tor formations of Danian and Maatrichtian age respectively. The formations consist of deep ocean sediments (pelagic) of organic origin composed mainly of coccoliths (de Gennaro et al. 2004). Coccoliths are the skeletal debris of unicellular algae called Coccolithophorids that produce spherical calcareous exoskeletons called coccospheres (Figure 4.3). The size of the coccospheres ranges from 10 to 30 µm and that of the coccoliths from 2 to 20 µm. The size of the coccoliths and differences in the depositional environments in the form of coarser carbonate debris, such as foraminiferal remains and small amounts of noncarbonated material, mostly silica and clay, results in the different relationships between porosity and permeability of the Ekofisk and Tor formations.

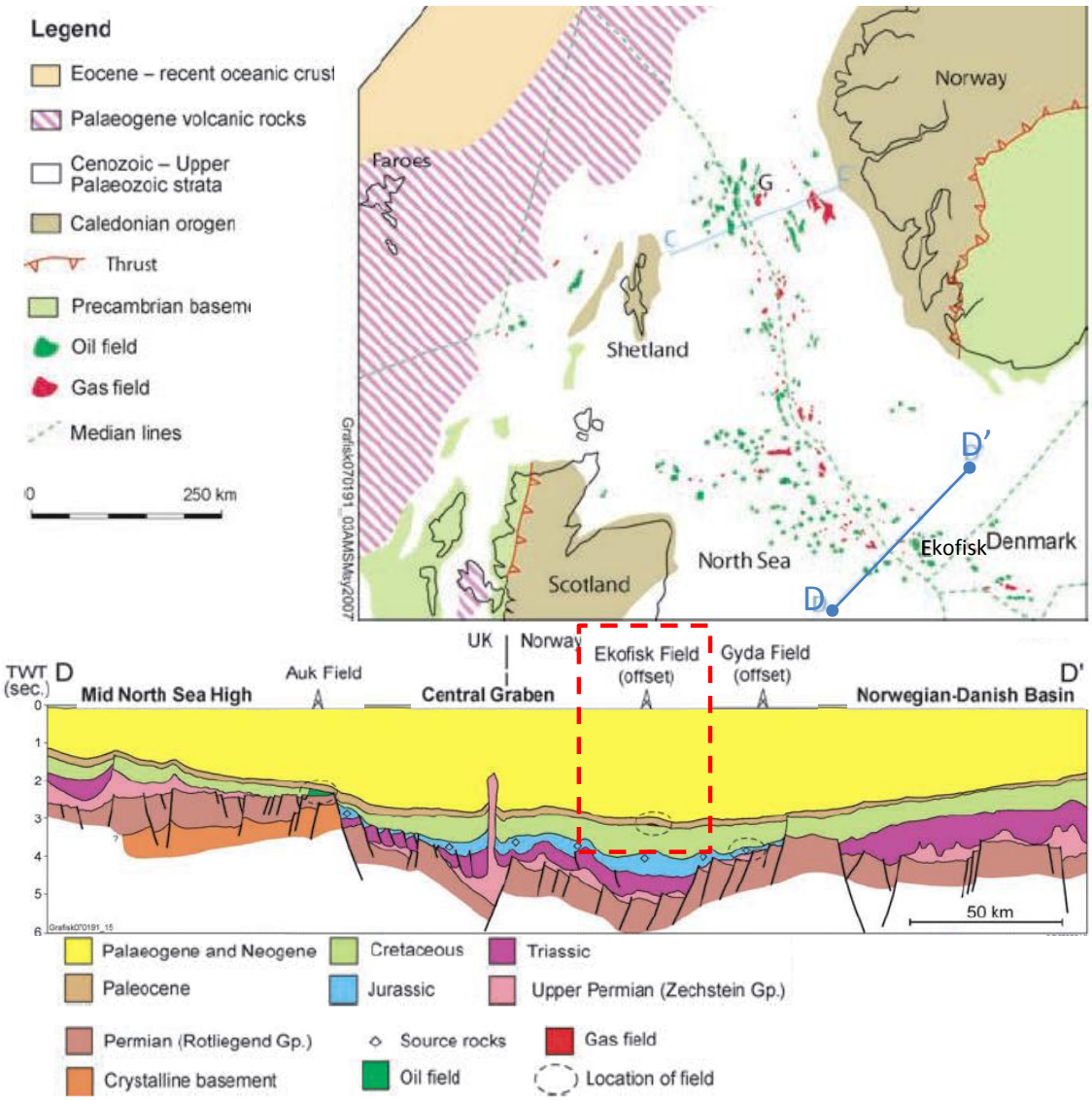

Figure 4.1 Above: oil and gas fields on the northern North Sea. The Ekofisk field is located along the transect D-D'.Below: geological cross-section of Ekofisk's petroleum system (Spencer et al., 2008).

Due to the nature of the chalk constituents and to the presence of overpressured hydrocarbons, the reservoir's porosity is very high (up to 50%). However, since the coccolith's platelets are held together by cementation, the matrix permeability is very low, typically 1 to 5 mD. Nonetheless, due to extensive natural fracturing caused by the diapiric nature of the structure, the effective permeability is considerably higher, ranging from 1 to 100 mD.

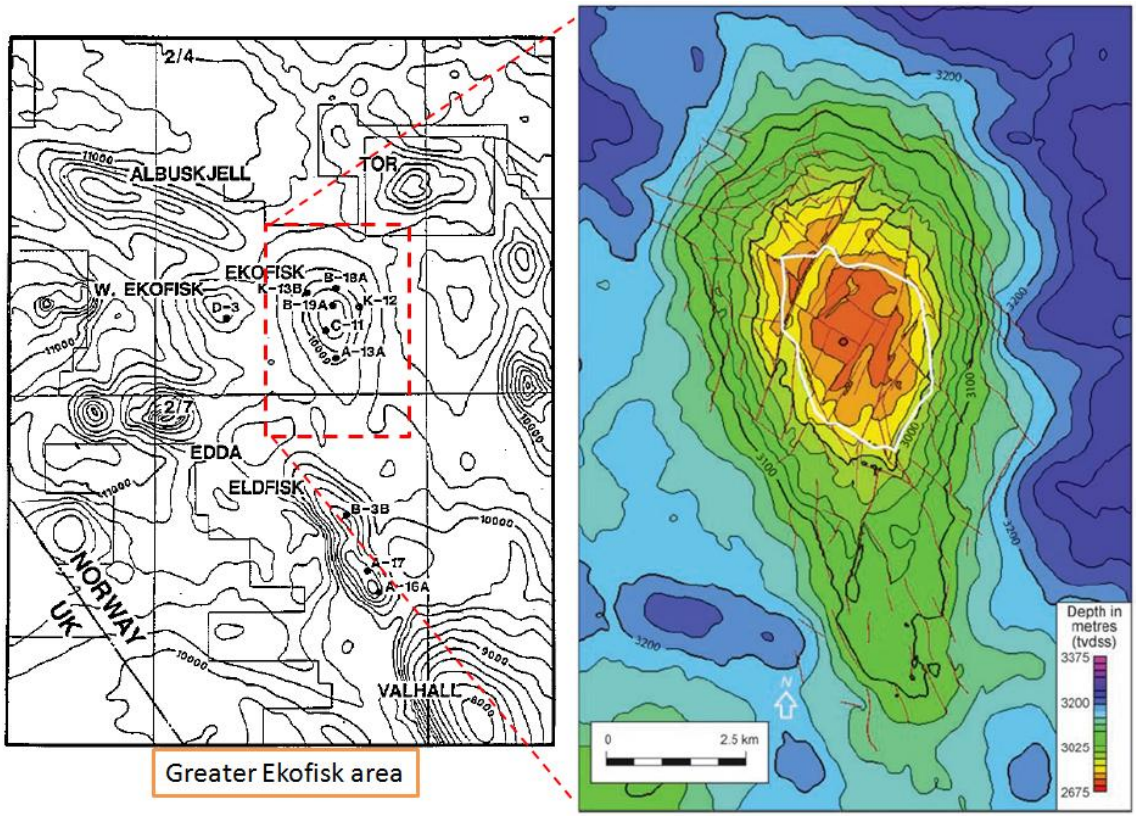

Figure 4.2 Left: depth map at the top of the chalk group of the Greater Ekofisk area, after Sulak and Danielsen (1989). Right: Ekofisk field structure map of the top of the Ekofisk formation, after Spencer et al. (2008). The top of the structure delineated by the white line corresponds to an area of very poor seismic imaging caused by a gas cloud.

The fairly stable conditions during chalk sedimentation produced a rather continuous background of chalk deposition interrupted only by intrusive bodies of chalk material in the form of turbidites, slumps, and debris flows (Johnson et al. 1989). The Ekofisk formation is separated from the underlying Tor formation by a basal low porosity clay-rich interval, the Ekofisk Tight Zone (Figure 4.4). The fracture system and low matrix permeability play a major role on the initial field conditions and field production; i.e. drilled wells have encountered multiple oil water contacts (Spencer et al. 2008).

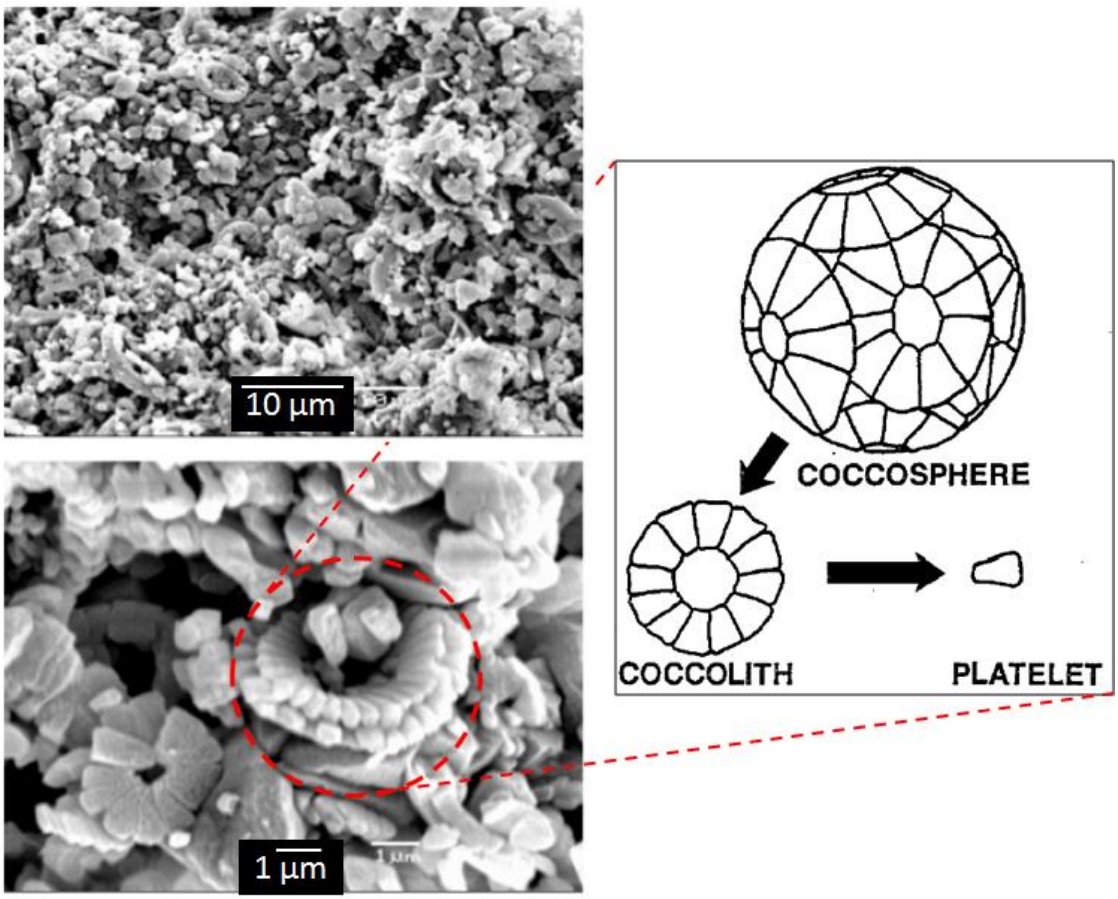

Figure 4.3 Left: Scanning electron microscope images of chalk sediments at two different magnifications (de Gennaro et al., 2004). Right: schematic representation of the Coccolithophorids' structure and constituents (Sulak and Danielsen, 1989).

The field was discovered in 1969 by Phillips Petroleum Co. Norway. The first phase of production started in 1971 from four exploration wells in order to determine whether pressure depletion would lead to a decrease in effective permeability through fracture closure and thus to a decrease in production. The field initially produced 39° API oil, with a solution gas-oil ratio of 1547 scf/bbl. In 1974 field development started properly, after no evidence of permeability reduction was observed.

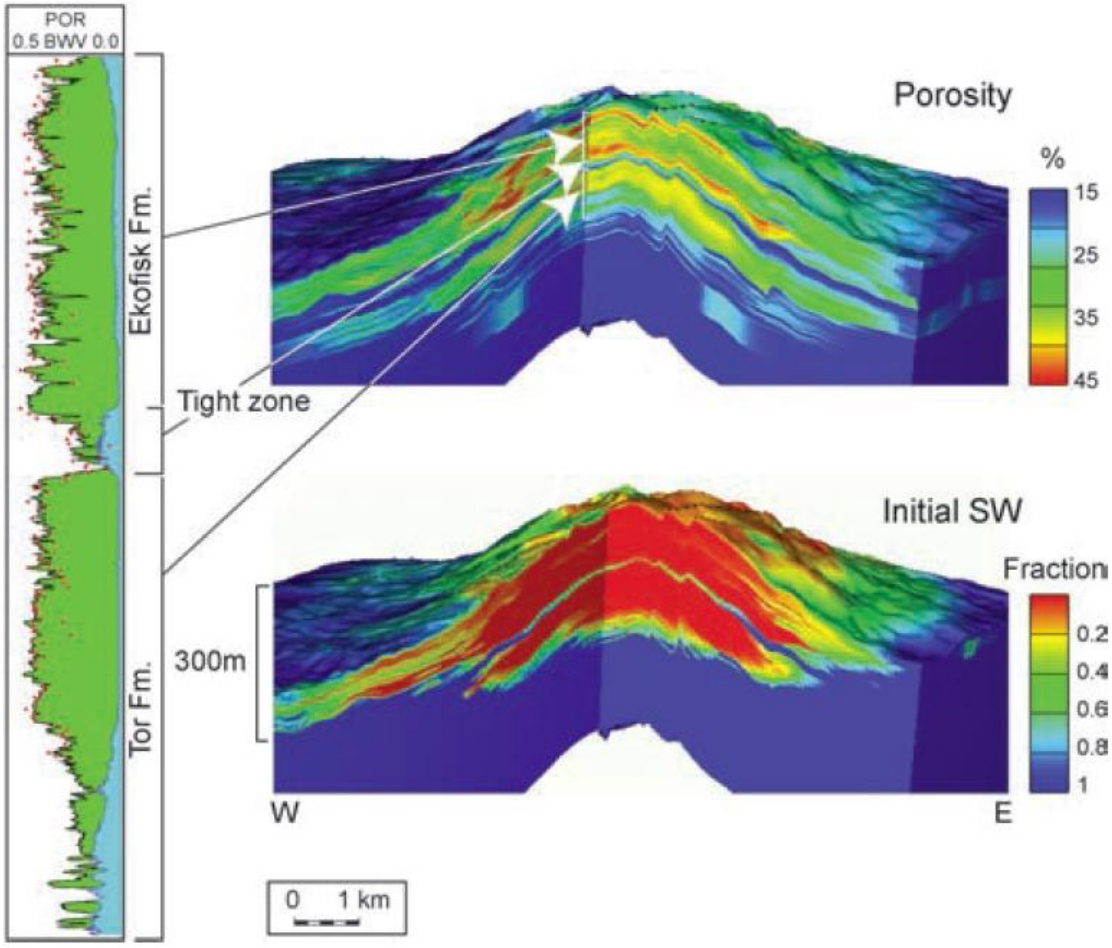

Figure 4.4 Cross-section of the Ekofisk geomodel showing initial porosity and water saturation. The Ekofisk and Tor reservoirs are separated by the low-porosity tight zone. Low matrix permeability and high capillary pressure results in a highly gradational oil-water contact (Spencer et al., 2008).

After subsidence was discovered in 1984 an extensive gas injection program started, followed in 1987 by a full field water flood. However, subsidence continued unabated and consistently higher than predicted. In the period between 1994 and 1998, despite the fact that as much fluid or more was being injected as produced per day, the subsidence rate remained almost constant at around 40 cm/year (Chin and Nagel, 2004). As of August 2002 the total subsidence at the top of the Ekofisk structure had reached 8.26 m. Nonetheless, the subsidence rate has now slowed down to about 0.1-0.15 m/yr in 2005 (Ottemöller et al. 2005). In order to accurately monitor compaction, a programme was started in 1985, where wells were dedicated strictly for this purpose. At the dedicated wells, radioactive markers (bullets) are shot into the formation at regular intervals before setting the casing (Menghini, 1989). Compaction is then measured by running a

gamma ray log and measuring changes in the distances between radioactive markers. Figure 4.5 shows the compaction logs from well 2/4 C11A.

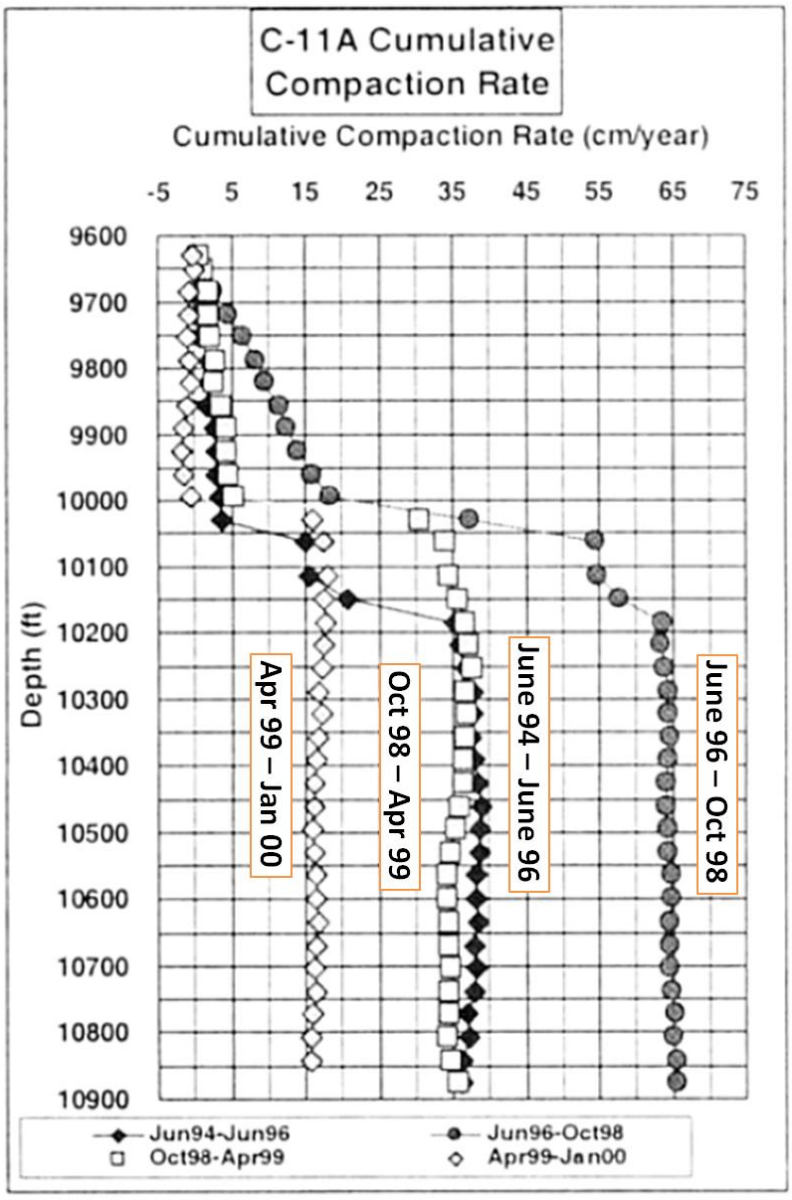

Figure 4.5 Sample compaction logs from the 2/4 C11A compaction monitoring well (Nagel, 2001).

In addition to radioactive markers, detailed time-lapse bathymetry has also been acquired. Figure 4.6 shows the differential bathymetry map computed between the 1999 baseline and the monitor acquired in 2001, 2 months after the 7th of May seismic event (Ottemöller et al., 2005). The central and southern part of the field exhibit subsidence as expected. However, an anomalous seafloor uplift observed in the north, has been

identified with unintentional water injection in the overburden and as the potential cause of the earthquake.

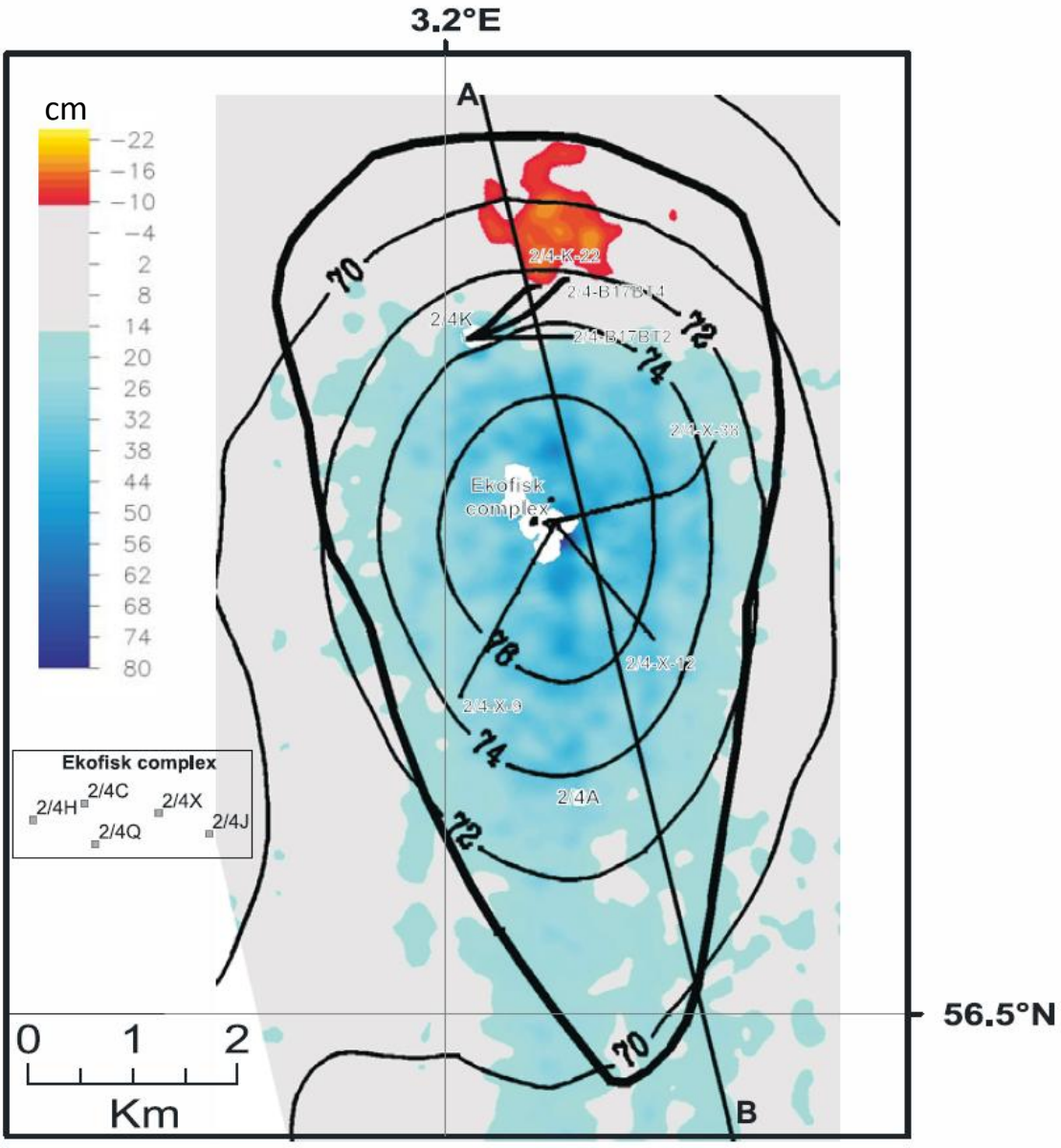

Figure 4.6 Time-lapse bathymetry map between the 1999 and 2001 surveys. The map (colour bar) is in centimetres. The contour lines are in decimetres and indicate the total subsidence up to 2001 (Ottemöller et al. 2005).

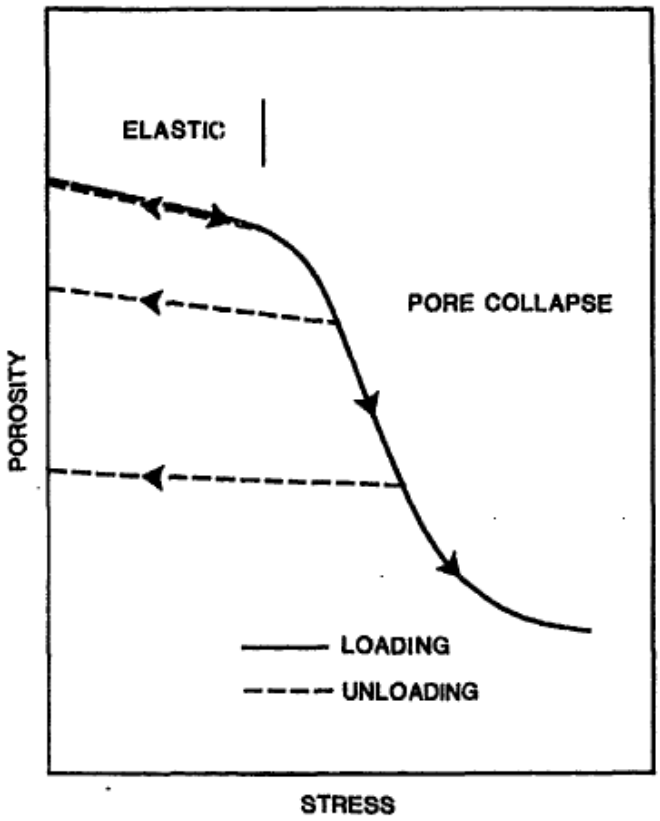

Figure 4.7 Sample porosity/effective stress curve for the Ekofisk chalk. Under low loading stresses, the chalk deforms elastically. At higher stresses though, the coccolith's structure breaks and the pore space collapses. This process is irreversible and the chalk experiences much larger compressibilities than during its elastic phase (Johnson et al., 1989).

4.2 Chalk behaviour and reservoir compaction

The fact that predicted compaction consistently underestimated the actual compaction at Ekofisk supplies evidence of the complexity of chalk mechanics. It was first believed reservoir compaction to be mostly plastic, in the form of shear failure of the chalk grains. However, after the events of 1984, when the Ekofisk storage tank was found to have sunk by almost 4m far surpassing the estimates, the mechanisms of pore collapse were exposed. Figure 4.7 shows a sample chalk hysteresis curve of effective stress versus porosity of an uniaxial-strain test where two regions are clearly visible; elastic region and irreversible pore collapse. The curve however, is controlled by the initial porosity of the samples. Nonetheless, the porosity/effective stress compaction curves for a given chalk type appear to converge to a common trend line in the pore collapse regime (Figure 4.8).

Still, long after field-wide water injection has been undertaken, high-rate subsidence continued, leading to the discovery of water weakening, the mechanisms of which are not yet fully understood. One theory points out to the effects of capillary pressure, where irreducible water saturation will give rise to very strong capillary forces providing an important contribution to the strength of the rock. On the other hand, when the sample becomes water saturated these capillary forces should disappear explaining the observed behaviour. However, tests on this theory have been so far inconclusive (Risnes and Flaageng, 1999). The other culprit is related with chemical process induced by sea water flooding, whereby temperature changes are no longer negligible (Madland et al. 2009). In this scenario, the flooding with seawater at high temperature induces chemical reactions that cause the precipitation of minerals containing calcium and magnesium. This precipitation, in turn leads to the dissolution of the chalk structure itself.

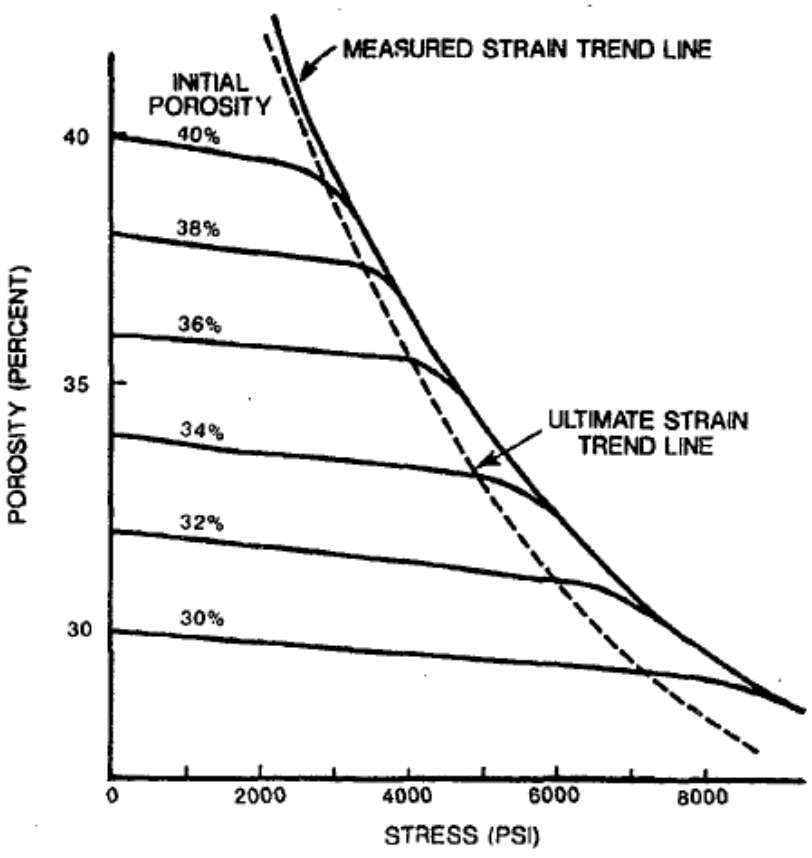

Figure 4.8 Uniaxial-strain compaction curves for different initial porosity samples for the Upper Ekofisk formation showing the strain trend line as function of effective stress (Johnson et al., 1989).

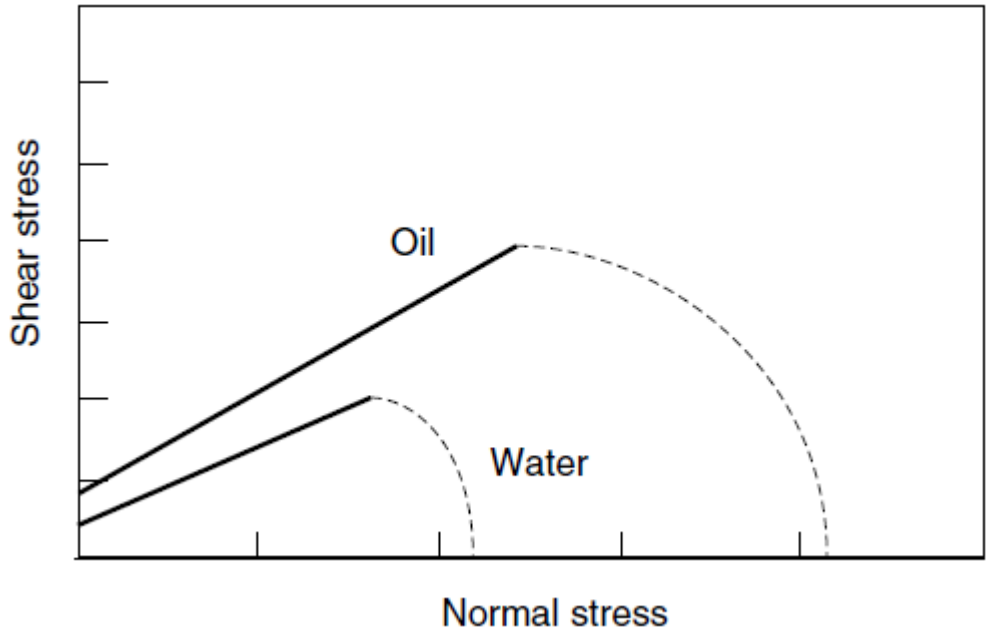

Figure 4.9 Sample Mohr-Coulomb failure diagram for oil and water saturated chalk (Risnes and Flaageng, 1999).

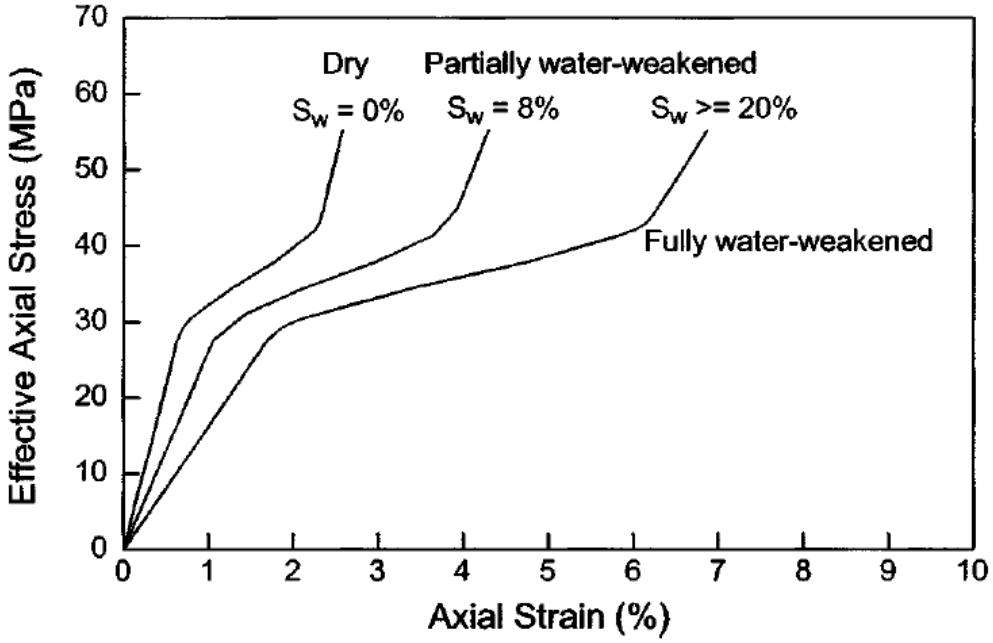

Figure 4.10 Stress-strain relations as a function of water saturation for a sample with 36% initial porosity (Chin and Nagel, 2004).

The effects of water weakening are first visible in that oil saturated chalk appear to be 2-3 times as strong as water saturated samples (Risnes and Flaageng, 1999), as illustrated

in Figure 4.9. This further complicates the stress-strain behaviour of chalk, as samples with the same porosity, will display different curves for different water saturations (Figure 4.10).

4.3 Time-lapse seismic surveys over Ekofisk

Despite numerous publications and studies regarding the Ekofisk compaction, comparatively not much has been done, or at least made public, regarding time-lapse seismic monitoring. The same can be said about published geomechanical model studies of the field, which, excluding academic works, practically stopped after the merger of Phillips Petroleum Co. (the field operator) and Conoco Inc. Meanwhile, neighbouring analogous fields like Valhall have lead the way in time-lapse monitoring, pioneering what is now known as Life of Field Seismic or LoFS; permanent multi-component (4C) sensor arrays installed on the seabed over which a repeatable source is fired.

Year	Contractor	Technology	Configuration	Acquisition style
1989	Geco/Prakla	Conventional	2 source, 2 streamers	Steer vessel for coverage
1999	Geco/Prakla	Conventional	2 source, 4 streamers	Steer vessel for coverage
2003	WesternGeco	Conventional	1 source, 8 streamers	Steer vessel for coverage
2006	WesternGeco	Q-Marine	1 source, 8 streamers	Steer vessel and streamers for coverage
2008	WesternGeco	Q-Marine	1 source, 8 streamers	Steer vessel, source, and streamers to duplicate 2006

Table 4.1 Different seismic surveys acquired over Ekofisk (Haugvaldstad et al. 2010).

Nonetheless, time-lapse surveys have been acquired in Ekofisk with the first monitor in 1999, followed by subsequent ones in 2003, 2006 and 2008. The baseline survey dates from 1989. However, only the last two surveys have been dedicated to maximize

repeatability. Table 4.1 shows the acquisition characteristics of the different surveys and reflects the advance in acquisition technologies.

The lack of 4D-seismic studies in Ekofisk could in part be explained by the particular challenges involved; i.e. low seismic repeatability (only the last two surveys are dedicated 4D) and a seismic obscured area. The seismic obscured area or gas cloud covers the central part of the field and is caused by the presence of both gas and variations of pore pressure in the overburden. Figure 4.11 shows the effects of the gas cloud on an RMS-amplitude seismic cross-section, where most of the central part of the field is obscured; including reservoir and overburden.

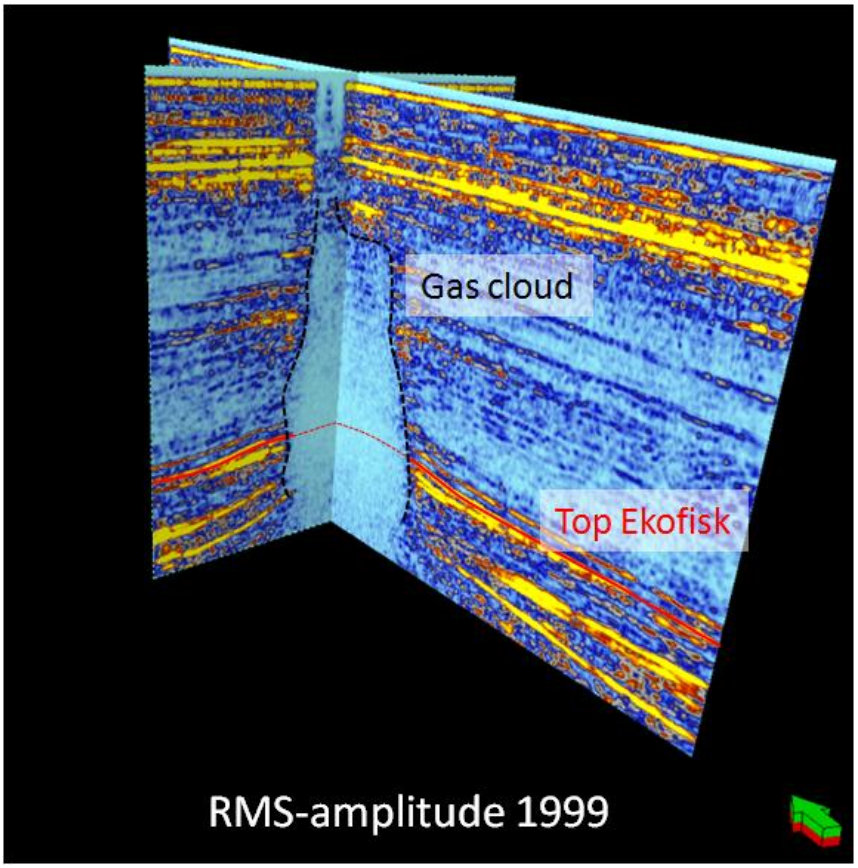

Figure 4.11 RMS-amplitude cross-section of the 1999 survey, showing the effects of the overburden gas cloud. The position of the top reservoir is shown as a red line.

Despite having been on stream for over 40 years, ConocoPhillips (the field operator) estimates recoverable oil at April 2011 of about 111.2 million scm, or roughly 50% of the oil originally in place (NPD, 2011). This, and new acquisition and processing

techniques have seen in the last two years, an increased interest on time-lapse seismic in Ekofisk. Starting with the reprocessing of the existing seismic surveys (Figure 4.12) and culminating in the installation of a LoFS array with a first acquisition scheduled for the end of 2010 and expected to be repeated approximately every six months thereafter (Haugvaldstad et al. 2010).

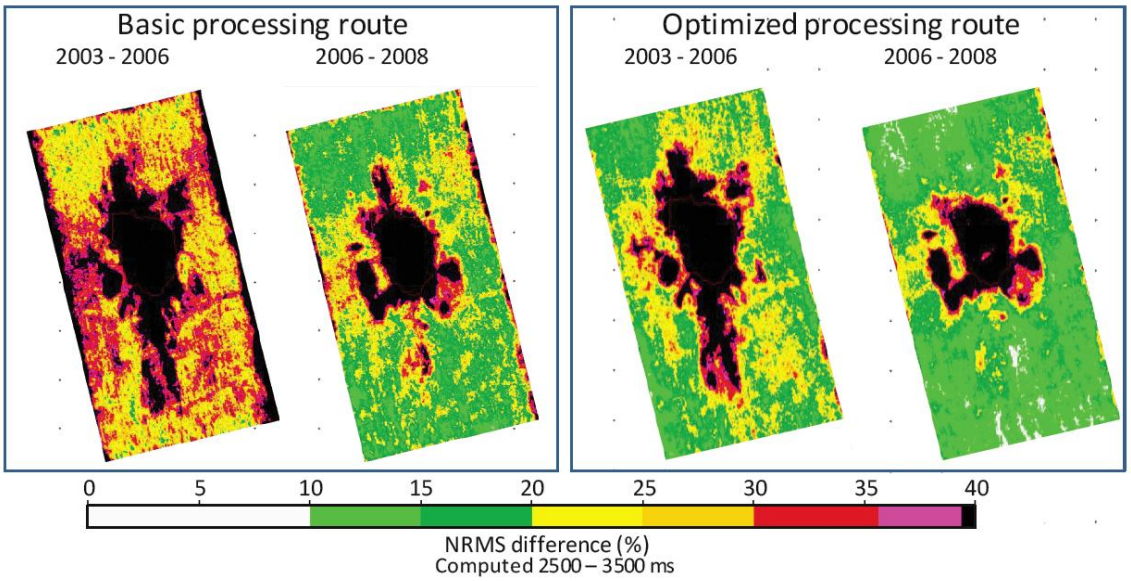

Figure 4.12 NRMS difference maps showing the differences between the old and the reprocessed seismic, resulting in an NRMS as low as 10% in the areas not affected by production.

In this chapter, the Wiener-filter method is applied on all five seismic vintages. However, in order to do so, a full field geomechanical model is needed with the purpose of approximating the impulse response. Additionally, time-strains for all vintages are computed using the common 1989 survey as baseline resulting in 4 time-strain cubes.

4.4 Ekofisk geomechanical model

A geomechanical model was supplied by ConocoPhillips, yet it soon emerged that there were problems with it, as it had been built to study surface subsidence and its effects on the surface production infrastructure alone, as opposed to well-casing integrity and reservoir management. Figure 4.13 shows the originally supplied overburden solid

density, where it can be observed that it is only well defined in the central part of the reservoir where the production infrastructure is located. For this reason, the geomechanical model has been rebuilt based on the supplied reservoir simulation model and interpreted overburden horizons.

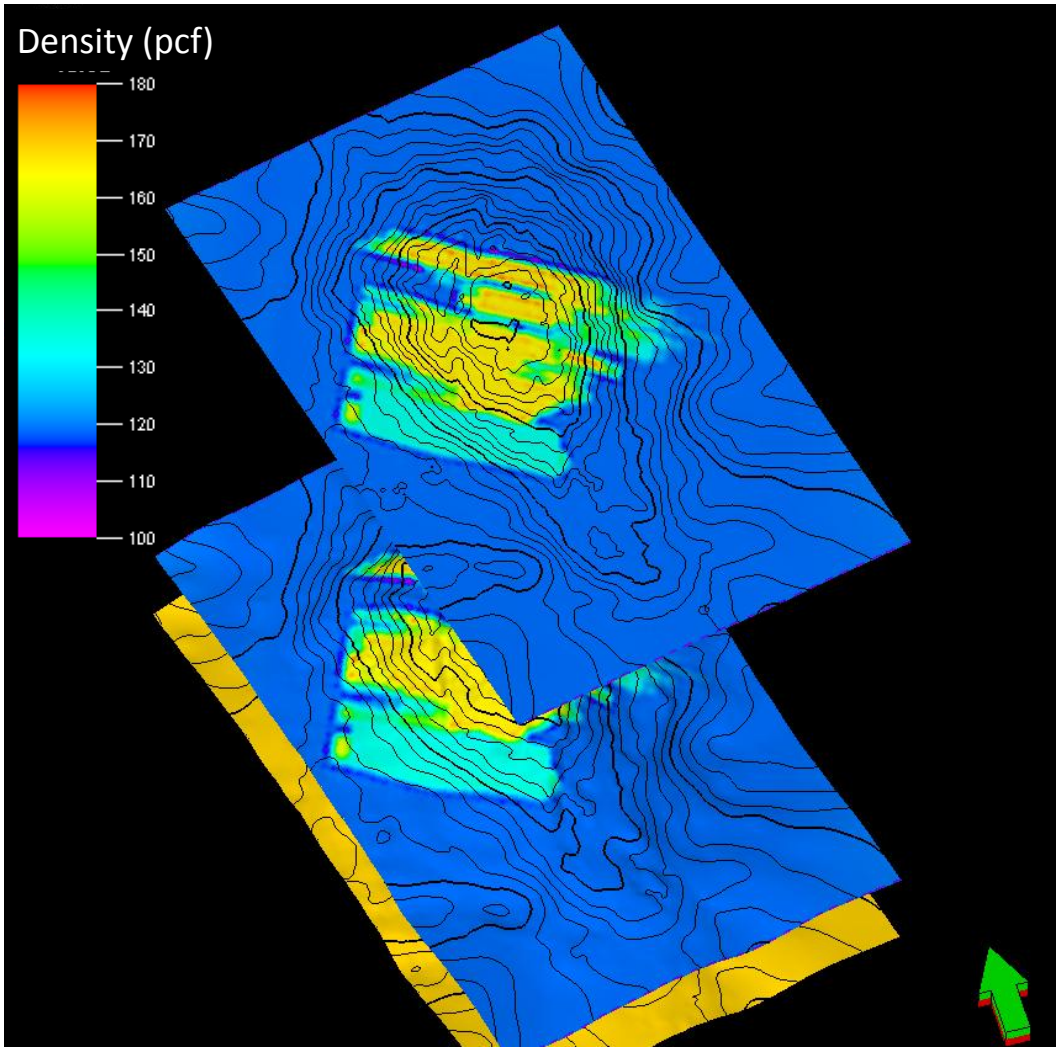

Figure 4.13 Overburden solid density in pounds per cubic foot, of the subsurface model supplied by ConocoPhillips showing values only where production infrastructure is concerned.

Layer No.	Young's modulus GPa	Poisson's ratio	Formation
1-3	0,08	0,15	Overburden
4	0,2	0,33	
5-8	0,21	0,36	
9	0.23-7.3	0.09-0.27	**Top Ekofisk**
10	0.11-7.4	0.09-0.33	
11	0.17-7.3	0.09-0.31	
12	0.2-7.3	0.09-0.30	
13	0.13-7.3	0.09-0.32	
14	0.45-7.3	0.09-0.21	Tight zone
15	0.14-6.8	0.09-0.32	**Top Tor**
16	0.19-3.7	0.09-0.30	
17	0.33-7.3	0.09-0.25	
18	0.8-7.3	0.09-0.13	Base chalk
19-20	13,7	0,25	Basement

Table 4.2 Petroelastic properties of the Ekofisk geomechanical model.

Since for the purposes of calculating the Wiener filters an approximate subsurface model is sufficient, i.e. only small changes at a time are simulated, the model is set as linear elastic. This is also because no real data has been supplied nor is readily available in order to input actual compaction curves to the simulator. Nonetheless, the new elastic properties are based on published empirical relationships for North Sea chalk (Fjær et al. 2008). Based on a large amount of outcrop and reservoir chalk data in the North Sea, the following trends correlating porosity with mechanical properties have been identified

$$E = 22.5e^{-11.2\phi} \tag{4.1}$$

$$H = 13.6e^{-9.29\phi} \tag{4.2}$$

where E and H given in MPa, correspond to the Young's modulus and uniaxial compaction modulus respectively and ϕ is porosity given as a fraction. All overburden parameters have been kept unchanged, as the provided values are similar to those of neighbouring Valhall field (Corzo, 2009). The new model consists of 282x179x20 cells including a sideburden of three cells in each lateral direction. Excluding the sideburden, all cells have a regular size as required by the Wiener-filter method of 50x50 m. Table

4.2 shows the range of values of the Young's modulus and Poisson's ratio for each model layer.

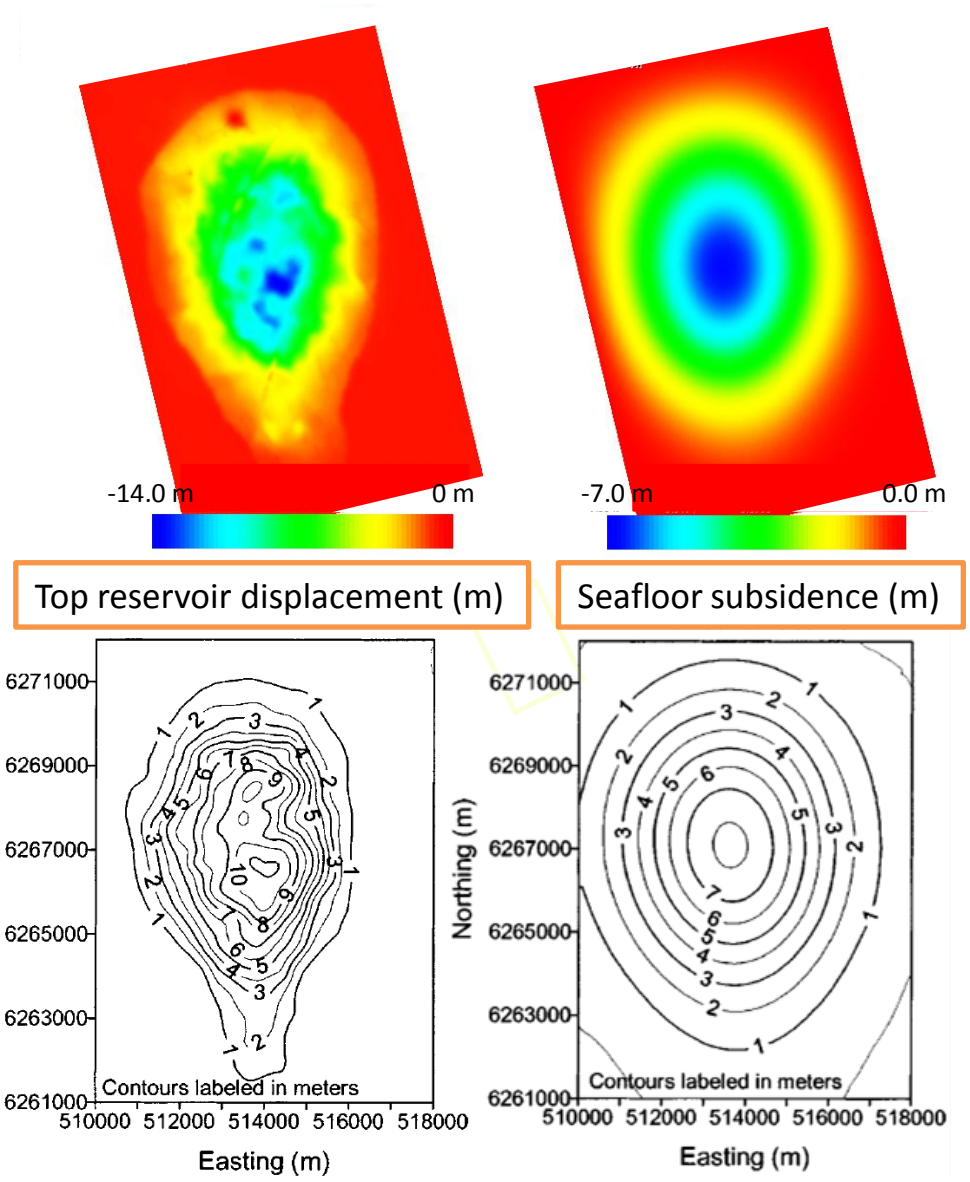

Figure 4.14 The figure shows the simulation results of the new geomechanical model (top maps) compared with those published by Chin and Nagel (2004). The vertical displacement maps at the top reservoir are displayed on the left and seafloor subsidence on the right.

As only the results of the reservoir simulation model for the seismic times and not the model itself were provided, it was not possible to do a fully coupled fluid flow and geomechanics simulation. Therefore, only a one-way coupling is considered, where the pressure changes from the reservoir model are fed to the geomechanical model in order

to simulate the subsurface strains. Figure 4.14 shows simulation results of the new model for 1999 pressure changes compared with the simulation results presented by Chin and Nagel (2004) for 2000. It can be observed that the modelled vertical displacements are in agreement with those published and additionally with the observed seafloor subsidence shown in Figure 4.6. This proves that the model although simple, is adequate for the purpose of calculating the Wiener filters.

4.5 Calculating the time-shifts

Time-shifts measured by 1D cross-correlation methods, where individual traces between base and monitor survey are compared for a given time window, although fast, are prone to noise. This is especially accentuated when considering their derivative; the time strains, resulting in poor lateral resolution and low signal to noise ratio. Therefore, in this project a method developed by Hale (2009) is employed for the calculation of the time-shifts. This method, instead of a 1D cross-correlation calculates the displacements in all three dimensions (warping). It does so first, by calculating for a given image sample or search window defined by the user, the local phase-correlation. In this step, in order to improve the spatial resolution, whitening and smoothing filters are applied to both vintages before correlation. The second step consists of a cyclic search, whereby a cyclic sequence of correlations and shifts along each spatial dimension are applied to the image. At a given iteration step, the shifts found in the previous step are applied to one of the images before correlation. Then a new set of shifts are calculated; first vertically and then in the horizontal direction. This process is repeated until all shifts become negligible. Figure 4.15 shows the 2-D shifts estimated on the first four cycles of an image synthetically warped vertically and horizontally. As a rule of thumb, four iterations seem to be sufficient for the warp-vector to converge; not only for the synthetic example but for observed time-lapse seismic as well. In this chapter, only the vertical component of the warp-vector (time-shifts) is used, the nature of the lateral shifts, is examined in Chapter 6.

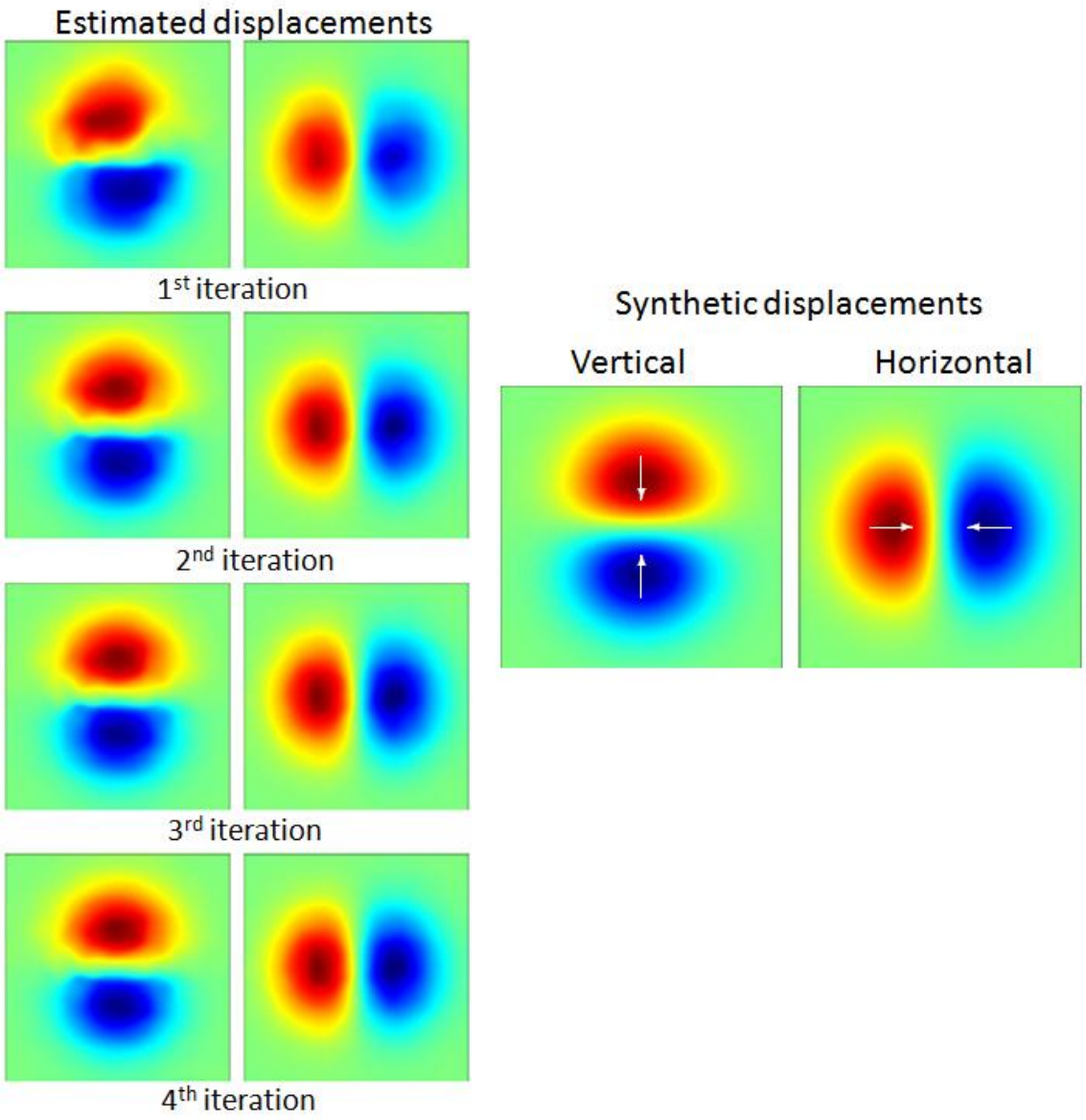

Figure 4.15 Four consecutive cycles (left) estimating 2-D shifts of an image originally warped as shown on the right figures (Hale, 2009).

For the study in this thesis the time-shifts have been calculated in four iterations using a search window of 15x12x12 samples in the vertical, in-line and cross-line directions respectively, with sampling intervals of 4 ms and 12.5 m. This procedure was applied to all time-lapse vintages. The results for the 1989-1999 and 1989-2003 periods is shown in Figure 4.16.

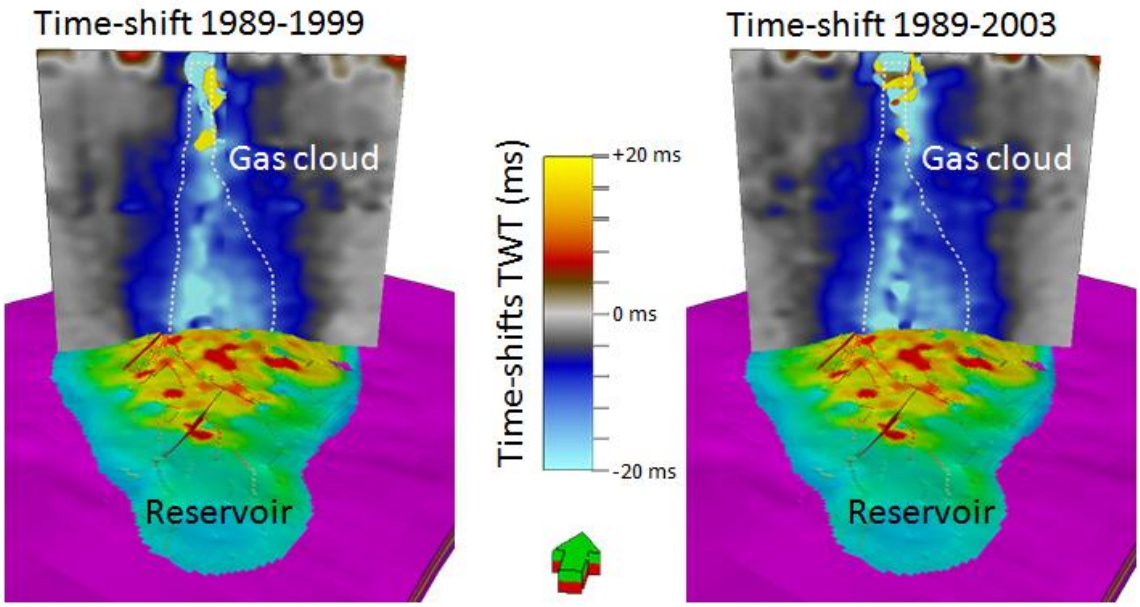

Figure 4.16 Time-shift cross-section for the first two monitor surveys calculated with the 3D warp method. Also shown is the initial reservoir model porosity at the top Ekofisk Formation. The dashed line shows the boundary of the obscured area as observed in the RMS cube (Figure 4.11).

The large window size and the filters included in the warping algorithm yield relatively smooth time-shifts, with the added benefit of reducing the obscured area of the gas cloud. A more comprehensive study of the effects of different window sizes is presented in Chapter 5. The dashed lines in Figure 4.16 delimit the extent of the gas cloud as observed in the RMS-amplitude cube (Figure 4.11). However, unlike conventional 1D cross-correlation, with warping meaningful time-shifts can to some extent be observed inside this boundary. Having calculated the time-shifts, the time-strains are obtained by calculating the derivative with respect to time e.g. the slope of the time-shift traces. This step is necessary in order to calculate the physical vertical strains of the overburden needed to apply the Wiener-filters.

Given the nature of the obscured area that thins out upwards away from the reservoir; an overburden horizon was selected such that it is far enough from the reservoir that the obscured area is minimized, but not too far that too much information is lost by attenuation of high-frequency information. The selected horizon, corresponds to the 6th surface from top to bottom of the geomechanical model, and is located approximately 1000 m above the top reservoir. Stratigraphically, this corresponds to the zone immediately below the Miocene marker. This zone is about 200m thick, along which

the measured time-strains have been vertically averaged in order to have more robust data, and strains that correspond to the thickness of the cells in the geomechanical model. By comparing via equation (1.10) these time-strains for each time-lapse time step with the corresponding simulated vertical strains, an R-factor of 10 has been chosen to calculate vertical strains from observed time-strains. Though this value is by no means a perfect estimate, the nature of the Wiener filters implies that any inconsistency within R translates into a scale factor on the final result. Although an R of 10 is double that which has been estimated by Janssen et al. (2006), their estimates were for the overburden as a whole, not just one formation as presented here. Given that the overburden is composed of different materials described by different elastic constants, there is no reason why a single R-value should be sufficient to describe them all.

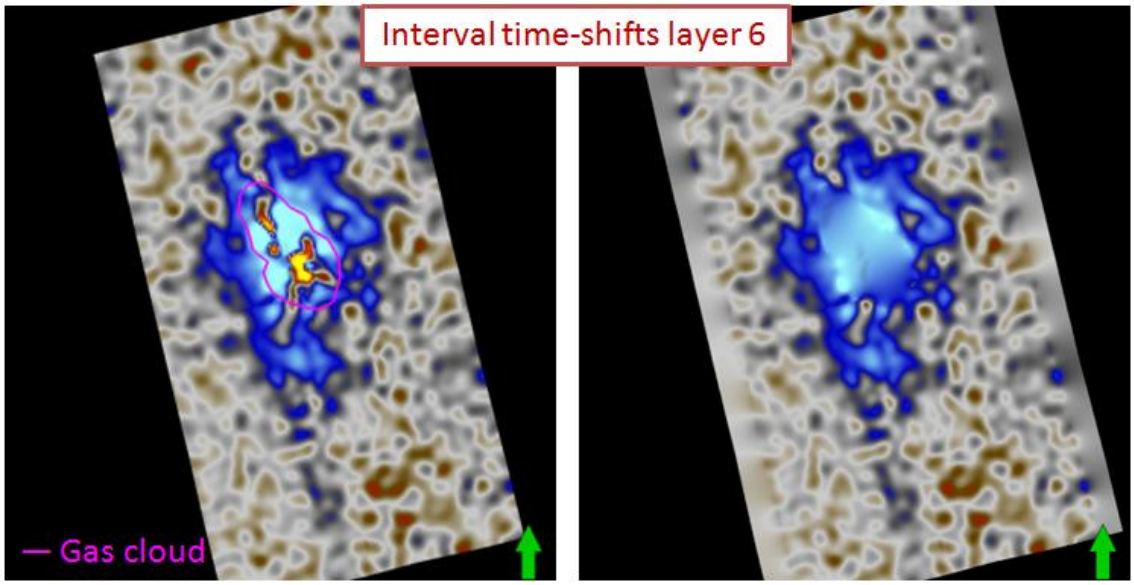

Figure 4.17 Interval time-strains at horizon 6. The left map shows the measured data and the boundary of the area affected by the gas cloud. The data inside this boundary is removed and replaced by linear interpolation (right map).

Nonetheless, even 1000m above the reservoir the effects of the gas cloud on the seismic are considerable, generating some impossible patterns as a by-product of correlating noise with noise from monitor and base surveys. Specifically, only an increase of the overburden seismic travel-times is expected and geomechanically consistent, therefore ruling out as non-physical the anomalies observed in Figure 4.17 inside the gas cloud. For this reason, the data inside the area affected by the gas cloud on layer 6 is removed

and replaced by a linear interpolation as shown in Figure 4.17. The reason for this is that when deconvolving the time-shifts with the Wiener-filters, the interpolated data will have a far smaller negative impact on the estimated reservoir compaction, than the highly noisy data inside the gas cloud.

4.6 Segmentation and Wiener-filters

In order to calculate the Wiener-filters, a record of how the system responds to localized perturbations, i.e. the impulse response, is needed. Since the overburden's response depends largely on structure, the Ekofisk geomechanical model has been divided in five segments based on dip azimuth and dip angle (each segment has largely the same slope). A sixth segment corresponds to the area outside the reservoir, shown in dark blue in Figure 4.18. In each of these segments (excluding the sixth) identical pressure change synthetic sources are placed to simulate the subsurface response to it using the geomechanical model in terms of reservoir volumetric strain and overburden vertical strain (Figure 4.19). The sources consist of a -100 KPa pressure change peak that decays to zero in the next three cells (i.e. 150 m). As used in Chapter 3, sources are stacked on top of each other permitting discrimination between the two reservoir formation; i.e. Ekofisk and Tor. Figure 4.19 shows a synthetic source on the central segment of the Ekofisk formation and the simulated overburden and reservoir strains.

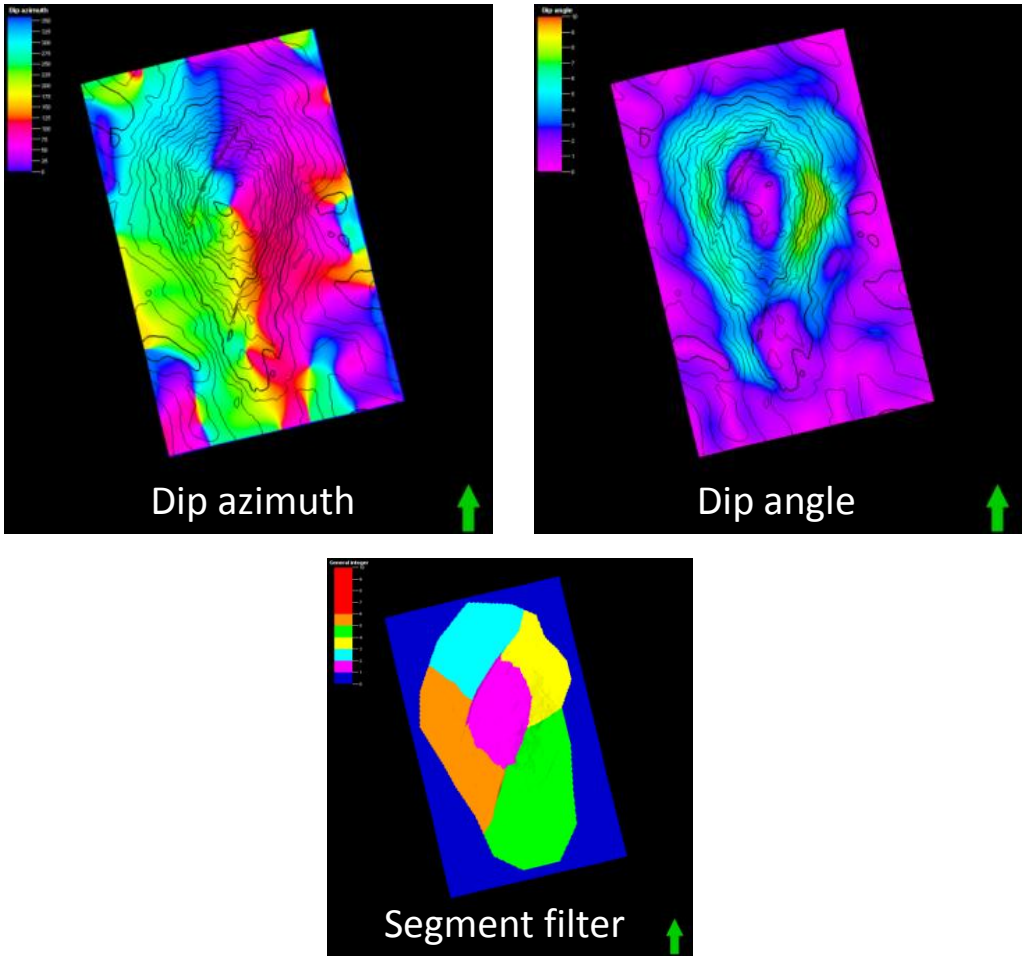

Figure 4.18 Segmentation of the Ekofisk model: based on the dip azimuth and dip angle maps, the Ekofisk model is divided into zones with similar structure, upon which a synthetic source is placed to calculate the segment's Wiener-filter.

In total, ten sources are placed, one for each segment (x5), and one per reservoir unit (x2). Once the calculated Wiener-filters are applied, this results in an equal number of maps of estimated reservoir compaction; that is five for each formation. The final result is a stack of maps, where each segment is calculated separately. For example, for a given segment, the estimated compaction using a source located in that segment will be weighted more in stacking than the other source results; e.g. 4/8 for the source inside the segment and 1/8 for the remaining four sources. The stacking is done in order to increase the signal to noise ratio and to ensure smooth overlapping at the segment boundaries. For the sixth segment all compaction maps are weighted equally.

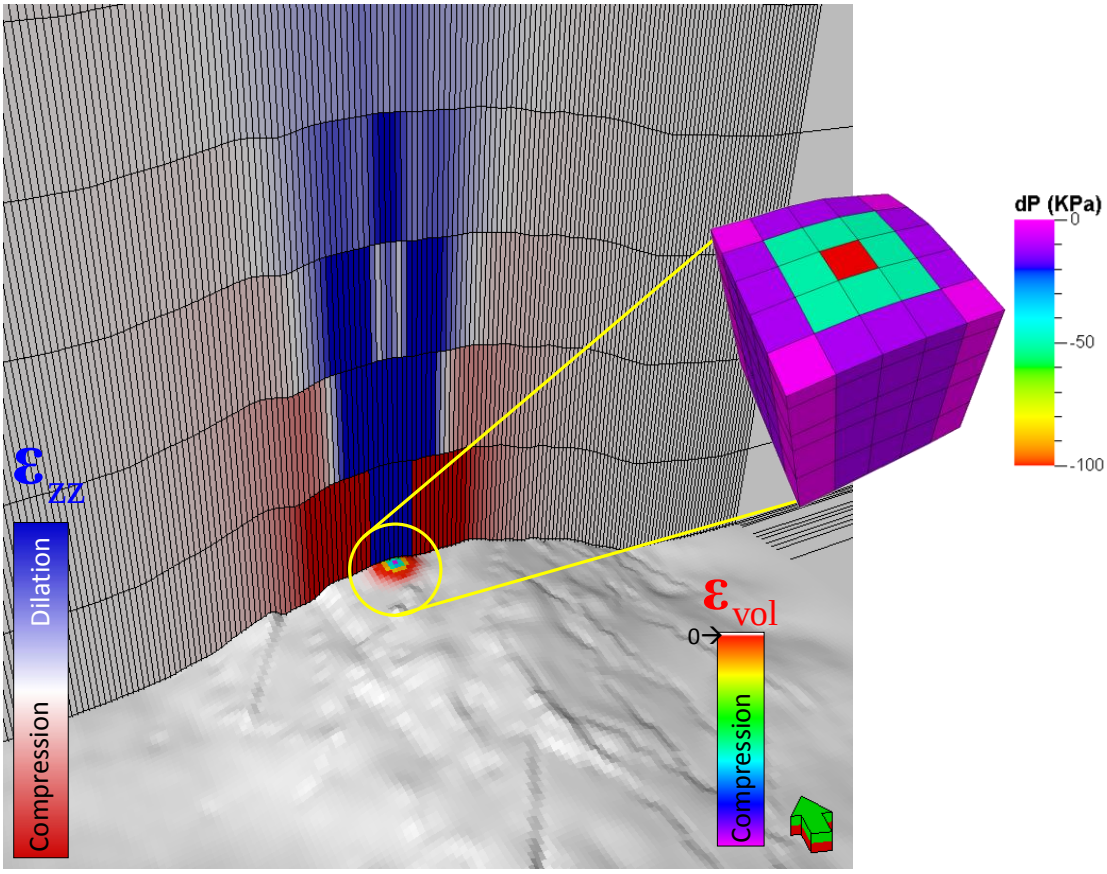

Figure 4.19 Synthetic source and simulated overburden vertical strain and reservoir volumetric strain, located in the central segment of the Ekofisk formation. The source consists of a -100 KPa pressure change peak that decays to zero in the next three cells (i.e. 150 m).

4.7 Wiener-filter results

With the final estimated reservoir volumetric strain maps from the Wiener-filters, changes of mean effective stress are also calculated as given by equation (3.4). However, in the Ekofisk case, porosity changes are no longer negligible. Recall that the bulk modulus has been calculated using equations (4.1) and (4.2) as functions of porosity. Therefore, for each time-lapse time-step *i*, the reservoir's porosity ϕ_i, is updated in terms of the initial porosity ϕ_0, with the estimated volumetric strain ε_{vol}^i, as

$$\phi_i = (1-\phi_0)\varepsilon_{vol}^i \tag{4.3}$$

Consequently, to each seismic time-step corresponds a new set of elastic constants and the mean effective stress change is now

$$\langle \Delta\sigma_i' \rangle = K_i \varepsilon_{vol}^i \tag{4.4}$$

where $K_i = K(\phi_i)$ is the updated bulk modulus of the ith seismic time-step.

For the present study, given the complexity of the field and the large amount of data, the decision was made with ConocoPhillips to concentrate in a smaller area of 4x4.5 km, just south of the crest and outside the obscured zone. Although Wiener filters have been used on the entire field, only the section shown in Figure 4.20 has been analyzed. Figure 4.20, Figure 4.21 and Figure 4.22 show the results for the Ekofisk formation for the 1989-1999, 1989-2003 and 1989-2006, and 1989-2008 periods respectively. Additionally, Figure 4.22 also shows results for the intermediate steps 1999-2003 and 2003-2008.

The overburden dimensionless interval time-strains $(\Delta t/t)$ upon which the Wiener-filters operate, are displayed along with the estimated volumetric strain and mean effective stress changes (in bar) for the Ekofisk formation. In general, the fact that the overburden interval time-strains look different from the estimated reservoir compaction, prove that inversion with Wiener-filters is not just mapping overburden deformation into the reservoir, but that as demonstrated in Chapter 2, it takes overburden heterogeneity and structure into account.

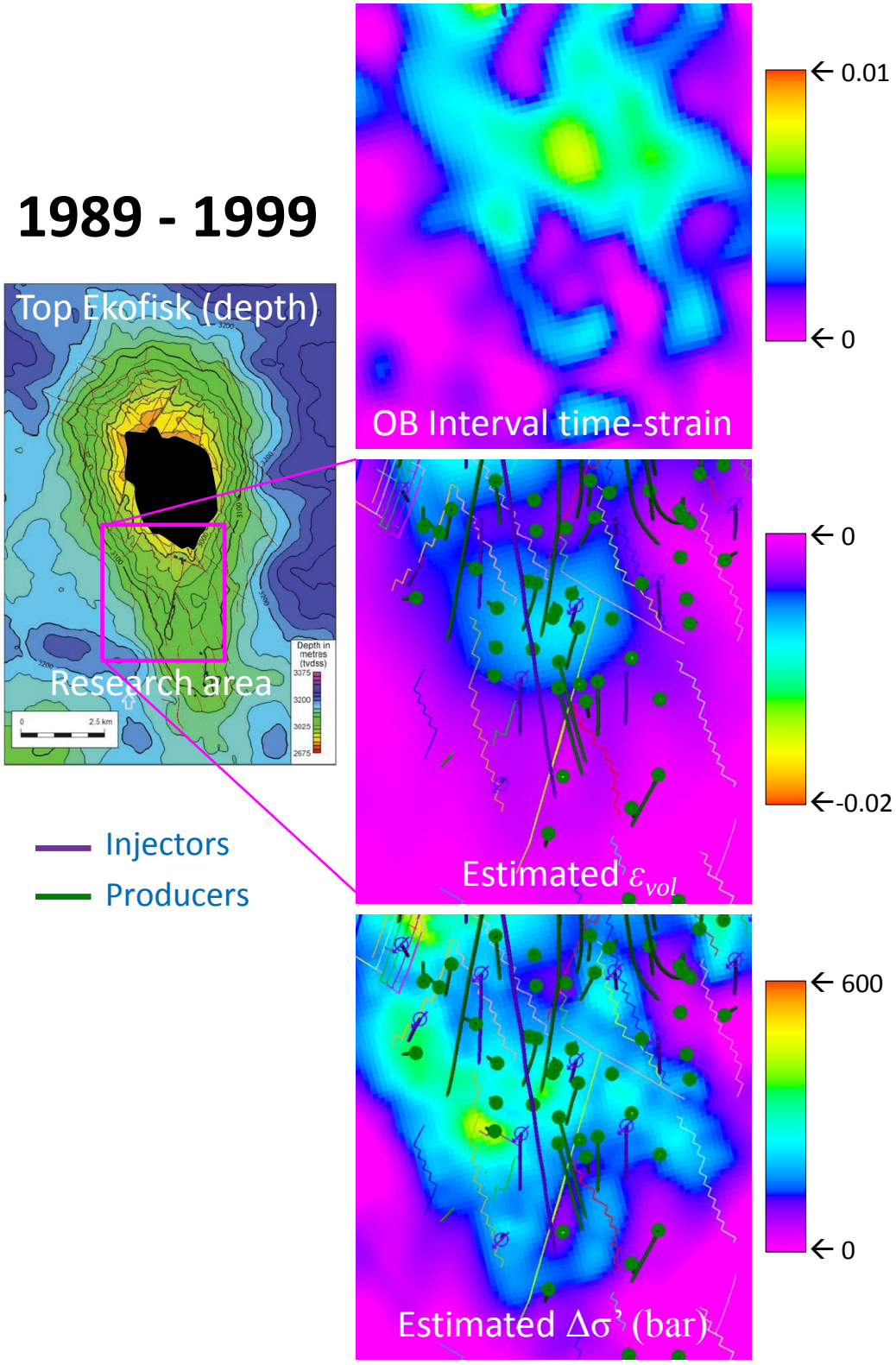

Figure 4.20 The structural map on the left shows the relative location of the study area. The results for the time-lapse period 1989-1999 are displayed on the right, where the top figure corresponds to the overburden interval time-strains of layer 6 used as input to the Wiener-filters. Below are the estimated volumetric strain at the Ekofisk formation and the calculated changes in mean effective stress (bar).

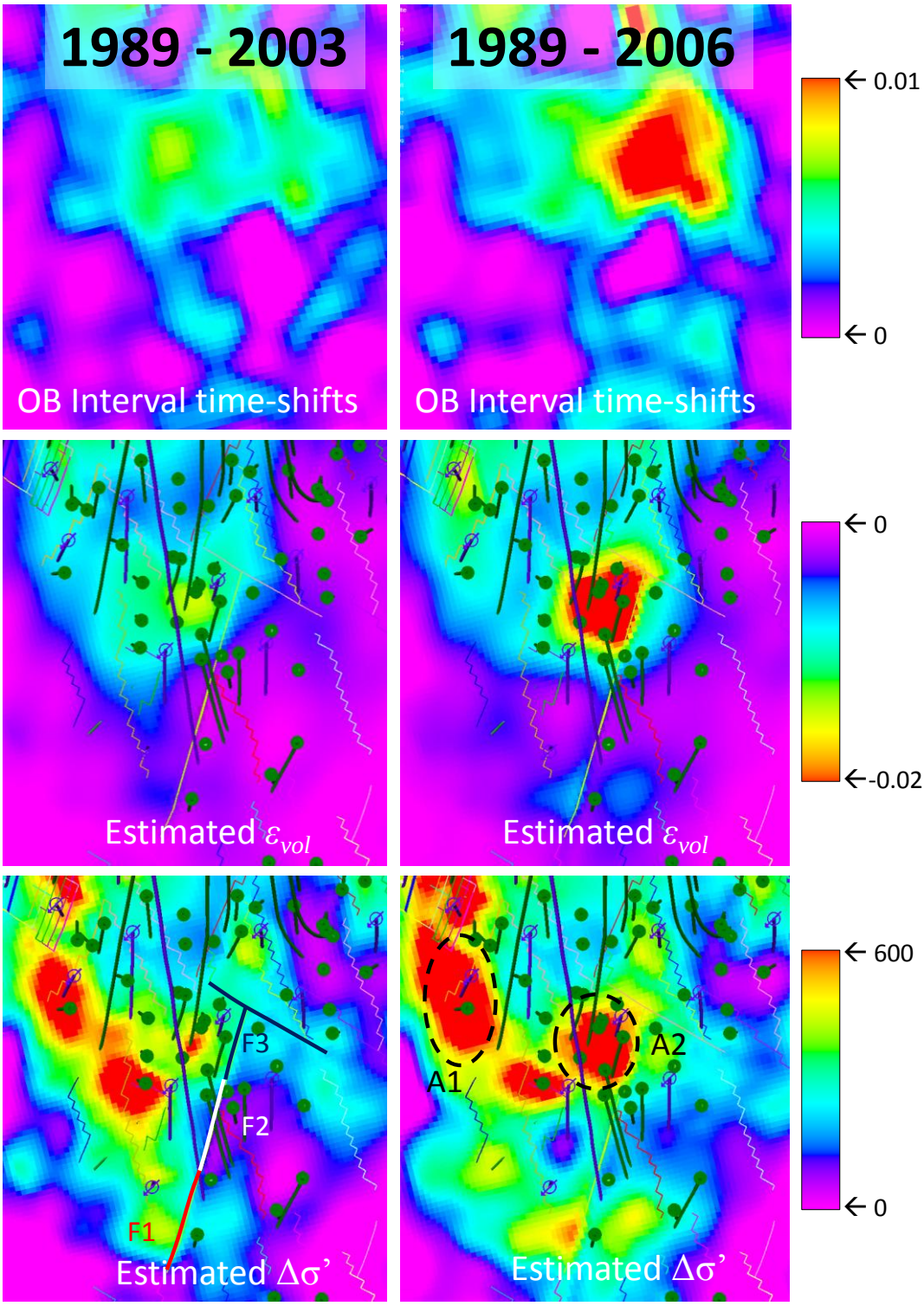

Figure 4.21 Results for the 1989-2003 and 1989-2006 on the left and right columns respectively, showing overburden interval time-strains (top), estimated volumetric strain (middle) and estimated mean effective stress change (bar) for the Ekofisk formation.

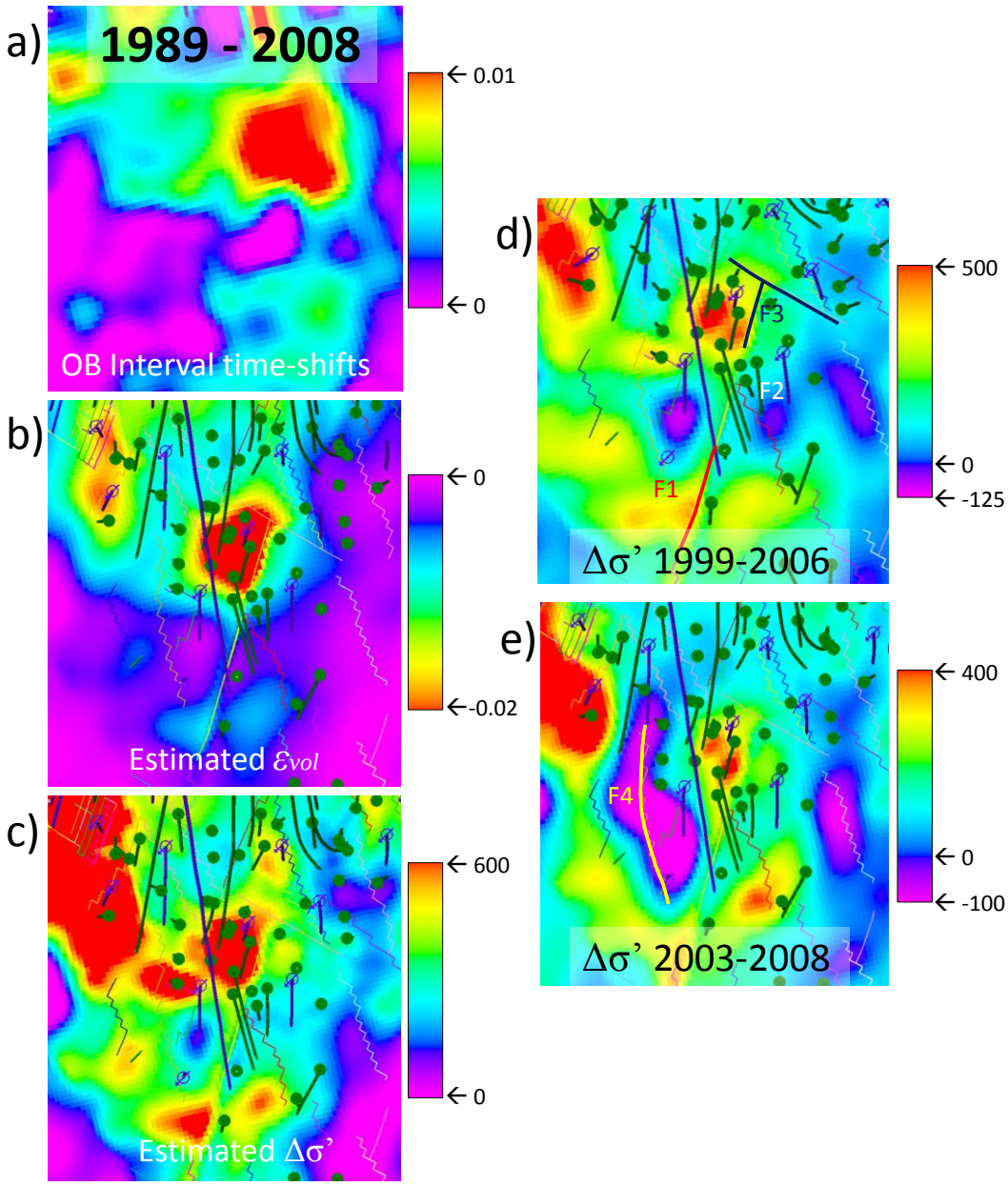

Figure 4.22 Results for the 1989-2008 period on the left column (a), (b) and (c). The right column shows the estimated mean effective stress changes (bar) for the intermediate periods 1999-2006 (d) and 2003-2008 (e).

Overall, results with the base survey (1989) as an initial state, all show widespread compaction and increase in effective stress. Note also that the overall polarity of the estimated mean effective stress is positive, meaning a net increase in compressive stress despite extensive water injection. These results agree with field observations, since despite water injection subsidence has never stopped. Therefore, regardless of injection there is still a net field-wide compression.

The estimations for the time-lapse period 1989-2003 (Figure 4.21) in addition to corroborate the previous observations, may give some indication of the transmissibility of the central fault. The fault, located at the centre of the research area and running south-west to north-east is highlighted in three segments labelled F1, F2 and F3 on the 1989-2003 effective stress map (Figure 4.21). Assuming that the mean effective stress changes are mostly caused by depletion, the producer nearest to the east side of fault F1 appears to be depleting form the west side of the fault. Additionally, as the southern segment of the fault appears permeable from the observations, the middle segment F2, does not and the near zero effective stress changes associated with pressure support from the injectors, do not appear to propagate westwards.

After 2003, the 1989-2006 and 1989-2008 results show a good correlation of mean effective stress changes with most well locations; largely, near zero to low values around injectors. Nonetheless, well status and well activity was not available for this study. However in some cases, where injectors are very close to producers (areas A1 and A2 encircled in the 1989-2006 effective stress map -Figure 4.21), only strong compressive stresses are visible. This could be an indication that these areas are being effectively water swept. This, in hand with depletion and water weakening, gives rise to the high estimated volumetric strain. In other words, water injection per se does not give rise to water weakening and measurable compaction, it is the process of replacing oil with water that does, and is enhanced if the overall final pore pressure is less than the initial one. Also visible after 2003, is the equalization of mean effective stress at both sides of the F2 section of the central fault. Provided these changes can be attributed only to changes in pore pressure, the observations may indicate that the F2 section of the central fault has ceased to act as a seal, allowing the equalization of pore pressure at both sides of the fault; a direct evidence of seal fracture. The results for the 1989-2008 time-lapse period agree with the above observations and emphasize the added value of the Wiener-filter method which could give an indication of injection fronts, drainage areas and fault transmissibility.

A better understanding of the field's performance can be attained by looking at the intermediate mean effective stress changes of recent surveys shown in Figure 4.22, as compaction and depletion are more under control and the quality of the 4D seismic improves. With regards to the A2 area mentioned above, west of the F3 fault, some resolution of the injector can be attained as opposed to the 1989-2006 map; i.e. the

strongest stresses are now around the producers. This is clearer still, in the 2003-2008 map.

For the intermediate time-steps Figure 4.22 (d) and (e), negative effective stress changes can be observed suggesting that such areas have experienced an increase in pore-pressure and perhaps some dilation relative to the time-lapse observation period and not that net compaction is being reversed, since, as has been discussed above, the reservoir's net strain has always been compressive. The 1999-2006 results show across both segments F1 and F3 of the central fault contrasting mean effective stress changes. This could indicate that to some extent these segments act as flow barriers, whilst the F2 segment looks now largely open. Additionally, if one assumes that zero mean effective stress corresponds to the front of the pressure wave from the injectors, the injection front is clearly visible and could be tracked at both ends of the F3 fault. Note however, that the mean effective stress changes for this interval are relative to whatever state the reservoir was prior to 1999. In other words, negative effective stress changes indicate that the pore pressure has increased above the confining stress at the start of the observed interval, in this case 1999. This may give rise to the opening of fractures, provided the excess pore pressure is above the tensile strength of the rock.

The assumption that negative mean effective stress changes can be associated with injection fronts alone, implies neglecting total stress changes or overburden relaxation as this will happen on a large scale instead of locally. Under this assumption, the distinctive feature observed in the 2003-2008 map (Figure 4.22) of negative mean effective stress changes concentrated along the fault labelled F4, could be interpreted as the water from nearby injectors flowing along the fault. This hypothesis is not unlikely, given that the primary mechanism for fluid flow in chalk is fracture permeability. However, it does contradict the results from the reservoir simulation (Figure 4.23), which instead expects the waterfront along the central fault (F1 and F2 segments). Though, it is worth mentioning that several issues have been recognized in the model and that it does not correspond to the latest history matched reservoir model, which was not available for this study.

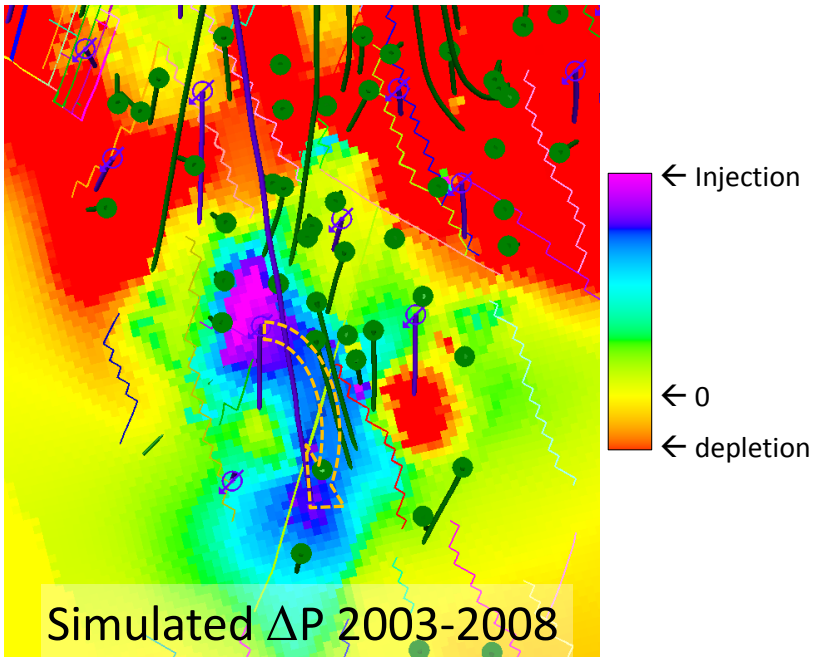

Figure 4.23 Simulated pressure change of the Ekofisk formation for 2003-2008 time-lapse period, from a history matched reservoir model

A less detailed analysis of the Tor formation is presented in Figure 4.24, since it is not the main producer. Results for all time-lapse years are not shown, but rather just a few intermediate stress changes. In the same way as before, interpreting negative stresses as an indication of the position of the injection fronts allows to track them through time. The other possibility, that such stress changes are a product of decrease in total stress might not be negligible in the Tor formation since a considerable weight in the form of extracted hydrocarbons is being removed from the overlying Ekofisk formation. However, this effect is hard to quantify and will be ignored. Therefore, by observing the evolution of the negative mean effective stress changes, it can be speculated that the seal on the central fault has been fractured in the F2 segment after 2003 (dashed red circle 1999-2006 and 1999-2008 maps). The above hypothesis is consistent with what has been suggested in the Ekofisk formation and additionally hints to the precise location of the possible fracture. Moreover, the insinuation of fracturing in both Ekofisk and Tor if correct suggests that either the fracture propagated between both formations through the tight zone, or that the tight zone in this area was permeable to begin with.

The simulated pressure change shown in Figure 4.24, has two clear differences with the observed mean effective stress changes: first, the highest depletion appears on the west side of the F3 fault segment, whereas the stress changes 1989-2008 show it on the east

side. Second, the stress changes seem to spread farther south than the simulated depletion indicates.

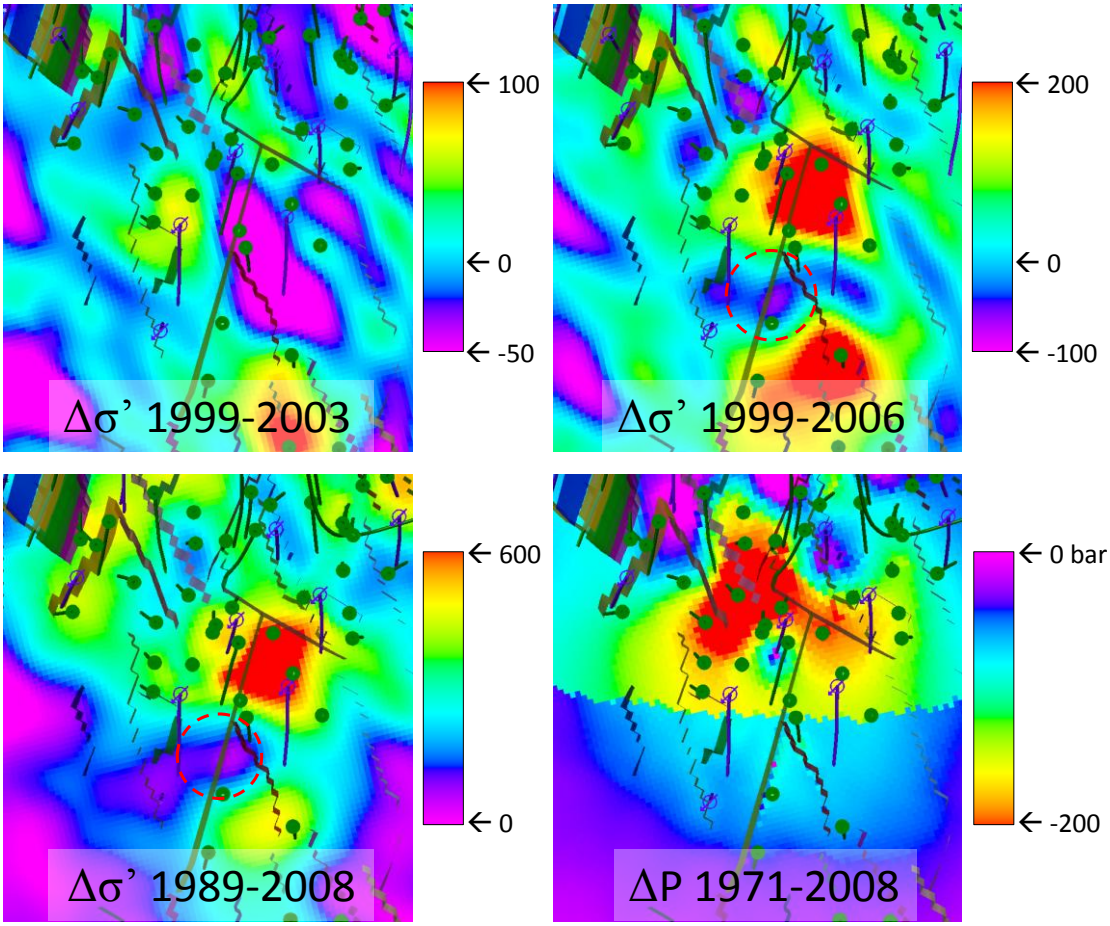

Figure 4.24 Estimated mean effective stress changes (in bar) of the Tor formation (1999-2003 top left, 1999-2006 top right and 1989-2008 bottom left) and simulated pressure change (bottom right).

4.8 Conclusions

The Ekofisk field, the largest of its kind in the North Sea, has been under production for 40 years. The complex behaviour of the reservoir rock, the large number of wells and the suboptimal quality of the seismic imaging (e.g. obscured area), make any study on the field very challenging. On top of this, not all well locations and well information in the form of well status and well activity was available for this study.

In addition to the above, the fact that the base survey was taken 18 years after production started in 1971, means that reservoir conditions at the acquisition time have a large uncertainty, making the interpretation of observations more difficult. Correlation of observations with known well activity will provide a tool to tie in the overburden derived observations to hard data at the reservoir helping to understand the nature and timing of the Wiener-filter results.

Nonetheless, this study has proven that a simple geomechanical model able to describe the overburden's gross deformation is sufficient to calculate the Wiener filters. Additionally, this research has provided information that could be used to determine the following parameters to update the simulation model:

1. Position of the injection front
2. Fault transmissibility
3. Possible hydraulic fracturing
4. Drainage areas
5. Flow paths

Information on the movement of the water fronts, in addition to the observed drainage areas not present in the simulation model if confirmed by well data, will prove the value of the Wiener-filter method as a tool to update the simulation model.

The current state of the reservoir rock in terms of tensile strength is hard to guess, given that most of it has experienced some amount of compaction, even pore collapse and perhaps water weakening. As a consequence, injection of high pressure fluid into the formation may result in the opening of fractures that may result in ineffective water sweep, if changes in the tensile strength of the rock are not accounted for. Consequently, getting the initial reservoir conditions or for that matter the conditions at a seismic survey time right, are of outmost importance. However, in mature and complex fields like Ekofisk such characterization proves very difficult at best. Nevertheless, Wiener-filters and its application to time-lapse seismic provide the means to monitor undesired effects related to production and reservoir management.

Chapter 5

5 Seismic time-lapse analysis at the South Arne field, Danish North Sea

South Arne is a chalk field of similar characteristics to Ekofisk, whereas in Ekofisk the Ekofisk formation is the main reservoir horizon, at South Arne production takes place mainly from the underlying Tor formation. The reservoir structure is an elongated double-dipping anticline with the long axis oriented NW-SE and a graben-like structure (with same orientation) on the crest at the north shoulder (Figure 5.1). Production started in 1999 from horizontal wells parallel to the axis of the reservoir, interleaved with water injectors. Production has been enhanced by induced vertical fractures. A high repeatability time-lapse seismic has been acquired with baseline survey in 1995 and monitor in 2005.

In this chapter, I again use overburden time-lapse time-shifts and derived time-strains to compute reservoir compaction using the Wiener filter method. Special attention is given to the effect of using different methods of time-shift computation. I compare time-strains as calculated from warping (Hale, 2009) using four different window sizes, and time-strains computed using 1D cross-correlation. The vertical components of the warp vectors, the time-shift, are compared with those obtained from 1D cross-correlation. Overburden time-strains from all five time-shift cubes are inverted using Wiener-filters that have been calculated using a geomechanical model. The geomechanical model is based on the reservoir model and calibrated to match bathymetry observations. The Wiener-filter results are analyzed in comparison with reservoir model predictions and time-lapse seismic attributes. The results agree with observations and together with the time-lapse seismic attributes permit resolution between Tor and Ekofisk formations.

5.1 Field description

The South Arne field is located in the Danish sector of the North Sea. The structure is an elongated Cretaceous inversion ridge situated on the western margin of the Tail-End Graben (Cipolla et al., 2007), with the long axis oriented north-west to south-east (Figure 5.1). The crest of the reservoir on the north shoulder has the best reservoir quality and presents a graben-like structure formed by post-depositional faulting (Figure 5.2), oriented parallel to the main axis. The reservoir laying at about 2900 m depth, is a high porosity low permeability chalk of Maastrichtian and Danian age, comprising the Tor and Ekofisk formations, respectively. A hard, low porosity interval at the bottom of the Ekofisk formation, known as the Tight zone, separates the two formations. Virgin reservoir pressure is 440 bar and reservoir temperature of 115ºC. The reservoir is low to moderately naturally fractured. The combined thickness of the Ekofisk and Tor reservoir varies from 10 to 150m and is located unconformably between thick shale layers.

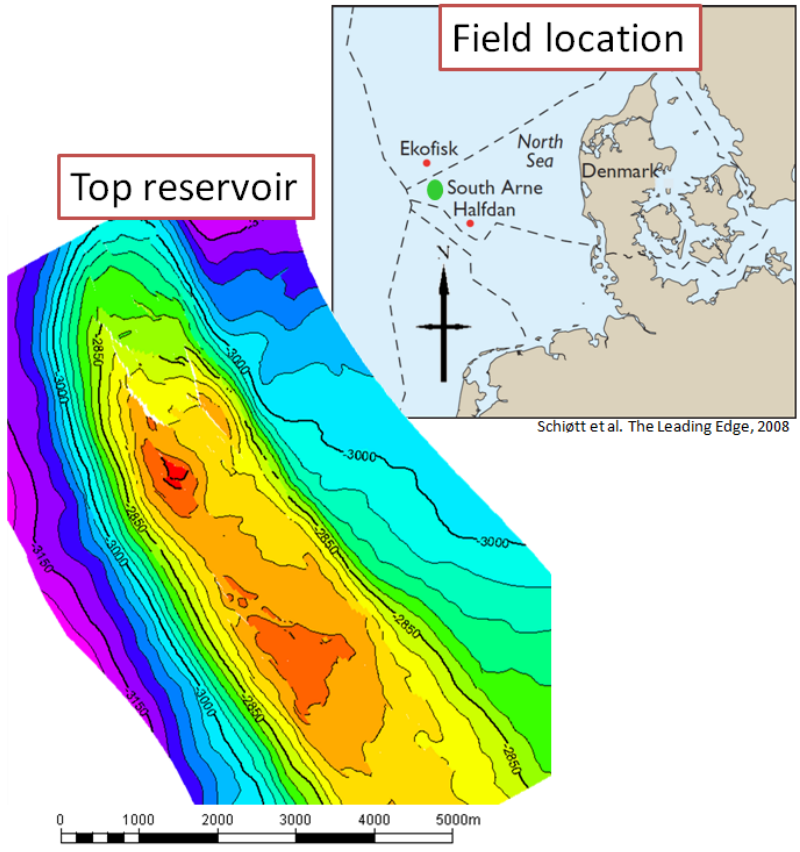

Figure 5.1 South Arne field location and depth map at top reservoir.

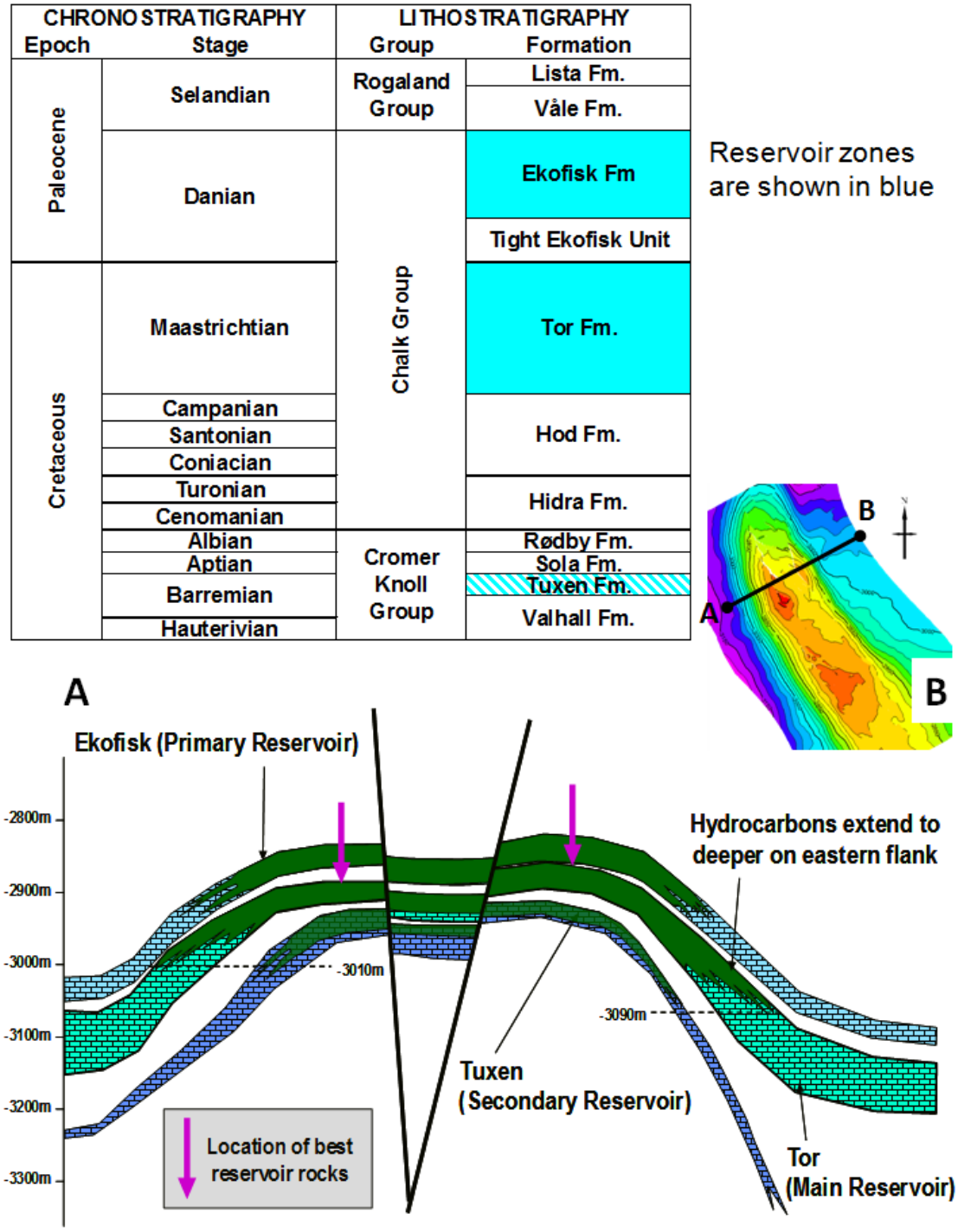

Figure 5.2 Stratigraphic column and geological cross section of the South Arne reservoir (images shown with permission from Hess internal report).

The best quality reservoir rock lies on the north flank in the Tor formation with porosities ranging from 20 to 45%. Reservoir permeability ranges from 0.1 to 10 mD, with fractures and faults providing the main contribution. The reservoir is thinner towards the crest of the structure and thins down to an unconformity southwards along the crest. Down dip on the other hand, the chalk sequence thickens (Figure 5.3), whilst

at the same time porosity and permeability decrease considerably (Mackertich and Goulding, 1999). As a consequence pressure support from the aquifer is negligible, since the oil water contact lies on the distal part of the structure where the permeability is lowest.

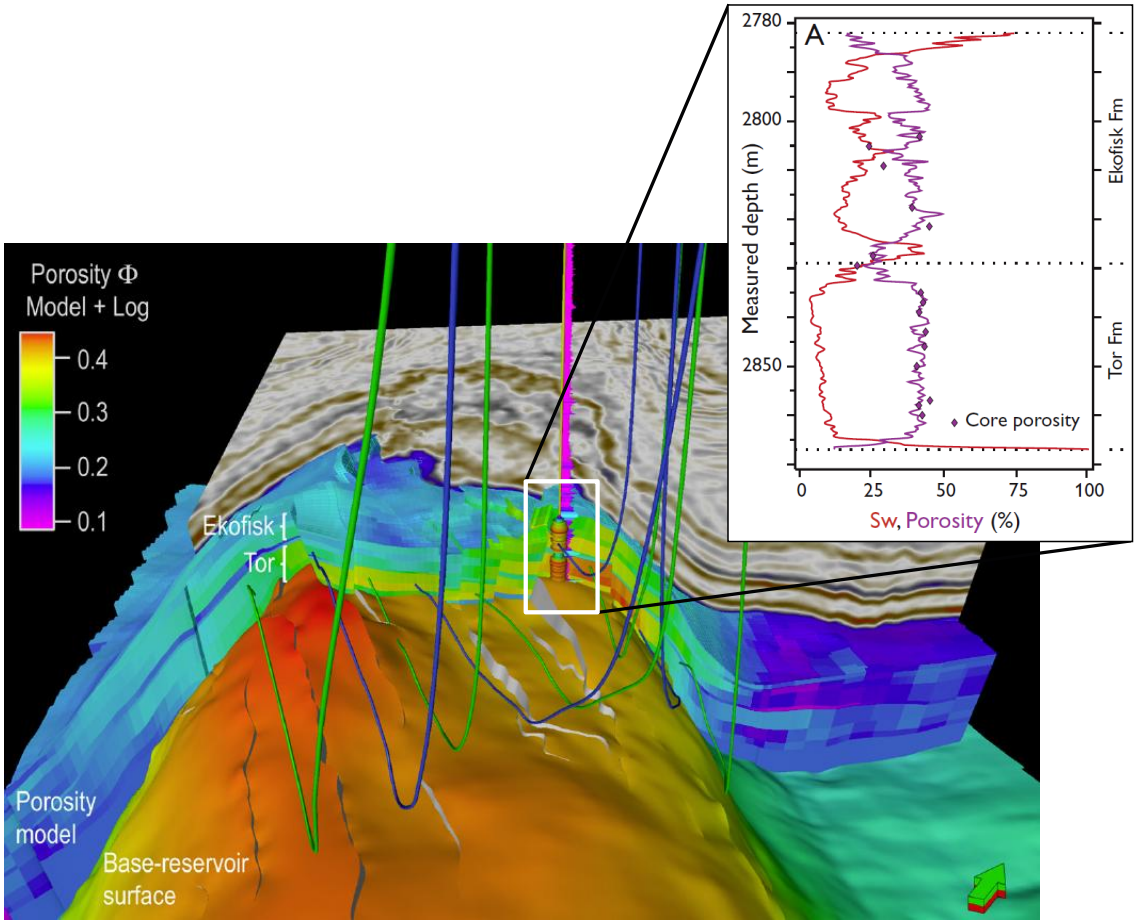

Figure 5.3 Three dimensional view of the north section of the field (Herwanger et al., 2009). The reservoir's porosity model section shows the highest porosities towards the crest with reservoir thickness thinner than on the flanks and a clear division between Ekofisk and Tor formations. The base reservoir surface highlights the field's configuration, where the graben structure is clearly visible. The log data (Japsen et al., 2005) shows the porosity (estimated from the density log) and water saturation (Sw), revealing the Tor formation as the better reservoir.

The field came onstream in 1999 from horizontal wells drilled parallel to the natural fracture orientation. The initial wells were placed on the upper third of the Tor formation to account for a better communication between the Ekofisk and Tor reservoirs. All wells have been completed with multiple induced vertical hydraulic

fractures. After an initial pilot project, a field wide water injection program started in 2000, with injectors drilled parallel and interleaved to producers (Wesnæs et al., 2002). Although most of the drive energy for hydrocarbon production comes from water injection, it is estimated that on the crest of the reservoir, up to 20% of the drive comes from compaction (Herwanger et al., 2009).

In spite of the efforts to maintain voidage there are quite large pressure variations in the reservoir. This is partly due to internal flow barriers. Gas is coming out of solution in some parts of the field, and compaction is occurring due to pressure draw down. Maximum compaction over the reservoir interval has been estimated at about 1 m as constrained by the time-lapse seismic data (Schiøtt et al., 2008). The time lapse seismic data in hand with geomechanical modelling has also been used to improve the understanding of the expected stress and strain changes of the field.

5.2 Time-lapse seismic data

A preproduction baseline survey was shot in 1995 and a monitor survey in 2005. Both are towed streamer with the second being a Q-marine survey. In order to maximize repeatability, the monitor survey was acquired with steerable streamers used to match as close as possible the baseline geometry. During the 2005 acquisition, due to production infrastructure i.e. the platform and a shallow buoy, two significant holes are present in the acquisition coverage (Figure 5.4). Prior to migration, these holes were filled with 1995 vintage data.

The final cubes for 4D analysis correspond to equivalent stacks, with a processing sequence designed to maximize repeatability in areas where time-lapse differences were not expected. The overlap areas of the two surveys were processed through an identical processing route. The final stacked cubes were generated at a trace spacing of 12.5 m x 25 m, at 2 ms sample interval, and to 7000 ms data length. The resulting repeatability is excellent, with NRMS (Kragh and Christie, 2002) of about 12%. However, reservoir imaging is obscured by a gas cloud over the crest (Figure 5.5).

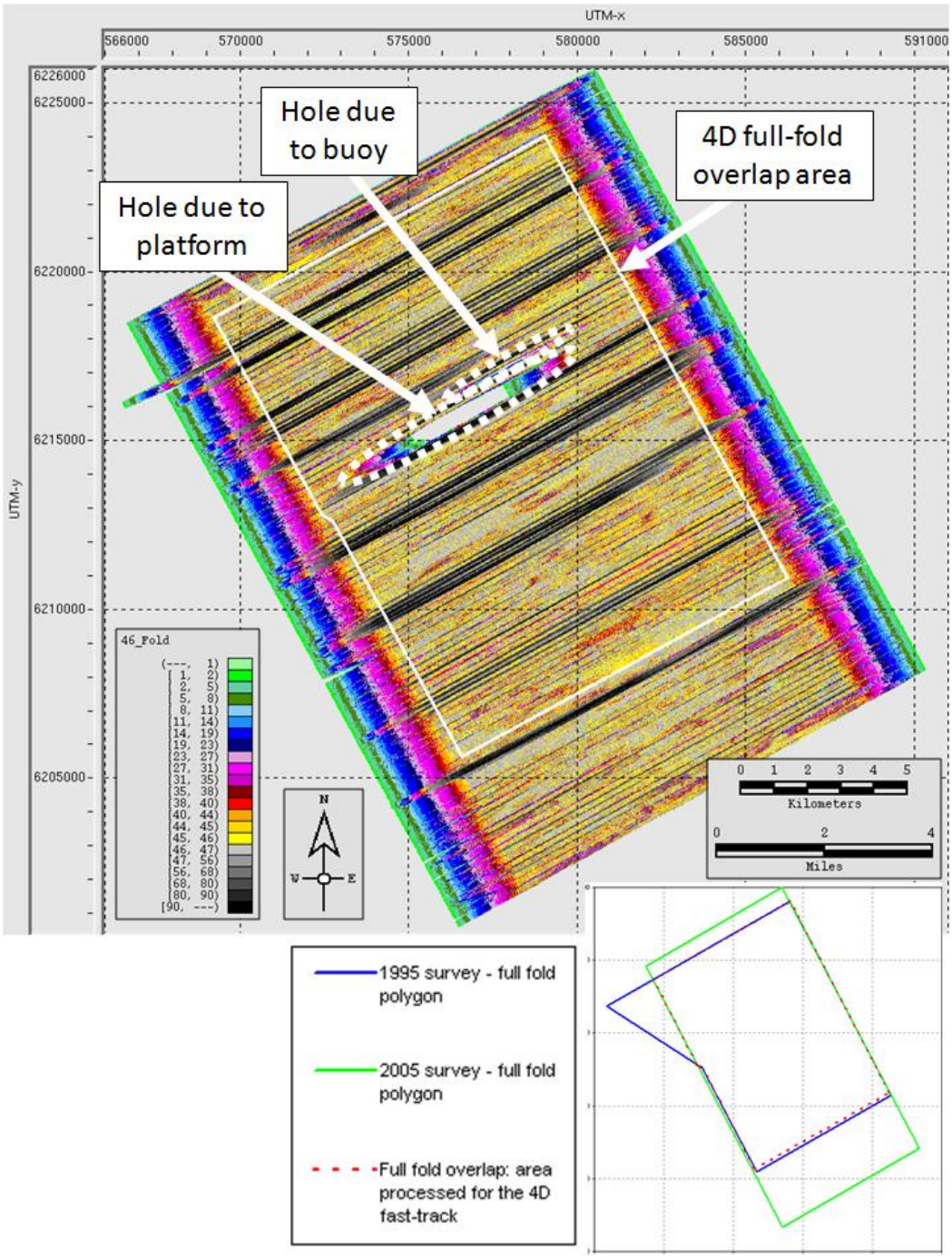

Figure 5.4 Acquisition geometry of the monitor survey, showing the full-fold area and data holes due to surface infrastructure. The lower figure shows the full-fold areas covered by the two surveys shown in blue and green for the baseline and monitor surveys respectively and the full-fold overlap area for the 4D study (Groombridge, 2006).

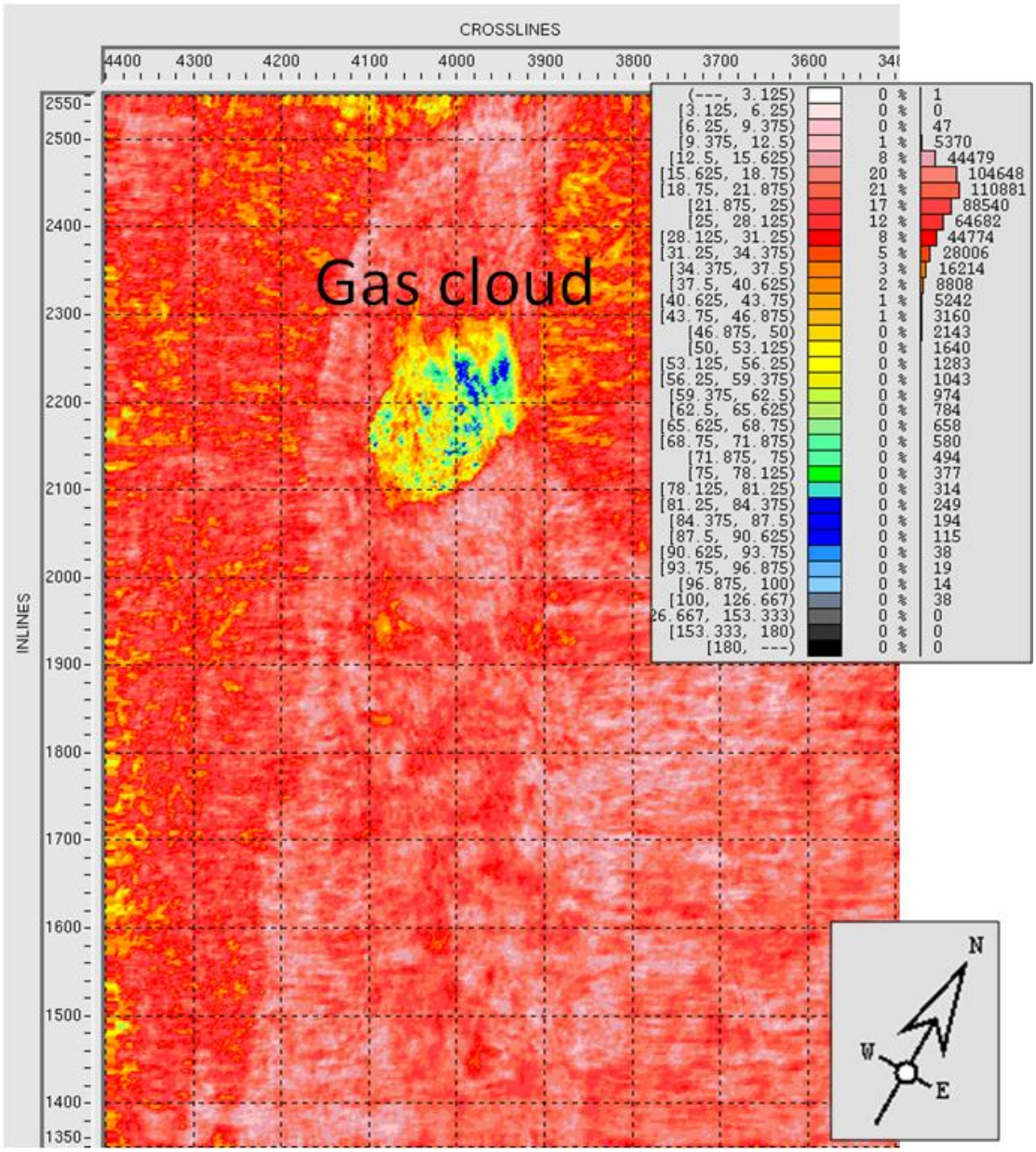

Figure 5.5 High-resolution 4D NRMS computed over time window 2.6 s – 2.9 s, showing the gas cloud over the crest and very high repeatability everywhere else (Groombridge, 2006).

5.2.1 Use of time-lapse seismic data on South Arne

Chalk reservoirs are naturally prone to compaction. However, the mechanisms through which they compact are various; i.e. elastic deformation, pore collapse and water weakening. In the latter scenarios of plastic deformation, the constituency of the reservoir rock changes severely. In order to be able to track fluid movements and depletion from time-lapse seismic attributes a thorough understanding of these changes

is key. To quantify the changes that compaction has had on the reservoir, Hess commissioned the 4D campaign and has carried out a series of studies with the time-lapse data. After the 4D parallel processing of the seismic surveys, a simultaneous 4D Amplitude Versus Offset (AVO) inversion followed to derive acoustic impedance, Poisson's ratio and related 4-D changes (Herwanger et al., 2009; Schiøtt et al., 2008).

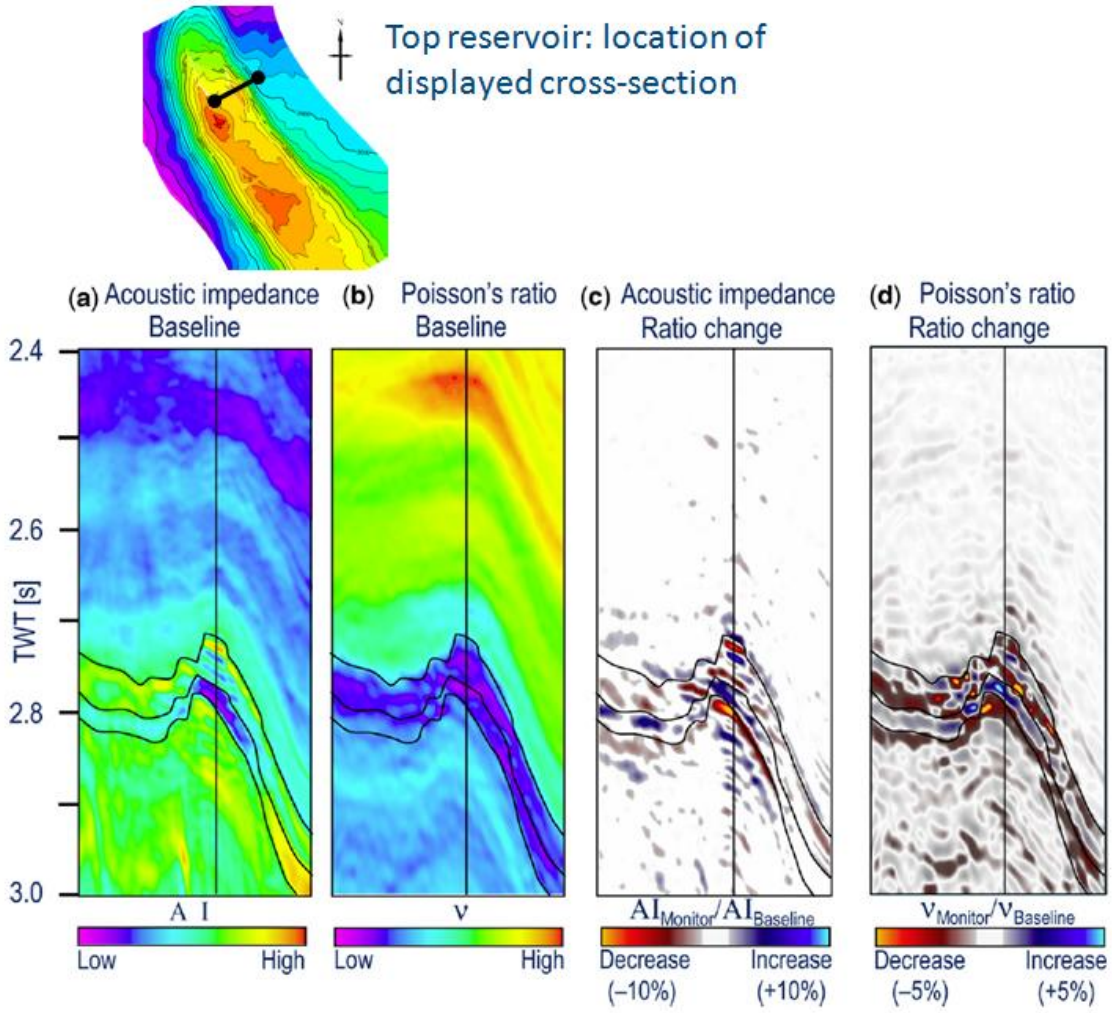

Figure 5.6 Inversion results of acoustic impedance (a), Poisson's ratio (b) for the baseline, and time-lapse ratio changes of acoustic impedance (c) and Poisson's ratio (d). The location of the displayed cross-section is indicated in the top reservoir map inset (Herwanger et al., 2009).

3D AVO inversion exploits the dependency of the reflection coefficients with incidence angle. The reflection coefficients determine the amplitude of the reflected waves and are governed by the property contrast at the materials' interface. For normal incidence waves, the reflection coefficient at a given interface can be described only in terms of

the acoustic impedance of the two materials (Mavko et al., 2009). At incidence angles other than 0º, the reflection coefficient will depend not only on the acoustic impedances, but on the Poisson's ratios and incidence angle (Shuey, 1985). In order to estimate these quantities, seven angle-band stacks (ranging from 0 to 35º) are inverted using simultaneous 3D and 4D AVO inversion (Rasmussen et al., 2004) of the two seismic vintages. The resulting properties are 3D cubes of acoustic impedance and Poisson's ratio using the same sampling as the input seismic. Figure 5.6 shows inversion results for a cross-section across the eastern edge of the graben; acoustic impedance (a) and Poisson's ratio (b) at the baseline time. The inverted time-lapse properties correspond to the ratio changes of acoustic impedance (c) $AI_{monitor}/AI_{baseline}$ and Poisson's ratio (d) $\upsilon_{monitor}/\upsilon_{baseline}$.

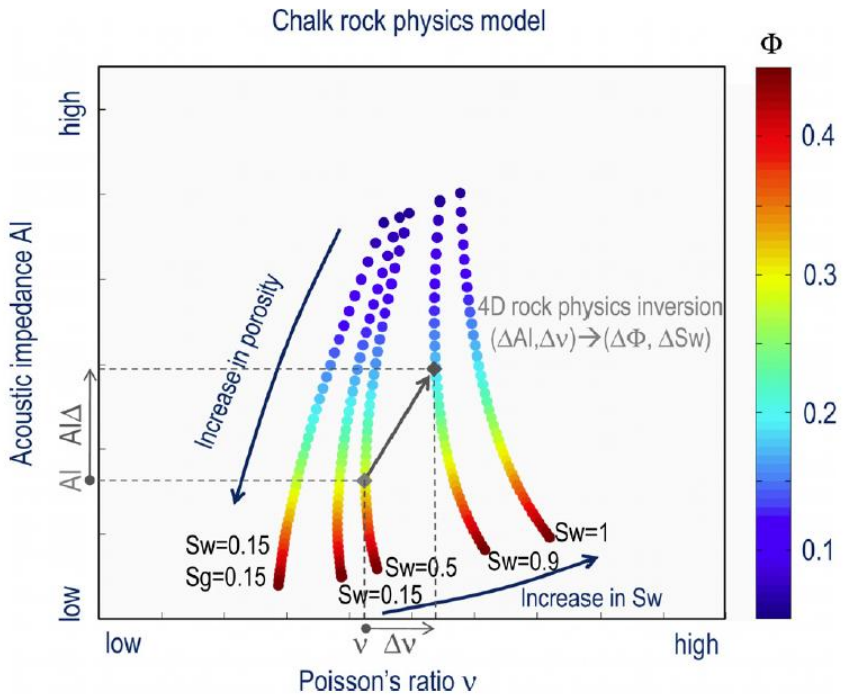

Figure 5.7 Rock physics model for South Arne chalk (Herwanger et al., 2009). Acoustic impedance versus Poisson's ratio; the different curves correspond to constant values of fluid saturation and each point corresponds to a different value of porosity as given by the colour bar on the right.

In order to understand how these changes in acoustic impedance and Poisson's ratio manifest themselves in the reservoir in light of reservoir engineering parameters, a calibrated rock physics model is necessary. The acoustic properties of the reservoir rock

are controlled by multiple factors like depositional environment and diagenesis. Therefore the rock physics model needs to be calibrated for each reservoir unit using well-log data. North Sea chalk has been extensively analyzed and several studies have established trends relating acoustic and reservoir properties (Gommesen et al., 2007; Japsen et al., 2004; Fabricius et al., 2007). All trends agree in the case of the South Arne chalk, that acoustic impedance is a good porosity indicator, whereas Poisson's ratio responds mostly to fluid saturation changes. The AVO inverted properties are translated to reservoir engineering parameters using the rock physics model shown in Figure 5.7. In this way, acoustic impedance and Poisson's ratio changes can readily be expressed as water saturation and porosity changes.

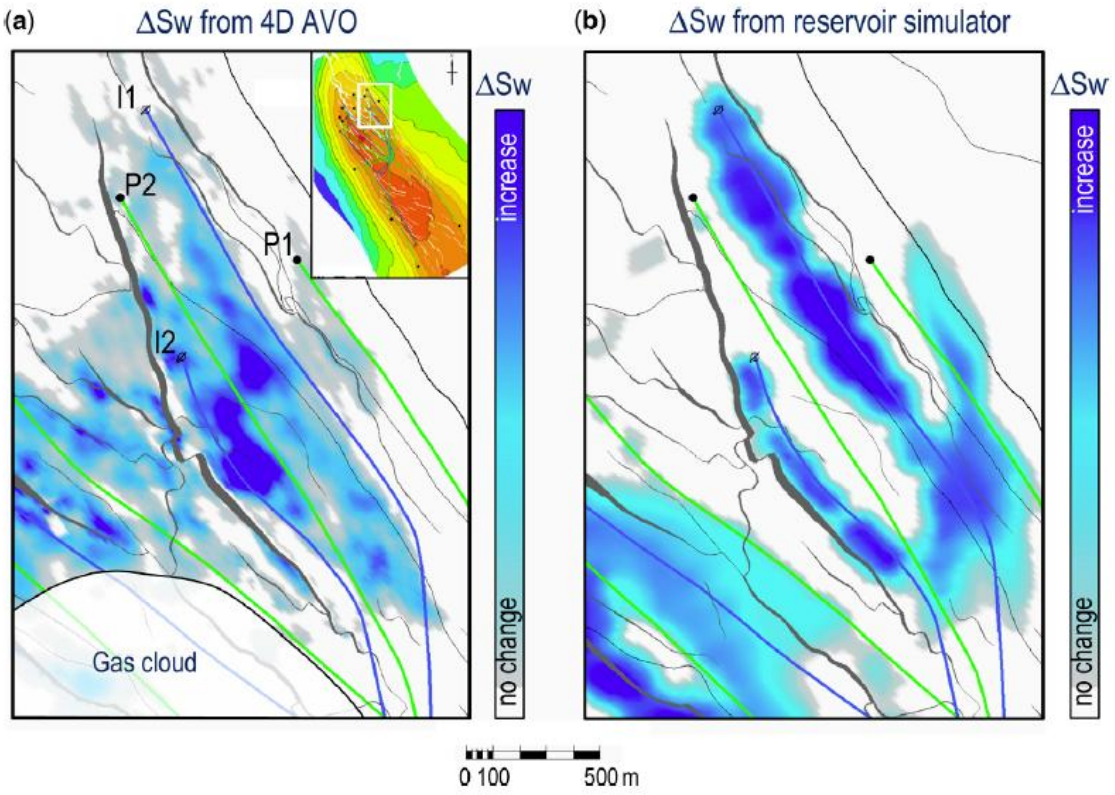

Figure 5.8 Maps of water saturation changes of the Tor formation as estimated from the 4D AVO inversion (a) and predicted by the reservoir simulation model (b) (Herwanger et al., 2009).

A vertical average along the Tor formation of the water saturation change estimated from the 4D AVO inversion is displayed in Figure 5.8a. Figure 5.8b shows for comparison, the corresponding saturation changes predicted by the reservoir model.

Visual comparison of the two maps (Figure 5.8 a and b) reveals a more heterogeneous and fault-controlled water pathways than predicted by the simulation model.

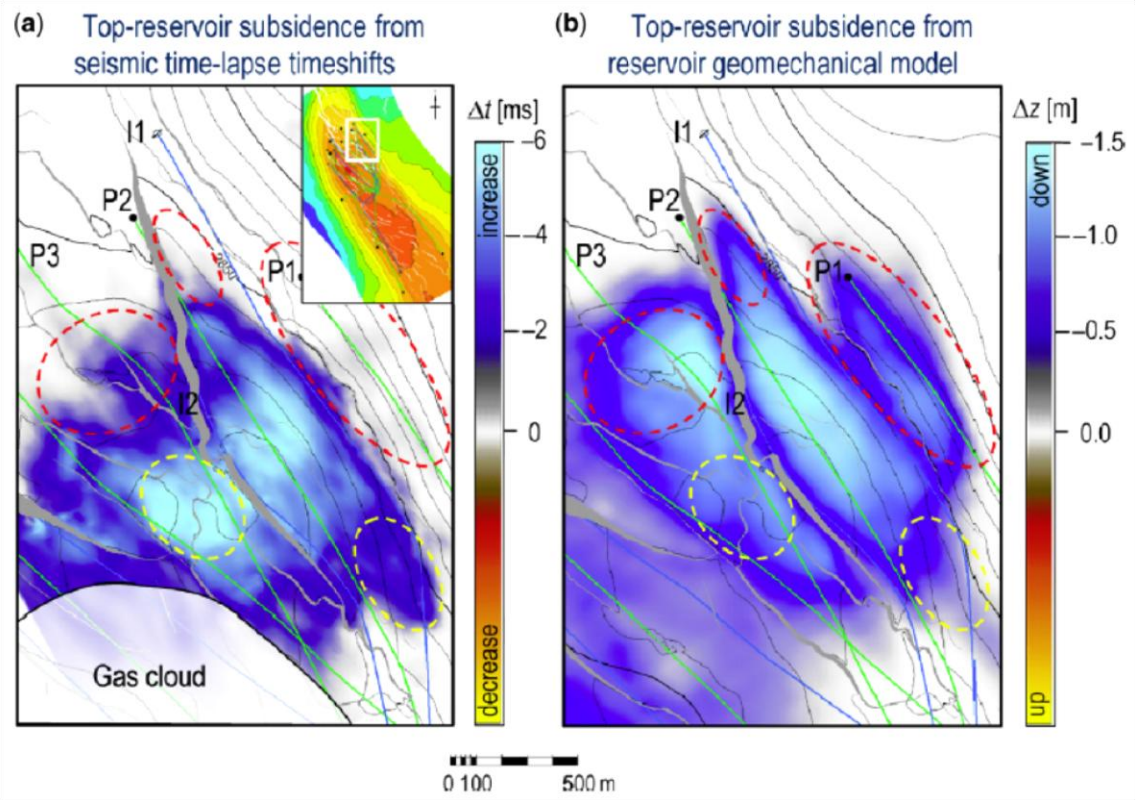

Figure 5.9 Displacements of the top reservoir observed as travel-time changes from measured time-lapse seismic (left figure) and predicted displacements from the geomechanical simulation model (right figure). The inset map on the top left, shows the location of the displayed area (Herwanger et al., 2009).

In addition to the 4D seismic programme, Hess commissioned a full-field geomechanical model to be built in order predict reservoir compaction and the associated impacts on reservoir performance. Mainly for the installation of production infrastructure, but also to monitor subsidence and as a calibration tool for the geomechanical model, bathymetry surveys coinciding with the time-lapse seismic times have also been acquired. Nonetheless, discrepancies between the predicted reservoir subsidence and the observed time-shifts at the top reservoir evidence the need for a recalibration of the simulation model (Figure 5.9). Qualitative differences between the observed time-shifts and predicted reservoir subsidence are highlighted in Figure 5.9. Features shown in the seismic but not in the simulation model are indicated with yellow circles and conversely red circles indicate features pertaining to the simulation model

only. Worth highlighting is the predicted compaction around the P1 and P3 producers not observed in the time-lapse map.

Still much more information is encoded in the time-lapse signal that has not yet been decoded by previous published studies. Among the issues to be solved by analysis of the time-lapse data are: a) further refinement of reservoir compaction for better understanding and quantification of production drive energy and to identify possible hazards to the production infrastructure; b) identification of sealing and conductive faults and favoured flow paths; c) quantification of saturation and pressure changes. To further understand the processes in motion inside the reservoir triggered by hydrocarbon production, a coalescence of full-field geomechanics and reservoir engineering is necessary. Wiener-filters provide a mean to link overburden changes to the reservoir and in hand with time-lapse seismic attributes provide valuable additional information for reservoir management.

5.3 New geomechanical model to calculate Wiener-filters

As with previous applications, a full-field geomechanical model is necessary to calculate the Wiener-filters that approximate the subsurface behaviour. A new model is built, based on the latest history-matched reservoir model. Following the same procedure as in Ekofisk, the reservoir elastic constants are calculated from the Fjær et al. (2008) empirical relations. Since the purpose of the model in this study is only to provide the means to calculate the Wiener-filters, no faults are modeled and all materials are linear elastic. The overburden properties were left unchanged from those used by Hess in previous studies (Schiøtt et al., 2008). The resulting model, the same used in Chapter 2 for the sensitivity analysis, is 105x106x42 cells including sideburden, overburden and underburden. Excluding the sideburden, all cells are regular in lateral dimensions with a size of 50m x 100m. The geomechanical grid has the same orientation as the seismic acquisition geometry in order to facilitate a better coupling between the model predictions and time-lapse atributes.

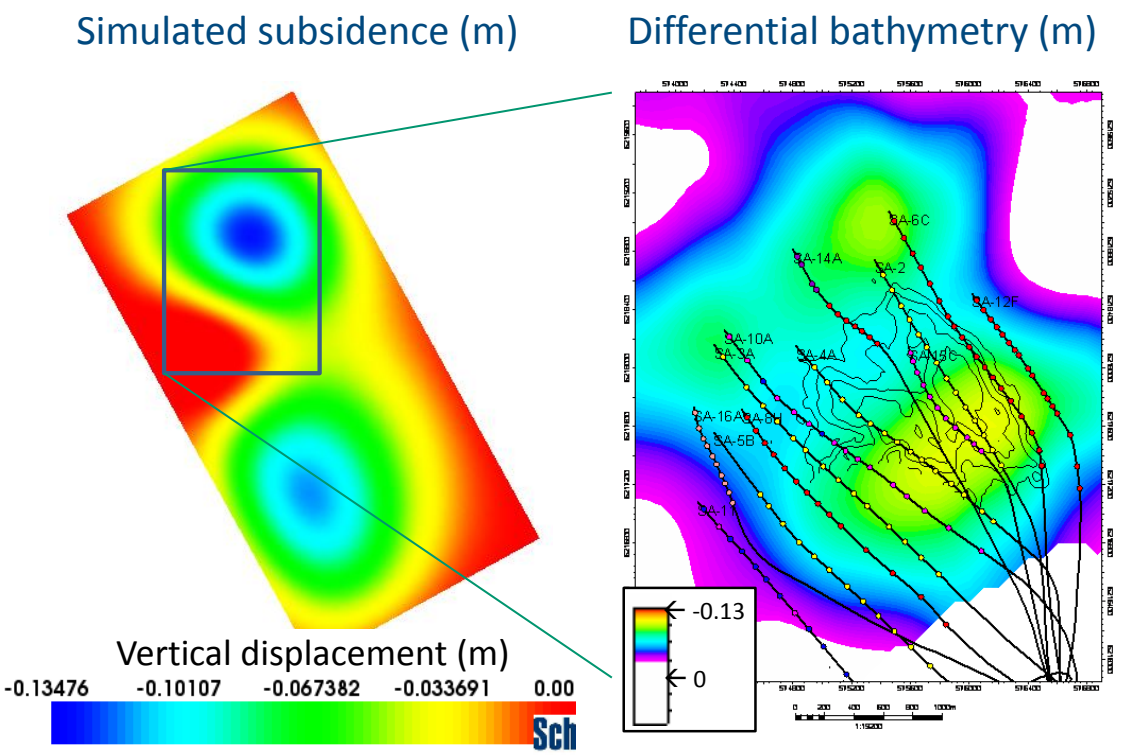

Figure 5.10 Seafloor subsidence maps from the geomechanical simulator covering the whole field (left) and differential bathymetry with well locations of the northern crest of the reservoir (right).

As a mean to calibrate the geomechanical model, an uncoupled simulation is run using as input pressure changes from the reservoir model corresponding to the seismic time-lapse period. The predicted seafloor subsidence is compared with the actual subsidence from differential bathymetry measurements. The resulting subsidence maps are shown in Figure 5.10. Although the measured differential bathymetry is too noisy and has had to be extensively filtered to provide a reliable outline of the subsidence bowl, it does provide a measure of the magnitude. Both subsidence maps agree with the maximum magnitude (roughly 13 cm), though they differ on the shape and in particular the simulated data is considerably smoother. This feature is to be expected from a simulation model and even more if it does not consider the effect of overburden faults, like the model under discussion. Nonetheless, the features observed on the bathymetry map, cannot be taken as definite given the noisy nature of the data. Figure 5.11 shows the differential bathymetry data, both before and after filtering. Striation patterns are visible on the raw data in the acquisition direction, a possible consequence of poor repeatability. Thus, the separate blobs observed on the detailed bathymetry (Figure 5.10) could be explained as an artefact of the data. Still, the gross agreement on the size

and depth of the subsidence bowl, confirms that the simple geomechanical model is accurate enough for the purposes of calculating the subsurface's Wiener-filter.

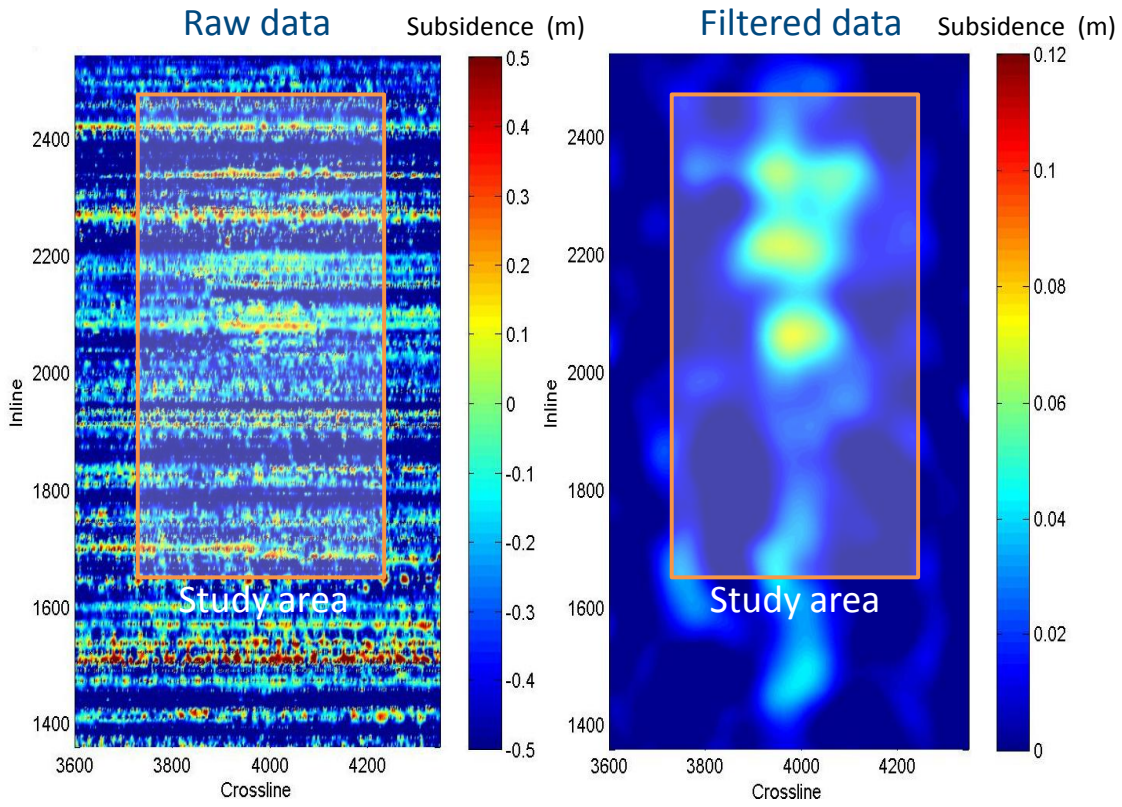

Figure 5.11 Measured differential bathymetry with the highlighted area corresponding to the reservoir and area covered by the geomechanical model. The left map corresponds to the raw bathymetry difference; the right map to the bathymetry difference after filtering in both inline and cross-line directions.

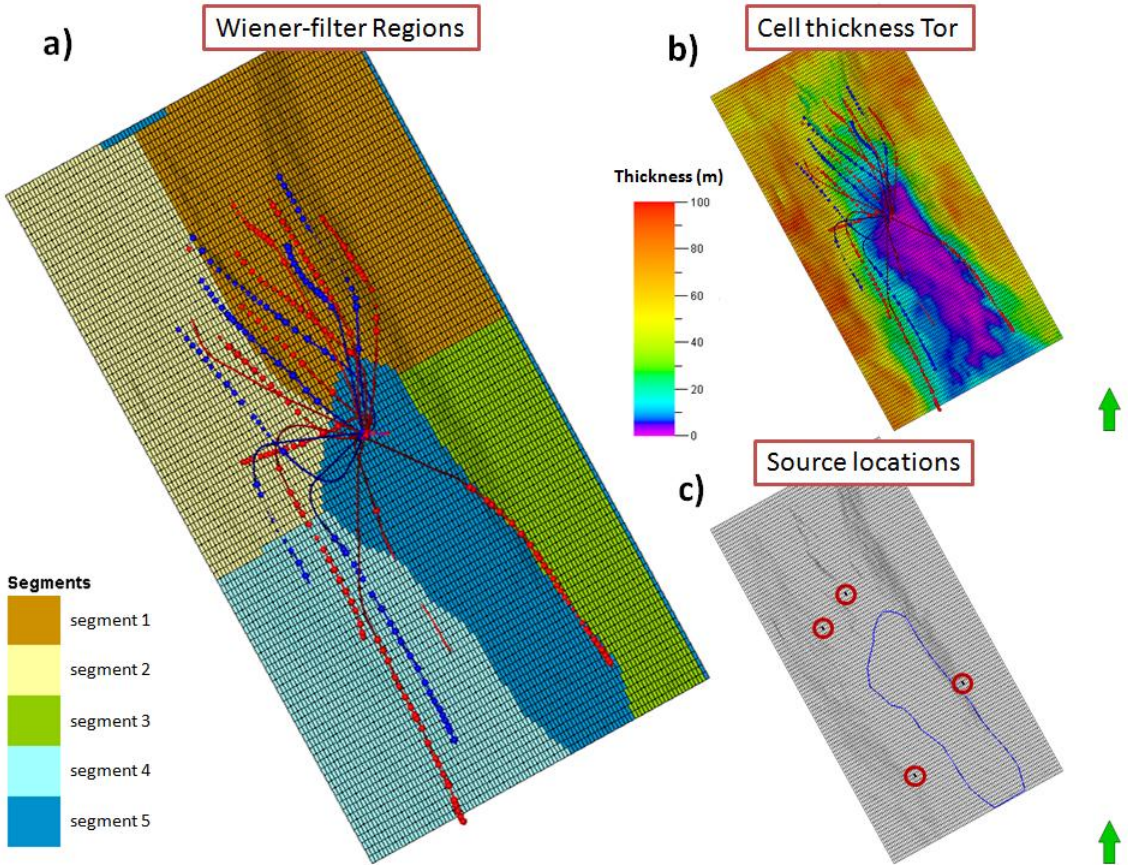

Figure 5.12 (a) Division of the reservoir in segments for application of the Wiener-filters. (b) Thickness map of the Tor formation showing the eroded ridge corresponding to segment 5. (c) Map showing the location of the sources used to calculate the Wiener-filters.

The procedure to calculate the Wiener-filters is the same employed for previous applications; i.e. a source or localized perturbation is given as input to the geomechanical model. This procedure is repeated and a simulation is run with identical sources placed in different locations. The criterion to select the different locations is to identify areas where measurable reservoir changes are expected to happen and to separate those areas into regions with different geometry i.e. dip angle and azimuth. South Arne has been divided into five such segments (Figure 5.12a). However, sources are placed in only four of them. Since segment 5 comprising the southern crest of the reservoir is largely eroded (Figure 5.12b) with poor reservoir quality and mostly beyond seismic resolution, no sources are placed there. Additionally, as shown in Chapter 2, the largest error of the Wiener-filter estimations corresponds to segment 5. Therefore, four sources are used located as shown in Figure 5.12c for each of the reservoir units; Ekofisk and Tor for a total of eight sources.

The Wiener-filters are applied to overburden time-strains at the Horda formation, roughly 400 m above the reservoir (Figure 5.13). The selected layer, corresponding to model horizon 16 is about 200 m thick and has been chosen according to the results of the sensitivity analysis (Section 2.5). The result after deconvolving the time-strains with the Wiener-filter is a different volumetric strain map for each Wiener-filter. Since the error of the inversion results increases with the distance from the source location, the final maps are obtained by stacking the volumetric strain maps at each reservoir segment with different weights. For a given segment, the results of the filter corresponding to a source located in that segment are weighted 3/6 whereas results from all other filters are weighted 1/6, so that all weights add up to one. This applies to segments 1 to 4, the results for segment 5 are weighted all equally (i.e. ¼). The reason behind the weighted stacking is to increases the signal to noise ratio and ensure a smooth overlap between segments.

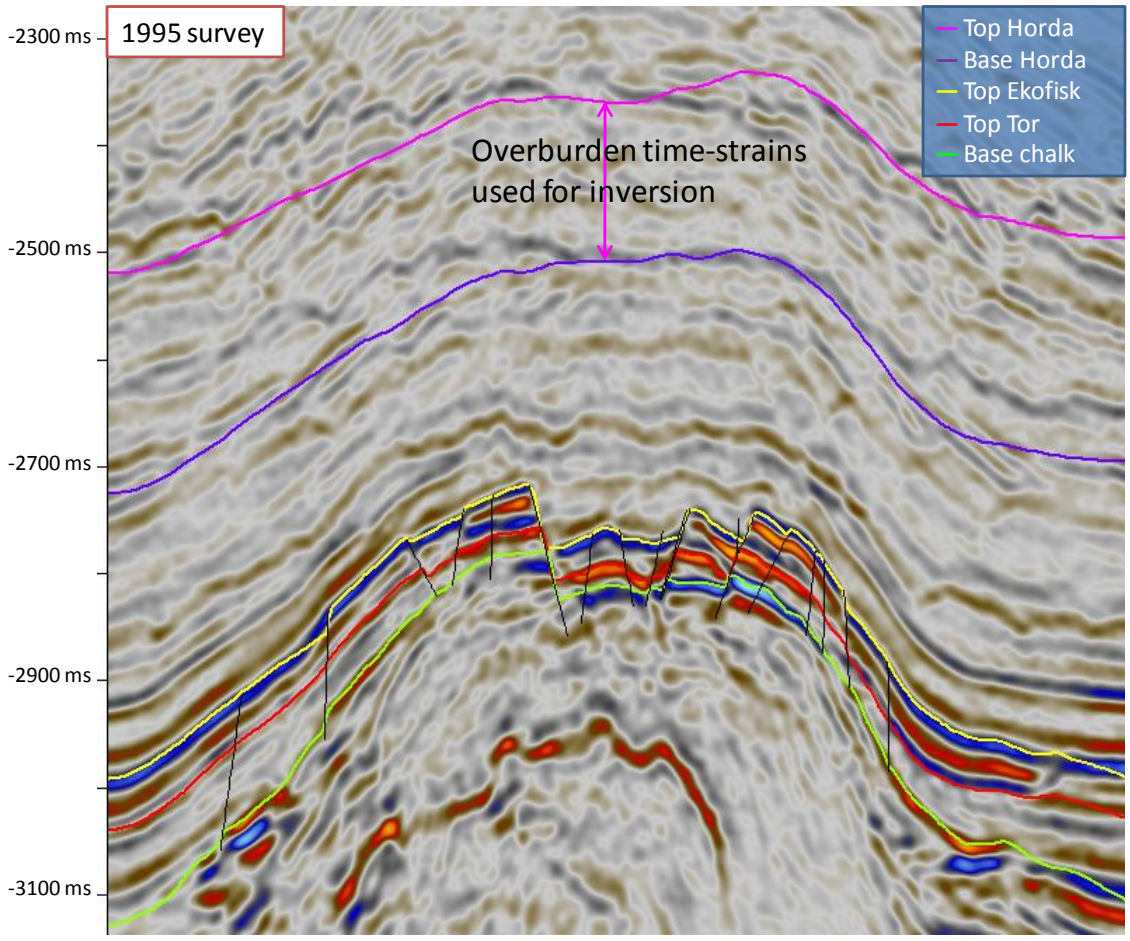

Figure 5.13 Inline seismic section of the baseline survey across the graben structure in the northern part of the reservoir. The line shows the position and thickness of the reservoir and the Horda formation employed to calculate the overburden interval time-strains used for the inversion.

5.4 Time-shift cubes for different correlation windows

In this chapter, in addition to the overburden inversion, the robustness of the time-lapse data is analyzed. For this purpose, five different time-strain cubes are calculated. The cubes are then deconvolved with the calculated Wiener-filters resulting in five separate sets of reservoir volumetric strain maps, as described above. Comparing these maps and the time-strains themselves gives a measure of the robustness of the data. The importance of this test lies in that there is no standard method to calculate the time-shifts and that they all yield slightly different results.

Here, five time-shifts cubes are compared; four have been calculated using the 3D warp method discussed on Section 4.5 and the remaining with 1D cross-correlation. The warp cubes are calculated using four different search windows; i.e. 15x12x12, 15x9x9, 12x9x9 and 10x5x5. The search windows are given in units of sampling interval in the vertical (2 ms), inline (12.5 m) and crossline (25 m) directions. The fifth cube has been provided by Hess and has been calculated using trace-by-trace cross-correlation (1D cross-correlation) being the most widely used method. Figure 5.14 shows time-shifts cross-sections from all five cubes. The cubes are arranged in descending order in terms of the size of the search window, starting with 15x12x12 and finishing with the 1D cross-correlation cube. All cubes display roughly the same magnitude of time-shifts ±4 ms. However, the resolution changes drastically; i.e. larger search windows yield smoother time-shifts. Although by visual comparison, the 1D cross-correlation results appear of higher reolution and better quality, which may explain why this method is the most accepted, the time-strain maps tell another story.

Figure 5.15 shows the overburden time-strain maps at the Horda formation in the same order as the time-shifts' cross-sections (Figure 5.14). All time-strains from the warp method display to some extent, the same discernible features. However, the signal to noise ratio decreses significantly along with the size of the search window, which effectively acts as a low pass filter. At the end of the spectrum is the 1D cross-correlation map, where little to no patterns can be identified above the noise, suggesting that most of the 4D noise is at the higher frequencies. Additionally, the area obscured by

the gas cloud dominating the centre of the map is not present on the warped time-shifts. Recall that the warp method calculates the phase correlation which is insensitive to white noise, whereas 1D cross-correlation operates in the time domain where amplitudes are mostly obscured inside the gas cloud. Therefore, it can be concluded that the obscured area is dominated by white noise impeding static imaging of the reservoir. However, dynamic changes can be measured with warping and phase correlation.

The consistency of the time-strains can also be examined when using them as a reservoir time-lapse seismic attribute. To this purpose, reservoir interval time-strains are calculated by integrating vertically the time-strains between top and base reservoir on a trace-by-trace basis. The resulting map displays the changes in seismic travel-times of the reservoir interval alone. Figure 5.16 shows the interval time-strains of the reservoir Tor formation, for a sector covering the crest of the reservoir as indicated on the map inset. The results corroborate the observations from the overburden time-strains; i.e. resolution along with noise increasing with smaller correlation windows. However in the case of the 1D cross-correlation interval time-shift map, some information can be observed above the noise level on the rim of the obscured area. Nonetheless, the data is still dominated by the gas cloud and a part of the reservoir remains obscured. The meaning of the reservoir's interval time-strains will be discussed later in the results section (Section 5.5). The reservoir sector shown in Figure 5.16 is the focus area for this study and will be henceforth discussed in detail, including the results of the overburden inversion along with time-lapse surface attributes.

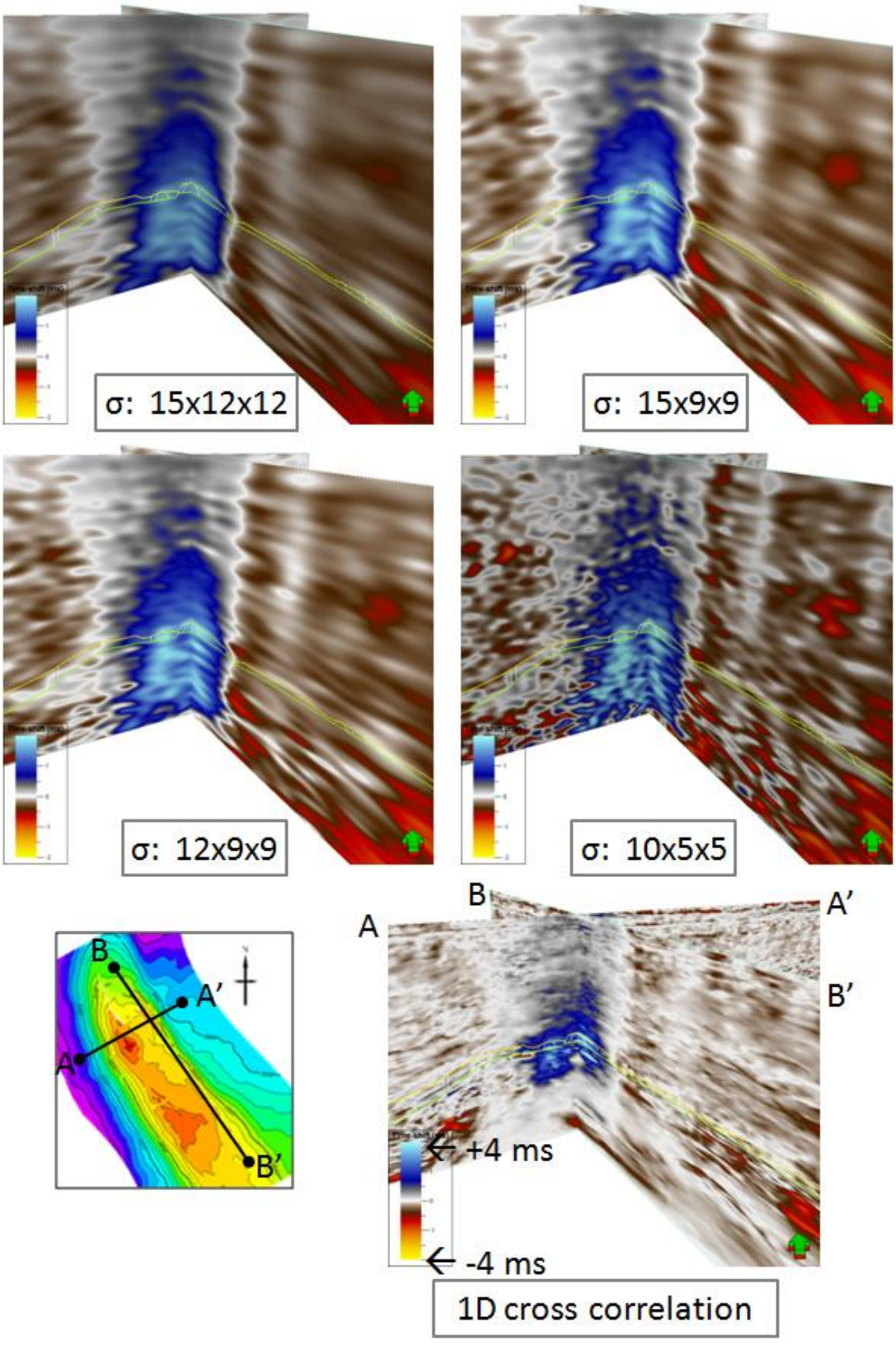

Figure 5.14 Inline and crossline sections of the time-shift cubes. The upper four have been obtained by calculating the 3D warp vector using the indicated search windows. The lower cube corresponds to time-shifts from 1D cross-correlation. The cross-sections shows are located as shown on the map inset.

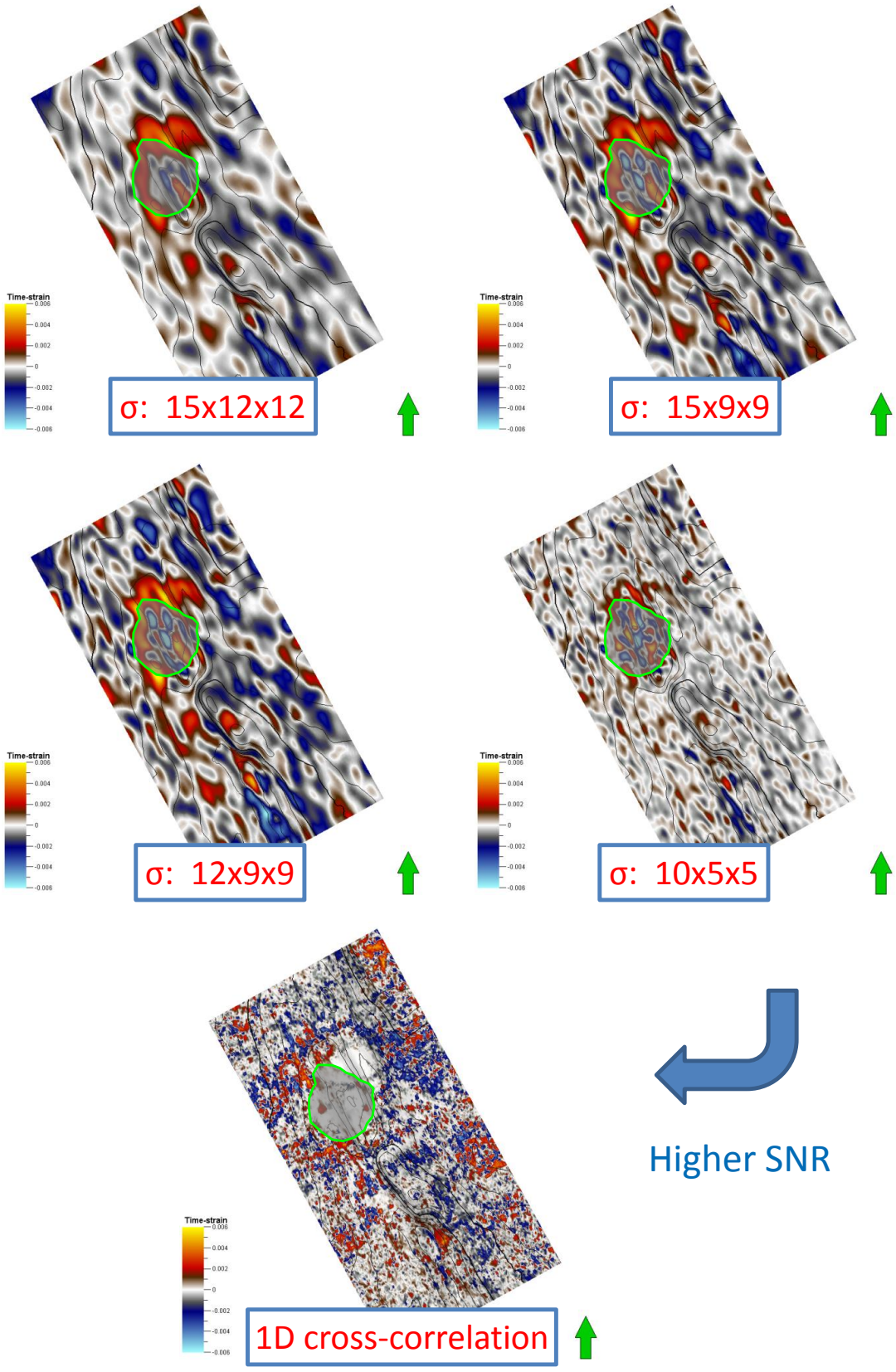

Figure 5.15 Time-strain maps from all five time-shift cubes at layer 16 vertically averaged along the thickness of the Horda formation roughly 200 m. The area of the Horda formation affected by the gas cloud is delineated in bright green in all maps.

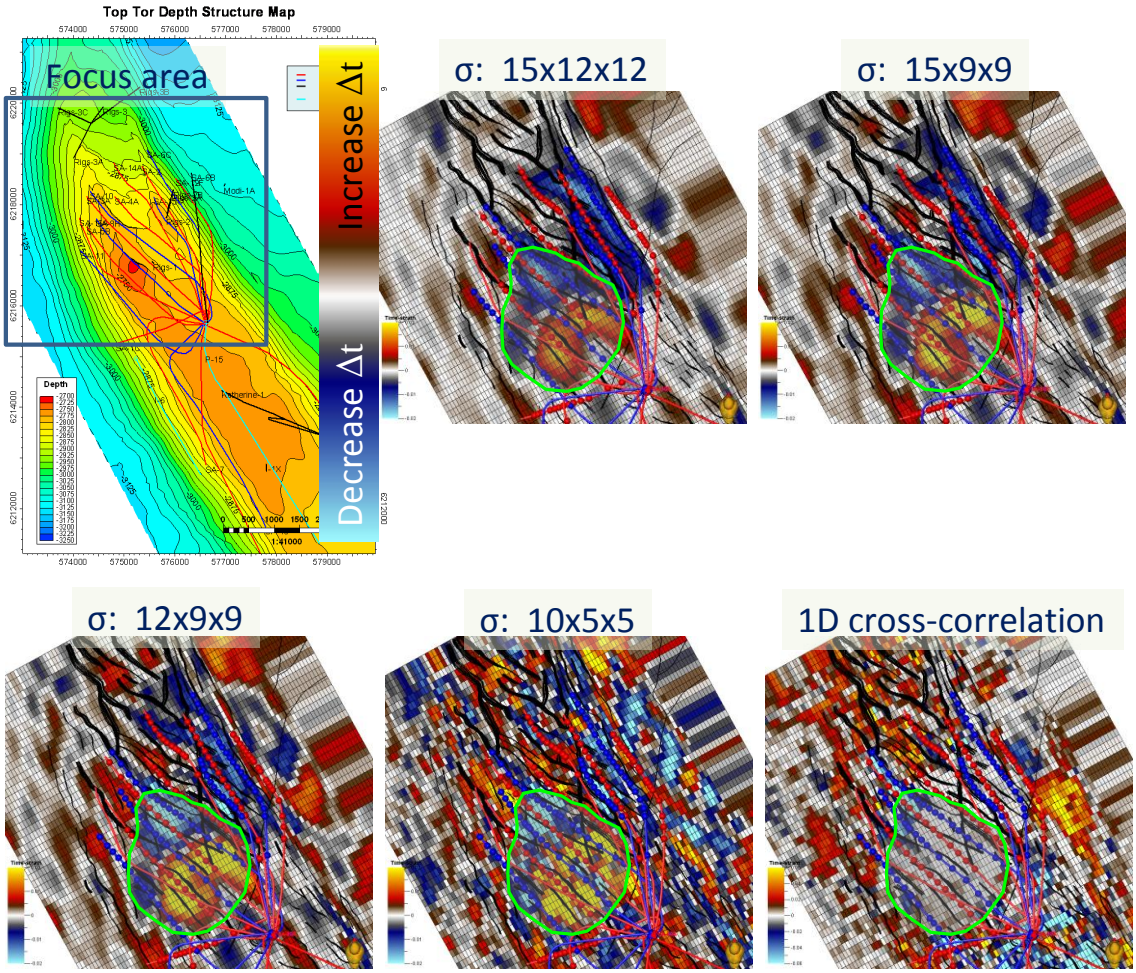

Figure 5.16 Interval time-strains of the Tor formation, covering the northern crest of the reservoir as indicated in the map inset. The maps are generated from the different time-strains cubes and show in light green the outline of the area affected by the gas cloud.

5.4.1 Cross-equalization and amplitude changes

In addition to provide useful insight into the reservoir's dynamics as a surface attribute, time-shifts are also used in realigning the monitor and base surveys. The fact that time-shifts are measurable means that reflector positions and seismic velocities have changed due to production activity. Therefore, seismic events will appear shifted for different seismic times. As a consequence, reservoir models built after some seismic interpretation will disagree with the seismic from a different acquisition time. Consequently, seismic surface attributes, be it time-lapse or static from different seismic time-steps, cannot be used or will yield inaccurate results if the time-shifts are ignored. Realigning the seismic events using the time-shifts is therefore necessary. This process is commonly known as cross-equalization, or more aptly morphing (Grandi et. al, 2010),

since cross-equalization specifically refers to 1D corrections; i.e. subtracting time-shifts measured by 1D cross-correlation. Whereas morphing refers to shifting each sample in three dimensions as given by the local warp vector.

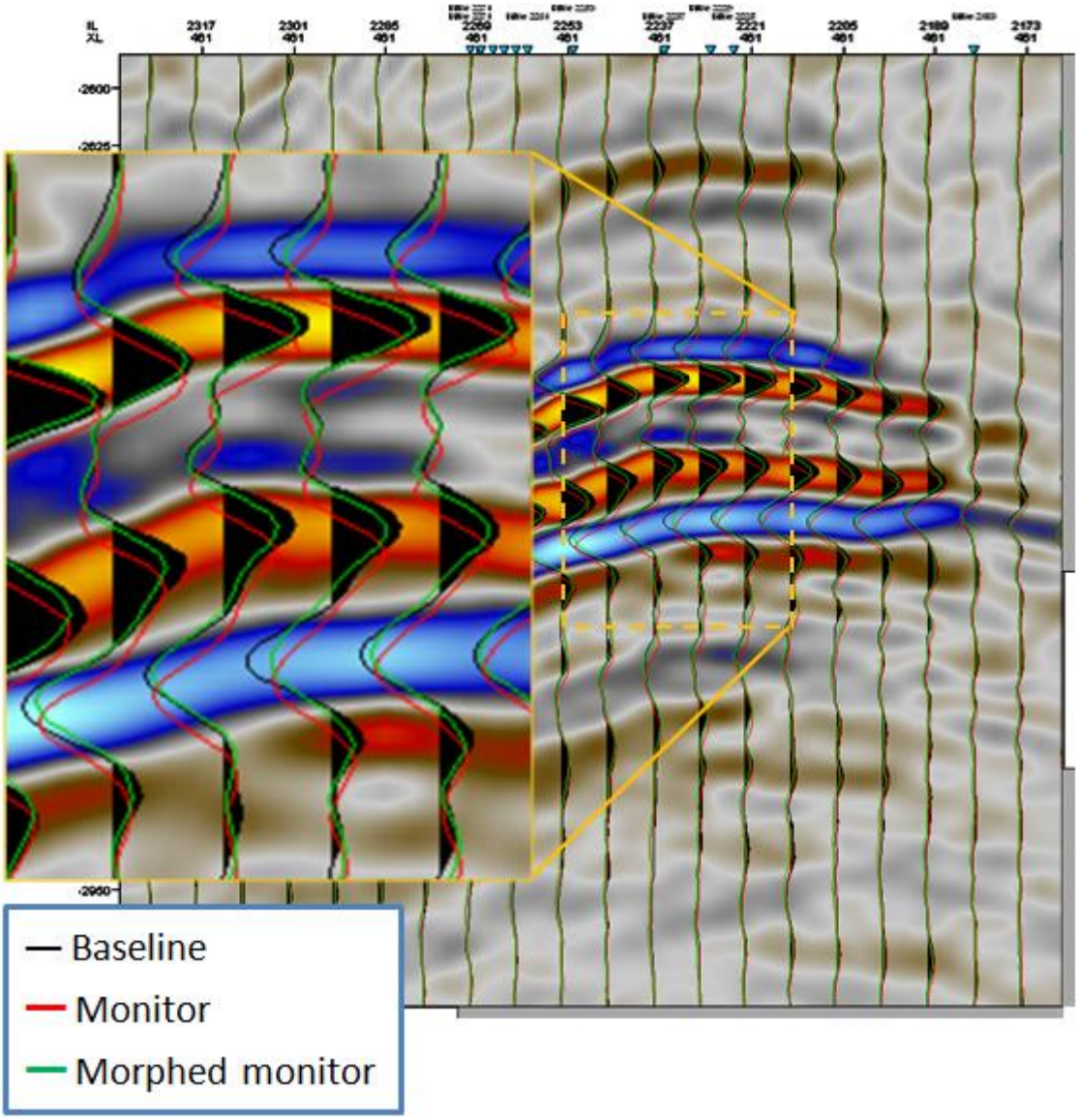

Figure 5.17 Comparison of seismic traces of the baseline (black wiggles and background image) and monitor (red traces) surveys, showing misalignment due to production induced velocity changes and interface displacements. The morphed monitor survey (green traces) show a very good alignment of events relative to the baseline survey.

A useful and the most commonly used reservoir time-lapse seismic attribute is amplitude changes. Since seismic reflection amplitudes are given by the contrasts in acoustic impedance across an interface, acoustic impedance changes inside the reservoir

give rise to seismic amplitude changes between baseline and monitor surveys. However, in order to calculate accurate 4D amplitude changes, both baseline and monitor surveys must be aligned; i.e. seismic events should be in phase and differing only by their amplitude. Figure 5.17 shows a comparison of seismic traces from baseline and monitor surveys. The baseline survey corresponds to the seismic background image and the superimposed black seismic traces. The traces of the monitor survey shown in red, clearly display both time-shifts and amplitude differences, despite the fact that both datasets have been processed in parallel. On the other hand, the morphed monitor survey, shown as green traces, shows a good alignment with the baseline survey, and events differ only by their amplitude. 4D amplitudes combined with interval time-strains and the results of the Wiener-filter overburden inversion will be discussed in the following section.

5.5 Wiener-filter results and time-lapse attributes

In the previous sections observation of the different overburden and reservoir time-strain maps (Figures 5.14 and 5.15) have revealed the advantage of warping over the supplied 1D cross-correlation cube, at least for the data set under discussion. Here the effect that the different time-strains have on the overburden inversion using Wiener-filters is examined. Exploiting the fact that the signal to noise ratio changes with the size of the correlation window, a study of the stability of the inversion method is performed. Specifically, this attempts to answer the question of how much noise proves too much for the Wiener-filter inversion. For this purpose, all five overburden time-strains (Figure 5.15) are deconvolved using the set of Wiener-filters and the results stacked as described in Section 5.3. This results in five sets of reservoir volumetric strain maps for the Ekofisk and Tor formations. The results for the Tor formation corresponding to the focus area are shown in Figure 5.18. The volumetric strains are displayed on the reservoir grid including the faults and wells; producers are shown in red and injectors in blue. Well completions are shown as spheres along the well paths. The maps are labelled according to the time-strains used for deconvolution.

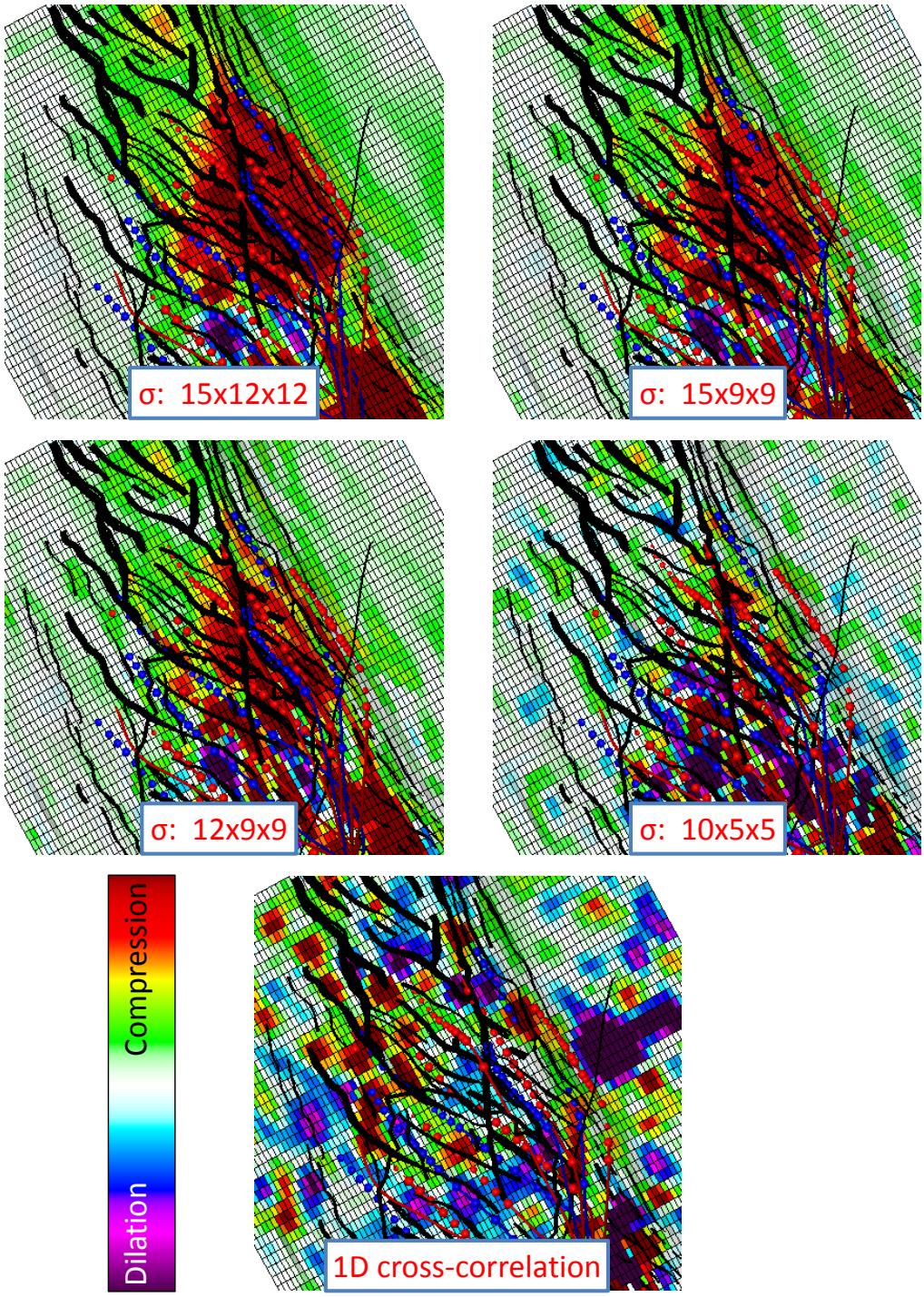

Figure 5.18 Estimated volumetric strain maps obtained by deconvolution of the overburden time-strains shown in Figure 5.15. The maps are labelled according to the method or correlation window used to calculate the respective time-strain cubes. The reservoir model faults are displayed in black, superimposed on the geomechanical model grid.

From a qualitative point of view only, all four volumetric strains maps corresponding to the warp cubes, exhibit the same patterns. Even the results from the 10x5x5 cube show some consistency. However the "mottled" behaviour of the 10x5x5 map reveals we are

nearing the limits of the Wiener-filter method, where the inversion starts to be unstable. In fact, the results from the 1D cross-correlation are past that limit and no similarity with the other maps can be observed. Additionally, no correlation with faults or well locations can be identified unlike with the previous maps, indicating that the results are of no value to our analysis. Recall that the coefficients of the Wiener-filters are calculated by least-squares and that during that process a Thikonov-type regularization is used (Aster et al., 2005). However, no regularization parameter and no amount of damping manage to improve the results from the 1D cross-correlation time-strains. Nevertheless, the question arises of whether the inversion is unstable and cannot cope with very noisy data, or that the data is not appropriate to begin with. Observing the overburden time-strains (Figure 5.15) supports the latter statement.

5.5.1 Discussion

Here the estimated volumetric strains, effective stress changes, reservoir time-strains and amplitude changes for the Ekofisk and Tor formations are examined together. Even the tight zone is discussed together with the structural map. To facilitate the interpretation of the results, relevant maps are display side by side for each reservoir layer. Henceforth, unless stated explicitly otherwise, all maps shown have been derived or calculated from the 15x9x9 time-strain cube. The Tor formation being the main reservoir is discussed first.

Figure 5.19 shows the estimated volumetric strain (a) and mean effective stress change (b) in addition to the interval time-shift (c) and 4D amplitude (d) maps for the Tor formation. The 4D amplitudes have been calculated by estimating the mean amplitude difference between top and base reservoir, relative to the baseline and morphed monitor surveys. I introduce the concepts of hardening and softening, defined as decrease (negative interval time-strains) and increase (positive interval time-strains) of seismic travel times respectively. This should not be confused with actual physical hardening of the reservoir rock, since travel-time changes are given both by thickness and velocity changes. The interval time-strains (Figure 5.19c), are clearly associated with the wells and bounded by faults. Examination of field data (i.e. well completions and production logs) reveals a strong correlation between hardening and water injection activity. Hydrocarbon production on the other hand, takes place in both hardening and softening areas.

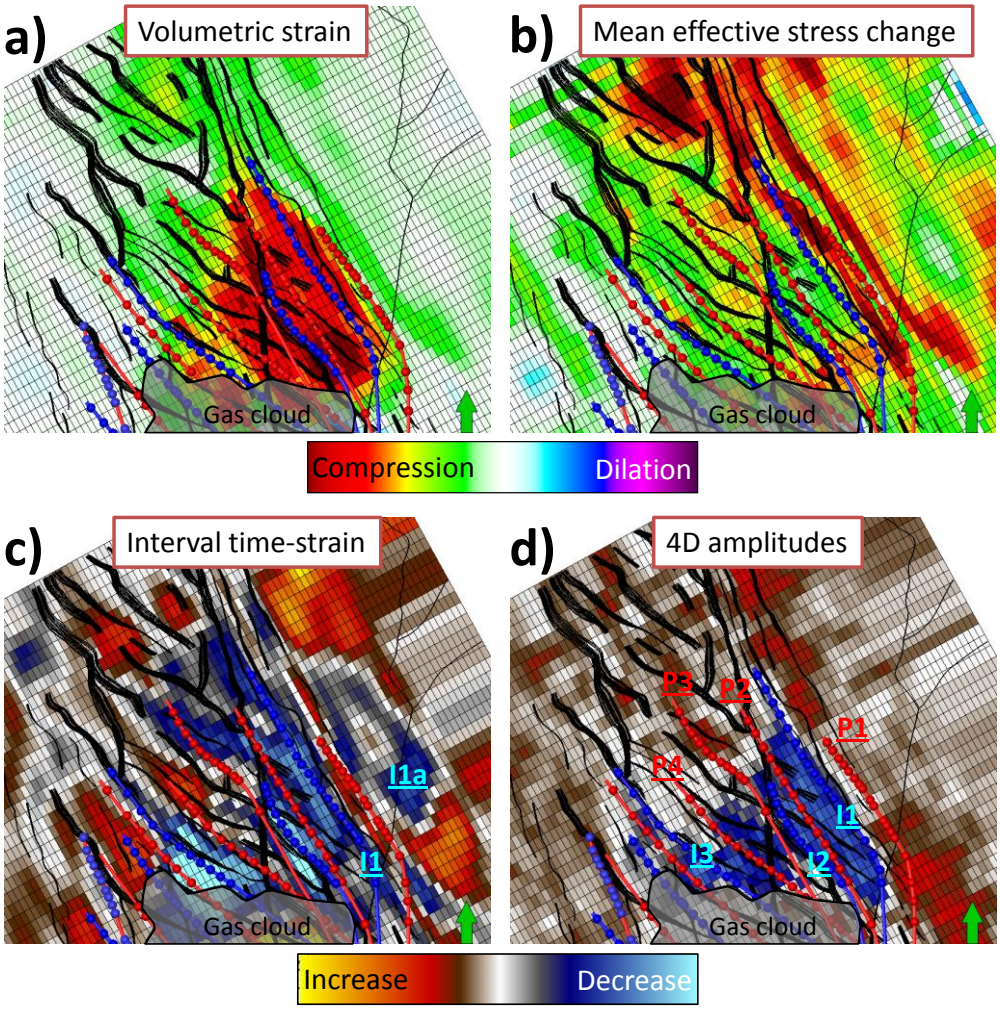

Figure 5.19 Time-lapse results for the Tor formation, showing the estimated volumetric strain (a), the mean effective stress change (b), the interval time-shift (c) and the 4D amplitudes. Relevant well names for further discussion are shown in the lower maps.

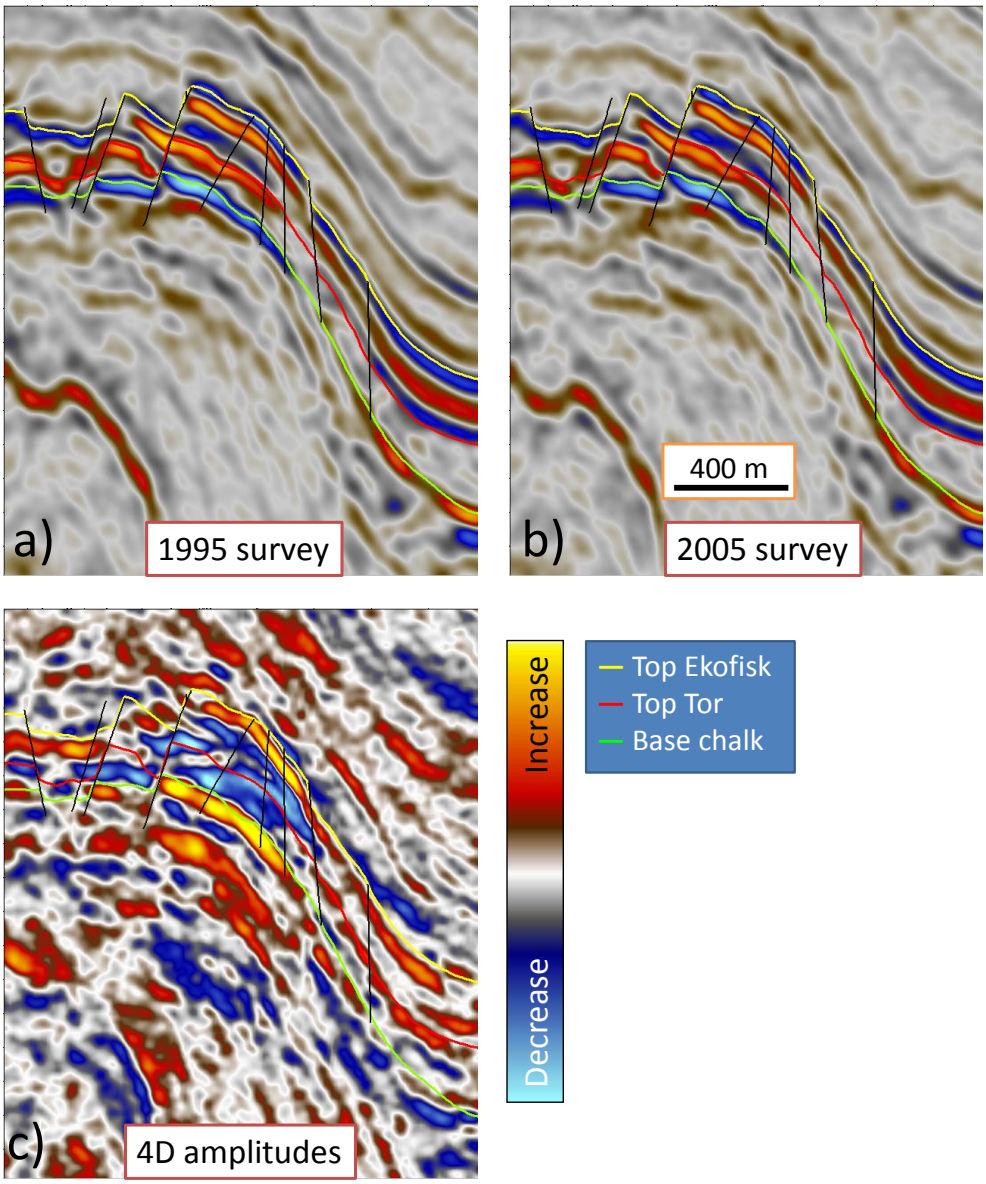

Figure 5.20 Inline seismic cross section with interpreted reservoir horizons and faults, located across the eastern high of the structure. Images correspond to the 1995 baseline survey (a), the 2005 monitor survey (b) and 4D amplitude changes (c).

Amplitude changes are caused by changes in the reflection coefficient of an interface, which is a function of the acoustic impedances on both sides. Therefore, to understand the meaning of 4D amplitude maps, one should first examine the nature of the seismic reflections at the reservoir horizons. Figure 5.20a shows an inline section of the baseline survey across the eastern edge of the graben on the crest of the reservoir structure. The interpreted formation tops indicate that the top Tor is associated with a seismic peak, whereas top Ekofisk with a trough followed by a peak, separating the upper and lower Ekofisk reservoir. Small changes in travel time and amplitudes are visible on the

seismic events of the monitor survey (Figure 5.20b). The corresponding 4D amplitude changes after morphing are shown in Figure 5.20c and clearly indicate a decrease of amplitudes in Tor and lower Ekofisk and an increase on the upper Ekofisk.

4D amplitudes express the contrast at the interface. However, neglecting changes of acoustic impedance in the overlying formation means that amplitude changes can be linked directly to acoustic impedance changes of the underlying layer. In the case of South Arne, this assumption is reasonable, as the changes taking place in Tor are bound to be considerably larger than in Ekofisk and the same applies to the upper Ekofisk relative to the cap rock. Therefore, a decrease in amplitude at the Tor formation (Figure 5.19d) corresponds to a decrease in the contrast and thus, to a decrease of the acoustic impedance inside the reservoir. The area of highest compaction, as given by the estimated volumetric strain map (Figure 5.19a), corresponds roughly to the hardening associated with the injectors and the decrease of acoustic impedance. Therefore, it can be concluded that hardening is caused by reservoir compaction and thus, the decrease in acoustic impedance can only be linked to water weakening and/or pore collapse together with pressure depletion. As a consequence, these overlapping areas correspond to effective water swept production. Softening on the other hand, can be associated with producers alone and hence pressure drop with minor to no water saturation changes and minor compaction.

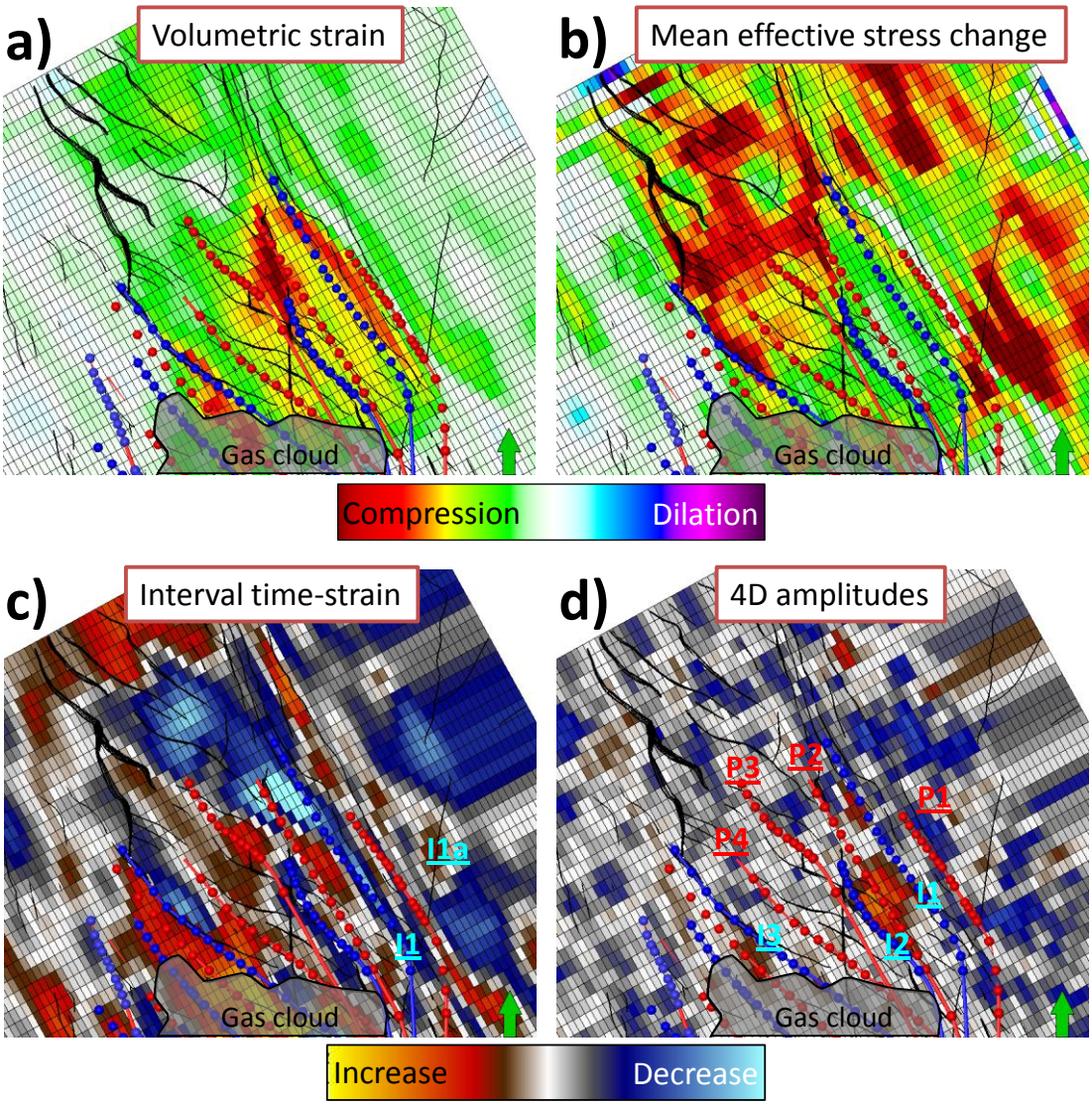

Figure 5.21 Time-lapse results for the Ekofisk formation, showing the estimated volumetric strain (a), the mean effective stress change (b), the interval time-shift (c) and the 4D amplitudes.

The estimated change in effective stress (Figure 5.19b), shows a remarkable correlation of high stress concentrations along certain faults, in addition to a general slight increase in the area where production is taking place. The highest observed stress anomaly is located along the faults to the north-east on both sides of producer P1. This is unsurprising, as the producer sits between two faults and is down-dip of injector I1 which may add to the effect. The stress build-up along the faults might be due to build-up of differential pressure indicating that the fault is sealing and therefore that the injector is not providing pressure support, a fact that has been confirmed by production data. Combining this information with the time-strain map, it can be speculated that the water is instead flowing north and possibly seeping through the tight zone into the

Ekofisk formation providing additional support to the producers in the central area. It is also visible on the interval time-shift map (Figure 5.19c), the open sidetrack well I1a that has been plugged, and the area to the south-east of this that producer P1 is draining.

Figure 5.21 shows the results of the upper reservoir (Ekofisk formation), displaying the estimated volumetric strain (a) and mean effective stress change (b) in addition to the interval time-shift (c) and 4D amplitude (d) maps. As explained before, the Ekofisk formation has a lower permeability, product of higher clay and silicates content. This fact could explain the high compaction more concentrated along the producers and along nearby faults that provide the flow pathways, instead of a more widespread behaviour when compared with the Tor formation. The interval time-shift map (Figure 5.21c) can be interpreted as for Tor formation; i.e. depletion in hand with water flooding gives rise to hardening and depletion without considerable water saturation changes and minor to no compaction shows up as softening.

The similarity between the Ekofisk and Tor compaction patterns indicate the permeable nature of the tight zone. More evident along faults especially those with injectors nearby i.e. wells I1 and I3. In the case of injector I1 and considering the estimated change in mean effective stress (Figure 5.21b) this could indicate that the water has flowed along the adjacent fault to the north-west where it has made its way from Tor to the Ekofisk Formation giving pressure support to the producers in the central area. This scenario is illustrated more clearly in Figure 5.22, where the interpreted flow pathway from injector I1 is shown by the red arrows following the hardening parallel to the faults. The interval time-strains of the tight zone (Figure 5.22d) indicate where communication is taking place between the formations which is clearly along the faults. The injected water moves laterally crossing at roughly the same depth from the Tor (Figure 5.22b) to the Ekofisk formation (Figure 5.22a) across the graben boundary, where the two formations meet. This scenario is additionally supported by the estimated mean effective stress changes (Figure 5.21b) that show a high increase in the areas being swept by water, mainly inside the graben on the northern part of the reservoir. The wells in this area have shown better than expected production rates which have been attributed to higher fracture permeability, so much that a development program is underway to install a new platform and drill more wells to target this area. However, the water seepage scenario if correct can be readily identifiable by new wells and will certainly have an impact on the new development plan.

The amplitude changes for Ekofisk (Figure 5.21d) are too noisy or mostly low and only a small positive change along injector I2 can be unambiguously identified. Since the top of the formation is defined by a seismic trough, an increase in reflection amplitude can be associated with a decrease in acoustic impedance. However, this small area east of I2 does not experience hardening (Figure 5.21c) nor significant compaction (Figure 5.21a). Instead, some softening is visible. Since 4D amplitudes are sensitive mainly to saturation changes, this may imply gas coming out of solution accumulating in what corresponds to the high of the structure on the eastern flank. Injector I2, the only well completed in the Ekofisk formation, is clearly not giving pressure support to this high. Instead, the hardening associated with injection can be seen on a closer look west of the bounding faults (Figure 5.22d), i.e. on the graben area out of the reservoir structure. In fact, the first half of the perforated interval on the I2 well, has been plugged corresponding to the section possibly outside of the structure.

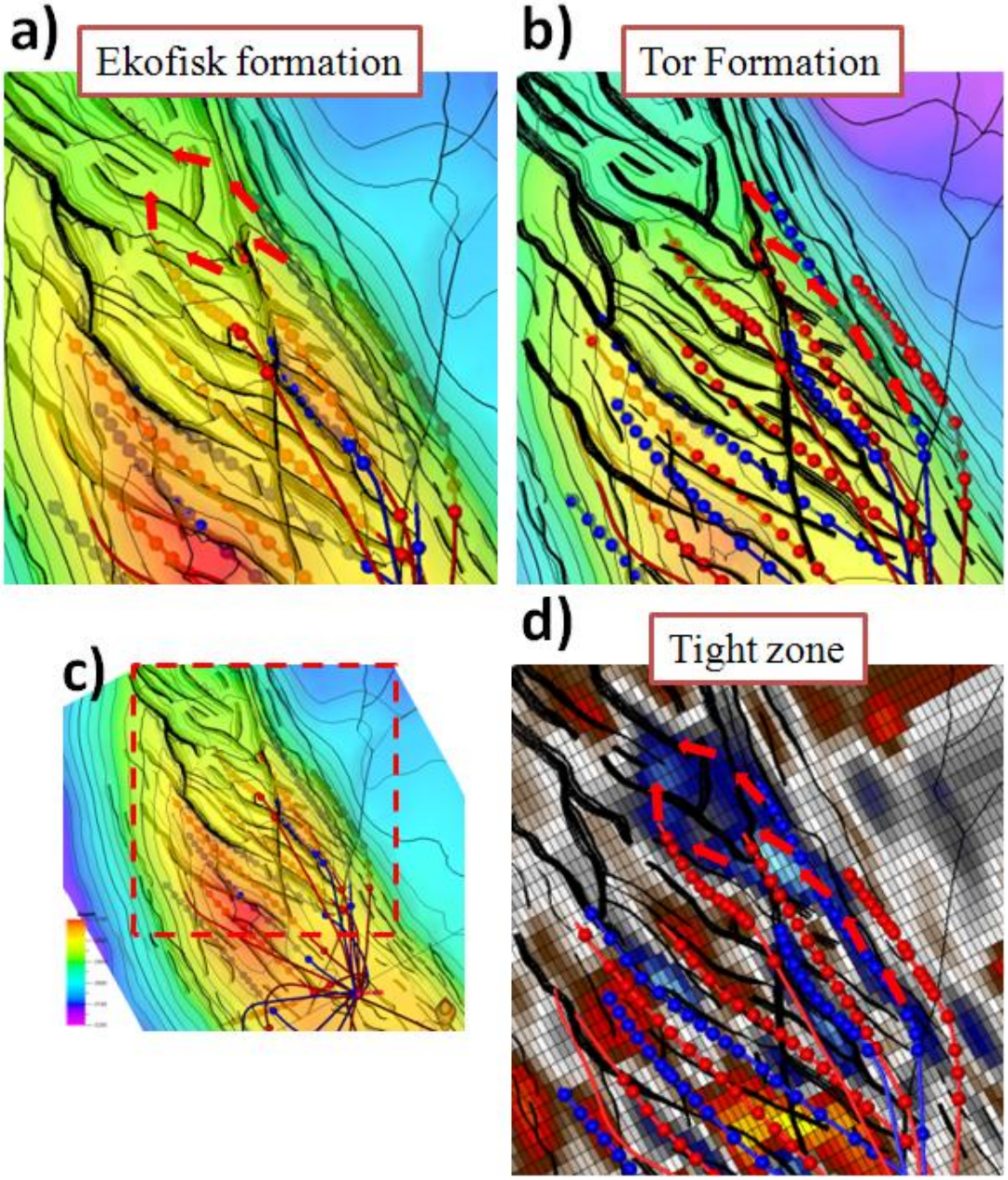

Figure 5.22 A zoom in on the focus area concentrating on the I1 injector as displayed on the map inset (c), showing the top Ekofisk (a) and Tor (b) depth maps and the interval time-strains at the tight zone (d).

5.6 Conclusions

The construction of a simple geomechanical model based on empirical relations is fast and has proven useful to model the gross subsurface deformation when compared with the measured bathymetry. A simple model like this is adequate for the purposes of calculating the subsurface's Wiener-filters though not for reservoir management.

However, a more detailed model will permit a full integration and better understanding of the different results and observations, not to mention the benefits for better reservoir management. In this respect, Wiener-filters can be used for constraining the geomechanical simulation parameters, as the predicted reservoir compaction should match that estimated from measured overburden strains.

The analysis of time-shifts calculated by two different methods, have shown that the results are not consistent. 1D cross-correlation commonly used to calculate time-shifts for cross equalization and subsidence studies, have proven unsuited for this study, since the time-strains from cross-equalization are too noisy and have very poor lateral continuity. On the other hand, warping time-strains are consistent in spite of changes in the size of the correlation window. Additionally, by operating in the frequency domain (phase correlation) it is possible to image inside the gas cloud indicating that the obscured area is mainly dominated by random noise, which impedes static imaging.

Warping and the associated morphing of the seismic permits the calculation of physically meaningful time-lapse amplitude changes. Nonetheless, being a static attribute, accurate recording of seismic amplitudes is very challenging. Particularly in fractured reservoirs like South Arne, where migration will fail to focus all of the seismic energy. This explains the suboptimum quality of the calculated amplitude changes, where small changes are lost and some changes appear where none should be; e.g. in the distal parts of the anticline. Despite these shortcomings, the measured amplitude changes are consistent with fault locations and give valuable information on saturation changes and water sweep efficiency. Additionally, the use of time-strains as a reservoir attribute proves a valuable tool, identifying drainage areas and discrimination between water swept regions from those experiencing pure depletion. Moreover, warping permits resolution of these changes at the different reservoir horizons.

Wiener-filters provide estimates of volumetric strain and mean effective stress changes in the reservoir that delineate the main compaction area and stress build-up at faults, indicating fracture controlled flow paths. When analyzed in conjunction with all of the time-lapse data; i.e. time-lapse attributes and overburden derived reservoir strain and stress changes, this allows us to draw a more complete picture of the processes inside the reservoir.

It has been identified that faults appear mostly impermeable to flows perpendicular to the fault surfaces, but facilitate flows parallel to them. With this in mind it is possible to distinguish the drainage area and the position of the water front. All these features can be delineated in each reservoir formation, including the tight zone, indicating the zones with better vertical connectivity. This has explained the good performance of the producers north of the crest due to unintentional water support from injector I1 that has in turn failed to support production downdip at P1. These observations are not expected from the reservoir model and could have a considerable impact on the future development plan of the field. As a result, Wiener-filters have provided valuable information that could be used to update both the geomechanical and reservoir models on a dynamic basis from measured time-lapse seismic.

Chapter 6

6 Analysis of lateral shifts observed in 4D seismic data

Conventional 4D seismic workflows all include parallel processing of the seismic vintages, whereby in order to maximize repeatability, speedup processing time and reduce costs, the same velocity model is applied to all surveys. However, if time-shifts are measurable, velocity changes have occurred and neglecting them while processing affects the final seismic images. It is thought that overburden velocity changes acting as low velocity lenses affect the seismic raypaths which, after migration with the baseline velocity model gives rise to apparent lateral shifts of the sideburden. Additionally, in compacting reservoirs actual lateral strains occur and the sideburden moves inward, towards the centre of the reservoir. However, warping measured seismic lateral shifts show apparent shifts that contradict the physical strains, as they appear too large in comparison and point away from the reservoir.

This chapter looks into the nature of lateral shifts, tracking their origin as both real physical lateral displacements of the sideburden and apparent shifts as a processing artefact. To this end, pre and post-production synthetic seismic are generated from a full-field subsurface synthetic model that has been strained according to a coupled fluid-flow and geomechanics simulation. Two monitor surveys are generated; one processed with the baseline velocity model and the other taking overburden velocity changes into account. Warp fields for the two cases are calculated and analyzed together with the physical strains from the geomechanical simulation.

6.1 Introduction

Compacting reservoirs are accompanied by a complex response of the subsurface; i.e. overburden, underburden and sideburden rocks reaccommodate to fill-in the reservoir's shrinking space. The commonly studied overburden extensions, thought to be mostly vertical displacements, in conjunction with its associated changes in the seismic velocities, manifest themselves as travel-time differences or time-shifts in time-lapse seismic data. Sideburden displacements, on the other hand, are thought to be mostly horizontal and according to the geomechanical simulations, directed towards the centre of the reservoir. However, publications on observed lateral shifts in compacting reservoirs have all reported an apparent discrepancy; that measured displacements are too large and point in the wrong direction, i.e. away from the reservoir (Hall, 2006 and Hale, 2007). Although vertical shifts or time-shifts have been studied thoroughly, little attention has been paid to lateral shifts and their peculiar behaviour.

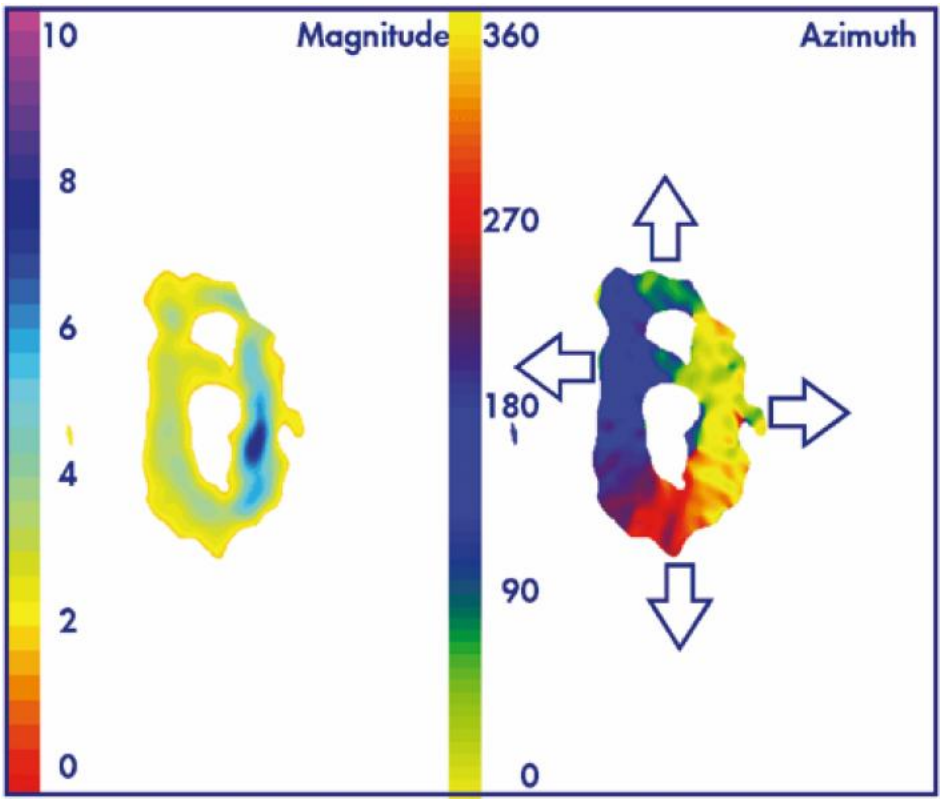

Figure 6.1 Map view of the observed lateral shifts around Shearwater. The left map represents the magnitude of the shifts in metres, whereas the right map shows the azimuthal direction of the shifts (Cox and Hatchell, 2008).

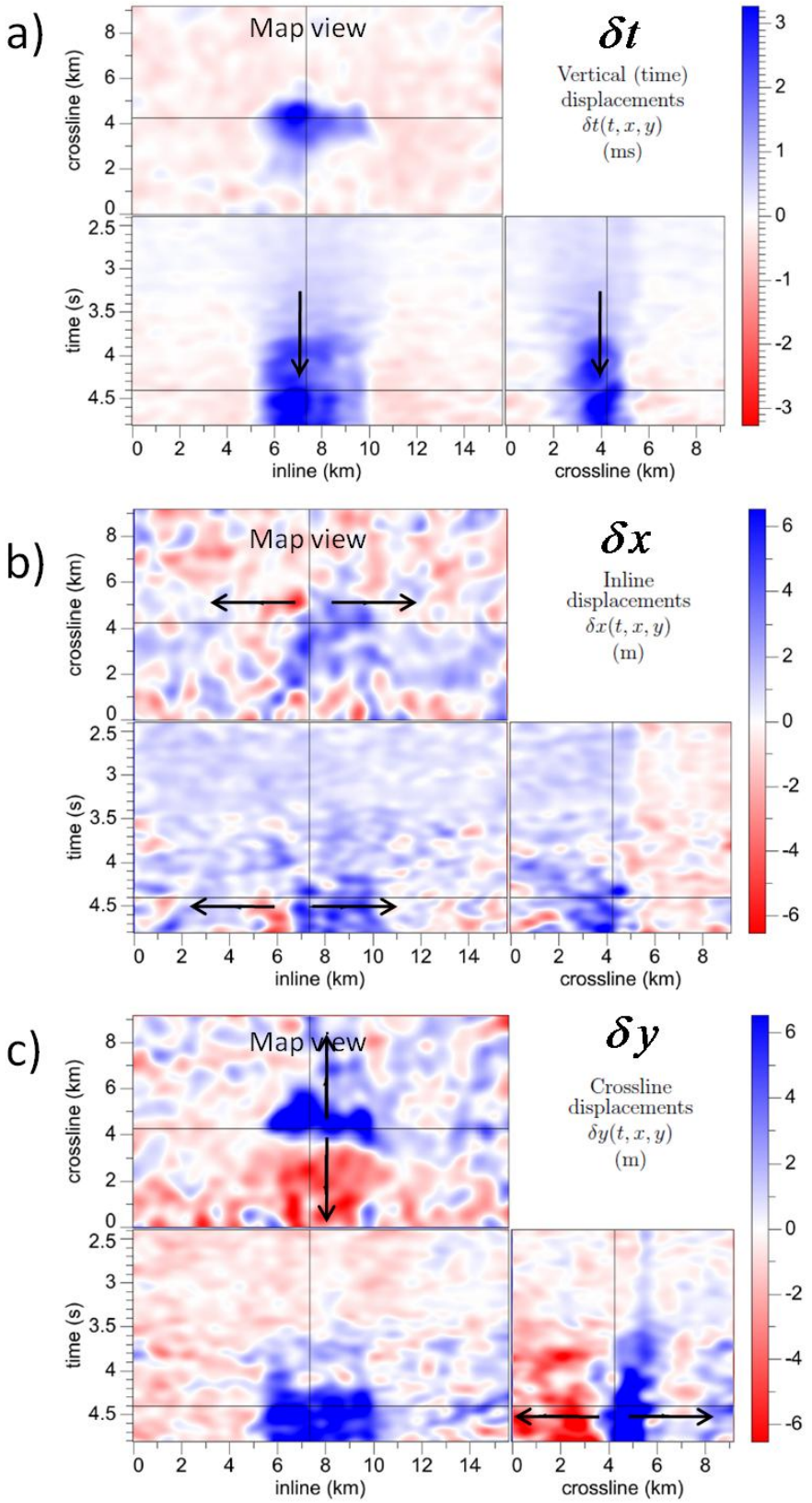

Figure 6.2 Warp field measured at Shearwater showing shifts in all three spatial directions; i.e. vertical time-shifts (a), lateral inline shifts (b) and shifts in the crossline direction (c). The panels display a time slice map view and inline and crossline sections (Hale et al., 2008).

Cox and Hatchell (2008) using Dave Hale's warping method (Hale, 2009) presented a study on measured lateral shifts from the Shearwater field. Shearwater is an HP/HT reservoir with very similar characteristics as neighbouring Elgin (see Chapter 3). In their study they reported time-shifts of up to 8 ms and most strikingly, lateral shifts of up to 8 m. Figure 6.1 shows the measured lateral shifts, where apart from the large magnitude of the observed displacements, even more remarkable is their direction; away from the reservoir. Taking into account that for compacting reservoirs expected lateral displacements are to be inward towards the centre of the reservoir, the observed displacements cannot represent real physical movements of the subsurface, but must have its cause in a different phenomenon. Figure 6.2 shows sections of the measured warp field in all three spatial dimensions; i.e. vertical time-shifts (Figure 6.2a), inline shifts (Figure 6.2b) and crossline (Figure 6.2c). The time-slice and inline and crossline sections, all show for the lateral shifts, an apparent outward movement of the reservoir, whilst the time-shifts representing a slowdown of the overburden, behave as expected.

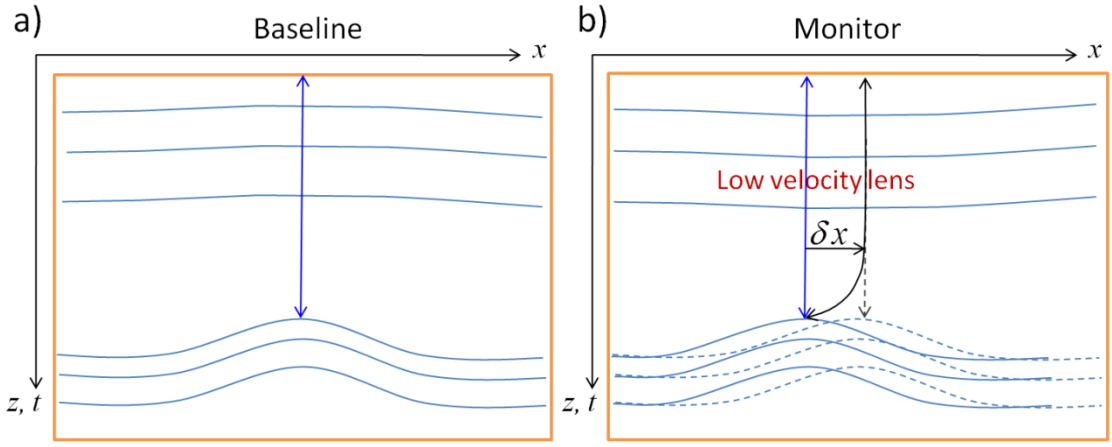

Figure 6.3 Schematic representation of the effects that overburden slowdown acting as low velocity lenses have during migration if the velocity changes are ignored in the monitor survey. Panel (a) shows the baseline survey migrated with the correct velocity model as opposed to a monitor survey (b) migrated using an incorrect (baseline) velocity model. The resulting apparent lateral shifts δx, are greatly exaggerated for demonstrational purpose (redrawn after Hale et al., 2008).

Cox and Hatchell (2008) first suggested that the apparent inconsistency observed in lateral shifts lies in the fact that in most 4D projects the base and monitor surveys are migrated using the same velocity model. Thus, the known velocity changes that take place in the overburden as a consequence of overburden relaxation, are ignored during

the monitor's processing. Nonetheless, if non-negligible time-shifts can be measured, equally non-negligible velocity changes have occurred. As a consequence, areas that have experienced relaxation appear as *low velocity lenses* when compared with the baseline survey, where seismic raypaths will behave differently. The process through which these low velocity lenses can affect the final seismic image if migrated with the incorrect baseline velocity model, is illustrated in Figure 6.3. Figure 6.3a shows a schematic of a baseline survey where a migration velocity model has been constructed so that all image rays are vertical at the surface. For a monitor survey on the other hand, the seismic rays will bend differently while passing through the low velocity lens and if migrated with the baseline velocity model, subsurface points will be imaged on the wrong locations appearing shifted laterally by an amount δx (Figure 6.3b).

Under this hypothesis, the authors presented two methods for modelling the lateral shifts: one based on raytracing and using a subsurface geomechanical model, and the second based on an analytical relation from which the lateral shifts are to be derived directly from the measured time-shifts. Both methods were put to test on the Shearwater field achieving good agreement with the observed data.

This current study aims to test Cox and Hatchell's hypotheses on a synthetic data set, which has been carefully constructed to resemble the Ekofisk field. The choice to use synthetic data was made in order to control all variables and thus the processes by which observed lateral shifts are created. Additionally, it is investigated whether or not and by what fraction the observed shifts correspond to actual lateral physical displacements and if they can be measured by including the overburden velocity changes in the processing.

6.1.1 Correcting the lateral shifts with raytracing

Cox and Hatchell, based on Shearwater data built a geomechanical model to simulate the production life of the field and the associated overburden strain. The overburden velocity changes can then be expressed in terms of the simulated vertical strains and the R factor (as explained in Section 1.4.1), via the relation

$$\frac{dv}{v} = -R\varepsilon_{zz} \tag{6.1}$$

The calculated velocity strains are used to update the baseline velocity model resulting in a *strained velocity model* for the monitor survey. Using the strained velocity model the monitor survey is de-migrated and re-migrated again using ray tracing and the baseline survey's velocity model. The differences between the subsurface points before de-migration and after re-migration correspond to the apparent lateral shifts predicted to occur as a result of the low velocity lenses in the overburden.

6.1.2 Lateral shifts and the time-shift potential

Under the premise that the information about the velocity changes is contained within the measured time-shifts, Cox and Hatchell introduced the *time-shift potential* in order to link vertical and lateral shifts. The time-shift potential is defined as

$$\phi(t) \equiv -\int_0^t \left(\frac{{v_0}^2}{2} \delta t \right) dt \tag{6.2}$$

from which the vertical and lateral shifts are calculated by differentiation (Hale et al. 2008):

$$\begin{aligned} \delta x &= \frac{R}{R+1} \frac{\partial \phi}{\partial x} \\ \delta y &= \frac{R}{R+1} \frac{\partial \phi}{\partial y} \\ \delta t &= \frac{-4}{{v_0}^2} \frac{\partial \phi}{\partial t} \end{aligned} \tag{6.3}$$

Equation (6.2) has the advantage that in order to calculate the apparent lateral shifts (equations (6.3)), no geomechanical simulation is necessary, only the initial velocity model v_0, and the measured time-shifts δt. However, in order to derive the time-shift potential, several important assumptions were made; mainly that the overburden is defined by a simple constant velocity v_0 that is perturbed by a small velocity change

αv_0, where $\alpha \ll 1$. Thus, the overburden velocity at the time of the monitor survey reads

$$v(x, y, z) = v_0[1 + \alpha(x, y, z)] \tag{6.4}$$

The time-shift potential is derived using the Born approximation for the two-way travel time with the perturbed velocity and minimizing with respect to the incidence angle keeping only first-order terms of α.

6.2 The synthetic model

In order to investigate the lateral shifts, a coupled geomechanics and reservoir model roughly based on Ekofisk data is constructed. The model is different and simpler than the one discussed on Chapter 4. It is composed of 92x100x9 cells (Figure 6.4a) of regular lateral spacing of 200x200 metres. The reservoir model includes the sideburden with an areal extent of 20x18.4 km as shown in Figure 6.4b. The reservoir is defined by two layers of a combined thickness of approximately 200 m. The upper reservoir has the best reservoir qualities and is where the producing wells are completed. The porosity ranges from 10% to 35% on the crest of the structure (Figure 6.4b). The blocky nature of the reservoir properties is due to limitations on the simulation package used for this study. However, this ensures a very particular compaction pattern that has an equally particular imprint on the modelled time-lapse seismic.

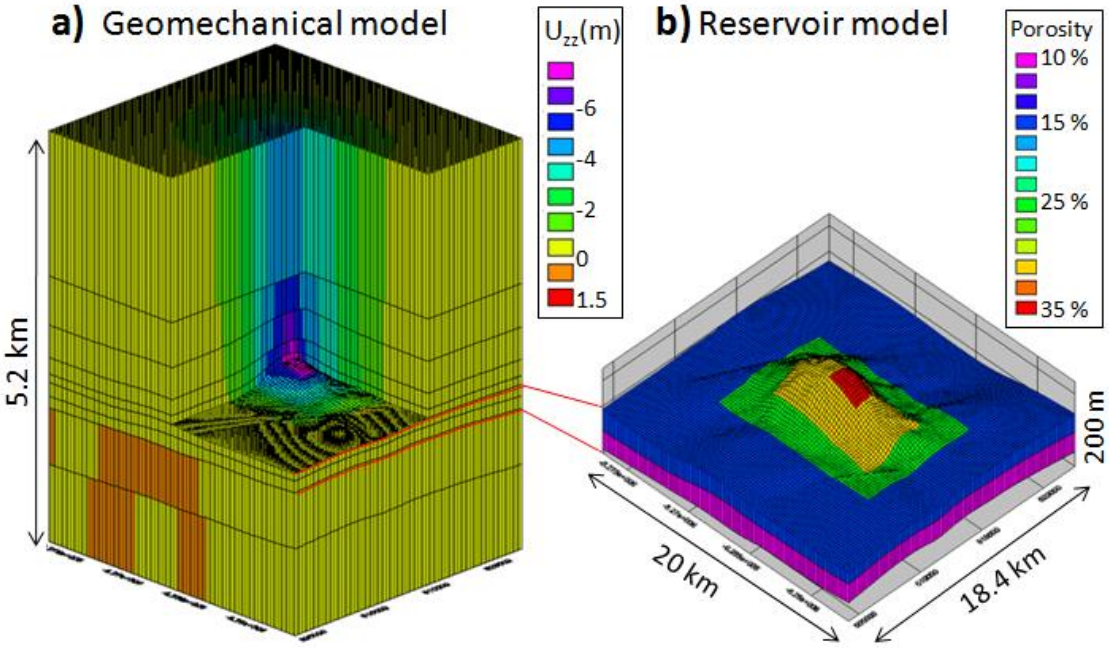

Figure 6.4 Reservoir (b) and full field geomechanics model (a) illustrating the model's dimensions. The geomechanical model shows the modelled vertical displacements in metres where negative is downwards. The reservoir model shows the initial porosity in percentage of the upper reservoir formation.

The geomechanical model consists of different linear elastic materials (Table 1). The overburden and underburden layers are laterally homogeneous. The mechanical properties of the overburden and underburden are calculated from empirical relations for North Sea shales as a function of P-wave velocity (V_p) measured from sonic logs (Horsrud, 2001); the Young's and shear modulus read

$$\begin{aligned} E &= 0.076 * V_p^{\,3.23} \quad \text{Young's modulus} \\ G &= 0.03 * V_p^{\,3.3} \quad \text{Shear modulus} \end{aligned} \tag{6.5}$$

the Poisson's ratio is obtained by the known relation $\upsilon = \frac{E}{2G} - 1$. The reservoir mechanical properties on the other hand, are based on the reservoir model; i.e. using the same empirical relations for North Sea chalk employed on Chapters 4 and 5. However, the Poisson's ratio ν, is taken from literature (Fabricius et al., 2007).

Unit	E [GPa]	ν	ρ (kg/m^3)	V_p [m/s]
OB shale	0.7845	0.2042	2000	2060
OB shale	0.7969	0.2038	2090	2070
OB shale	0.7131	0.2067	2000	2000
OB shale	0.8220	0.2030	2100	2090
OB shale	0.8608	0.2018	2115	2120
Ekofisk Fm	0.45 - 3.35	0.02 - 0.2	2110	2400
Tor Fm	0.78 - 7.34	0.03 - 0.25	2180	2500
UB shale	1.5629	0.1863	2300	2550
UB shale	1.8798	0.1816	2400	2700

Table 6.1 Summary of mechanical properties used for geomechanical and baseline seismic modelling, including from left to right: Young's modulus (E), Poisson's ratio (υ), density (ρ) and P-wave velocity (V_p). The properties are ordered from top (sea floor) overburden (OB) to the underburden (UB) bottom of the model. Elastic properties inside the reservoir Ekofisk and Tor formations range according to porosity.

Twenty years of simulated production are modelled using a coupled reservoir and geomechanics simulator (Settari and Walters, 1999; Sen and Settari, 2005), resulting in an Ekofisk-like depletion and compaction scenario, together with the overburden displacement field. Pressure changes of up to 220 bar are achieved, resulting in roughly 7-8 m displacement at the top of the reservoir and about 4 m of sea floor subsidence (Figure 6.4a). Production comes from eight multi-lateral wells drilled roughly symmetrically around the flanks of the anticline structure and completed in the upper reservoir layer (Figure 6.5). No injection is modelled assuming a pressure depletion drive only. Depletion results in lateral shifts of up to 1.5 metres in both inline (Figure 6.6a) and crossline directions (Figure 6.6b), always towards the centre of the reservoir.

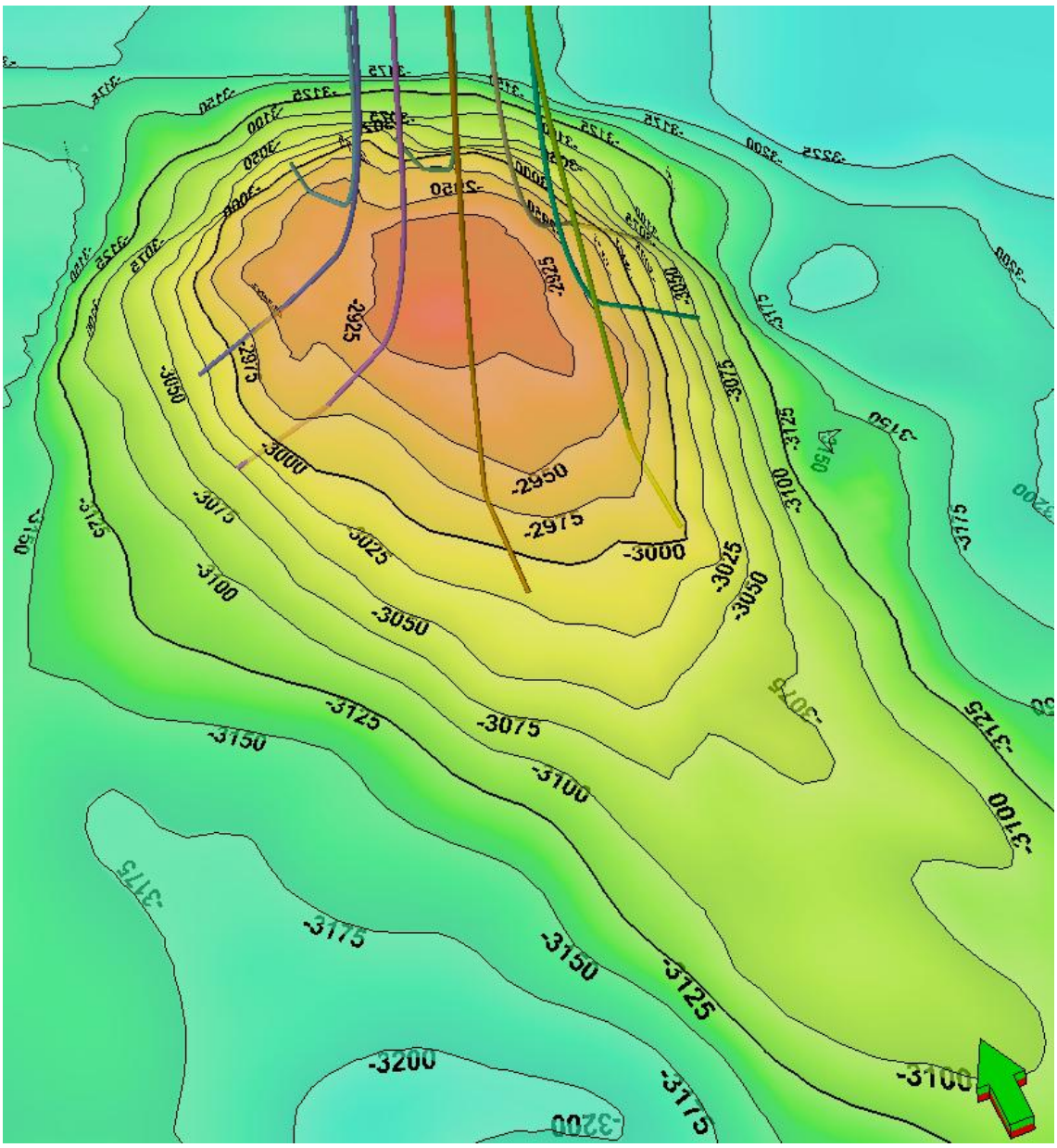

Figure 6.5 Top reservoir structure showing the drilled wells distributed around the flanks of the anticline and completed in the upper reservoir only.

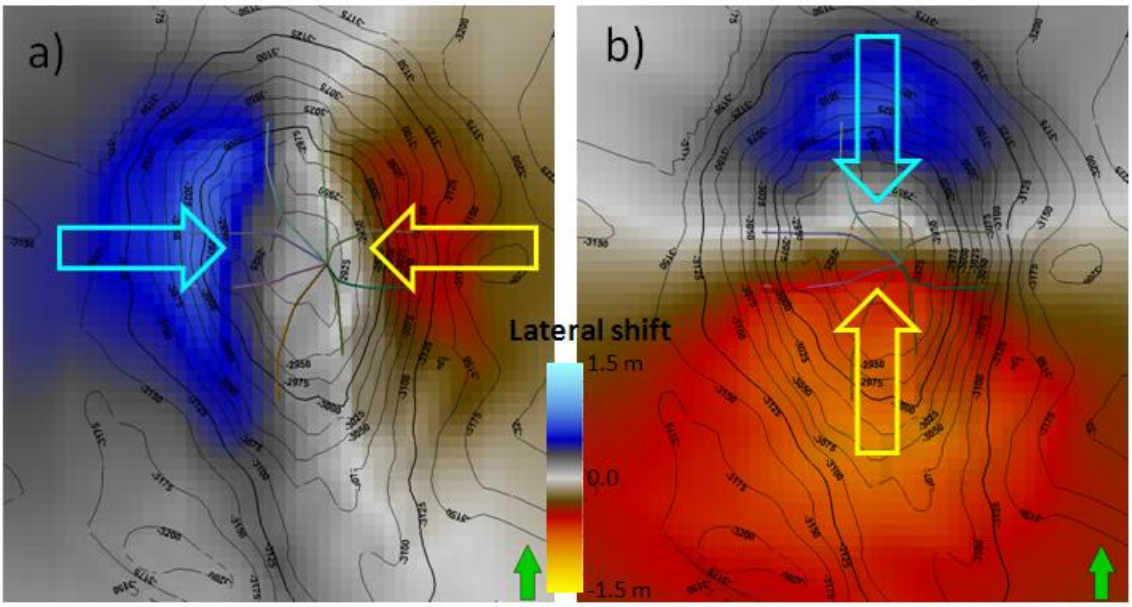

Figure 6.6 Simulated inline (a) and crossline (b) lateral displacements at the top reservoir. All simulated shifts point towards the centre of the reservoir.

The pre- and post-production grids (deformed according to the simulated displacements) are used for seismic modelling. The baseline velocity model is constructed using a sonic log averaged over each material as defined in the geomechanical model. The V_p/V_s ratio is obtained from literature on North Sea shales and chalks (Holt and Fjaer, 2003 and Japsen et al. 2004 respectively). Real seismic acquisition geometries and a Ricker 30Hz zero phase wavelet are used to generate synthetic pre-stack baseline and monitor shot gathers by propagating wavefronts through the subsurface model. The acquisition geometries are based on the Ekofisk streamer data for the 1999 and 2003 surveys. Figure 6.7 shows the streamer data for the 1999 and 2003 surveys, where the undershoot area due to the surface infrastructure is clearly visible. The seismic modelling area is indicated by the yellow rectangle. In order to avoid undershoot problems especially where the highest compaction takes place, shot and receiver pairs are selected outside this area and are moved to obtain a regular seismic coverage. The monitor survey includes not only displaced horizons as dictated by the geomechanical simulation, but also updated seismic velocities to account for the production induced compression and relaxation of the materials. Updating of the seismic velocities is done following Cox and Hatchell's first method: where the velocity changes δv are calculated using the R-factor and simulated vertical strains via equation (6.1). R-values of 5 and 2 for the overburden and reservoir formations respectively are selected as reported by Janssen et

al. (2006). The seismic modelling for this study has been done by Domes (2010) as part of his PhD project at the Edinburgh Time-lapse Project using NORSAR software.

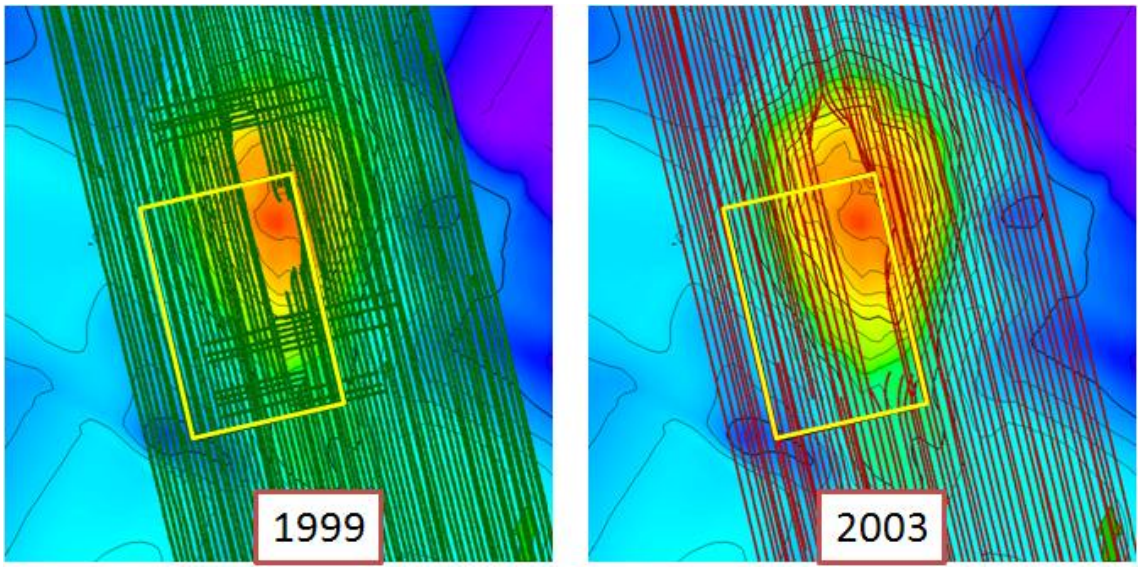

Figure 6.7 Observed acquisition geometry over Ekofisk field for the 1999 and 2003 surveys used as baseline and monitor surveys respectively for this study. The yellow rectangle delimits the seismic modelling area.

Even though the geomechanical simulation covers the entire field, due to computational constraints, the seismic modelling is only performed on a subset (4km x 6km) of the modelled field, comprising the highest compaction area and the south-west flank of the structure. Figure 6.8a Shows the acquisition geometry relative to the top reservoir structure covered by the simulation model. Time-lapse trace selection is done based on minimizing the $\Delta S+\Delta R$ measure. Subsequently, the seismic data is processed using pre-stack Kirchhoff time migration, with two sets of migration velocities; the baseline case, and the strained velocity model after equation (6.1). This yields two different monitor datasets: one processed with the baseline model in accordance with standard time-lapse worflows and the other with the strained velocity model. The workflow is explained in Figure 6.9. The resulting baseline and two monitor surveys are used to calculate the corresponding warp fields. This yields two sets of warp fields; i.e. *normal* and *strained*, generated using the baseline and strained velocity models respectively. Note that for all monitor data the strained velocities are included in the seismic modelling. The difference lies in the processing; where for one case the velocity changes are ignored in

migration (normal) and included in the other (strained). Figure 6.8b shows seismic cross-sections of the baseline survey.

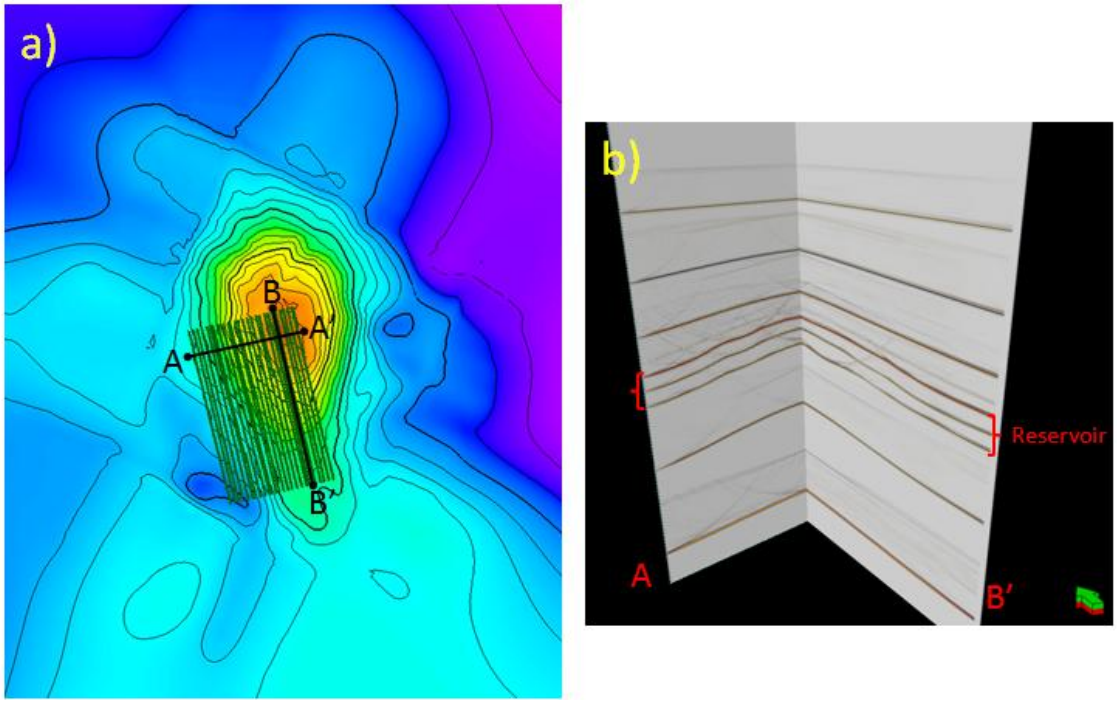

Figure 6.8 Acquisition geometry of the baseline survey (a) and seismic cross-sections of the baseline survey (b). The reservoir is indicated with the red brackets.

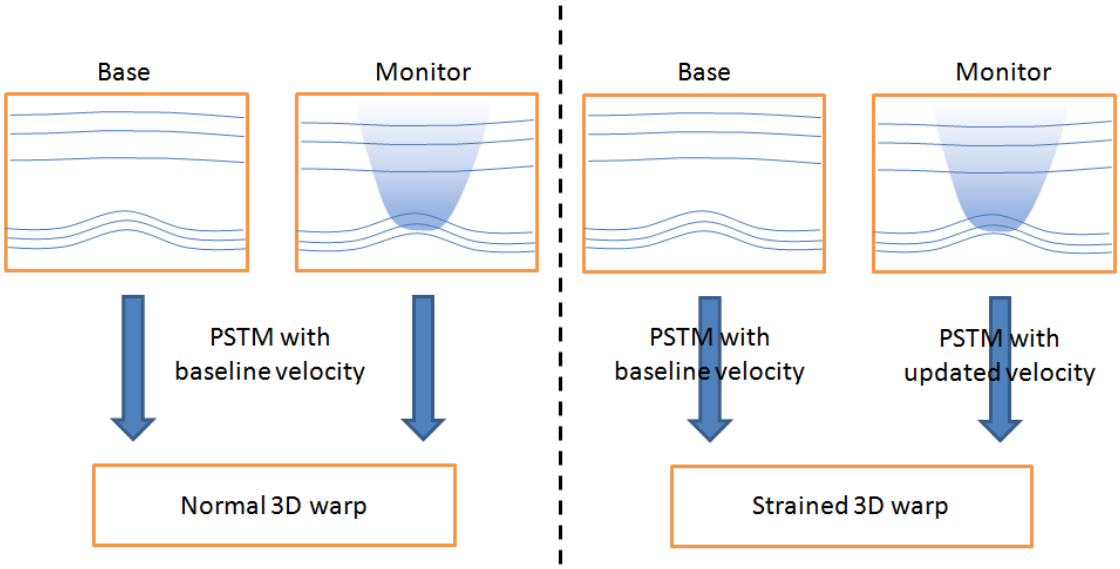

Figure 6.9 Schematic workflow to calculate the "normal" and the "strained" warp vectors.

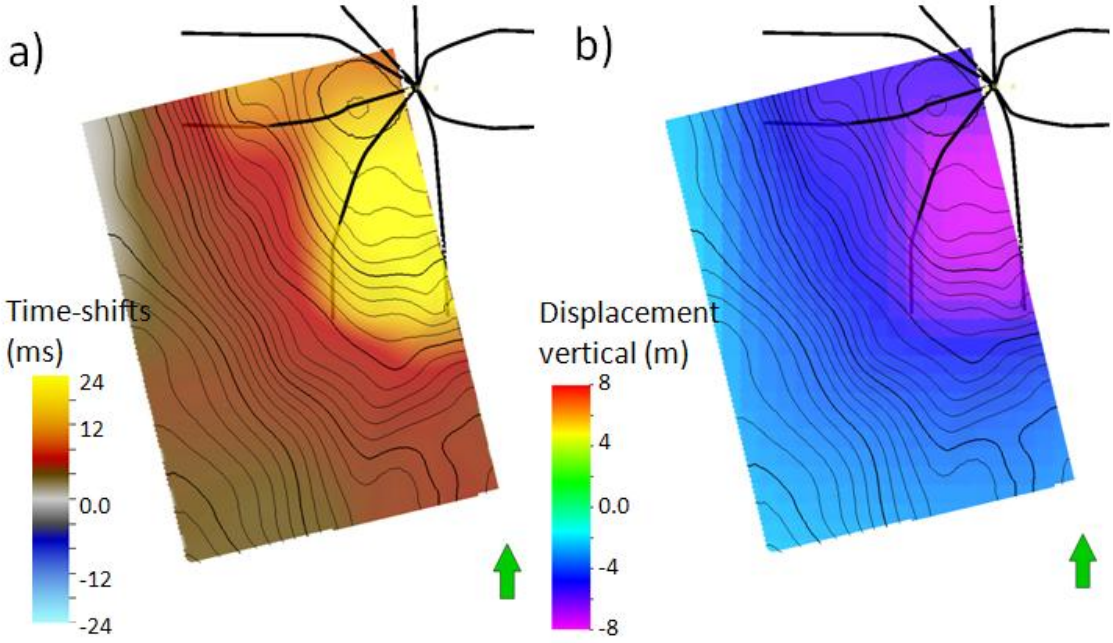

Figure 6.10 Time-shifts at the top reservoir (a) in milliseconds and simulated vertical displacements (b) at the same horizon (top reservoir) in metres.

Both normal and strained warp fields are calculated using the same correlation window of 15x12x12 for sampling intervals of 4ms vertically and 25m laterally. The calculated normal time-shifts of up to 24ms TWT, are roughly the same magnitude as those reported on Ekofisk in 1999 (Guilbot and Smith, 2002). The calculated normal time-shifts at the top reservoir (Figure 6.10a) delineate very clearly the main compaction area (Figure 6.10b) defined by the high porosity section.

6.3 Observed apparent lateral shifts

The resulting lateral shifts are displayed in Figure 6.11 and Figure 6.12 for the inline crossline directions respectively. The figures show the reference lateral physical displacements obtained from the geomechanical simulation (a) with a dashed line that delimits the seismic modelling area. The arrows indicate the direction of the displacements, which is inwards towards the centre of the reservoir. The other two panels correspond to the normal (b) and strained (c) apparent lateral shifts. As observed by Cox and Hatchell, the observed (apparent) lateral shifts conflict with the ones from the geomechanical simulation pointing mostly away from the reservoir and of a

magnitude far too great to be real. Though, this agrees with their hypothesis, accounting for these velocity changes during processing appears to make no difference.

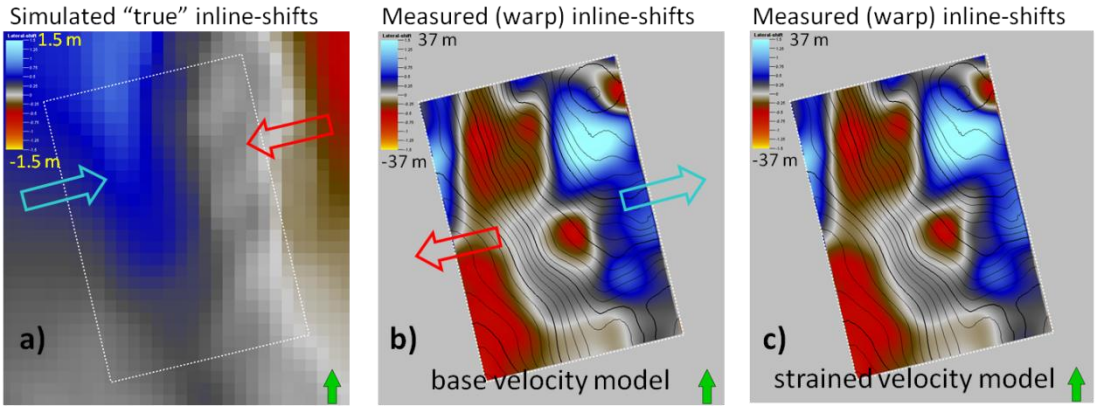

Figure 6.11 Observed displacements in the inline direction for the three cases: a) displacements from the reference geomechanical model. The dashed white line rectangle delineates the extent of the seismic modelling area. b) Displacements from the normal and strained (c) warp fields. The coloured arrows indicate the direction of the observed displacements.

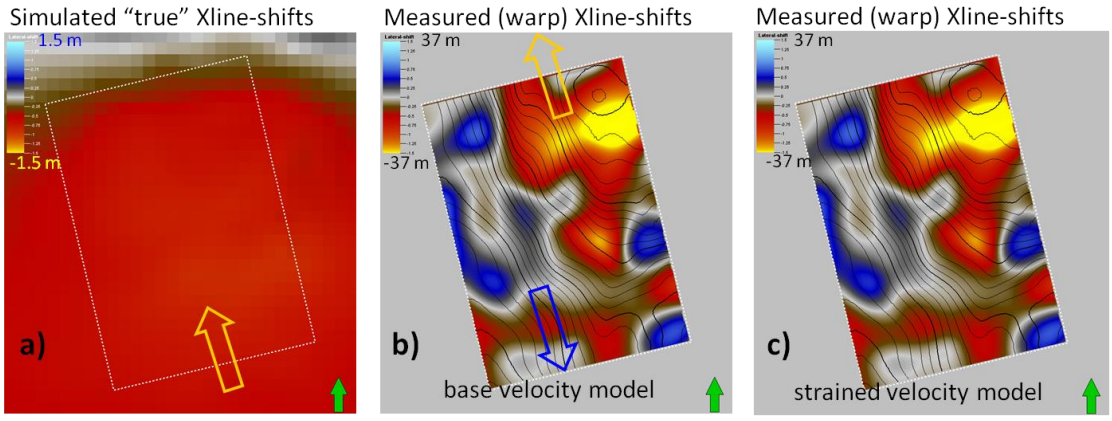

Figure 6.12 Observed displacements in the crossline direction for the three cases: a) displacements from the reference geomechanical model. The dashed white line rectangle delineates the extent of the seismic modelling area. b) Displacements from the normal and strained (c) warp fields. The coloured arrows indicate the direction of the observed displacements.

It was anticipated that including the velocity changes into the migration velocity, would have corrected the effects of migrating with the baseline velocity model, resulting in lateral shifts with the right magnitude and direction. However, the lateral shifts from the

strained velocity model exhibit the same characteristics as those obtained with the incorrect velocity model. Furthermore, the corrections are too small to make any visible difference. In both inline and crossline cases (Figure 6.11 and 6.12) the warp field lateral displacements look very different in character (apart from direction and magnitude) to the reference displacements from the geomechanical simulation, an indication that the measured time-lapse lateral shifts are an artefact not directly related to the physical lateral displacements. The cause of which, may be twofold: First, the synthetic seismic is defined only at the interfaces or model horizons (i.e. the only place where reflections take place; Figure 6.8b) and so would the time-lapse signal which might not be adequately measured by the warping method. Second, pre-stack time migration might not capture all lateral displacements, for which pre-stack depth migration (PSDM) would have been more adequate. Unfortunately PSDM is outside our capabilities in terms of time, computational resources and expertise. This could also explain why accounting for the overburden velocity changes during processing makes little to no difference to the measured apparent lateral shifts.

In addition to the above, as is the case with the Ekofisk field, the synthetic model shows that most of the strain takes place inside the reservoir with the overburden layers offering very little resistance to subsidence. In other words, negligible stress arching occurs and the overburden sinks experiencing large vertical displacements with relatively little vertical strain (Figure 6.13). Therefore, seismic time-lapse time-strains in the overburden are dominated largely by ray-path length changes rather than velocity changes. Consequently both normal and strained calculated time-shifts at the top reservoir (Figure 6.14 a and b respectively) are nearly indistinguishable from each other differing only by about 5 % (Figure 6.14c); the amount of time-shifts caused by velocity changes alone.

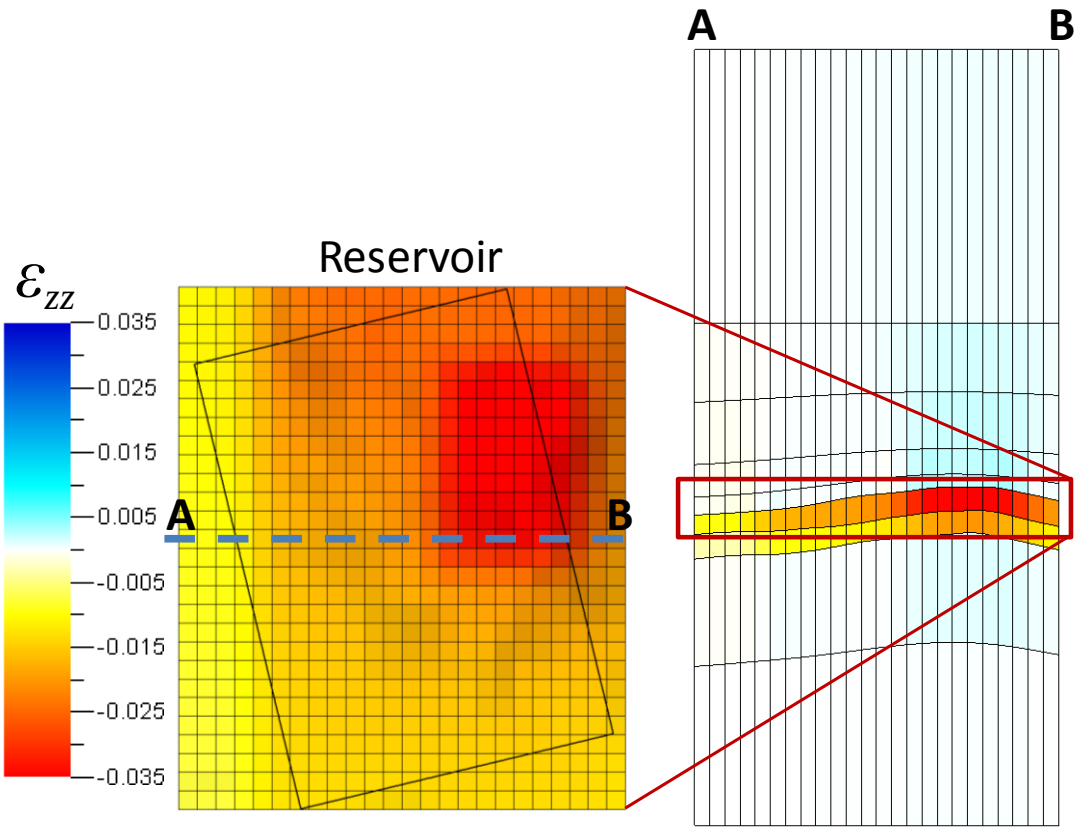

Figure 6.13 Simulated vertical strains at the top reservoir (left) and vertical cross section (right) including the overburden and underburden.

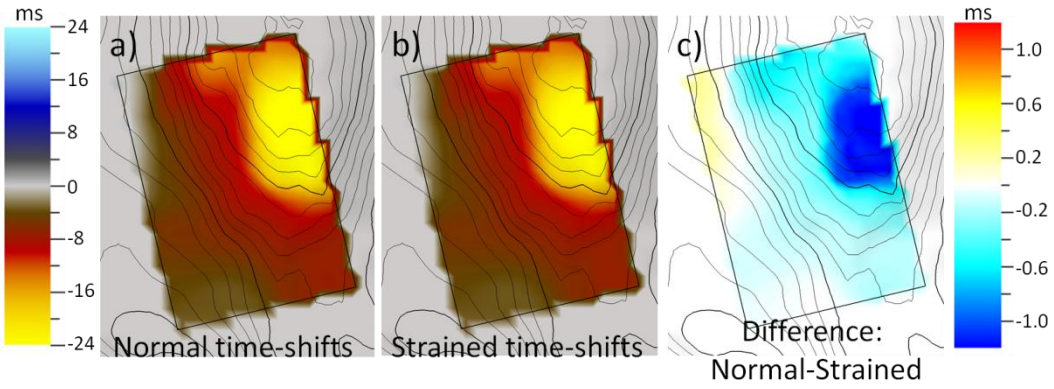

Figure 6.14 Time-lapse time-shifts at the top reservoir using the normal velocity model (a) and the strained velocity model (b). The difference between the two time-shifts (c) indicates the time-shifts caused only by velocity changes; about 5% of the total.

Figure 6.15 shows the residuals or difference between the strained and normal observed lateral shifts for the inline (a) and crossline (b) directions. The well trajectories of the

simulated production wells are shown as black lines. Remarkably, the residuals correlate very well with well activity, with displacements always inwards towards the wells and, aside from the magnitude of the differences, the maps have some resemblance to the simulated/real lateral strains (Figure 6.16). This however, can be explained as that when applying the velocity strains to the monitor survey during pre-stack time migration, the apparent lateral shifts are untouched, only vertical travel-times are affected. Therefore, the time-shifts caused by changes in velocity are removed leaving only the differences due to travel paths caused by subsidence. Thus, the residuals (Figure 6.15) show a mixture of real physical lateral strains and the effects of velocity changes on the vertical travel times. Separating these two effects, should require pre-stack depth migration.

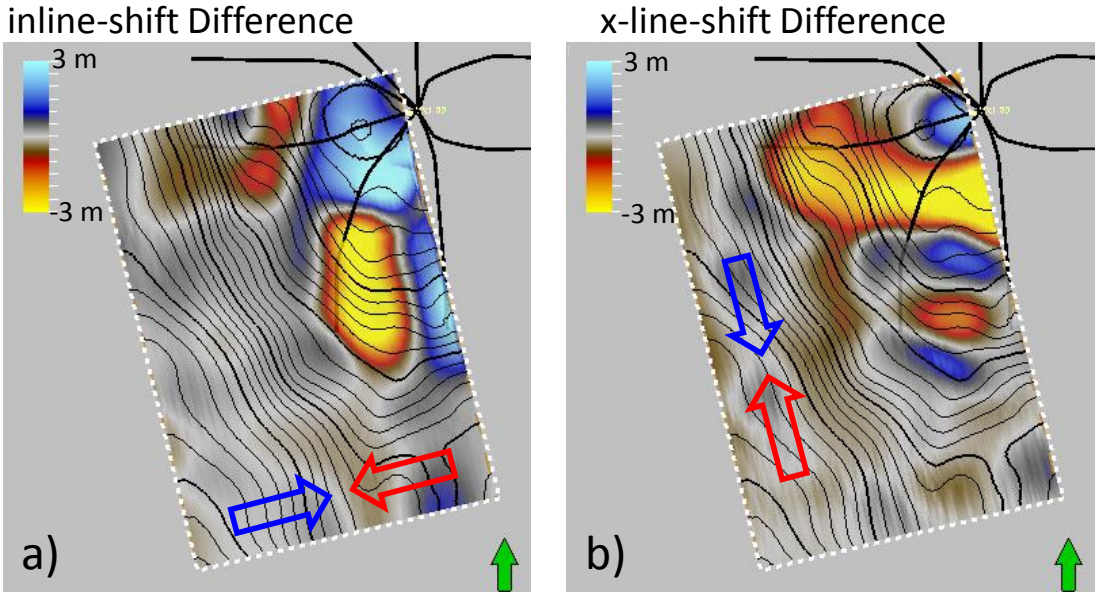

Figure 6.15 Difference map at top reservoir between normal and strained lateral shifts. a) inline-shift difference. b) x-line shift difference.

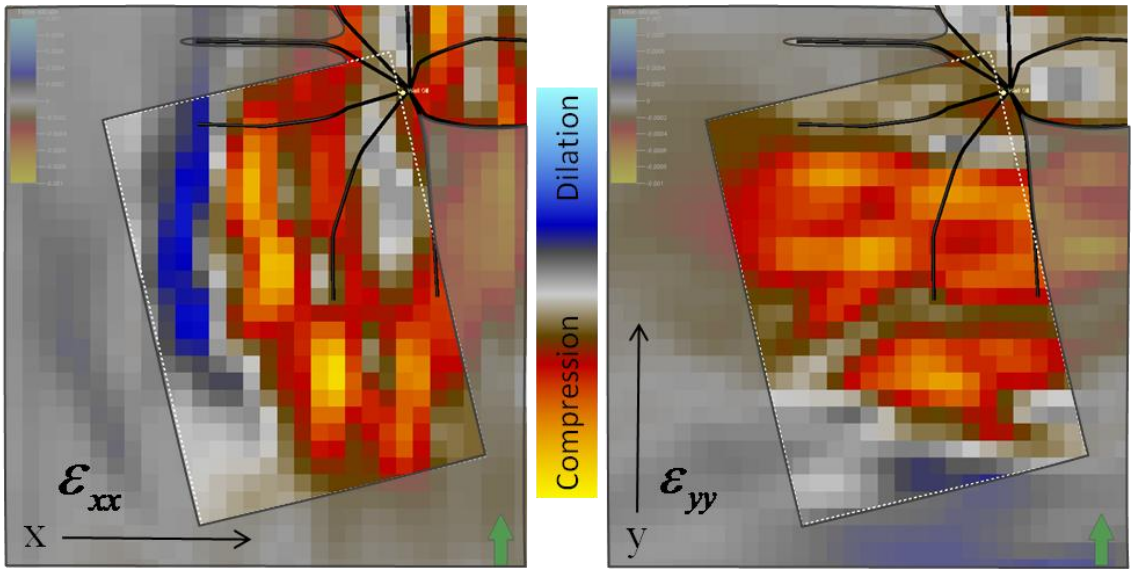

Figure 6.16 Simulated lateral strains at the reservoir horizon in x and y-directions as indicated. Hot colours indicate compression and cold colours dilation.

Nonetheless, the large apparent lateral shifts remain unexplained, as shifts of up to 40 metres, cannot be attributed only to time migration and as has been shown above, neither to processing with an inadequate velocity model as that accounts in this case for about 10% of the difference. It is possible then, that the apparent shifts are an artefact created by the way the warp vector is measured. First of all, in dipping planes like the flanks of the anticlinal structure modelled in this study, it is difficult to separate vertical from lateral displacements. Second, accurate measurement of lateral shifts requires that individual seismic events can be unequivocally laterally resolved; i.e. that the seismic amplitudes associated to a subsurface event (inside the correlation window) can be distinguished from that of the neighbouring seismic traces. However, the choice of homogeneous seismic velocities in each layer of the model (Table 6.1) results in a constant acoustic impedance contrast across each subsurface interface and thus, to constant reflection amplitudes (Figure 6.17). Therefore, in areas of similar structure as shown in Figure 6.17, when calculating the warp vector seismic events will be hard to resolve laterally resulting possibly in inaccurate measurement of lateral shifts.

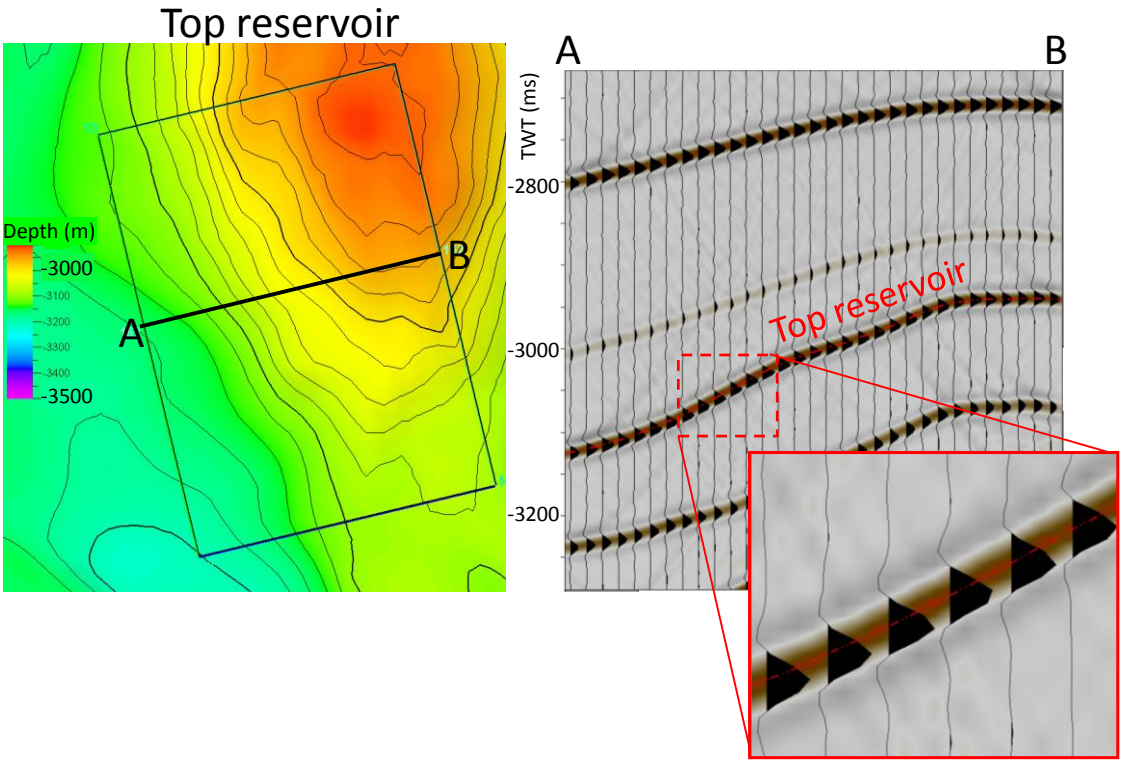

Figure 6.17 Inline seismic cross section of the baseline survey showing the reflection amplitudes every fourth seismic trace highlighting the top reservoir, emphasizing the difficulty when calculating the warp vector of resolving laterally the one trace from another.

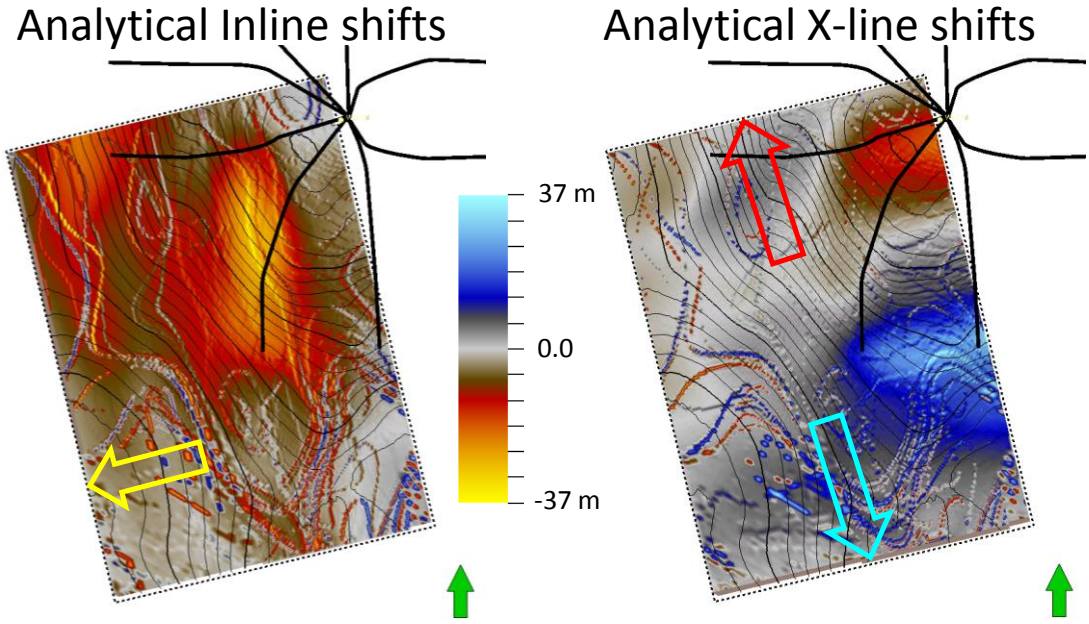

Figure 6.18 Calculated lateral shifts using the time-shift potential for the top reservoir in the inline direction (left panel) and x-line direction (right panel).

On the other hand, the analytical lateral shifts from the time-shift potential seen in Figure 6.18, although they exhibit the same magnitude, are considerably smoother and of different character as the observed ones (Figure 6.11 and Figure 6.12). The observed noise in the maps, is due to the fact that the modelled seismic is not defined in between reflectors and thus the time-shift potential at the interface introduces some numerical instabilities. These instabilities, together with the uncertainty associated with measuring the lateral shifts may explain the discrepancies between the calculated and measured lateral shifts.

6.4 Conclusions

The results of this study place geomechanics or the subsurface strains as the main contributor to the observed seismic time-lapse signal, whereas overburden velocity changes, prove inconclusive and do not in this particular case explain the modelled time-lapse lateral shifts. There is no apparent correlation observed between the lateral displacements generated by the geomechanical simulation and those measured from the modelled seismic, indicating that the latter are an artefact of processing and the warping algorithm itself. Updating the velocity model seems to have little effect in correcting this mismatch.

One possible reason is the way migration handles the data and therefore, that pre-stack time-migration does not capture the lateral velocity variations introduced in the strained velocity model, implying that the presented analysis should be carried out using PSDM algorithms. However, migration alone cannot be responsible for the large observed lateral shifts. On the other hand, it has been shown that only a small part of the measured apparent lateral shifts can be attributed to overburden velocity changes and actual physical displacements. The large remaining difference is believed to be an artefact caused by the warping algorithm itself unable to laterally diferentiate individual seismic events due to the characteristics of the modelled synthetic seismic.

Whatever the cause of the apparent lateral shifts, taking the difference between the strained and normal observed lateral shifts removes it. The residual contains only the

information that is introduced in updating the velocity model. Consequently, observed apparent lateral shifts are still poorly understood and with only a handful of publications addressing the subject, it remains an open research area. The potential benefits of understanding time-lapse lateral shifts include measurement of lateral strains for well stability and detection of shear planes in order to mitigate parallel-slip and fault reactivation.

Chapter 7

7 Conclusions and recommendations for future work

In this project I have examined production induced subsurface deformations and treated them as a signal that originates inside the reservoir triggered by production activity. This signal filtered by the earth is recorded in the form of time-lapse seismic data, and the challenge is to fully decode the information contained in the time-lapse seismic data. Integration of reservoir geophysics with field-wide geomechanics as pursued in this thesis, seeks to improve our understanding of the different processes that originate and shape the seismic time-lapse signal. This understanding permits us to mitigate undesired effects such as subsidence and allows us to infer what is happening inside the reservoir through what we can see in the overburden with the recorded time-lapse signal. In this way, the overburden time-lapse seismic now is able to provide an additional control over reservoir compaction, depletion and injection areas that should supplement the existing information.

More explicitly, in this thesis I have studied how to measure time-shifts, what geomechanical processes give rise to those time-shifts, and how and where these geomechanical effects are generated inside the reservoir. The main focus of this research has been mainly on the latter question; i.e. how to relate the signal generated inside the reservoir to what is recorded in the overburden as time-shifts; i.e. to improve the commonly used Geertsma approach. By postulating the problem as a transmitter (reservoir) and receiver (overburden) configuration I have been able to forgo an explicit description of the physical processes that shape this signal to be replaced by an implicit linear filter. In this study, the linear filter has been approximated as a Wiener filter calculated directly from the data. As a result, I have been able to achieve greater accuracy than with explicit Geertsma type Green's functions with considerably lower computing time.

7.1 Summary

In complex reservoirs and in a world demanding energy security, a thorough understanding of a producing reservoir translates into better field management and consequent higher recovery factors at a higher profit. This understanding comes only by integrating all disciplines i.e. “surface geophysics” (e.g. seismic acquisition and imaging), “subsurface engineering” (e.g. well integrity and seafloor subsidence), reservoir geophysics and reservoir engineering. However, in order to do so, the processes through which reservoir activity affects the surrounding rocks and translates into time-lapse seismic differences must be readily understood. This understanding comes in the form of geomechanics and rock physics. Originally restricted to computer simulation models of the subsurface, now geomechanics has time-lapse seismic to directly update the subsurface model and thus reservoir management decisions.

This project has focused on the relationship between the overburden and the reservoir. Although previous works have addressed the need of solving the inverse problem between the overburden and the reservoir, they are either too simple or overly complex. Here, I have proposed an intermediate step by approximating the solution with available data. In order to do so, I have reformulated the problem to be analogous to the analysis of time series. In this way, by considering the reservoir as a transmitter whose signal is filtered by the medium it propagates (i.e. the overburden), where it is recorded in the form of vertical strain by the receiver (i.e. the overburden), I have been able to find an approximate solution to this filter from the available field data. In this thesis, I have used geomechanical models as data to simulate the behaviour of these filters assuming they are linear and time invariant. Therefore, I have been able to find an approximate solution in the form of Wiener filters. The resulting Wiener filters describe the deformations of the overburden caused by reservoir production activity. The ensuing modelling error although still high is significantly lower than regularly used techniques like Geertsma, representing a valuable contribution to this area of research. Furthermore, in addition to being able to approximate a solution from the available data, Wiener filters have the advantage that by operating via convolution they are very fast to apply. Not only can reservoir data be convolved with the filter to estimate overburden deformation, but more importantly, the overburden strain can be deconvolved using the

inverse filter to estimate changes inside the reservoir. In this way each monitor survey provides an indirect measure of the evolution of the field.

7.2 Assumptions and its implications

There are two main assumptions behind this work; first, that the measured overburden time-strains are directly proportional to the physical vertical strains. This proportionality is described by the R factor and although there is still controversy about its nature, it is widely accepted. Even though in this research it has been used in all field applications for consistency with published works, thanks to the way filters operate the R factor could be ignored. Since convolution satisfies the associative arithmetic property (Bracewell, 1999), we have that

$$\begin{aligned} f^{-1} * \varepsilon_{zz} &= f^{-1} * \left(\frac{1}{(1+R)} \frac{dt}{t} \right) \\ &= \frac{1}{(1+R)} \left(f^{-1} * \frac{dt}{t} \right) \end{aligned} \tag{7.1}$$

thus, direct deconvolution of the time-strains yields

$$\begin{aligned} f^{-1} * \frac{dt}{t} &= (1+R) f^{-1} * \varepsilon_{zz} \\ &= (1+R)\varepsilon_{vol} \end{aligned} \tag{7.2}$$

where f is the Wiener filter, ε_{zz} is the overburden vertical strain and dt/t the measured time-strains. As a consequence, R acts only as a scale factor for the estimated reservoir volumetric strain ε_{vol}. Therefore, unless one is concerned with the actual physical magnitude of the reservoir's volumetric strains, we can do without R and its associated uncertainties. Nonetheless, while I have pointed out the need for different R values on the overburden as a function of different rock formations, some authors have hinted to an anisotropic and/or horizontally heterogeneous nature of R (Herwanger, 2008; Sayers, 2006). If such are the circumstances, and if dR/dx and dR/dy is non negligible, a thorough characterization of R will be necessary before an overburden inversion can be

performed. However, studies on this regard are scant and therefore any lateral variations of R have been ignored for this research. The exact nature of R lies outside the scope of this thesis.

The second assumption, that the subsurface process is linear and time-invariant has an important implication on the type of reservoir information that can be estimated using Wiener filters. Ideally we would like to estimate reservoir pressure changes as has been presented before by Du and Olson (2001) and Hodgson et al. (2007). However, pressure changes are not the deciding factor directly responsible for compaction, but effective stress changes instead, which govern the fractional change of volume inside the reservoir. Reservoir volumetric strain in turn, dictates the resulting subsurface deformation. Thus, inverting for reservoir pressure changes from overburden deformation will require pressure changes to be directly proportional to volumetric strain. However, mature compacting fields do not behave linearly and the changes in total stress are non negligible. Moreover, the governing factors are usually too complex to characterize with the typically scant available information. For this reason, volumetric strain changes and mean effective stress changes (provided a reasonable assumption of the effective bulk modulus) in my belief and in agreement with other studies (Corzo, 2009; Hodgson, 2009), are the only parameters that can be estimated through inversion of measured time-shifts.

Estimation of reservoir pressure changes is still possible, though it will involve the adoption of field-specific rock physics models, in addition to some type of supplementary data. For example, provided the inverted estimates of reservoir volumetric strain, chalk fields still require saturation estimates for a complete characterization of the reservoir pressure. The studies in this thesis have shown that the overburden on the other hand can be regarded as a linear process that can be approximately described with Wiener filters.

7.3 Lateral variability, errors and the Wiener filters

The sensitivity analysis presented in Chapter 2, showed that the effects of structure and general heterogeneity of the subsurface on the Wiener filters are non negligible. As a

consequence, this leads to the introduction of multiple sources in order to minimize the effects of lateral variability on the calculated Wiener filters and its solutions. The implementation of several sources consequently leads to the issue of how to combine the different estimates of reservoir volumetric strain. By applying the Wiener filter technique to a naturally compartmentalized field like Elgin, the natural answer to this question was to place a source roughly in the middle of each reservoir compartment. The Elgin approach was extended to the remaining field applications, where in the absence of clear natural compartments, artificial segments were defined in terms of similar structure and a generally slow lateral variability. Therefore, some segments are bounded by faults where the reservoir properties change abruptly, while others are simply defined by structure.

Moreover, although not included in this thesis, the use of multiple sources can be used to quantify the error associated with to the overburden inversion. By modifying the definition of the mean standard deviation given by

$$\boldsymbol{\sigma} = \sqrt{\frac{1}{N}\sum_{i=1}^{N}\left(\boldsymbol{\varepsilon}_{vol}^{i} - \left\langle \boldsymbol{\varepsilon}_{vol} \right\rangle\right)^{2}} \tag{7.3}$$

where $\boldsymbol{\varepsilon}_{vol}^{i}$ is the estimated volumetric strain map resulting from applying the Wiener filter of the ith source to the measured overburden strain; $\left\langle \boldsymbol{\varepsilon}_{vol} \right\rangle$, instead of an arithmetic mean is the map resulting after stacking all N overburden inversions, where N is the number of sources used.

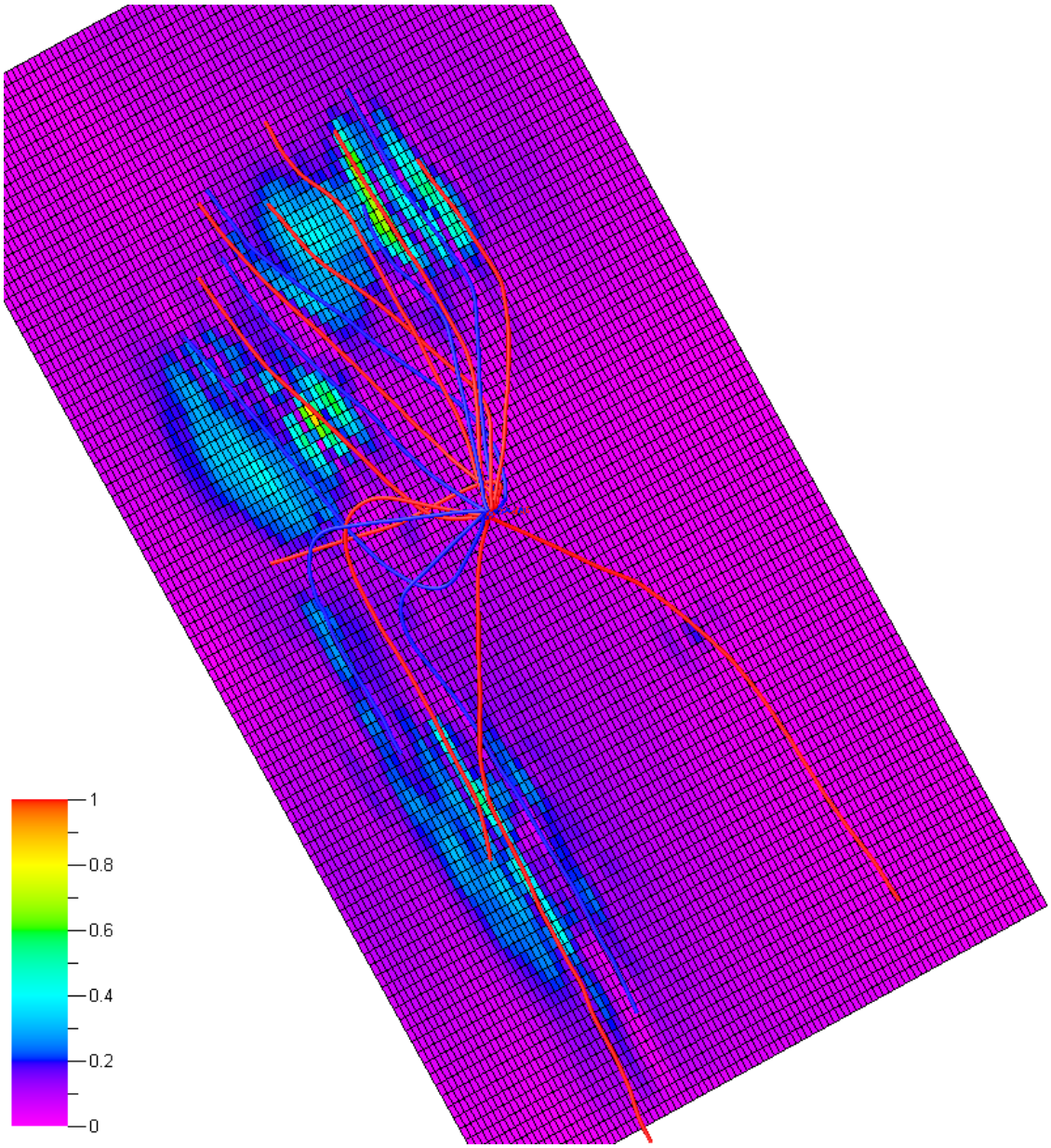

Figure 7.1 Modified normalized mean standard deviation of the estimated volumetric strain for the Tor formation (Figure 2.12e) for the synthetic example used in Chapter 2.

Figure 7.1 shows a map of the modified normalized mean standard deviation of the estimated volumetric strain for the Tor formation shown in Figure 2.12e. Not surprisingly, the results show that there is larger uncertainty where larger changes in the reservoir have taken place. However, what can be very valuable to know is that there is high confidence in the areas where little to no changes are predicted. In this thesis the number of sources for a given reservoir formation is at the most 5, which is too low to give $\boldsymbol{\sigma}$ (modified mean standard deviation) a real statistical significance. If the Wiener filter technique were to be automated in order to make the inclusion of more sources

less cumbersome, $\boldsymbol{\sigma}$ maps could be very useful by quantifying the confidence of the overburden inversion. Along the same lines, something similar could be done with the measured overburden time-strains used for the inversion; i.e. in fields with multiple seismic vintages (ideally with LoFS), the dispersion or $\boldsymbol{\sigma}$ could be quantified for the cross-equalized seismic cubes. The resulting *time-lapse uncertainty*, when combined with that from the overburden inversion, could give an actual physical error of the overall time-lapse analysis.

7.4 Stacking multiple-source inversions

In order to automatize the Wiener filter method and use a larger number of sources, the use of segments to average or stack the different estimations must be discarded. As a consequence, some weighting function dependent on the source location has to be defined. Additionally all weighting functions should be zero at the other source locations and all should add up to one everywhere. Figure 7.2 shows a preliminary test for one such set of weighting functions. The map corresponds to the estimated volume changes of the synthetic example used in Chapter 2 (Figure 2.12e). The resulting NRMSE is of 35%, a 1.1% improvement when compared with the previously used segments from the same four sources. The weighting function used for this test for the ith sources is defined as

$$w_i(\mathbf{x}) = \left[\frac{1}{N} + \frac{(N-1)}{N} e^{-\beta^2 \left\| \mathbf{x}-\mathbf{x}_i \right\|} \right] \prod_{j \neq i}^{N} \left(1 - e^{-\beta^2 \left\| \mathbf{x}-\mathbf{x}_j \right\|} \right) \tag{7.4}$$

where N is the total number of sources, $\mathbf{x}_i$ is the location of the source, $\left\| \mathbf{x}-\mathbf{x}_i \right\|$ is the Euclidean distance between the observation point and the source and β is a free parameter that controls the decay rate of the exponential functions.

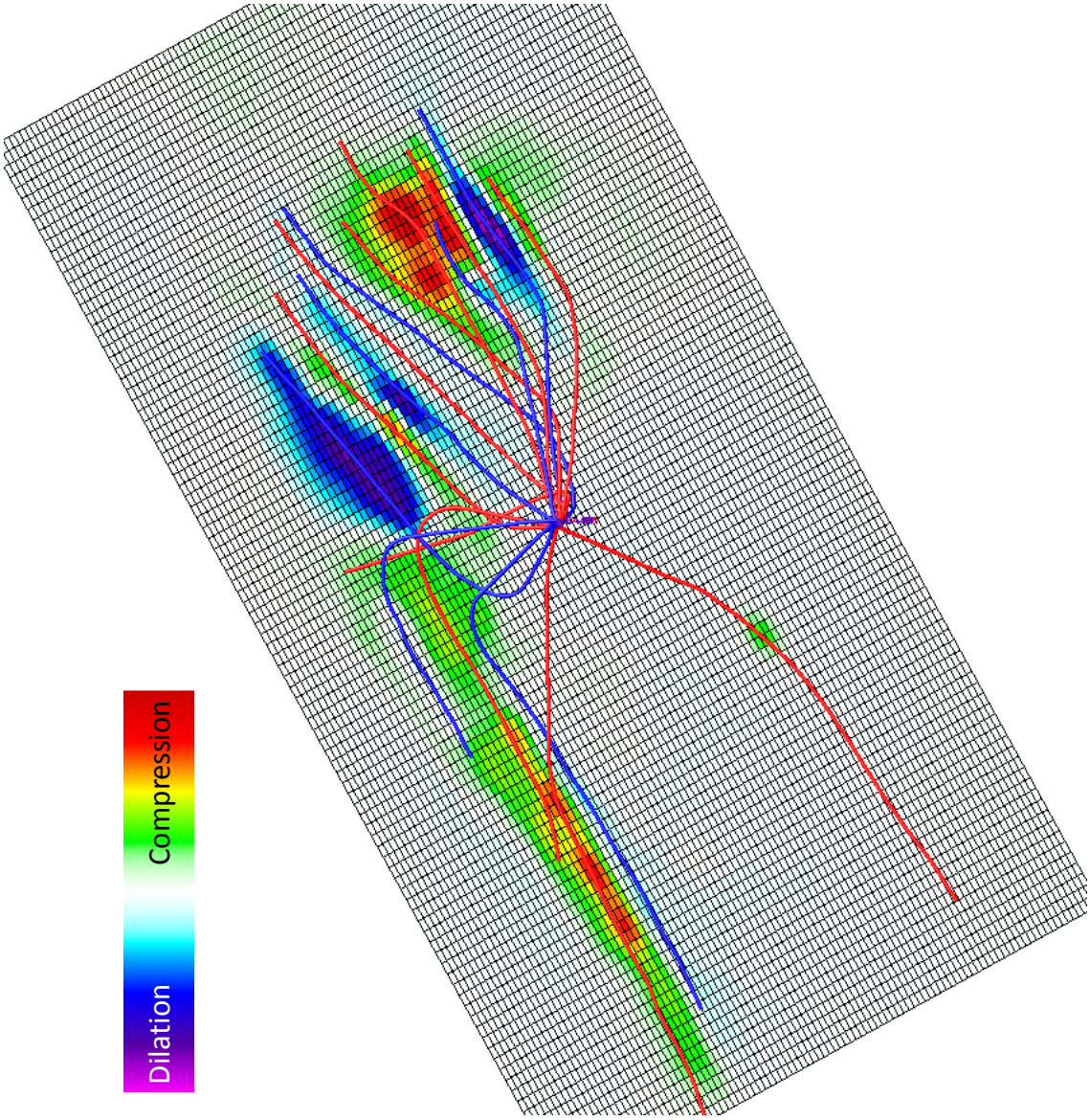

Figure 7.2 Estimated volumetric strain for the Tor formation (Figure 2.12e) of the synthetic example used in Chapter 2. The map has been calculated with a weighting function of the type described in equation (7.4).

Equation (7.4) satisfies all conditions; i.e. that the individual weights are never less than 1/N except at other source locations where it is zero and that the sum of all weights

$$w_T = \sum_{i=1}^{N} w_i \tag{7.5}$$

is equal to one. Although equation (7.4) represents an improvement over the segment-based stacking, it is not significant and further tests should be carried out using perhaps

wider Gaussian-type distributions or possibly some type of nearest-neighbours interaction.

7.5 Vertical resolution

Vertical resolution or the discrimination of different reservoir units from overburden inversion, as has been presented in this thesis, is based on the assumption that the total overburden strain can be expressed as a linear combination of contributions from the different reservoir formations. For example, given a reservoir composed of L different reservoir layers, with a source location $\mathbf{x}_i$ and sources $\boldsymbol{\varepsilon}_{vol}^{i,\lambda}$ placed on top of each other and the corresponding Wiener filters $f_{i,\lambda}$, with $\lambda = 1, 2, \ldots, L$, the overburden strain reads

$$\boldsymbol{\varepsilon}_{zz}^{i} = \sum_{\lambda=1}^{L} f_{i,\lambda} * \boldsymbol{\varepsilon}_{vol}^{i,\lambda} \tag{7.6}$$

In other words, the total overburden strain can be expressed as the sum of the partial strains $\boldsymbol{\varepsilon}_{zz}^{i,\lambda}$, caused by each source. However, this assumption entails that there is no interaction or interference between sources; i.e. that the reservoir formations are isolated. Intercommunication between reservoir units or interference between volumetric strains will cause the assumption to break. The extent of this rupture is unknown and should be further investigated. Moreover, if one of the reservoir formations contributes with most of the production and thus to the compaction, a linear combination of sources will tend to impose that solution on neighbouring formations even if they are inactive. Therefore, the linear combination approach used in this research should be improved by perhaps an additional term accounting for interaction between layers or by replacing it with an altogether different approach.

7.6 Multichannel formulation and other filter types

In order to overcome the challenge posed by multilayered reservoirs to overburden inversion, it should be possible to extend the present formalism of Wiener filters to that of multichannel systems. In the way it has been developed in this thesis the system is composed of a single input and a single output, that are related by a single channel Wiener filter. However for the analysis of time series and image processing, the formalism exists in literature (Treitel, 1970) for multichannel digital filtering, where a multichannel describes the relation between multiple inputs and outputs. In this way, multiple overburden strains could be simultaneously deconvolved (inverted) to multiple reservoir units. Moreover, although in this research I have focussed on the application of Wiener filters alone, there is no reason why other types of filters could not replace them. For example, the introduction of Kalman filters (Kalman, 1960) would overcome the restriction of time-invariance inherent to Wiener filters.

7.7 Further recommendations: R factor and warping

For a successful integration of geomechanics with all subsurface disciplines, as pursued in this thesis, several challenges remain. There are at least two topics that should be addressed more thoroughly before overburden inversion can be used on a regular basis. The first, is to define the nature and characteristics of the R factor and the second should be to reach a consensus on how time-shifts should be measured as the different techniques available and the effects of different correlation windows has not been fully addressed.

A more detailed modelling in the same lines as that presented in Chapter 6, combining geomechanical modelling and raytracing aimed at matching real observed field data, could indicate whether the R factor is heterogeneous and/or anisotropic. Additionally, having a precise synthetic record on the behaviour of R, could indicate if it can be expressed in terms of known elastic constants or if it is an independent parameter that should be determined separately.

The warping method should be modified to calculate simultaneously not only the warp components, but also the amplitude changes. The calculation of these time-lapse quantities should be done all in phase-space, i.e. while calculating the phase-correlation as explained in Section 4.5. Thus, the resulting warp vector and amplitude changes will be insensitive to white noise. Furthermore, additional tests should be carried out comparing the different available methods to calculate time-shifts and a more thorough analysis in the effects of the different search or correlation windows. This could help establish a consensus on how time-shifts are best measured.

7.8 Future of the method

As the frontiers of oil exploration move towards more complex assets under the shadow of long term high oil prices and growing governmental concern over energy security, oil companies' policies may shift from higher immediate profits to higher ultimate recovery factors and thus, higher long term profits. In this scenario provided the field exhibits overburden time-shifts, the Wiener filter technique could be used on a regular basis. The technique can help in monitoring depletion and flooding, thus providing the necessary information for optimum reservoir management and achieve higher ultimate recovery factors. Similarly, the same can be said for carbon capture projects monitored with 4D seismic, where the method could provide information on the advance of gas saturation fronts and monitor the accumulation of high effective stresses to prevent seal fracture and subsequent CO_2 leakage. To this end, the Wiener filter technique when fully mature, could be incorporated as a part or plug-in of an industry standard geomechanical simulator, such that each time the subsurface model is updated a new set of Wiener filters will be generated without any user interaction other than the model update. This in turn will yield an updated estimate of reservoir strain and effective stress changes for each seismic time-lapse vintage for all reservoir formations. Finally, as the installation of permanent ocean bottom sensors becomes common, it is not hard to imagine the possibility of measuring the Wiener filters directly from the field at a relatively low cost. This will require that an isolated depletion in the reservoir (e.g. from a small reservoir compartment), could be associated to the measured time-lapse time-shifts from whence the Wiener filter can be calculated.

References

Albert, L. (2001). *Houston Wet*. Retrieved 2010, from Rice University: http://www.rice.edu/~lda/wet/bwood/drop/index.htm

Allen, D. & Mayuga, M. (1970). The Mechanics Of Compaction And Rebound, Wilmington Oil Field, Long Beach, California, U.S.A. In I. A. Sciences (Ed.), *Land subsidence: proceedings of the Tokyo Symposium; Studies and reports in hydrology, 8.* Tokyo.

Arfken, G. B., & Weber, H. J. (2001). *Mathematical methods for physicists.* Academic Press.

Aster, R. A., Borchers, B., & Thurber, C. H. (2005). *Parameter Estimation and Inverse Problems.* Elsevier Academic Press.

Audet, D., & Fowler, A. (1992). A mathematical model for compaction in sedimentary basins. *Geophysical Journal International, 110*, 557-590.

Beaumont, E. A., & Foster, N. H. (2001). *Exploring for Oil and Gas Traps* (1st ed.). AAPG.

Boade, R., Chin, L., & Siemers, W. (1989). Forecasting of Ekofisk Reservoir Compaction and Subsidence by Numerical Simulation. *Journal Of Petroleum Technology*, 723-728.

Boeas, M. L. (1983). Mathematical Methods in the Physical Sciences. John Wiley and Sons.

Bouchon, M. (1981). A simple method to calculate green's functions for elastic layered media. *Bulletin of the Seismological Society of America , 71*, 959-971.

Bracewell, R. (1999). *The Fourier Transform and Its Applications* (3rd Edition ed.). New York: McGraw-Hill.

Bruno, M. S. (2002). Geomechanics and Decision Analyses for Mitagation Compaction-Related Casing Damage. *SPE Drilling and Completion, SPE 79519*, 179-188.

Burns, F. E., Burley, S. D., Gawthorpe, R. L., & Pollard, J. E. (2005). Diagenetic signatures of stratal surfaces in the Upper Jurassic Fulmar Formation, Central North Sea, UKCS. *Sedimentology , 52*, 1155-1185.

Carnec, C., & Fabriol, H. (1999). Monitoring and modeling land subsidence at the Cerro Prieto geothermal field, Baja California, Mexico, using SAR interferometry. *Geophysical Research Letters, 26*, 1211-1214.

Chin, L. Y., & Nagel, N. B. (2004). Modeling of Subsidence and Reservoir Compaction under Waterflood Operations. *International Journal of Geomechanics*, 28-34.

Chow, Y. L., Yang, J. J., & Howard, G. E. (1991). Complex Images for Electrostatic Field Computation in Multilayered Media. *IEEE Transactions on Microwave Theory And Techniques, 39*, 1120-1125.

Cipolla, C. L., Hansen, K. K., & Ginty, w. R. (2007). Fracture Treatment Design and Execution in Low-Porosity Chalk Reservoirs. *SPE Production & Operations, 22* (1), *SPE 86485*, 94-106.

Corzo, M. M. (2009). *Pressure estimation using time-lapse seismic in compacting reservoirs.* Edinburgh: PhD Thesis, Heriot-Watt University, Institute of Petroleum Engineering.

Cox, B., & Hatchell, P. (2008). Straightening out lateral shifts in time-lapse seismic. *First Break, 26*, 93-98.

de Gennaro, S., Onaisi, A., Grandi, A., & Neillo, V. (2008). 4D reservoir geomechanics: a case study from the HP/HT reservoirs of the Elgin and Franklin fields. *First Break, 26*, 53-59.

de Gennaro, S., Schutjens, P., Frumau, M., Fuery, M., Ita, J., & Fokker, P. (2010). The Role of Geomechanics in the Development of an HPHT Field. *44th US Rock Mechanics Symposium.* Salt Lake City.

de Gennaro, V., Delage, P., Priol, G., Collin, F., & Cui, Y.-J. (2004). On the collapse behaviour of oil reservoir chalk. *Geotechnique , 54* (6), 415–420.

der Knaap, V., & der Vlis, V. (1967). On the Cause of Subsidence in Oil-producing Areas. *7th World Petroleum Congress Mexico D.F.; Proceedings, 3.* Mexico D.F.

Domes, F. (2010). *The influence of overburden on quantitative time-lapse seismic interpretation.* Edinburgh: PhD Thesis, Heriot-Watt University, Institute of Petroleum Engineering.

Du, J., & Olson, J. E. (2001). A poroelastic reservoir model for predicting subsidence and mapping subsurface pressure fronts. *Journal of Petroleum Science and Engineering, 30*, 181-197.

Dusseault, M. B., Bruno, M. S., & Barrera, J. (2001). Casing Shear: Causes, Cases, Cures. *SPE Drilling & Completion, SPE 72060*, 98-107.

Dusseault, M. B., Yin, S., Rothenburg, L., & Han, H. (2007). Seismic monitoring and geomechanics simulation. *The Leading Edge, v. 26*, 610-620.

Fabricius, I. L., Røgen, B., & Gommesen, L. (2007). How depositional texture and diagenesis control petrophysical and elastic properties of samples from five North Sea chalk fields. *Petroleum Geoscience, 13*, 81-95.

Fares, N., & Li, V. (1988). General image method in a plane-layered elastostatic medium. *Journal of Applied Mechanics, 55*, 781-785.

Fjær, E., Holt, R., Raaen, A., Risnes, R., & Horsrud, P. (2008). *Petroleum related rock mechanics* (2nd Edition). Elsevier Academic Press.

Fokker, P. A., Muntendam-Bos, A. G., & Kroon, I. C. (2007). Inverse Modelling of Surface Subsidence to Better Understand the Earth's Subsurface. *First Break, 25*, 101-105.

Garcia, A., Grandi, A., & McBeth, C. (2010). Time-shift inversion for dynamic reservoir characterization in the Elgin field. *SEG Annual Meeting.* Denver.

Geertsma, J. (1973). A Basic Theory of Subsidence due to Reservoir Compaction: The Homogeneous Case. *Verhandelingen Kon. Ned. Geol. Mijnbouwk. Gen., 28*, 43-62.

Geertsma, J. (1966). Problems of Rock Mechanics in Petroleum Production Engineering. *Proceedings Of The First Congress International Society Of Rock Mechanics,*Lisbon, 585-594.

Gommesen, L., Fabricius, I., Mukerji, T., Mavko, G., & Pedersen, J. (2007). Elastic behaviour of North Sea chalk: A well-log study. *Geophysical Prospecting, 55*, 307-322.

Gonzalez, R. C., & Wintz, P. (1983). *Digital Image Processing.* Addison-Wesley Publishing Company.

Grandi, A., Rahmanov, O., Neillo, V., Soyeur, C., Bourgeois, F., Deplanté, C., et al. (2010). Time lapse monitoring of the Elgin HPHT field. *72nd EAGE Conference & Exhibition incorporating SPE EUROPEC.* Barcelona.

Grandi, A., Wauquier, S., Cumming, H., Deplanté, C., & Hubans, C. (2009). Quantitative 4D time lapse characterisation: three examples. *SEG International Exposition and 79th Annual Meeting*, Houston, 3815-3819.

Greaves, R. J., & Fulp, T. J. (1987). Three-dimensional seismic monitoring of an enhanced oil recovery process. *Geophysics, 52*, 1175-1187.

Greaves, R. J., Fulp, T. J., & Head, P. L. (1983). Three-dimensional seismic monitoring of an enhanced oil recovery project. *SEG Technical Program Expanded Abstracts,* 476-478.

Groombridge, P. (2006). *Data processing report for HESS Limited.* HESS Limited. WesternGeco.

Gubbins, D. (2004). Time Series Analysis and Inverse Theory for Geophysics. Cambridge University Press.

Guilbot, J., & Smith, B. (2002). 4-D constrained depth conversion for reservoir compaction estimation: Application to Ekofisk Field. *The Leading Edge, 21*, 302-308.

Hale, D. (2009). A method for estimating apparent displacement vectors from time-lapse seismic images. *Geophysics, 74* (5), 99-107.

Hale, D., Cox, B., & Hatchell, P. (2008). *Apparent horizontal displacements in time-lapse seismic images.* Center for Wave Phenomena. Colorado School of Mines.

Hall, S. A., MacBeth, C., Barkved, O. I., & Wild, P. (2002). Time-lapse seismic monitoring of compaction and subsidence at Valhall through crossmatching and interpreted warping of 3D streamer and OBC data. *SEG Int'l Exposition and 72nd Annual Meeting.* Salt Lake City, Utah.

Hatchell, P., & Bourne, S. (2005). Rocks under strain: Strain-induced time-lapse time shifts are observed for depleting reservoirs. *The Leading Edge, 24*, 1222-1225.

Hatchell, P., van den Beukel, A., Molenaar, M., Maron, K., Kenter, C., Stammeijer, J., et al. (2003). Whole earth 4D: reservoir monitoring geomechanics. *SEG 2003 Expanded Abstracts*, 1330-1333.

Haugvaldstad, H., Lyngnes, B., Smith, P. J., & Thompson, A. I. (2010). Ekofisk time-lapse seismic - A story if continuous improvement, *72nd EAGE Conference & Exhibition Incorporating SPE EUROPEC.* Barcelona: EAGE.

Herwanger, J. (2007). Linking Geomechanics and Seismics: Stress-Effects on Time-Lapse Seismic Data. *EAGE Distinguished Lecturers Series.* London.

Herwanger, J. (2008). R We There Yet? *70th EAGE Conference & Exhibition.* Rome.

Herwanger, J. V., Schiøtt, C. R., Frederiksen, R., Vejbæk, O. V., Wold, R., Hansen, H. J., et al. (2009). Applying time-lapse seismic methods to reservoir management and field development planning at South Arne, Danish North Sea. *Petroleum Geology: From Mature Basins to New Frontiers – Proceedings of the 7th Petroleum Geology Conferenc*, London, 523-535.

Herwanger, J., Palmer, E., & Schiøtt, C. R. (2007). Field Observations and Modeling Production-Induced Time-Shifts in 4D Seismic Data at South Arne, Danish North Sea. In EAGE (Ed.), *69th EAGE, Conference & Exhibition*, (p. Extended Abstracts IO16). London.

Hodgson, N. (2009). Inversion for reservoir pressure change using overburden strain measurements determined from 4D seismic. Edinburgh: PhD Thesis, Heriot-Watt University, Institute of Petroleum Engineering.

Hodgson, N., Macbeth, C., Duranti, L., Rickett, J., & Nihei, K. (2007). Inverting for reservoir pressure change using time-lapse time strain: Application to Genesis Field, Gulf of Mexico. *The Leading Edge, 26*, 649-652.

Horsrud, P. (2001). Estimating Mechanical Properties of Shale From Empirical Correlations. *SPE Drilling & Completion, SPE 56017, 16*, 68-73.

International Energy Agency. (2005). Resources to Reserves, Oil & Gas Technologies for the Energy Markets of the Future. IEA.

Irikura, K. (1986). Prediction of strong acceleration motions using empirical Green's function. *Proc. 7th Japan Earthquake Engineering Symposium*, Tokyo, 151-156.

Janssen, A. L., Smith, B. A., & Byerley, G. W. (2006). Measuring velocity sensitivity to production-induced strain at the Ekofsk Field using time-lapse time-shifts and compaction logs. *SEG Annual International Meeting*, New Orleans, 200-3203.

Japsen, P. (1998). Regional Velocity-Depth Anomalies, North Sea Chalk: A Record of Overpressure and Neogene Uplift and Erosion. *AAPG Bulletin, 82* (11), 2031-2074.

Japsen, P., Bruun, A., Fabricius, I. L., & Mavko, G. (2005). Identification of hydrocarbons in chalk reservoirs from surface seismic data: South Arne field, North Sea. *Geological Survey of Denmark and Greenland Bulletin, 7*, 13-16.

Japsen, P., Bruun, A., Fabricius, I., Rasmussen, R., Vejbæk, O., Pedersen, J., et al. (2004). Influence of porosity and pore fluid on acoustic properties of chalk: AVO response from oil, South Arne Field, North Sea. *Petroleum Geoscience, 10*, 319-330.

Johnson, J. P., Rhett, D. W., & Siemers, W. T. (1989). Rock Mechanics of the Ekofisk Reservoir in the Evaluation of Subsidence. *Journal of Petroleum Technology*, 717-722.

Kalman, R. E. (1960). A New Approach to Linear Filtering and Prediction Problems. *Transaction of the ASME—Journal of Basic Engineering, 82*, 35-45.

Kennett, B. (1983). *Seismic Wave Propagation in Stratified Media.* Cambridge University Press.

Key, S. C., Pederson, S. H., & Smith, B. A. (1998). Adding value to reservoir management with seismic monitoring technologies. *The Leading Edge*, 515-519.

Kragh, E., & Christie, P. (2002). Seismic repeatability, normalized rms, and predictability. *The Leading Edge, 21*, 640–647.

Kuvshinov, B. N. (2007b). Analytical geomechanical models - insightful, fast, cheap. *Offshore, 67* (4).

Kuvshinov, B. N. (2007a). Reflectivity Method for Geomechanical Equilibria. *Geophys. J. Int., 170*, 567-579.

Kvendseth, S. S. (1988). Giant Discovery A History of Ekofisk Through the First 20 Years. Philips Petroleum Company Norway.

Landrø, M., & Stammeijer, J. (2004). Quantitative estimation of compaction and velocity changes using 4D impedance and traveltime changes. *Geophysics, 69*, 949-957.

Loos, J. M. (1973). In Situ Compaction Measurements in Groningen Observation Wells. *Verhandelingen Kon. Ned. Geol. Mijnbouwk. Gen., 28*, 79-104.

Mackertich, D. S., & Goulding, D. R. (1999). Exploration and appraisal of the South Arne Field, Danish North Sea. In G. Society (Ed.), *Petroleum Geology Conference series*, London, 959-974.

Madland, M., Zangiabadi, B., Korsnes, R., Evje, S., Cathles, L., T.G., K., et al. (2009). *Solving the chalk mystery.* Retrieved 2011, from PHYSORG.com: http://www.physorg.com/news159792763.html

Mavko, B. G., Mukerji, T., & Dvorkin, J. (1998). *The Rock Physics Handbook: Tools for Seismic Analysis in Porous Media.* Cambridge University Press.

Mavko, B. G., Mukerji, T., & Dvorkin, J. (2009). *The Rock Physics Handbook: Tools for Seismic Analysis in Porous Media* (2nd Edition). Cambridge University Press.

Meling, L. M., & Lehne, K. A. (1993). Description and Interpretation of North Sea Fractured Chalk Formations, *SPE Middle East Oil Technical Conference & Exhibition*, Bahrain, *SPE* 25640, 371-381.

Menghini, M. L. (1989). Compaction Monitoring in the Ekofisk Area Chalk Fields. *Journal of Petroleum Technology*, 735-739.

Menke, W. (1984). Geophysical Data Analysis: Discrete Inverse Theory. Academic Press.

Mindlin, R. D., & Cheng, D. H. (1950). Nuclei of Strain in the Semi-Infinite Solid. *Journal of Applied Physics*, 926-930.

Mobach, E., & Gussinklo, H. J. (1994). In-situ Reservoir Compaction Monitoring in the Groningen Field, *Eurock SPE/ISRM Rock Mechanics in Petroleum Engineering, SPE 28094,* 535-547.

Mogi, K. (1958). Relations between the eruptions of various volcanoes and the deformations of the ground surface around them. *Bulletin of the Earthquake Research Institute , 36*, 99-134.

Nagel, N. B. (2001). Compaction and Subsidence Issues Within the Petroleum Industry: From Wilmington to Ekofisk and Beyond. *Phys. Chem. Earth (A), 26*, 3-14.

NPD. (2011). *Norwegian Petroleum Directorate*. Retrieved April 27, 2011, from http://www.npd.no/engelsk/cwi/pbl/en/field/all/43506.htm

Otnes, R. K., & Enochson, L. (1978). *Applied Time Series Analysis* (Vol. 1 Basic Techniques). John Wiley and Sons.

Ottemöller, L., Nielsen, H. H., Atakan, K., Braunmiller, J., & Havskov, J. (2005). The 7 May 2001 induced seismic event in the Ekofisk oil field, North Sea. *Journal of Geophysical Research, 110*, 1-15.

Pan, E. (1997). Static Green's Functions in Multilayered Half Spaces. *Appl. Math. Modelling, 21*, 509-521.

Pierce, R. L. (1970). Reducing land subsidence in the Wilmington oil field by use of saline waters. *Water Resour. Res., 6*, 1505-1514.

Pratt, W. E., & Johnson, D. W. (1926). Local subsidence of the Goose Creek oil field. *Journal of Geology, 34*.

Ramirez, M. O., & Zubillaga, J. (1987). Applications of Well Logging for Compaction and Subsidence Studies in the Orinoco Oil Belt, Venezuela. In SPE (Ed.), *62nd SPE Annual Technical Conference and Exhibition.* Dallas.

Rasmussen, K. B., Bruun, A., & Pedersen, J. (2004). Simultaneous seismic inversion. *EAGE 66th Conference & Exhibition.* Paris.

Rickett, J., Duranti, L., Hudson, T., & Hodgson, N. (2006). Compaction and 4-D time strain at the Genesis Field. *SEG Annual Meeting.* New Orleans.

Risnes, R., & Flaageng, O. (1999). Mechanical Properties of Chalk with Emphasis on Chalk-Fluid Interactions and Micromechanical Aspects. *Oil & Gas Science and Technology – Rev. IFP, 54*, 751-758.

Robinson, E. A., & Treitel, S. (1967). Principles Of Digital Wiener Filtering. *Geophysical Prospecting, 15*, 311 - 332.

Sayers, C. M. (2005). Sensitivity of elastic wave velocities to reservoir stress path. *SEG 2005 Annual Meeting.* Houston.

Sayers, C. M. (2006). Sensitivity of time-lapse seismic to reservoir stress path. *Geophysical Prospecting, 54*, 369–380.

Schiøtt, C. R., Bertrand-Biran, V., Hanse, H. J., Koutsabeloulis, N., & Westeng, K. (2008). Time-lapse inversion and geomechanical modelling of the South Arne field. *First Break, 26*, 85-91.

Segall, P. (1992). Induced stresses due to fluid extraction from axisymmetric reservoirs. *Pure and Applied Geophysics, 139*, 535-560.

Sen, V., & Settari, A. (2005). Coupled geomechanical and flow modeling of compacting reservoirs. *The Leading Edge*, 1284-1286.

Settari, A., & Mourits, F. (1998). A coupled reservoir and geomechanical simulation system. *SPE Journal*, 219-226.

Settari, A., & Walters, D. A. (1999). Advances in Coupled Geomechanical and Reservoir Modeling With Applications to Reservoir Compaction. *SPE Reservoir Simulation Symposium.* Houston, *SPE 74142.*

Shuey, R. T. (1985). A Simplification of the Zoeppritz Equations. *Geophysics, 50* (4), 609-614.

Spencer, A. M., Briskeby, P. I., Christensen, L. D., Foyn, R., Kjølleberg, M., Kvadsheim, E., et al. (2008). Petroleum geoscience in Norden – exploration, production and organization. *Episodes, 31* (1), 115-124.

Staples, R., Ita, J., Burrell, R., & Nash, R. (2007). Monitoring pressure depletion and improving geomechanical models of the Shearwater Field using 4D seismic. *The Leading Edge*, 636-642.

Suiak, R., & Danielsen, J. (1989). Reservoir Aspects of Ekofisk Subsidence. *Journal of Petroleum Technology*, 709-716.

Tarantola, A., & Valette, B. (1982). Generalized nonlinear inverse problems solved using least squares criterion. *Reviews of Geophysics and Space Physics, 20* (2), 219-232.

Taylor, N., Ben-Brahim, L., Tindle, C., Joffroy, G., Hubans, C., & Onaisi, A. (2007). Elgin-Franklin 4D Seismic – Encouraging Results for Reservoir Monitoring & Development Planning. *EAGE 69th Conference & Exhibition.* London.

Tikhonov, A. N., & Arsenin, V. Y. (1977). *Solutions of ill-posed problems.* New York: V. H. Winston and Sons.

TOTAL S.A. (2002). Retrieved from http://total.com/MEDIAS/MEDIAS_INFOS/2155/EN/elgin-franklin-VA.pdf

Treitel, S. (1970). Principles of digital multichannel filtering. *Geophysics, 35*, 785–811.

van Ditzhuijzen, P. J., & de Wool, J. A. (1984). Reservoir Compaction And Surface Subsidence In Tne Central Luconia Gas Bearing Csrbonates, Offshore Sarawak, East Malaysia. *5th Offshore South East Asia.* Singapore.

van Opstal, G. (1973). The Effect of Base-Rock Rigidity on Subsidence Due to Reservoir Compaction. *Proceedings of the Third Congress of the International Society of Rock Mechanics.* National Academy of Sciences, W. D.

Vasco, D. W., & Ferretti, A. (2005). On the use of quasi-static deformation to understand reservoir fluid flow. *Geophysics, 70*, 013-027.

Vasco, D. W., Karasaki, K., & Doughty, C. (2000). Using surface deformation to image reservoir dynamics. *Geophysics, 65*, 132-147.

Velasco, A. A., Ammon, C. J., & Lay, T. (1994). Empirical Green function deconvolution of broadband surface waves; rupture directivity of the 1992 Landers, California (Mw = 7.3), earthquake. *Bulletin of the Seismological Society of America, 84* (3), 735-750.

Wesnæs, K., Hasbo, K., & Ginty, W. R. (2002). Hydraulic Fracture Spacing in Horizontal Chalk Producers: The South Arne Field. *SPE Western Regional/AAPG Pacific Section Joint Meeting.* Anchorage, Alaska: SPE 76722.

Wiener, N. (1964). Extrapolation, interpolation and smoothing of stationary time series. The M.I.T. Press.

Williamson, P., & Cherrett, A. (2007). A New Approach to Warping for Quantitative Time–Lapse Characterisation. *EAGE 69th Conference & Exhibition*, (p. P064). London.

Yerkes, R. F., & Castle, R. O. (1970). Surface Deformation Associated With Oil And Gas Field Operations In The United States. *Land subsidence: proceedings of the Tokyo Symposium; Studies and reports in hydrology, 8.* Tokyo.

Yudovich, A., Chin, L., & Morgan, D. R. (1989). Casing Deformation in Ekofisk. *Journal Of Petroleum Technology*, 729-734.